MINISTRY OF EDUCATION AND SCIENCE
RUSSIAN FEDERATION
Federal State Autonomous Educational Institution of Higher Education
Immanuel Kant Baltic Federal University

On the rights of the manuscript

OMELYANCHIK ALEXANDER SERGEEVICH

MAGNETIC ANISOTROPY OF OXIDE NANOARCHITECTURES

Specialty 1.3.12 (01.04.11) – "Physics of magnetic phenomena"

Dissertation for the degree of
Candidate of Physical and Mathematical Sciences

Supervisor:
candidate of physical and mathematical sciences,
associate professor RODIONOVA V. V.

Co-supervisor:
Ph.D. physical chemistry, professor PEDDIS D.

Kaliningrad
2022

Table of contents

Introduction

The interest in developing magnetic nanoparticles (MNPs) and magnetic nanohybrids (MNHs) consisting of nanosized magnetic materials and studying their magnetic properties increases continuously. Magnetic nanohybrid are materials composed of two or more distinct magnetic phases existing in synergy and coupling. Under the term "magnetic", we understand materials in which at least one of the phases has a long-rage magnetic order, for example, ferro- (FM), ferri- (FiM) or antiferromagnetic (AFM). At the nanoscale, the terms "composite" and "hybrid" are synonyms since the chemical bonds or interactions between two phases are unavoidable. This bonding leads to the achieving new properties of hybrid material which do not present in a simple mechanical mixture of components [1].

In literature, it is more common under the term MNHs to designate materials composed of magnetic transition metal-based oxide or metal component coupled with plasmonic noble metal [2,3], diamagnetic organic [4,5], functional carbon/graphene [6,7] or silica [8] counterpart in form of nanoheterostructures. The main distinctive feature of the listed combination is their multifunctionality. Recently, a lot of attention was devoted to the synthesis of multifunctional MNH combining structural, optical, mechanical, rheological, catalytical properties which do not exist in nature. That is important to meet the requirements of new technologies, such as magnetic recording, ferrofluids, catalysis, biomedicine. The new and perspective directions where MNH find application were forecasted[1]:

a) Spintronics using organic and inorganic magnetic building blocks down to the molecular level;

b) Spin "nano" processing for energy-saving magneto-logic devices and microprocessors based on spin-dynamics;

c) Magnetic storage materials using three-dimensional self-assembled hierarchies;

d) Materials for magnetic refrigeration.

---

[1] https://ec.europa.eu/futurium/en/content/magnetic-nanohybrids-nanomagnets-and-nanomagnetic-devices-energy-conserving-applications

The consciousness and research of MNPs and MNHs, which include a ferromagnetic or ferrimagnetic (F(i)M) component, is one of the most demanded areas in science and technology in the last two decades. The reasons are:

- progress in research methods and methods for the synthesis of nanostructured materials;
- the emergence of new devices and areas of fundamental research where such materials are demanded;
- the modern trend towards miniaturization, which is being addressed by creating multifunctional materials.

In literature it is presented several classifications of nanohybrids (no specified for magnetic) by different factors [9,10]:

- Level of correlation
    - Weak interacting (for example, electrostatic or magnetostatic);
    - Strong interacting (for example, covalent or exchange).
- Morphological characteristic
    - 0-D: core/shell, dumbbell-, Janus-like, encapsulated mesoporous and hollow nanoparticles of different shapes;
    - 1-D: nanowires or nanotubes covered, partially covered, encapsulated or decorated with nanoparticles;
    - 2-D: nanostructured and nanopatterned thin films, multilayer thin films, nanoplates and microdisc;
    - 3-D: bulk matrix filled with 0-, 1- and 2-D nanostructures including hierarchical and self-assembled structures.

More specified classification of MNH can be given as follow:

- Class I: multimagnetic MNHs consisted of two or more F(i)M materials with different kinds of anisotropy (for example, magnetically soft and hard) or antiferromagnetic material;
- Class II: magnetic/non-magnetic MNHs consisted of F(i)M phase covered, coupled with non-magnetic (dia- or paramagnetic) shell or incapsulated in the matrix or layered structures;

- Class III: topological MNH is the class of material where the second phase is surface which could be of the same chemical composition but different magnetic properties;
- Class IV: MNH with special magnetic phenomenon arise on the interface between two magnetic or non-magnetic phases.

Listed above classes of MNHs can coexist, for examples, the core/shell MNPs consisting of magnetically hard and soft materials covered with an organic shell is categorized as a 0-D MNHs of Class I/II. In case F(i)M/AFM thin film with evidenced exchange bias coming from the interface can be categorized into 2-D MNH of Class I/IV.

The first class of MNHs consisted of several magnetic phases is a well-known way to tune the magnetic properties of the material. Indeed, the coupling of magnetically soft and hard phases affects the hysteretic properties of such material. This approach is widely studied for improvement of the energy product $(BH)_{max}$ of exchange-spring magnets for permanent magnets [11]. Magnetic phases with high anisotropy usually have relatively low saturation magnetization and Curie temperature. Coupling a magnetically hard phase with magnetically soft results in hysteresis with higher performance. Theoretically, $(BH)_{max}$ value of the exchange-spring magnet can exceed about three times commercially available permanent magnets and reach 120 MGOe [11].

The second class of MNHs consisted of "magnetic" material embedded or coupled with "non-magnetic" is probably one of the most pronounced classes of MNH because of its native multifunctionality and vivid difference in physical properties of counterparts. Indeed, as we mentioned before in this paragraph, most of the cases of using the term "magnetic nanohybrid" applied to Class II. A remarkable example of the application of Class II MNH is biomedicine [5]. Here, coupling of magnetic phases with non-magnetic carried to combine magnetic properties with functions of biomolecules (drugs, gens, enzymes, etc.), the biocompatibility of silica, gold or polymers; or to add particular optical properties of semiconductor quantum dots. In biomedical applications, magnetism can be applied for magnetic hyperthermia treatment or magnetic resonance imaging (MRI) diagnostics purposes, while the second phase, for example, plasmonic one for additional bioconjugation with different biomolecules and optical sensing [2]. To date several chemical synthetic strategies to synthesize MNHs in form of core/shell, dumbbell-like and nanoflower nanoparticles of different sizes and shapes [12,13].

The Class III of MNHs is material with the strong influence of surface spins. Hybrids of this class can be chemically homogenous but because of the surface spins forming a magnetically anomalous region can be considered a two-phase system. In magnetic nanostructures, the strong influence of surface manifest in reduction of saturation magnetization and increased anisotropy [14,15]. A vivid example of this class of MNHs is a hollow particle because in this case the influence of surface is doubled. Indeed, hollow structures have two surfaces (internal and external). Typical magnetic hysteresis of such particles is characterized by high saturation and closure fields [16].

Class IV is MNHs with the strong influence of interface between two phases on magnetic properties of the whole system with phenomenon arises because of the contribution of interphases spins. In the case of two magnetic phases, a very important phenomenon of the exchange bias (EB) can be observed [17]. In *M-H* hysteretic measurements this phenomenon is displayed by the shift of hysteresis after induction of the preferential orientation of pinned spins on the interface between two phases. An important requirement to observe bias is the significant difference in anisotropy constant between two magnetic phases and more pronounced become in the case of AFM and F(i)M systems. The EB phenomenon was firstly discovered in a system of FM/AFM core/shell nanoparticles by Meiklejohn and Bean [18], who observed a horizontal shift of the hysteresis loop after cooling through the AFM Néel temperature, T_N (in the system with T_N of AFM lower than the FM Curie Temperature, T_C) in the presence of an applied magnetic field. The observation of such phenomenon has been then extended to interfaces between FiM and AFM as well as in FM/FiM [19,20] and AFM/AFM [21,22] systems. The key distinguishing feature of such systems is a family of interface spins with broken symmetry of exchange interaction which becomes pinned at a certain temperature and acts as an anchoring layer. The exchange bias in multilayered MNH of Class IV is the crucial phenomenon lied in the base of devices in spintronics based on magnetoresistance, in particular the giant magnetoresistance [23].

Transition metal oxides (TMO) is very rich in its variation family of materials that wide-spreading in the earth's crust [24,25]. Their rich variety of crystal chemistry turns into a unique plethora of physical properties related main to spin and electronic structures, making TMO both applicable in many technological fields of industry and interesting objects for fundamental research. Properly functionalized MNPs and MNHs consisting of iron oxides are currently being studied intensively for a range of biomedical applications [26–30], particularly for cancer treatment via both targeted hyperthermia and drug delivery, as well as in diagnostics, for example, in MRI for use as contrast agents. An array of MNP materials exist for these applications, with ferrimagnetic iron oxides (magnetite Fe_3O_4 and maghemite γ-Fe_2O_3) being of particular note due to a favorable compromise between biocompatibility and magnetic properties (saturation magnetization) [31–33]. The magnetic properties of iron oxide MNPs can be enhanced by doping with other metal ions, controlling their size and shape. The most significant advances in the use of MNPs appear to be related to the design of multifunctional platforms allowing simultaneous implementation of several diagnostic and therapeutic methods in the theranostic approach [34,35].

The main problem in understanding magnetic properties is the interconnection between the structural properties of oxides in form of nanohybrids and their magnetic properties. This dissertation is devoted to the study of the magnetic properties of nanostructures representing MNPs and nanohybrid TMOs. Several synthesis strategies were employed to obtain MNP systems of different sizes, chemical compositions and architectures (size, shape and order of layers of multiphase structures), and to discover the influence of those factors on magnetic properties. Their magnetic properties were investigated and analyzed.

Aims and objectives

The aim of this dissertation was to study the influence of the composition, morphology, and architecture of different nanostructures of magnetic transition metal oxides, including core/shell and hollow nanoparticles, on their magnetic properties.

In accordance with the goal, the following tasks were set:

1. To investigate the magnetic and structural properties of nanoparticles of cobalt ferrites doped with zinc and nickel produced by the sol-gel autocombustion method;
2. To refine the magnetic structure of a set of cobalt ferrite doped with zinc nanoparticles produced by the hydrothermal method. To develop a model of correlation between magnetic properties (i.e., measurements by SQUID magnetometry) and magnetic structure (i.e., Mössbauer spectroscopy under an intense magnetic field);
3. To study magnetization reversal processes and features arising from the structural and magnetic disorder in small nanocrystals of magnetic iron oxides and cobalt ferrites produced by the coprecipitation and sol-gel autocombustion methods;
4. To experimentally discover the changes in the magnetic properties of nanoparticles of magnetically soft iron oxides and magnetically hard cobalt ferrite in nonmagnetic surrounding in the ultra-small size range (less than 10 nm) with decreasing nanoparticle size and to separate the factors leading to such variations by a phenomenological approach;
5. To analyze the magnetic properties of the core/shell-type nanohybrids consisting of magnetic materials with magnetically soft, hard, or antiferromagnetic properties, as well as hollow nanoparticles. In particular, to investigate the systems with variable core and shell material compositions ($NiFe_2O_4$ и NiO), different thicknesses of the magnetically soft shell.

Statements for defense:

1. The reduction of cobalt in the nanoparticles of cobalt ferrites doped with zinc and nickel prepared by the sol-gel autocombustion method brings a reduction of the coercivity while the saturation magnetization has a non-monotonous character reaching maximum when the molar concentration of dopped elements was around 25%;
2. The interplay between the layer of canted magnetic moments of atoms at particle surface and magnetic structure of the particle core (i.e., inversion degree for spinel ferrite) defines the magnetic properties of nanoparticles, the surface factor dominates in particles below 5 nm especially in magnetically soft materials;
3. The core/shell nanoparticles with a magnetically hard core have a stronger anisotropy compared with an inverted soft/hard system. This is due to the proximity effect, which increases the anisotropy of the magnetically soft material during its epitaxial growth on the magnetically hard material;
4. The magnetically soft shell with a thickness below the unit cell for nickel ferrite increases the coercivity on 20% at low temperatures compared to uncoated cobalt ferrite nanoparticles with dimensions of 8 nm, which is associated with an increase in the degree of canting of the magnetic moments of the atoms at surface;
5. The epitaxial growth of a very thin (below 1 nm) antiferromagnetic layer of nickel monoxide on the cobalt ferrite core increases the coercivity of this system from 1.2 T to 2.0 T. The increase in anisotropy is stronger compared with those caused by the enhanced regime of canted magnetic moments of surface atoms of the same thickness soft shell on cobalt ferrite core of the same size;
6. The core/shell system consisting of ferrimagnetic and antiferromagnetic manganese oxide transforming into a hollow nanoparticle of ferrimagnetic manganese oxide loses the properties specific for exchange bias systems but increases the coercivity from 0.31 T up to 0.65 T due to the increased surface effect.

Personal participation of the applicant in obtaining scientific results

Setting the goal and objectives of the dissertation work, the construction of the plan for experimental research were carried out by A.S. Omelyanchik jointly with the scientific supervisors. Processing, description and analysis of the results of magnetic measurements, data from X-Ray diffractometry and electron microscopy were carried out by the candidate. Synthesis of some samples of MNPs, investigation of their thermal properties by differential scanning colorimetry and thermogravimetric analysis, as well as the study of their magnetic properties by vibrating sample magnetometry were performed directly by the author of the dissertation research at the Immanuel Kant Baltic Federal University (IKBFU). Partial fabrication of samples and attestation of their structural properties by X-Ray diffractometry were performed by the applicant during his fellowship at the University of Genova (Genova, Italy, under the supervision of Prof. Davide Peddis and Prof. Fabio Canepa), at the Chemical Department of Lomonosov Moscow State University (MSU, Russia), under the supervision of Prof. Alexander Majouga, within the work according to the grant of the Russian Foundation for Basic Research (№17-32-50202/18). The investigation of the magnetic properties of the samples by SQUID magnetometry was partially carried out by the author of this dissertation during his stay at the Institute of Materials Structure of the Italian Research Council (Rome, Italy, under the supervision of Prof. Davide Peddis) and at the National Research Center Kurchatov Institute (Moscow, Russia, under the supervision of Prof. Alexander Inyushkin) as part of the grant of the Russian Foundation for Basic Research (№ 16-32-50187/16). The processing, analysis, and description of all the results obtained, as well as the writing of articles, were performed directly by the author of the dissertation.

Reliability of the main results

The validity of the results obtained by the candidate is confirmed by the application of modern technologies and methods of synthesis of materials, the use of modern high-precision scientific equipment for the characterization of their structural, morphological and magnetic properties. The validity was also ensured by a set of complementary experimental techniques and computer modeling of some systems, the reproducibility of the results and the correspondence of the obtained results to the data of other scientific groups available in the literature. The results presented for the defense have been published in indexed journals (Web of Science, Scopus) and have been repeatedly presented at scientific seminars and conferences.

The practical significance of the work

The study of magnetic properties of metal oxide nanostructures made in the form of magnetic nanoparticles, including nanohybrids consisting of several magnetic phases, is an actual topic of basic research. For example, the determination of factors influencing the formation of magnetic anisotropy of complex nanostructures remains a difficult task due to a large number of interrelated factors: surface influence, interaction at the interface, interparticle interactions, the difference between the nanoparticle magnetic crystal structure and massive materials, consisting in particular in the spinel inversion degree. Thus, the magnetic properties of the system will be determined by the choice of chemical compositions, size, size distribution, shape, surface and interface properties, and a set of other factors.

Hence, the magnetic properties of nanostructures (saturation magnetization and anisotropy) are parameters that can be controlled to meet the requirements of various applications, such as biomedical applications or the use of magnetic nanoparticles as fillers for composite materials. The dissertation aims to experimentally investigate the magnetic properties and determine the mechanisms of formation of the relationship between the structural and magnetic properties of oxide nanoarchitectures. To achieve the goal, the dissertation work analyses the magnetic properties of a large number of different nanostructures fabricated by sol-gel autocombustion, coprecipitation and high-temperature decomposition methods, as composite nanostructures, monocrystalline nanoparticles, nanoparticles with core/shell structure, hollow nanoparticles, nanoparticles with different organic shells and particles embedded in inorganic matrices made of iron oxides with spinel structure, cobalt ferrites, doped cobalt ferrites, manganese and nickel oxides. Some of the studied materials were tested for application in biomedicine and their prospects were shown, and also some of the obtained samples of nanoparticles were used for manufacturing polymer magnetoelectric composites.

Approval of the work and publications

The main results of the dissertation were presented at 20 Russian and international conferences in the form of poster and oral reports (abstracts of which were published in the relevant proceedings): Italian School on Magnetism (Milan, Italy, 2016), XIV Kurchatov Youth Scientific School (Moscow, 2016), Moscow International Symposium on Magnetism (Moscow, 2017) International Baltic Conference on Magnetism (Kaliningrad, 2017, 2019, 2021), Phase Transitions, Critical and Nonlinear Phenomena in Condensed Matter Physics Conference (Makhachkala, 2017), Magnetic nanomaterials for biomedicine: synthesis, properties, application (Zvenigorod, 2017), Nanomaterials Applied to Life Sciences (Gijón, Spain, 2017), The 25th International Symposium on Metastable, Amorphous and Nanostructured Materials (Rome, Italy, 2018), 9th Joint European Magnetic Symposia (Mainz, Germany, 2018), IEEE International Conference on “Nanomaterials Applications & Properties” (Zatoka, Ukraine, 2018), 10th International Conference on Fine Particle Magnetism (Gijón, Spain, 2019), 5th International Conference on Nanoscience, Nanotechnology and nanobiotechnology (Brasilia, Brasil, 2019), Conference on Superconductivity and Functional Oxides (Santa Margherita Ligure, Italy, 2019), 2nd International Conference on Nanomaterials Applied to Life Sciences (Madrid, Spain, 2020), 4a Jornada Francisco Tourinho (Brasilia, Brasil, 2021/online), Advances in Magnetics (Moena, Italy, 2021/online), Congresso Nazionale della Società Chimica Italiana (Rome, Italy, 2021/online), International Conference Functional Materials (Alushta, 2021).

The list of the author's publications containing the results presented for the defense is given below.

The results of the dissertation were published in 7 publications indexed in the Web of Science and Scopus databases:

1. Omelianchik A., Singh G., McDonagh B.H., Rodionova V., Fiorani D., Peddis D., Laureti S. From Mn_3O_4/MnO core–shell nanoparticles to hollow MnO: evolution of magnetic properties // Nanotechnology. IOP Publishing, 2018. Vol. 29, № 5. P. 055703. DOI: 10.1088/1361-6528/aa9e59 (IF=3.874; WoS: Q2; Scopus: Q1)
2. Omelyanchik A., Singh G., Volochaev M., Sokolov A., Rodionova V., Peddis D. Tunable magnetic properties of Ni-doped $CoFe_2O_4$ nanoparticles prepared by the sol–gel citrate self-combustion method // J. Magn. Magn. Mater. Elsevier B.V., 2019. Vol. 476, P. 387–391. DOI: 10.1016/j.jmmm.2018.12.064 (IF=2.993; WoS: Q2; Scopus: Q2)
3. Omelyanchik A., Levada K., Pshenichnikov S., Abdolrahim M., Baricic M., Kapitunova A., Galieva A., Sukhikh S., Astakhova L., Antipov S., Fabiano B., Peddis D., Rodionova V. Green Synthesis of Co-Zn Spinel Ferrite Nanoparticles: Magnetic and Intrinsic Antimicrobial Properties // Materials (Basel). 2020. Vol. 13, № 21. P. 5014. DOI: 10.3390/ma13215014 (IF=3.623; WoS: Q1; Scopus: Q2)
4. Omelyanchik A., Salvador M., D’Orazio F., Mameli V., Cannas C., Fiorani D., Musinu A., Rivas M., Rodionova V., Varvaro G., Peddis D. Magnetocrystalline and surface anisotropy in $CoFe_2O_4$ nanoparticles // Nanomaterials. Multidisciplinary Digital Publishing Institute, 2020. Vol. 10, № 7. P. 1–11. DOI: 10.3390/nano10071288 (IF=5.076; WoS: Q1; Scopus: Q1)
5. Omelyanchik A., da Silva F.G., Gomide G., Kozenkov I., Depeyrot J., Aquino R., Campos A.F.C., Fiorani D., Peddis D., Rodionova V., Jovanović S. Effect of citric acid on the morpho-structural and magnetic properties of ultrasmall iron oxide nanoparticles // J. Alloys Compd. 2021. Vol. 883. P. 160779. DOI: 10.1016/j.jallcom.2021.160779 (IF=5.316; WoS: Q1; Scopus: Q1)

6. Omelyanchik A., Villa S., Singh G., Rodionova V., Laureti S., Canepa F., Peddis D. Magnetic Properties of Bi-Magnetic Core/Shell Nanoparticles: The Case of Thin Shells // Magnetochemistry. 2021. Vol. 7, № 11. P. 146. DOI: 10.3390/magnetochemistry7110146 (IF=2.193; WoS: Q3)
7. Omelyanchik A., Villa S., Vasilakaki M., Singh G., Ferretti A.M., Ponti A., Canepa F., Margaris G., Trohidou K.N., Peddis D. Interplay between inter- and intraparticle interactions in bi-magnetic core/shell nanoparticles // Nanoscale Adv. Royal Society of Chemistry, 2021. Vol. 3, № 24. P. 6912–6924. DOI: 10.1039/D1NA00312G (IF=4.553; WoS: Q2; Scopus: Q1)

Structure and scope of the dissertation

The dissertation consists of an introduction, five chapters with the main results and conclusions, a list of references consisting of 276 items. The total volume of the work is 217 pages of text, including 112 figures and 27 tables.

Chapter 1: Introduction to magnetism at the nanoscale

1.1 Magnetism and magnetic interactions

According to the classical theory of electromagnetism, the moving electrical charges generate the magnetic field (H) and they are affected by this field, thus the energy of the magnetic field is the measure of interaction of moving charges [36,37]. The intrinsic movement of the electron, its angular momentum (spin) is one of the main sources of magnetic properties of materials. The magnetic field is a vector field that interacts with a magnetic moment ($\boldsymbol{\mu}$). The magnetostatic interaction energy is

$$E = \mu_0(\boldsymbol{\mu} \cdot \boldsymbol{H}), \tag{1}$$

where μ_0 is the vacuum permeability. Since each magnetic moment is the source of the magnetic field, two magnetic moments placed at the distance r will interact with the energy depending on the mutual orientation of each magnetic moment (Figure 1 a):

$$E_d = \frac{\mu_0}{4\pi}\left[\frac{(\boldsymbol{\mu_i} \cdot \boldsymbol{\mu_j})}{r_{ij}^3} - 3\,\frac{(\boldsymbol{\mu_i} \cdot \boldsymbol{r_{ij}})(\boldsymbol{\mu_j} \cdot \boldsymbol{r_{ij}})}{r_{ij}^5}\right]. \tag{2}$$

This magnetostatic interaction energy is weak concerning two local (atomic) magnetic moments. For two magnetic moments with the magnitude of one Bohr magneton (μ_B) at a distance of 1 Å is ~0.05 meV (~10^{-23} J) which corresponds to the temperature energy of less than 1 K [38]. Thus, this energy is not enough to stabilize magnetic order at temperatures of hundreds of K (typical value of Curie temperature for ferromagnetic materials).

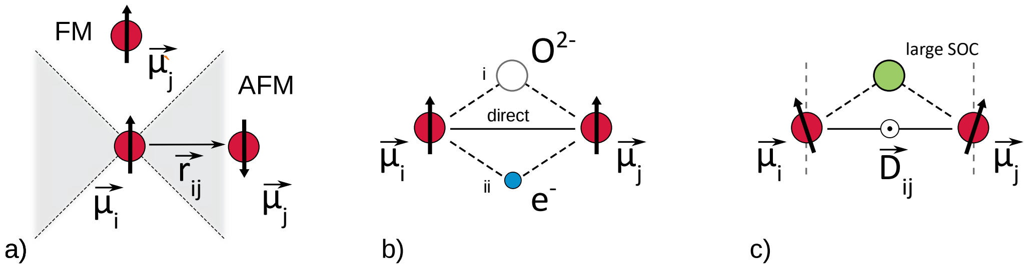

Figure 1. Illustration of a) magnetic dipole interactions; b) exchange interactions mechanisms: direct and indirect through (i) intermediate anions (for example oxygen) or (ii) conducting electrons; c) schematic representation of Dzyaloshinskii–Moriya interaction between two spins involving an atom with the large spin-orbit coupling.

The long-range magnetic order of individual atomic magnetic moments (spins) is provided by quantum-mechanical exchange interactions [39]. These interactions arise due to the overlapping of antisymmetric wave functions of identical particles under the Pauli exclusion principle. In the case of the *direct exchange*, the energy of two interacting spins can be described by the Heisenberg Hamiltonian:

$$\mathcal{H}_{exch.} = -\sum_{i\neq j} J_{ij}\boldsymbol{S_i}\cdot\boldsymbol{S_j} \begin{cases} J > 0 & - \quad \text{ferromagnetic coupling;} \\ J < 0 & - \ \textit{anti}\text{ferromagnetic coupling,} \end{cases} \tag{3}$$

where S is the spin operator and J_{ij} is the exchange integral. In the case of direct exchange interaction, which can occur in ferromagnetic metals (Fe, Co, and Ni), the J is in the range of 10–50 meV [38]. This strong interaction can provide long-range magnetic moment at very high temperatures (Curie temperatures for Fe, Co, and Ni are 1043, 1400, and 627 K, respectively).

Another type of direct exchange interaction is the *antisymmetric Dzyaloshinskii–Moriya* interaction (DMI) [40]. This occurs in non-centrosymmetric lattices or at interfaces [41–43]. This interaction can appear between two atomic spins with a neighboring atom having the large spin-orbit coupling (SOC) [44]. The Hamiltonian of DMI, in this case, can be written as follow:

$$\mathcal{H}_{DM} = -\boldsymbol{D_{ij}}\cdot\left(\boldsymbol{S_i}\times\boldsymbol{S_j}\right), \tag{4}$$

where $\boldsymbol{D_{ij}}$ is Dzyaloshinskii–Moriya vector. This interaction favors the perpendicular spin alignment competing with symmetric exchange interaction (Figure 1). However, the magnitude of $\boldsymbol{D}_{ij}$ is usually much smaller that J_{ij} and the resulting spin canting is the order of 1° [43]. Nevertheless, in some particular nanostructures magnetocrystalline anisotropy, symmetric and antisymmetric exchange interactions are of the same order (for example, of ~0.5 meV in ordered Fe–Pt alloys) [43]. In these situations, DMI induces the formation of chiral spin textures (e.g., skyrmions). In particular, DMI is responsible for weak ferromagnetism of some antiferromagnetic compounds (e.g., α-Fe_2O_3, $BiFeO_3$, Cr_2O_3, …). In nanoparticles magnetism, the essential role of DMI is in the spin canting phenomenon of surface spins [45] and magnetic distortion at crystal defects [46]. Moreover, an inverse DMI is consisting in the charge displacement (ferroelectricity) due to antisymmetric spin-exchange interactions [47]. In other words, this effect is responsible for the interaction of magnetic order and electric polarization in magnetoelectric multiferroics.

Except for the direct exchange, there are several *indirect mechanisms* for establishing the exchange interaction (Figure 1b) [39]. One of the mechanisms of indirect exchange is the *super-exchange interaction* mediated via intermediate anions (for example, O^{2-} in magnetic oxides). The super-exchange at 90° is the *double-exchange* mechanism arising between atoms with the mixed valence (for example, between Fe^{2+} and Fe^{3+} in Fe_3O_4). The interplay of super- and double-exchange interactions determines the long-range magnetic order in the spinel ferrites.

In conducting media, the *Ruderman–Kittel–Kasuya–Yosida* (RKKY) interactions mediated by conductive electrons through the hyperfine interaction are possible [39]. Although the RKKY interaction usually does not present in the most common FM spinel ferrites due to their insulating properties, in metallic systems, such as, FM particles embedded into a metallic matrix, it can play a determining role [48,49].

1.1.2 Magnetic anisotropy

The general expression for Hamiltonian eq.(3) has the isotropic character. In bulk materials, the *magnetocrystalline* anisotropy (K_{mc}) term is usually considered to be dominant. The K_{mc} originates from the spin-lattice coupling. In the total energy of the system, this interaction can be considered as an additional term in the Heisenberg Hamiltonian:

$$\mathcal{H} = -\sum_{i\neq j} J_{ij}(\boldsymbol{S_i}\cdot\boldsymbol{S_j}) - \frac{\lambda}{2}\sum_{i\neq j} S_i^z S_j^z, \tag{5}$$

where λ is the parameter of spin-lattice coupling. Thus, in FM materials, exchange and anisotropy terms balance at the scale of exchange-correlation length [50]:

$$L_0 = \varphi_0\sqrt{A/|K_l|}\,, \tag{6}$$

where $|K_l|$ is the absolute value of the local anisotropy constant, A is the exchange stiffness and φ_0 is the coefficient of proportionality ($\varphi_0 = 1$ in the Herzer's model). L_0 is a critical size below which local magnetic moments are aligned parallel due to exchange interaction. The exchange length L_{ex} results from the normalization of the natural exchange length L_0 by substituting the local magnetocrystalline anisotropy $|K_l|$ with the average anisotropy constant $< K >$. In materials with a structural correlation higher than exchange correlation length $d > L_{ex}$, spins have a non-collinear structure. In particular, the thickness of the Bloch domain wall can be defined as $\delta = \pi\sqrt{A/|K_l|}$. The typical scale of L_0 for ferromagnetic materials is tens or hundreds of nanometers, thus many nanoparticle systems belong to regime $d < L_{ex}$ [50]. In terms of the random anisotropy model (RAM) [50], the average anisotropy constant of exchange-coupled volume is

$$< K >= |K_l|\cdot(d/L_0)^6\,. \tag{7}$$

Considering that in Stoner–Wohlfarth (SW) model $\mu_0 H_C \sim K/M_S$ ($\mu_0 H_C$ is coercive field and M_S is the saturations magnetization) and other material` properties are constants which do not dependent on the particle size, one can show from eq.(7), that $\mu_0 H_C \sim d^6$ in the regime $d < L_0$ H is characterized by coherent behavior of all spins of the correlated volume.

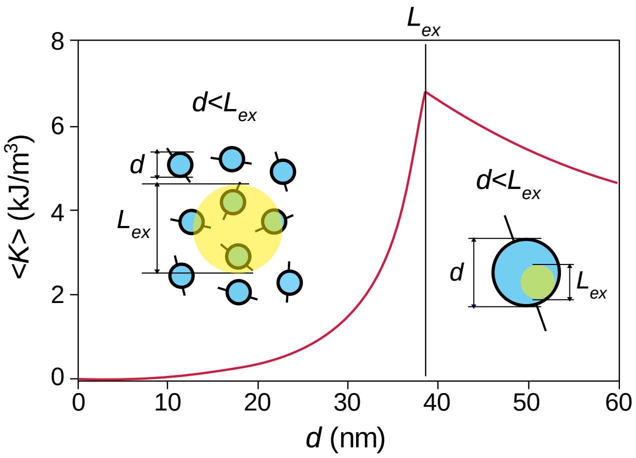

Figure 2. Theoretical grain size dependence of the effective anisotropy <K> for *bcc* $Fe_{80}Si_{20}$ (grains volume fraction 0.73). Reproduced from [51].

The cubic and uniaxial crystal symmetry are more common for magnetic materials and it gives rise to the corresponding magnetic anisotropy symmetry. Examples of materials with cubic magnetocrystalline anisotropy are pure metals (e.g., body-centered cubic (*bcc*) Fe) and spinel ferrites (γ-Fe_2O_3, Fe_3O_4, $CoFe_2O_4$, etc.), while materials with the hexagonal crystal structure such as hexagonal close-packed (*hcp*) Co, $SrFe_{12}O_{19}$ and $BaFe_{12}O_{19}$ hexaferrites have strongly pronounced uniaxial anisotropy.

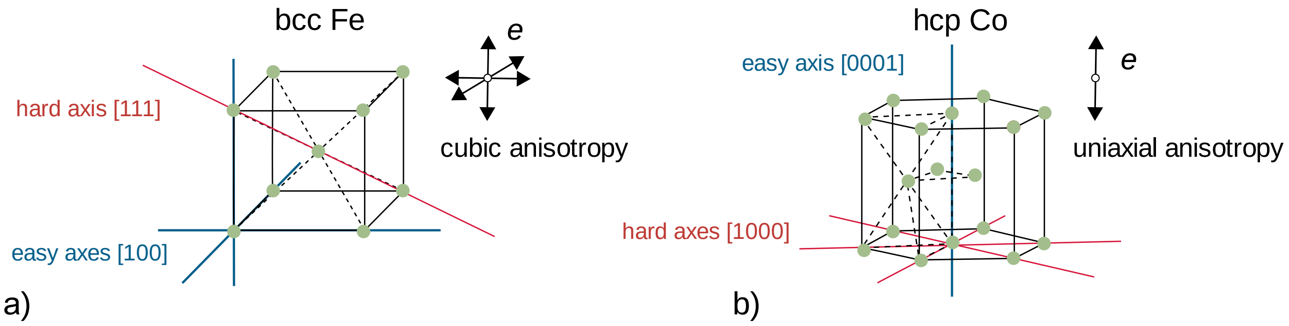

Figure 3. Schematic representation of anisotropy axes (e) in a) cubic and b) uniaxial anisotropy symmetry cases.

Considering the symmetry principle, Akulov showed the energy density of the magnetocrystalline anisotropy can be expressed phenomenologically [52,53]. For crystals with cubic energy anisotropy, it can be written in terms of the cosines of the directions of magnetization α_1, α_2 and α_3 according to three edges of the cube [100], [010] and [001] respectively. The crystal planes {100}, {010} and {001} are symmetry planes where the reflection in the plane leads to the change in the sign of the cosines. Thus, the anisotropy energy must be invariant concerning the replacement $\alpha_i \rightarrow -\alpha_i$. Consequently, the first term, satisfying the requirements of symmetry, in the energy expansion E_a will be the term proportional to the sum ($\alpha_1^2+\alpha_2^2+\alpha_3^2$). But $\alpha_1^2+\alpha_2^2+\alpha_3^2=1$, and the sum of the terms of the series containing α_i^2 will give the constant. The sum of the following non-zero terms of the 4th and 6th orders gives the main contribution to this expansion, and, after appropriate mathematical transformations, it can be demonstrated that

$$E_a^{cubic} = K_1V(\alpha_1^2\alpha_2^2 + \alpha_2^2\alpha_3^2 + \alpha_3^2\alpha_1^2) + K_2V\alpha_1^2\alpha_2^2\alpha_3^2, \tag{8}$$

where $\alpha_1 = \sin\theta\cos\varphi$, $\alpha_2 = \sin\theta\sin\varphi$, $\alpha_3 = \cos\theta$ and θ is the polar and φ is the azimuthal angle.

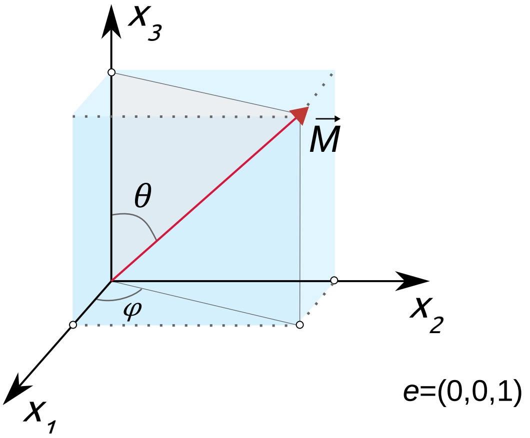

Figure 4. Schematic showing cartesian coordinate axes and corresponding angles to the definition of magnetic anisotropy for magnetization vector (M) in the system with uniaxial anisotropy.

In the case of uniaxial anisotropy, considering only terms of first and second orders, magnetic anisotropy energy can be expressed:

$$E_a^{uniaxial} = K_1V\sin^2(\theta) + K_2V\sin^4(\theta), \tag{9}$$

where K_x are the anisotropy constants, V is the volume of the particle and θ is the angle between the magnetic moment vector and the easy axis of particle anisotropy. In many cases, K_1 term dominates over the higher-order coefficients [54].

Here one can note that it is more common to observe the uniaxial anisotropy in many nanoparticle systems with the cubic magnetocrystalline anisotropy (most common case): the reason is the appearance of additional sources of magnetic anisotropy at the nanoscale. This is more pronounced in magnetically soft materials with a low value of magnetocrystalline anisotropy.

One of the most common and probably significant terms of magnetic anisotropy is the *surface* anisotropy arising from the symmetry breaking resulting in a reduction in coordination of surface spins. The linear trend according to eq.(18) in the dependence of the effective magnetic anisotropy constant versus the particle size was observed for metallic Fe particles [55]. In small ferrite nanoparticles, the change in surface-to-volume ratio is usually accompanied by a change in the properties of the particle core material (e.g., inversion degree), strongly affecting magnetocrystalline magnetic anisotropy making the linear rule eq.(18) more complicated [15].

The non-spherical shape of particles results in an additional increase in anisotropy due to additional magnetostatic energy. According to eq.(2), magnetostatic energy is strongly dependent on distance. One can consider the magnetic poles of single-domain (SD) particles as interacting magnetic moments producing demagnetizing field. Since in a spherical particle all orientations of magnetization are equivalent. However, in non-spherical particles, this phenomenon known as shape anisotropy can play a significant role, especially in elongated particles with, for example, ellipsoidal or rod-like shapes. For an ellipsoidal particle with major axis c and minor axes $a = b$, the magnetostatic energy can be written as [56]:

$$E_{shape} = \frac{1}{2}\mu_0 M_S^2 V (N_a - N_c)\sin^2\theta, \tag{10}$$

where N_a and N_c are demagnetizing factors for minor and major axes respectively, and θ is the angle between magnetization vector and c axis.

We should note that shape anisotropy in real systems is a more complicated phenomenon because of the geometric distortions of small particles and they only very approximately can be considered to be spherical or ellipsoidal. While the more realistic situation is an ensemble of particles with partially faceted and unfaceted surfaces which occurs due to chaotic processes of particle growth [57,58]. One can consider particle shape as an octahedron with additional filled or partially filed facets giving rise to increased uniaxial anisotropy.

1.1.3 Single-domain regime

In 1930 Frenkel and Dorfman predicted that small magnetic particles would transition from multi- (MD) to single-domain (SD) state [59]. This is because the magnetostatic energy becomes comparable with the energy required for the formation of a domain wall. In the case of an FM particle with diameter d, the total energy of the Bloch domain wall through the center of the particle is estimated as

$$E_w = \frac{\pi\gamma d^2}{4}, \tag{11}$$

where γ is the energy of the domain wall per unit area [60].

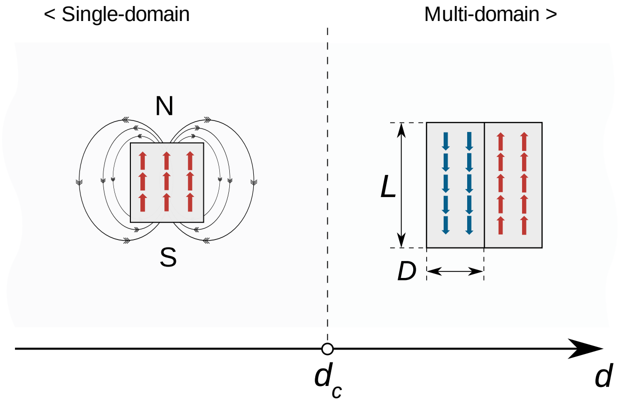

Figure 5. Schematic representation of the change in the magnetic structure of the material in the transition from MD to SD state.

While the magnetostatic energy can be estimated as

$$E_m = -\frac{\mu_0}{2} N_d M_S^2 V, \tag{12}$$

where M_S is the saturation magnetization of the spherical particle with the volume $V = \pi d^3/6$, μ_0 is the vacuum permeability and N_d is demagnetizing factor equal to 1/3 for the sphere. For multi-domain crystals with the slab-like domains and characteristics dimensions D and L ($D < L$) (Figure 5), the magnetostatic energy per unit area of the top surface was found to be $0.85\mu_0 M_S^2 D$ [60].

The total energy of the particle, E, is equal to the sum of the wall and magnetostatic energies (eq. (11) and (12), respectively). Thus, the critical diameter, d_c, at which the spherical particle contains only one domain can be defined as a diameter where this energy becomes zero:

$$d_c = \frac{18\gamma}{\mu_0 M_S^2}. \tag{13}$$

Thus, a particle less than d_c can be regarded as a saturated magnet or a magnetic dipole formed by a superposition of individual spins of the atoms that form this particle.

The total magnetic moment of an SD MNP is called *superspin* because it is formed by a superposition of many coherent spins. The typical value of the magnetic moment of one particle is 10^3–10^5 μ_B (μ_B is the Bohr magneton) [39]. The magnetic reversal mechanism of MNPs in the SD state is described by the Stoner–Wohlfarth (SW) model [61]. MNPs in this regime are characterized by a high value of remanent magnetization (M_R) and coercive field, because a uniformly magnetized particle is in the saturation state, and the magnetic moment can change orientation only by coherent rotation of all spins, which is energetically more expensive than magnetization reversal by non-coherent magnetization (e.g., domain walls motion or curling mode).

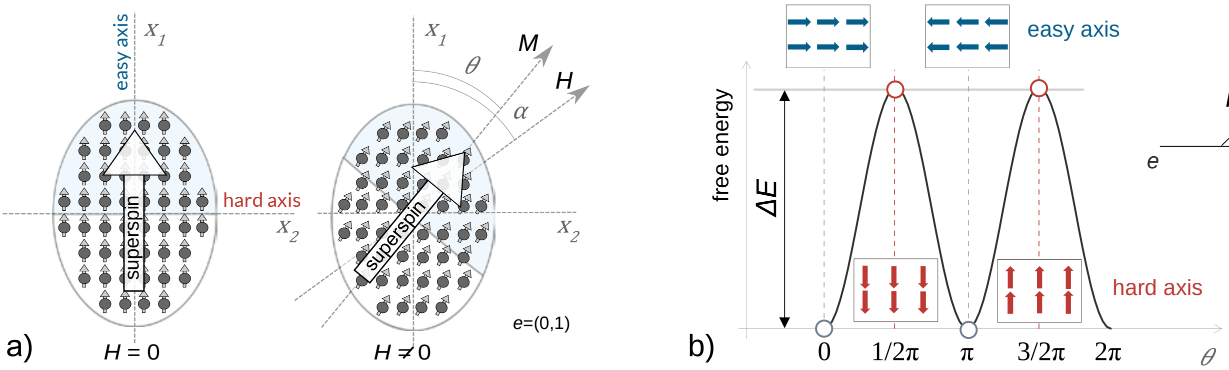

Figure 6. a) Schematic representation of a SW particle in the absence of a magnetic field and in a magnetic field; b) the angular dependence of the free energy on the volume of the SW particle in an external magnetic field.

Then one can express the magnetic anisotropy energy as $E_a = KVsin^2(\theta)$ and, in the presence of the external magnetic field two equivalent superspin positions are separated by an energy barrier (free energy) [62]:

$$\Delta E_a = KVsin^2(\theta) - \mu_0 M_S VHcos(\alpha - \theta), \tag{14}$$

where α is the angle between the axis of easy magnetization and the magnetic field (H). Free energy dependence according to eq.(14) is presented in Figure 6 b). In the absence of a magnetic field, the SW particle has two ground states with a minimum energy corresponding to the direction of the superspin collinear with the easy anisotropy axis. The direction of magnetization along the hard axis has a maximal energy. Thus, the parameter of the magnetic anisotropy describes the directional dependence of the energy of magnetic moment which depends on material properties, which will be described in detail in the further chapter.

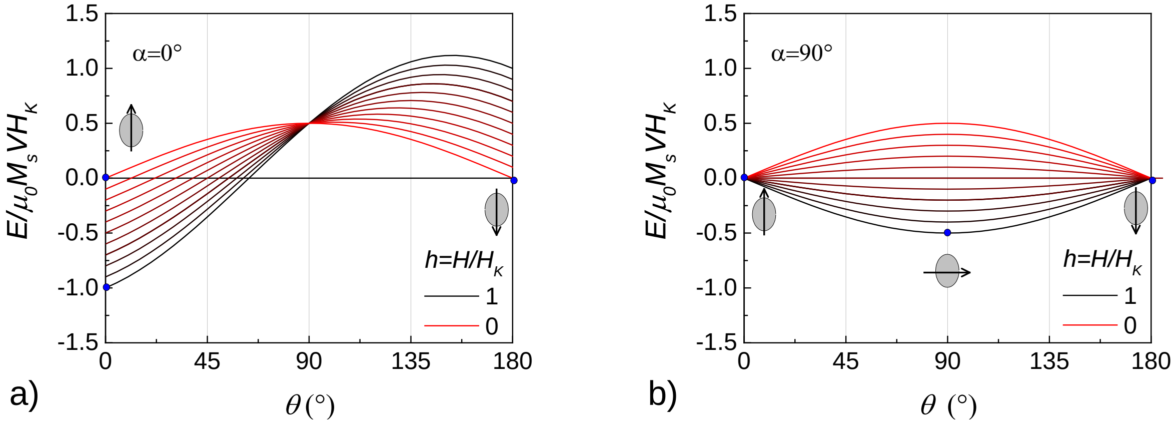

Figure 7. Normalized energy of SW MNP under applied magnetic field a) parallel and b) perpendicular to the easy axis of particle magnetic anisotropy axis.

The magnetization of a system of SW particles at low temperatures exhibits a hysteresis behavior in an external field. This hysteresis has a specific nature, and it was described within the framework of the SW model for uniaxial noninteracting particles. For an ensemble of SD particles with a random arrangement of easy axes, the magnetic hysteresis represents the superposition of all possible hysteresis for a single particle in different orientations considering field direction that can be obtained based on eq.(14) as graphically presented in Figure 6.

The energy of SW particle in the external field can be obtained from eq.(14):

$$\Delta E_a = KV\left(1 \pm \frac{H}{H_K}\right), \tag{15}$$

where $\mu_0 H_K$ is the anisotropy field given by

$$\mu_0 H_K = \frac{2K}{M_s}. \tag{16}$$

The eq.(16) is fundamental in the study of the magnetic properties of SW particles since it connects the main parameters of magnetic hysteresis (saturation magnetization, anisotropy constant, and anisotropy field which is proportional to the coercivity).

The extreme cases are the square hysteresis for the magnetization reversal of a particle along its easy axis, which occurs by the flip-flop reversal of all spins of the system when the value of the external field is equal to the anisotropy field. It was also shown for the case of an ensemble of SW particles that $H_C = 0.479 H_K$ and $M_R/M_S = 0.5$. Later, Néel generalized SW model to the case of particles with cubic anisotropy, then $M_R/M_S \sim 0.8$ and $H_C = \xi H_K$. Effective anisotropy in cubic systems is lower than in uniaxial [57]. Important to note that magnetic interparticle interactions also affect remanence and coefficient ξ.

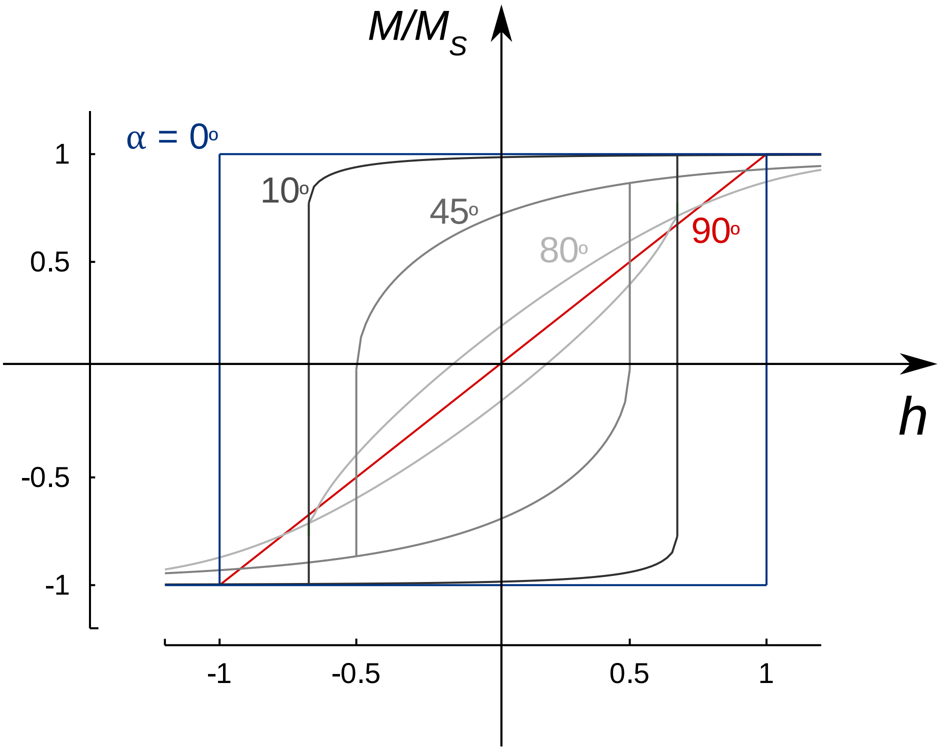

Figure 8. Calculated field dependence of magnetization for SW MNP in the magnetic field applied at different angles to the easy axis of particle magnetic anisotropy.

Table 1. Reduced remanence (M_R/M_S), reduced coercivity ($\xi = H_C/H_K$) and initial susceptibility ($\chi_i = (dm/dh)_{h\to 0}$) for the ensemble of randomly oriented noninteracting SD MNPs.

Anisotropy symmetry		M_R/M_S	$\xi = H_C/H_K$	χ_i
Uniaxial		0.5	0.479	0.667
Cubic	$K_1 > 0$	0.831	$0.320 < \xi < 0.335$	0.667
	$K_1 < 0$	0.866	$0.180 < \xi < 0.200$	1

Adapted from ref.[63] and references therein.

Kodama et al. suggested an approximation for $NiFe_2O_4$ MNPs, where the anisotropy field was estimated by the closure field of hysteresis $\mu_0 H_K \approx \mu_0 H_{irr}$ [64]. The close field $\mu_0 H_{irr}$ can be defined as a field at which the difference between the reduced magnetization of upper and lower branches of hysteresis reaches a certain value usually 1 or 3% depending on the quality of data.

Assuming that $\mu_0 H_C$ is mainly due to the switching of particle core while $\mu_0 H_{irr}$ is mainly attributed to the reversal of highly anisotropic surface spins, two values of anisotropy constant can be obtained from eq.(16):

$$K_{core} = \frac{\mu_0 H_C M_s}{2 \times 0.48}; \quad K_{eff} = \frac{\mu_0 H_{irr} M_s}{2}. \tag{17}$$

The difference between values of anisotropy constants in eq.(17) indicates an additional contribution, that at first approximation can be referred to as the surface [65]. One can also assume that the main contribution of the anisotropy of the core is the bulk magnetocrystalline anisotropy than $K_{core} \approx K_{bulk}$ [66]. With these considerations, the K_S for spherical MNPs can be expressed as follows [55]:

$$K_S = \frac{d\left(K_{eff} - K_{bulk}\right)}{6}. \tag{18}$$

The approximation $K_{core} \approx K_{bulk}$ is valid only in limited cases. Indeed, the K_{core} can be affected in nanoparticular systems due to other factors such as for example interparticle interactions, crystal defects, spin canting and cation distribution [15].

1.1.4 Interface effects

Intergranular exchange coupling in two-phase magnetic systems consisting of materials with magnetically soft and hard properties leads to significant variation in the magnetic properties of the entire system [67]. Depending on the magnetic properties of each phase, quality of interphase and structural properties of composite, hard-soft exchange-coupled nanocomposites can be classified as weak and rigidly coupled (Figure 9). For an ideal nanocomposite of extremely soft and hard phases, switching from (i) weak to (ii) rigid coupling happens when the critical scale of the soft phase (l^S) becomes lower then roughly twice of the thickness of domain wall in the hard phase $l^S < 2\delta^H$ (proportional to exchange correlation length L_0 in eq.(6)) [11]. In this regime also known as “exchange spring magnet”, spins of magnetic phase align collinearly with the spins of the hard phase, thus the entire anisotropy of these systems is higher than that of a system of non-interacting grains. Since many magnetically hard materials possess relatively low M_S, exchange spring magnets advance in reaching high energy product $(BH)_{max}$, a parameter important for permanent magnets [11,67]. Considering fractions $f^H$and f^S of soft and hard phases respectively (mass, volume or thickness of layer can be chosen depending on normalization of K and M_S), nucleation field can be written as follow [67]:

$$\mu_0 H_N \approx \frac{2(f^S K^S + f^H K^H)}{(f^S M_S^S + f^H M_S^H)}. \tag{19}$$

For systems with the thicker soft phase $l^S > 2\delta^H$, the reversal of the soft phase occurs much before the reversal of the hard one. The nucleation field of the soft phase in the weakly coupled systems given by

$$\mu_0 H_N^S \approx \frac{\pi^2 A_S}{M_S (l^S)^2}, \tag{20}$$

where l^S is the thickness of the soft phase [11].

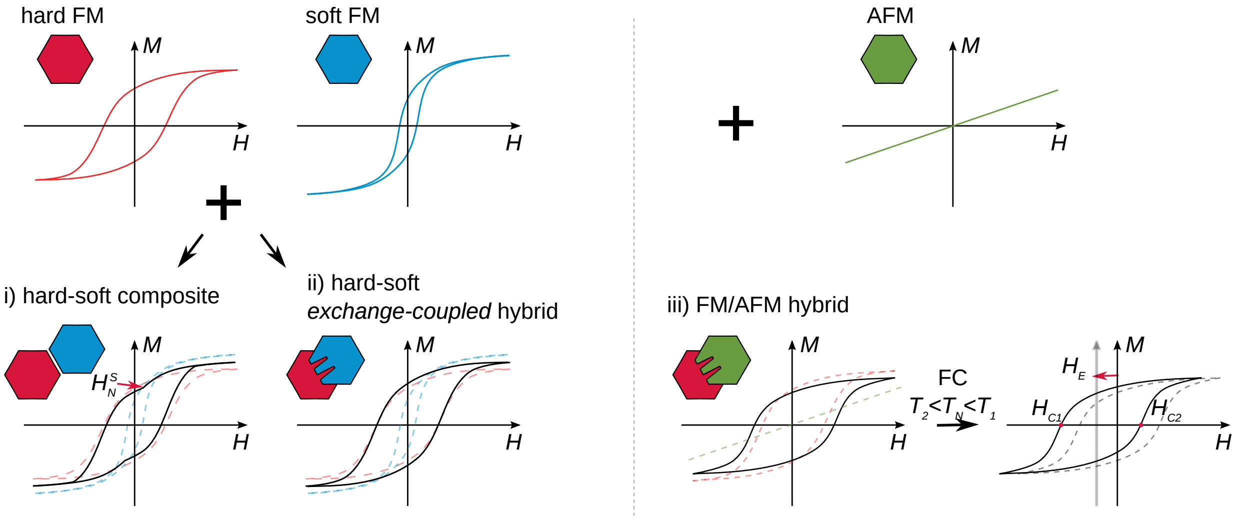

Figure 9. Scheme of the magnetic behavior of hard-soft nanocomposites with i) weak interphase coupling and ii) rigid exchange coupling, and an extremal case of the exchange-coupled composite of soft or hard FM with AFM.

In nanoparticle magnetism, particular attention is devoted to the bi-magnetic core/shell systems [68]. Bi-magnetic exchange-coupled systems possess some unique properties. Among these, there is an "exchange bias" phenomenon concluded in the horizontal bias of the *M-H* hysteresis cycle [17]. Firstly this phenomenon was observed in Co(FM)/CoO(AFM) nanoparticles after field cooling (FC) of the system from temperature T_1 above Néel (T_N) down to a low temperature T_2, where $T_C > T_N$ [18] (Figure 9). Phenomenologically it was explained due to the orientation of interface AFM spins above T_N collinearly with the spins of the FM phase via exchange interaction. These pinned AFM spins possess a high anisotropy due to exchange coupling with the AMF phase when it is ordered and they act as anchors promoting a certain orientation of the magnetization of the FM phase. The exchange bias field ($\mu_0 H_E$) is given by

$$H_E = \frac{|H_{C1} + H_{C2}|}{2}, \tag{21}$$

where H_{C1} and H_{C2} are coercivity field for left and right branches of the hysteresis cycle.

Notwithstanding this phenomenon was mainly considered to be a fingerprint of the AFM/FM systems, generally speaking, it can be observed in bi-magnetic soft-hard systems under specific conditions, for example in field range below switching field of hard phase after its magnetization. The exchange bias phenomena were discovered in many systems, including core/shell nanoparticles, layered thin films, etc. Exchange bias and related phenomena are fundamentally important for magnetoresistive devices [17]. Moreover, the exchange coupling of FM material with highly anisotropic AFM can increase its anisotropy to stabilize the small domain against thermal fluctuation in magnetic recording media [69].

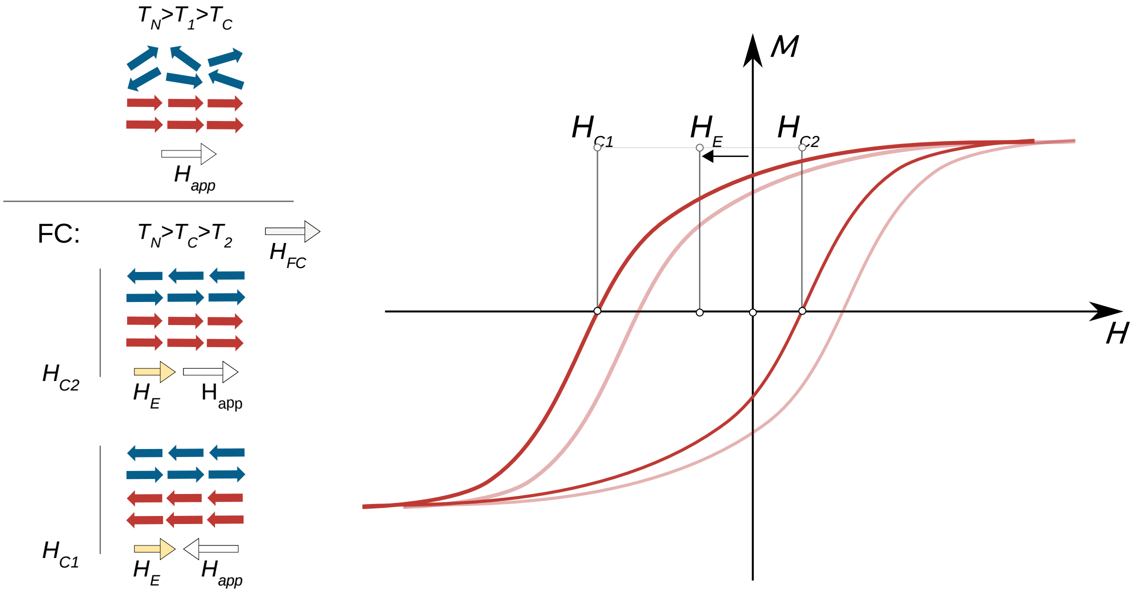

Figure 10. Schematic illustration of exchange bias phenomenon occurring after field cooling (FC) of the sample consisting of AFM and FM phases.

1.1.5 Non-collinear magnetism in nanoparticles

Non-collinear behavior of magnetization in MNPs occurs due to different reasons. E.I. Kondorsky (1952) drew attention to the fact that SD states are possible, in which the spins of the system are in incoherent states (pseudo-single-domain state), forming magnetic vortices or similar structures. Particles with sizes in which, for any values and directions, the magnetization remains homogeneous throughout the sample volume are *true* single-domain [62].

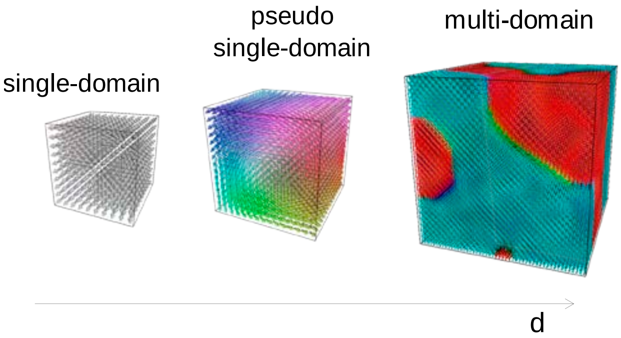

Figure 11. Evolution of the micromagnetic structure of cubical shape magnetic particle with the increase of the size. Micromagnetic simulation made via Spirit software. Colors correspond to the orientation of the magnetic moment.

In SD MNPs also possible non-collinear magnetization phenomena:

1. The frustration of surface spin due to lack of structural symmetry;
2. DMI-induced canting due to intraparticle interactions;
3. Defect-induced canting associated with DMI.

The listed-above mechanisms lead, in particular, to the spin canting – deviation of magnetization vector event at the high field from the direction of the field [70]. This canting leads to the reduction of the net particle magnetic moment and within a single particle, the angle of canting can be expressed as follows

$$\theta_{cant} \equiv \tan^{-1}\left(\frac{M_{perp}}{M_{par}}\right). \tag{22}$$

Interesting to note, that while in a single particle, the perpendicular component of magnetization was explained by the appearance of DMI interaction, in an assembly of interacting MNPs the correlation of perpendicular components of magnetization was observed and explained due to magnetic dipolar interparticle interactions [71].

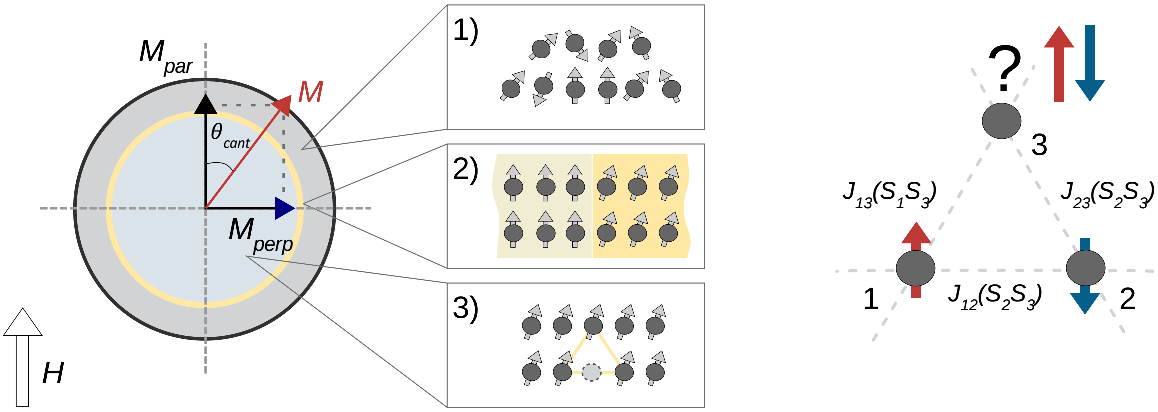

a) b)

Figure 12. a) Illustration of non-collinear spin structures which can arise in SD MNP via surface structural disorder (1), intraparticle interactions (2), and microstructural defects (3); b) Schematical representation of geometrical frustration of 3-spin structure.

At temperatures, lower than the glassy temperature (T_g), the magnetic structure of surface spins can be explained in an example of geometrical frustration in an AFM-coupled equilateral triangle of Ising spins. This configuration is possible on the surface due to the lack of symmetry and broken exchange interaction bonds of surface spins. The two-spin system of spin 1 "*up*" and spin 2 "*down*" is in minimum energy satisfying exchange interaction with exchange integral J_{12}. However, the third spin introduced into this system can not simultaneously satisfy the AFM interactions with both spins 1 and 2. The spin 3 has two energetically equivalent states separated by activation energy (ΔE_a). Thus, this system is frustrated and this frustration leads to a variety of cooperative spin states such as spin-glass or spin-ice. Spins in glassy states possess unique magnetic properties reveling in slow dynamics and high anisotropy.

In nanomagnetic systems, a magnetically disordered surface can be considered as an individual phase because the magnetic properties of surface material are different concerning the core. The thin surface layer (t_s) of iron oxide-based MNPs above T_g can be considered "magnetically dead" since it does not contribute to the net magnetic moment of the particle system [14,72,73]. Considering spherical or cubic particles having magnetically ordered core with diameter d_c and uniform magnetically frustrated shell with the constant thickness, M_S can be written as follows [74]:

$$M_S = M_S^{bulk}\left[1 - \frac{(d-2t_S)^3}{d^3}\right] \approx M_S^{bulk}\left[1 - \frac{6t_S}{d}\right]. \tag{23}$$

Significant reduction in magnetization takes place in very small particles where the volume of the disordered surface became comparable with the volume of a magnetic core with diameter. We should note that the “magnetically dead layer” is the model which not consider possible canting which occurs also in the particle core and possible crystal defects in the particle core [75,76].

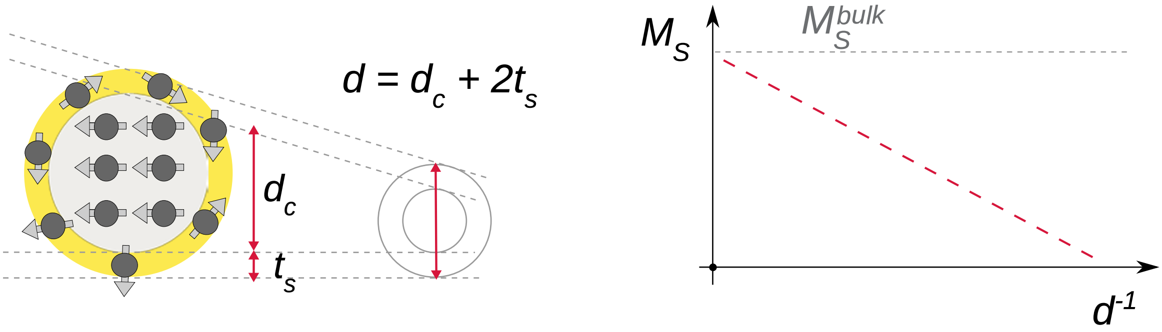

Figure 13. Phenomenological “magnetic dead layer” model.

The temperature dependence of saturation magnetization for cobalt ferrite MNPs is shown in Figure 14 a) [14]. The saturation magnetization decreases with decreasing average particle size. The decrease of magnetization with increasing temperature can be described by the general power law

$$M_S(T) = M_S^0(1 - BT^{\alpha}), \tag{24}$$

where α is Bloch exponent and B is Bloch constant. Both parameters depend on the particle size. For example, in bulk FM the Bloch exponent α is 3/2 which leads to the known Bloch low $M(T) \sim T^{3/2}$ for the temperature dependence of magnetization in the low-temperature range. For some oxides, for instance, for cobalt ferrite $\alpha = 2$ [77], however in many MNP systems, this value varies in a wide range. In ref. [14] α increased from 0.5 to 2.5 when particle size increased from ~4 to 11 nm. Also, the Bloch constant B decreases as the particle size increases. This divergence in the nanoparticle system concerning the bulk analogs was attributed to the different spin-wave structures of the nanoparticle core.

In the smallest nanoparticles at low temperatures, a sharp increase in magnetization can be observed (region <25 K in Figure 14 a)). At these temperatures, the frustrating surface spins become frozen and act in a spin-glass-like regime [14,78]. This is also accompanied by a sharp increase in magnetic anisotropy (Figure 14 b).

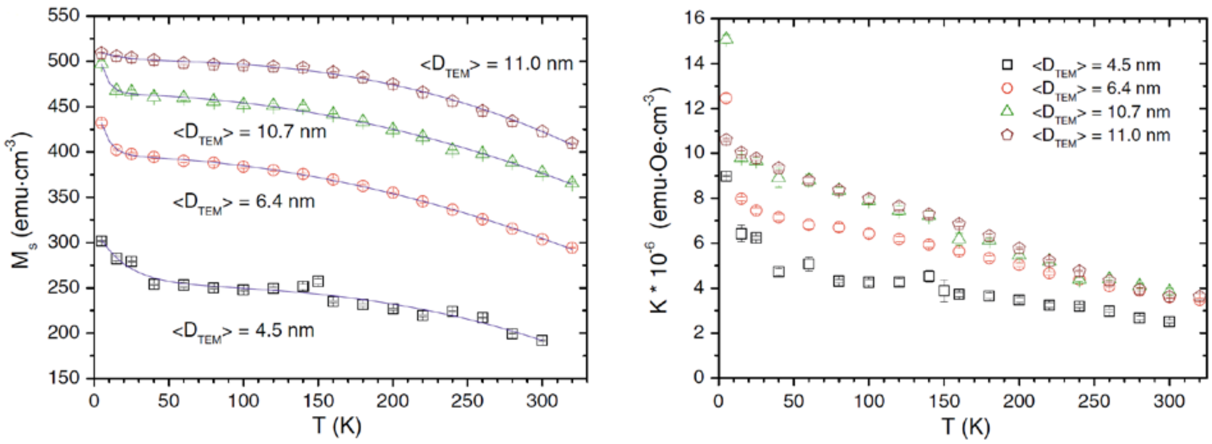

a) b)

Figure 14. a) Temperature dependence of saturation magnetization and b) magnetic anisotropy constant of cobalt ferrite nanoparticles. Reprinted from [14].

Thus, at low temperatures magnetically disordered layer transits from a “magnetically dead” (paramagnetic) state to a magnetically frustrated, spin-glass-like state characterized by the strong spin canting level and high anisotropy. The temperature dependence of the magnetic “dead layer” in cobalt ferrite MNPs from ref. [14] is shown in Figure 15 a). Interesting to note, that the level of disorder is also a function of the external magnetic field. Here we should highlight, that the difference in the meaning of structural disorder with the magnetic disorder, which, however, are correlating. While the size of the structurally disordered layer can be found from the difference of particle and crystalline sizes found from TEM and XRD analysis, the magnetic size is defined as the volume of material where spins are collinear and reverse via the coherent mode (for ferri- or ferromagnetic material in SD state). Recently, employing magnetic small-angle neutron scattering it was discovered, that an external magnetic field increases the magnetic volume of MNPs (Figure 15 b)). Thus, the magnetic moment of MNPs is increasing under the applied magnetic field due to the ordering action of this field. Magnetic alignment of structurally disordered surface spins in 14 nm cobalt ferrite MNPs, the magnetic field of about 1 T results in the increased magnetic volume, making it 20% larger than the structurally coherent core [79].

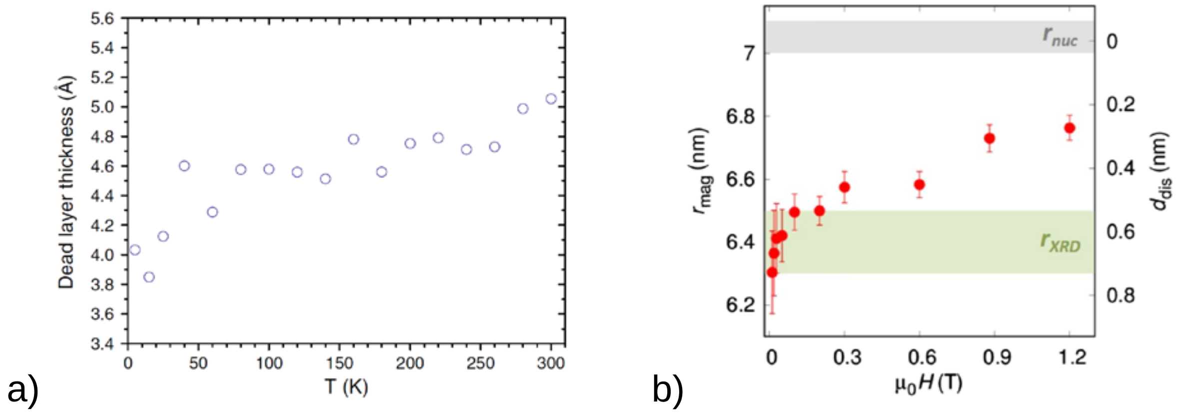

Figure 15. a) Temperature dependence of dead layer thickness (reprinted from [14]) and b) field dependence of disordered surface (d_{dis}) of cobalt ferrite MNPs (reprinted from [79]). r_{mag} is the radius corresponding to the magnetic, r_{XRD} – crystallite and r_{nuc} – total particle size.

It was observed that exchange-coupled FM/spin-glass systems can reveal a significant exchange bias field [80]. Interestingly, the glass-like frozen surface spins may act as a magnetically hard phase increasing anisotropy and leading to the intrinsic exchange bias effect in chemically single-phase systems [81,82]. In magnetically hard materials, DMI possibly stabilized spin canting is suppressed by singe-ion SOC and it is more significant in magnetically soft materials. For example, it was demonstrated that the spin canting angle in $CoFe_2O_4$ MNPs was 17° while it was 40° in softer Fe_3O_4 MNPs forming a core/shell-like structure [83].

The spin canting occurs not only in the surface spins but in the particle core as well. Moreover, canting of surface spins may induce the canting of the spins of particle core. The intraparticle effects can induce spin canting via the DMI, as was shown on ~7.4 nm core/shell $Fe_3O_4/Mn_xFe_{3-x}O_4$ MNPs with a 0.5 nm Mn-ferrite shell [71]. It was demonstrated that strong DMI can lead to frustration of the shell spins causing the canting of the net particle moment. The higher affinity of softer material to be canted can be used to modulate the magnetic structure of the core/shell nanoparticles. In this way, a thin layer of magnetically soft material deposited on the magnetically hard core can increase the magnetic anisotropy of the whole system [84]. This enhanced spin-canting phenomenon can be observed in the core/shell MNPs with the typical thickens of the soft shell thickness less than the size of the unit cell [84].

1.1.6 Superparamagnetism

Superparamagnetism (SPM) is a type of magnetic behavior that occurs in an ensemble of SD MNPs of small size. At relatively high temperatures, when the thermal energy is large concerning the magnetic anisotropy energy ($k_BT > KV$), the magnetization vector of a single particle can flip freely between two easy directions and therefore, its time average in the absence of an external magnetic field is zero. In such conditions, the assembly of MNPs behaves like a paramagnetic system with zero coercivity and remanence.

If MNPs can move, for example, if they are dispersed in fluid, Néel and Brownian relaxations of magnetic moment occur [85–87]. The Brownian relaxation describes the rotation of the MNPs in a fluid as a function of an AC magnetic field. The time required by the MNPs to change from the free rotation with the field to the blocked state is called Brownian relaxation time τ_B and is given by:

$$\tau_B = \frac{3\eta V_{hyd}}{k_BT}, \tag{25}$$

where k_B is the Boltzmann constant, T is the temperature, η is the viscosity of the carrier liquid, and V_{hyd} is the hydrodynamic volume of the particle. Néel relaxation, on the other hand, describes the rotation of the magnetization vector of the MNP toward the external AC magnetic field independent of surrounding molecules. The relaxation time is called Néel relaxation time τ_N, given by:

$$\tau_N = \tau_0 \exp\left(\frac{\Delta E_a}{k_BT}\right), \tag{26}$$

where ΔE_a is the activation energy, which is equal to the anisotropy energy KV of SD MNP and τ_0 is the relaxation time for a single relaxing unit. If both relaxation mechanisms are possible, the effective relaxation time is

$$\tau_{eff} = \frac{\tau_B \tau_N}{\tau_B + \tau_N}. \tag{27}$$

From the above equations, one can note that Brownian relaxation time varies with the hydrodynamic volume of the MNPs and with the fluid viscosity coefficient, e.g. in a gel, the particles are not able to easily rotate. On the contrary, Néel's relaxation time depends on the real volume of the nanoparticle (*V*) and the magnetic anisotropy energy constant (*K*).

The Néel–Arrhenius model considering thermally activated switching between different states is valid only for non-interacting magnetic particles [87]. To consider the effect of weak interparticle magnetic interactions, this expression can be written in the shape of Vogel–Fulcher (VF) model:

$$\tau_{VF} = \tau_0 \exp\left(\frac{\Delta E_a}{k_B[T`_B - T_0]}\right), \tag{28}$$

where T_0 is a measure of interparticle interactions and $T`_B$ is peak temperature equal to the blocking temperature of non-interacting particles.

Figure 16 a) shows the temperature dependence of the real part of magnetic susceptibility measured at different frequencies on 4.5 nm cobalt ferrite MNPs [14]. The peak value of $T`_{max}$ is often concidered to be the first approximation of the blocking temperatyure $T`_B$. Thus, the shift of $T`_{max}$ at different frequencies illustrate measuring-time dependence of the blocking temperature. Linear dependence $T`_{max} \times \ln(\tau/\tau_0)$ versus $\ln(\tau/\tau_0)$ is according to the VF model. Linear fit to the eq.(28) allows determine magnetic anisotropy constant and T_0.

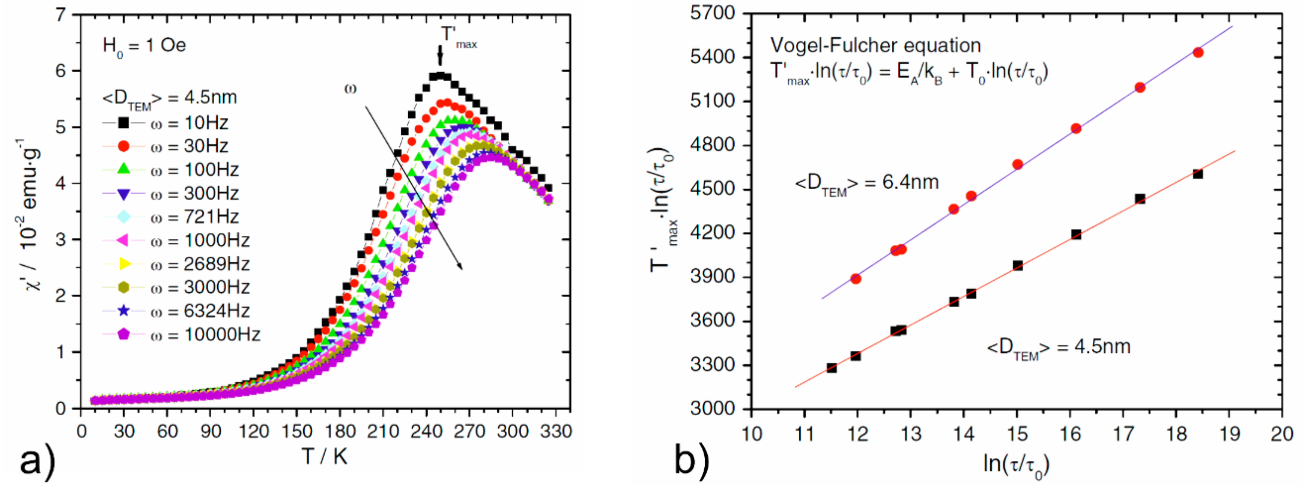

Figure 16. a) Temperature dependence of the real component of magnetic susceptibility and b) measuring time dependence of peak position of the real art of magnetic susceptibility fit with the Vogel–Fulcher equation. Reprinted from [14].

Given a specific particle size and for a particular experimental measuring time (τ_m), the temperature at which this transition occurs is defined as the blocking temperature (T_B) and corresponds to the condition $\tau_{B(N)} = \tau_m$. Thus, $\tau < \tau_m$ means that the relaxation during the experiment happens so quickly that only a time average of the magnetization is observed: the value of the coercivity and the remanent magnetization will tend to zero. Conversely, if $\tau > \tau_m$, the relaxation during the experiment is very slow and only static properties are observed, therefore, a completed hysteresis loop typical for any F(i)M material can be observed with non-zero values of $\mu_0 H_C$ and M_R. When the relaxation time and the measuring time become comparable and Néel relaxations dominate, the systems became "blocked" and the specific temperature for this state is called blocking temperature T_B. Using eq.(26), the T_B can be defined as:

$$T_B = \frac{KV}{k_B\, Ln\left({}^{\tau_m}/_{\tau}\right)}. \tag{29}$$

According to this definition, at T_B in the system, the half of particles (50%) are in the blocked regime and another half (50%) are in the SPM regime [54,88,89]. It should be noted that the time required to make a measurement is dependent on the equipment used: so, T_B for the same system of MNPs could be different depending on the technique used. Moreover, the definition of "superparamagnetic particles" according to eq.(29) has sense only with the defined time and temperature of the measurement, by default those conditions are room temperature (300 K) and characteristic time of DC-magnetometry (10^2–10^3 s).

Above T_B, an assembly of MNPs acts as paramagnet with zero values of remanence and coercivity [62]; the M-H behavior can be described by the Langevin function, i.e. the behavior of a system of classical paramagnetic moments, with the difference being that instead of individual magnetic moments of atoms, in case of a SPM system, we deal with giant magnetic moments (the magnetic moment of a single particle is also called a superspin). The general shape of the Langevin function for magnetization is [54,76,90]:

$$M = M_S^{`} \left(coth\mathcal{L} - \frac{1}{\mathcal{L}} \right), \tag{30}$$

where $\mathcal{L}$ is the Langevin parameter (the ratio of magnetic to thermal energy) equal to $\mu_0\mu H/k_BT$. For spherical particles, the magnetic moment of a single particle is $M_S` \times \pi d_m^3/6$, where $M_S`$ is saturation magnetization of bulk material (per unit volume) and d_m is the “magnetic diameter” of the particle.

The reduced magnetization M/M_S is a universal curve plotted in Langevin coordinates H/T [54]. That means, that the $M(H/T)$ curves, measured at different temperatures for an assembly non-interacting MNPs, will merge. Figure 17 shows the typical Langevin magnetization curve for an assembly of non-interacting MNPs which satisfy the classical scaling law of SPM [91]. The inset of this figure shows the case when the scaling law is not performed for the assembly of the same particles if they are not isolated and interact by the dipolar mechanism.

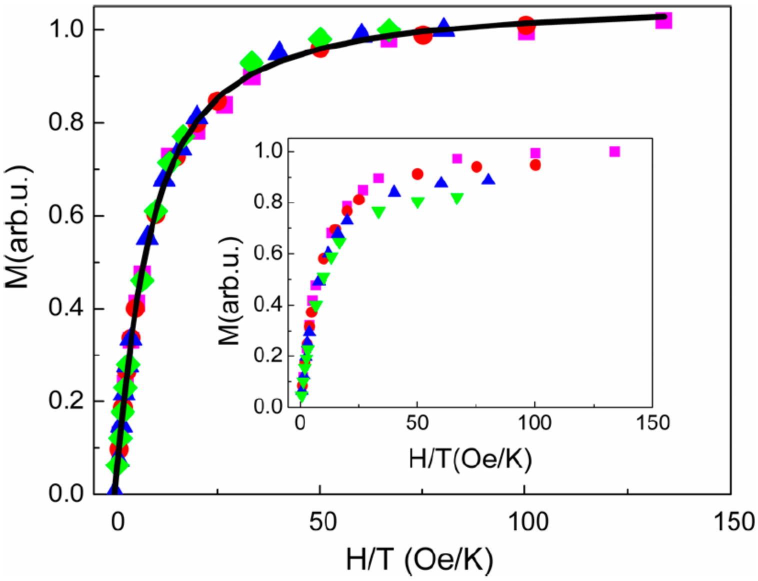

Figure 17. Field dependence of magnetization for ~5 nm iron oxide MNPs coated with SiO_2 plotted in Langevin coordinates. Symbols indicate experimental data at 150 K (square), 200 K (circles), 250 K (triangles), and 300 K (diamonds). The black line is the fit with the Langevin formula considering log-normal size distribution. Inset: the same MNPs without SiO_2 coating. Reproduced from [91].

Magnetization of small particles at finite fields will progressively reduce with the reduction of particle size due to thermal fluctuations. Figure 18 shows the magnetization normalized to saturation at fields in the range from 0.1 to 4 T. Bellow 10 nm even at the relatively high field this reduction becomes significant. Thus, the shape of non-interacting MNPs reflect is sensitive to the particle size. In particular, we will show below that the initial susceptibility $\chi_i = dM/dH\,(H \rightarrow 0)$ is proportional to the particle magnetic volume. However, to define the parameters of particle magnetic size from magnetic measurements in real systems, one shall consider the particle size distribution.

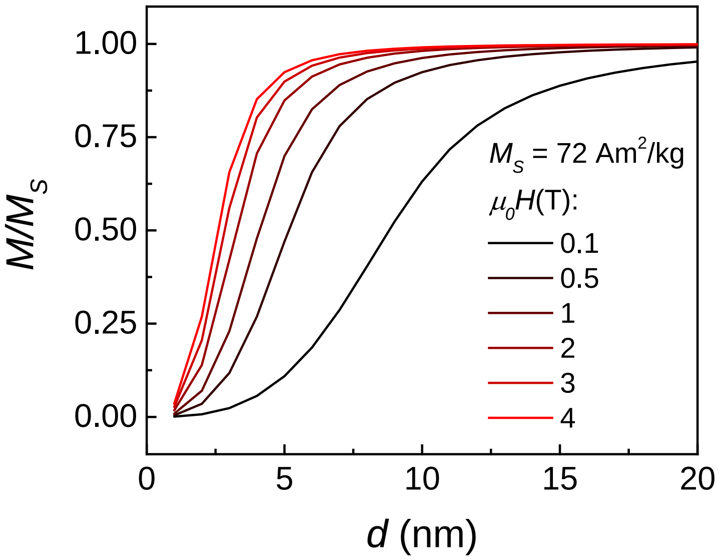

Figure 18. Magnetization at different fields normalized to saturation as a function of the diameter of spherical particles at 300 K.

A widespread method to define the magnetic size of SPM particles is performing a fitting of experimental *M-H* curves recorded above T_B using eq.(30). This procedure can by extended within the Langevin–Chantrell method in order to determine a distribution of magnetic moments, which is usually considered to be log-normal [90]. In the Langevin–Chantrell model the mean magnetic size (d_m) and its standard deviation (σ_{mag}) are free parameters. An alternative for this approach is a method of numerical inversion which is also a powerful method to resolve the distribution of magnetic moments but there is no need to restrict moment distribution to log-normal [92–94]. Figure 19 a) shows the SPM magnetization curve fitted with both approaches. Figure 19 b) shows the calculated magnetic size obtained from the numerical inversion method compared with the physical particle size from TEM measurements. The magnetic size is usually slightly smaller due to the presence of a non-magnetic layer of disordered surface spins.

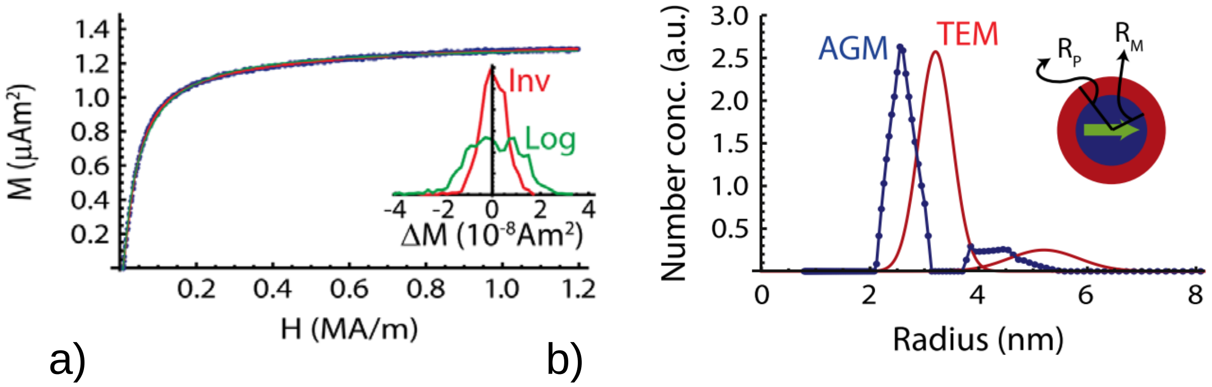

Figure 19. a) Field dependence of magnetization 6.4 nm iron oxide MNPs fitted with Langevin function considering lognormal size distribution (Log) and size distribution obtained by numerical inversion method (Inv). *ΔM* is the difference between fitted and experimental data; b) bi-modal size distribution of physical particle radius (R_p) obtained from TEM and the radius of the magnetic particle core (R_M) after the elaboration of alternating gradient magnetometry (AGM) measurements. Reprinted from [94].

Reduced magnetic susceptibility is the first derivative of reduced magnetization versus the field, $\chi = d(M/M_S)/dH$:

$$\chi = \chi_i \, 3/\mathcal{L} \; (\coth \mathcal{L} - 1/\mathcal{L}). \tag{31}$$

Thus, in low field approximation while magnetization approximately depends linear on the field, the susceptibility is equal to an initial susceptibility:

$$\chi_i = \frac{\mu_0 M_S^2 V}{3 k_B T}, \tag{32}$$

where $V = 4/3\pi r^3$ is the volume of spherical nanoparticle with dimeter $d = 2r$. This equation is the Curie law written for SPM particles [54]. In low magnetic fields, the magnetization of MNPs in the SPM state is a linear function $M(H) = \chi_i \mu_0 H$. The regime, where magnetization can be approximated by linear functions describes the dynamic magnetic behavior in the frame of the Linear Response Theory (LRT) [95].

In the framework of DC magnetometry, several methods can be used to determine blocking temperature from the temperature dependence of magnetization [96]. Usually, those approaches are based on the measurement of the magnetic moment in a small magnetic field (to be able to apply LRT) with different thermal and magnetic history [54,97]:

- Magnetization of zero-field cooled (M_{ZFC}) sample recording during the heating of sample previously cooled in the absence of the magnetic field;
- Magnetization of field cooled (M_{FC}) sample recording during the heating of sample previously cooled in the absence of the magnetic field.

Curie low for magnetization of SPM particles at temperatures above T_B is a superposition of ZFC and FC magnetizations. Bellow the T_B, the “frozen Curie low” from the SW model is [54,98–101]:

$$M_{ZFC}(T) = \begin{cases} \dfrac{\mu_0 M_s^2 VH}{3k_B T}; & T > T_B \\ \dfrac{\mu_0 M_s^2 H}{3K}; & T < T_B \end{cases} \tag{33}$$

$$M_{FC}(T) = \begin{cases} \dfrac{\mu_0 M_s^2 VH}{3k_B T}; & T > T_B \\ \dfrac{\mu_0 M_s^2 VH}{3k_B T_B}. & T < T_B \end{cases} \tag{34}$$

Considering, that at temperatures below blocking, the ZFC magnetization is small concerning FC ($M_{ZFC}\ (T) \approx 0$) and introducing δ function, which is $\delta(<0) = 0$ and $\delta(>0) = 1$, one can collapse eqs.(35) and (36) in

$$M_{ZFC}(T) = \frac{\mu_0 M_s^2 VH}{3k_B T}\delta\big(T - T_B(V)\big); \tag{35}$$

$$M_{FC}(T) = \frac{\mu_0 M_s^2 VH}{3k_B T}\delta\big(T - T_B(V)\big) + \frac{\mu_0 M_s^2 VH}{3k_B T_B(V)}\delta(T_B(V) - T). \tag{36}$$

Introducing volume distribution function $f(V)$:

$$M_{ZFC}(T) = \frac{\mu_0 M_s^2 H}{3k_B}\int_0^\infty \frac{V}{T}\delta\big(T - T_B(V)\big)f(V)dV\,; \tag{37}$$

$$\begin{aligned} M_{FC}(T) = {} & \frac{\mu_0 M_s^2 H}{3k_B}\int_0^\infty \frac{\mathrm{V}}{\mathrm{T}}\delta\big(\mathrm{T} - \mathrm{T_B}(V)\big)f(V)dV \\ & + \frac{\mu_0 M_s^2 H}{3k_B}\int_0^\infty \frac{\mathrm{V}}{\mathrm{T_B(V)}}\delta(\mathrm{T_B}(V) - \mathrm{T})f(V)dV, \end{aligned} \tag{38}$$

one obtains

$$M_{ZFC}(T) = \frac{\mu_0 M_s^2 H}{3k_B} \int_0^{\infty} \frac{V}{T} \delta\big(T - T_B(V)\big) f(V) dV\,; \tag{39}$$

$$\begin{aligned} M_{FC}(T) = {} & \frac{\mu_0 M_s^2 H}{3k_B} \int_0^{\infty} \frac{V}{T} \delta\big(T - T_B(V)\big) f(V) dV \\ & + \frac{\mu_0 M_s^2 H}{3k_B} \int_0^{\infty} \frac{V}{T_B(V)} \delta(T_B(V) - T) f(V) dV. \end{aligned} \tag{40}$$

The difference between the two functions is

$$\begin{aligned} M_{ZFC-FC}(T) & = M_{ZFC}(T) - M_{FC}(T) \\ & = -\frac{\mu_0 M_s^2 H}{3k_B} \int_0^{\infty} \frac{V}{T_B(V)} \delta(T_B(V) - T) f(V) dV. \end{aligned} \tag{41}$$

Defining a critical volume for the SPM regime as $V_c = k_B T_B / K \ln(\tau_m/\tau_0)$

$$M_{ZFC-FC}(T) = -\frac{\mu_0 M_s^2 H}{3K \ln\left(\frac{\tau_m}{\tau_0}\right)} \int_{T_B}^{\infty} f(T_B) d(T_B), \tag{42}$$

the first derivative is

$$\frac{dM_{ZFC-FC}(T)}{dT} = -\frac{\mu_0 M_s^2 H}{3K \ln\left(\frac{\tau_m}{\tau_0}\right)} f(T_B). \tag{43}$$

According to this definition, at T_B in the system, half of the particles (50%) are in the blocked regime and another half (50%) are in the SPM regime [54,88,89]. The approach to estimate T_B from ZFC and FC measurements was proposed by Micha et al. [96,102] based on an analysis of the distribution of T_B performed by differentiation of the difference between two curves:

$$f(T_B) \sim \frac{dM_{ZFC-FC}(T)}{dT}. \tag{44}$$

The average value of T_B can be defined from the integration of this function of searching for $d^2 M_{ZFC-FC}(T)/dT^2 = 0$ from the left of the ZFC peak position [100]. It should be noted that T_B obtained from ZFC–FC protocol is a function of the applied field and it is strongly affected by interparticle interactions [54,103]. A random anisotropy model (RAM) could be applied to obtain an intrinsic value of T_B which is not affected by interparticle interactions [104,105].

An alternative approach is the measuring of thermoremanent magnetization $M_{TRM}(T)$ recorded during the heating in zero magnetic fields of a sample previously cooled in a magnetic field. For a non-interacting MNPs ensemble [106]

$$M_{TRM}(T) = M_{FC}(T) - M_{ZFC}(T) + M_{IRM}(T), \tag{45}$$

where $M_{IRM}(T)$ is the isothermal magnetization recorded during the cooling of the sample without any applied magnetic field. For demagnetized samples $M_{IRM}(T)$ is negligible. Thus, the distribution of magnetic energy barrier ΔE_a is proportional to the first derivative of the thermoremanent magnetization term $f(\Delta E_a) \sim M_{TRM}(T)/dT$.

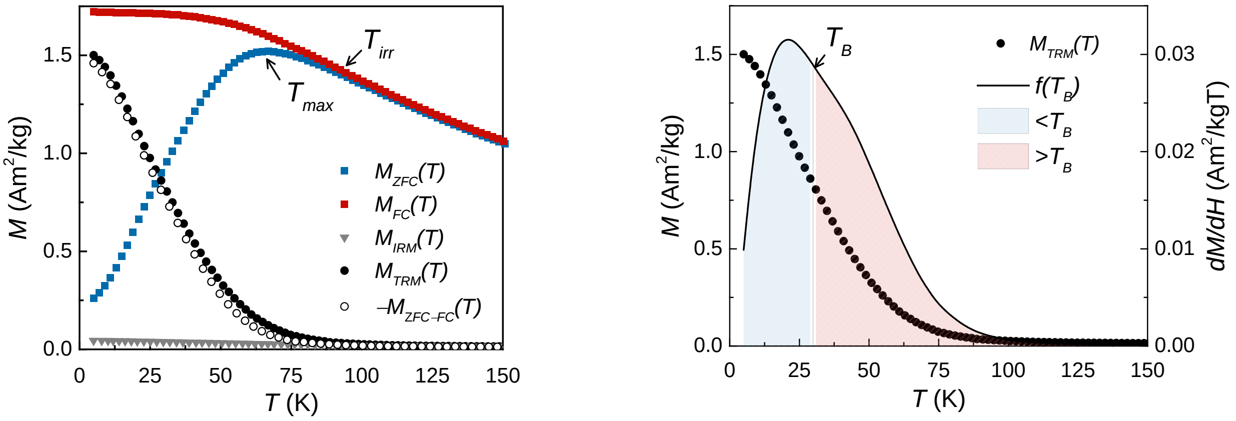

a) b)

Figure 20. a) Measured M_{ZFC}, M_{FC}, M_{TRM}, M_{IRM} and calculated $-M_{ZFC-FC}$; b) M_{TRM} and its first derivative of iron oxide MNPs. The measuring field is 1 mT.

The first approximation of T_B often used in literature is taken as the maximum of the ZFC magnetization curve (T_{max}), which usually has a peak-like shape. T_{max} is proportional to the value of T_B by a factor $\beta = 1.5–2$: $T_{max} = \beta T_B$ [107,108]. The constant β is because of log-normal particle size distribution. The irreversibility temperature (T_{irr}) is attributed to the splitting of ZFC and FC magnetizations: $M_{FC}(T_{irr}) - M_{ZFC}(T_{irr}) \rightarrow 0$. The T_{irr} has an important physical meaning since above T_{irr} all particles in the assembly are in the SPM regime.

1.1.7 Magnetically interacting nanogranular systems

Magnetic particles in ensembles generate magnetic field mutually changing local fields ($\mu_0 H_{loc}$) of neighboring particles making them different from external ($\mu_0 H_{ext}$):

$$\mu_0 H_{loc} = \mu_0 H_{ext} - N_p M, \tag{46}$$

where N_p is a demagnetizing factor of particle assembly. For an assembly of randomly packed spherical particles one can write demagnetizing factor as follow [109,110]:

$$N_p = \frac{1}{3} + f\left(N_s - \frac{1}{3}\right), \tag{47}$$

where f is the pacing factor N_S is a sample shape factor depending on its orientation regarding the magnetic field. In the simplest case of measurement of an in-plane component of magnetization of the sample if a form of the thin film N_S is 0 [110]. For powder samples in a typical capsule for laboratory static magnetometry $N_S \approx 0.28$, considering also packing factor of nanopowders to be $f \approx 0.3$, one can estimate $N_p \approx 0.32$ which is close to the demagnetizing factor of isotropic bulk (for the sphere or cube perpendicular to the plane $N = 0.33$) [111].

Besides demagnetizing effect, magnetostatic interactions among particles can vary the single-particle energy barriers in their assembly thus changing the energetical landscape of the entire system or even leading to a collective behavior [112]. Depending on particle anisotropy axes arrangement, packing factor and intrinsic particles` properties, dipolar interactions can be *positive* or *negative* [113]. Dominating negative types of dipolar interactions is probably more common for randomly distributed magnetic particles. This type of interaction leads to the linear decrease of coercivity:

$$\mu_0 H_C = \mu_0 H_C^0 (1 - f), \tag{48}$$

where $\mu_0 H_C^0$ is the coercivity of isolated particles.

In an ensemble of randomly distributed SD MNPs, assuming a point-dipole model (i.e., particles’ distance calculated from center-to-center), and defining the magnetic moment of a particle as $m = M_S \times V$, the energy due to dipole-dipole interactions can be approximated as:

$$E_{dip} \approx \frac{\mu_0}{4\pi}\left(\frac{m^2}{l^3}\right), \quad (49)$$

where l is the average interparticle distance from center-to-center.

Strong dipolar interactions can lead to the collective behavior of particles` superspins in *superferromagnetic* regime or *superspin-glass* (SSG) behavior characterized by magnetic memory and ageing effects [110,112,114]. Both SSG and atomistic spin-glasses are characterized by the frustration of unit magnetic moment in frozen metastable regime below glassy temperature (T_g) [115]. The units of SSG are particles superspins instead of individual spins for atoms in classical spin-glasses.

Glassing of SSG systems is reveling in ZFC–FC experiments similarly with the blocking of SPM particles by the appearance of the peak in ZFC magnetization; the difference of this process is the peak also in the FC curve (Figure 21) [116], which is not observed in weakly interacting SD MNPs. Another manifestation of collective dynamics of interacting systems is slow dynamics which can be observed in memory experiments. In a typical memory experiment, the reference ZFC magnetization is compared with the one performed after the "*stop&wait*" protocol where the cooling in zero fields performing with the delay at a temperature below T_g. The SSG system during this delay slowly relaxes to the energy minimum corresponding to metastable configuration formed by already blocked particles. The SSG system *remembers* this configuration and further ZFC magnetization paths in this region with the fall because the lowest energetical state with corresponding lower magnetization was *remembered* by the system. Thus, the difference between reference M_{ZFC} and M_{ZFC} recorded after *stop&wait* protocol exhibits a characteristic dip at the temperature at which the delay was performed (green line in the inset of Figure 21).

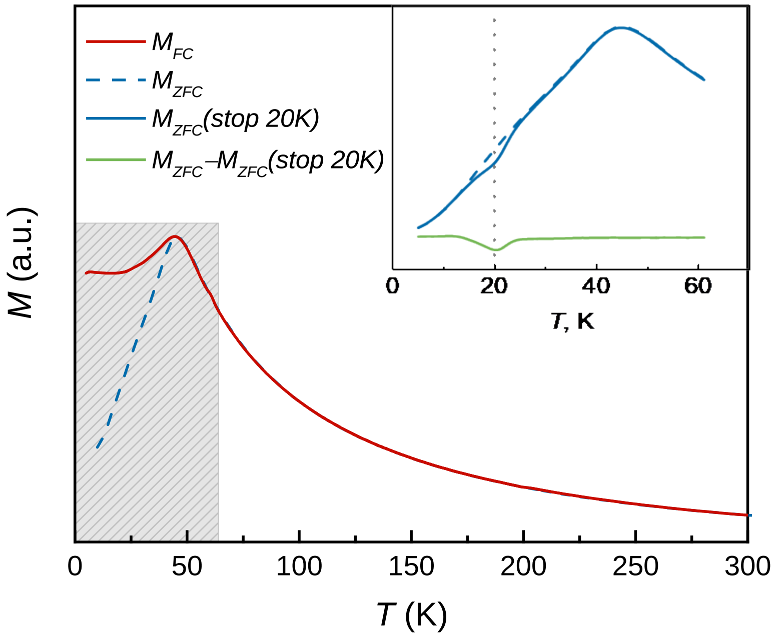

Figure 21. Temperature dependence of magnetizations performed following standard ZFC and FC protocols on a system of a strongly interacting system of $MnFe_2O_4$ MNPs. The inset shows the reference magnetization recorded after ZFC protocol, ZFC magnetization after *stop&wait* protocol, and their difference. Data adapted from [116].

Besides dipolar interactions, the exchange interactions between particles are also possible if particles are in direct contact. In the cases when exchange interactions between particles are dominating, the magnetization will tend to act coherently at the scale of the exchange interaction length (L_{ex}) higher than the particles size. The correlation length of interparticle (intergranular) interactions can be defined similarly with eq.(6) with A representing the intergranular exchange constant [54]. In terms of RAM this leads to the reduction of anisotropy by the root square of the number of correlating units ($n = (L_{ex}/d)^3$) due to a statistical fluctuation of easy axes [50]:

$$< K >= |K_1| \cdot n^{-\frac{1}{2}} = \ |K_1| \cdot \left(\frac{d}{L_{ex}}\right)^{\frac{3}{2}}. \tag{50}$$

Conclusions

From this overview, we note that magnetic properties at nanoscale change due to thermal fluctuation, changes of magnetic structure occurring at surface caused the broken exchange bonds and changes of magnetization reversal processes because of the unfavourability of a multi-domain state. As a result, the general picture of the change in the coercive force with decreasing material size can be described as follows::

1) Coercivity increases due to passing from incoherent magnetization mechanism to coherent and appearance of new sources of anisotropy;
2) Coercivity decreases because the magnetic anisotropy energy became lower than the thermal energy and thermal fluctuation became probable.

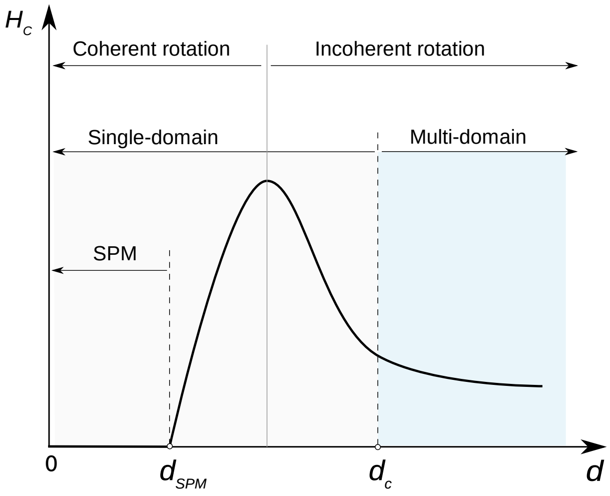

Figure 22. Phenomenological dependence of coercivity versus particle size.

Besides, the surface layer leads to a reduction of saturation magnetization, the appearance of such phenomena as exchange bias and manifestations of magnetically frustrated systems. Magnetic interactions occurring between particles also may drastically affect the anisotropy and may manifest in slow magnetic dynamics (magnetic memory effect). More changes occur due to changes in the structural properties of the material, which in their turn affect the magnetic properties. The next section is aimed to overview the changes in materials properties at the nanoscale affecting magnetic properties.

1.2 Magnetic materials: focus on oxides

This section is devoted to the magnetic transition metal oxides, first of all, to the magnetic and structural properties of spinel ferrites. Features in the properties are discussed in correlation with the synthesis method of these materials and nanohybrids composed of several layers of magnetic oxides with different magnetic properties.

1.2.1 Spinel ferrite structure

The atom of the transition group is one in which *d* sub-shell is partially occupied by electrons or which can give rise to cations with unfilled inner electron shells while outer shells are occupied by electrons [25]. In the frame of interest of this chapter, first, the transaction ions of the iron group with incomplete inner d^n shells because of their significant magnetic properties. Transaction metals are reactive and produce chemical bonds with oxygen through electrons of outer shells forming complex transition metal oxide (TMO). In TMO the cations are usually located in lattice sites of the substructure of closely-packed oxygen atoms referred as coordinations. The close-packing forms a face-centered cubic (*fcc*) (e.g., spinel ferrites or perovskites) or hexagonal close-packed (*hcp*) (e.g., hexaferrites) symmetry. In the cubic structure of close-packed oxygen lattice, metal cations can occupy the following positions [24]:

(i) octahedral with six oxygen neighbors;

(ii) tetrahedral with four oxygen neighbors.

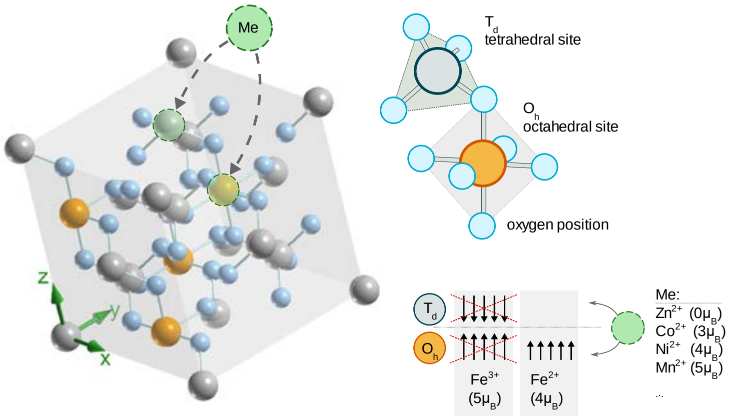

Figure 23. Schematic representation of spinel structure.

Spinel oxides ($Me^{2+}Me^{3+}{}_2O_4$) containing *3d* metals represent one of the most important classes of TMOs due to their rich crystal chemistry allowing for a fine-tuning of the magnetic properties. The spinel ferrite structure can be described as a cubic close-packed arrangement of O^{2-} anions, with Me^{2+} and Me^{3+} ions occupying tetrahedral and octahedral coordinated sites, termed as A- and B-sites, respectively. When the (A)-sites are occupied by M^{2+} cations and the [B]-sites by Me^{3+} cations, the structure is referred to as *normal* spinel, $(Me^{2+})[Me^{3+}]$. However, if the A sites are completely occupied by Me^{3+} and the B-sites are occupied by Me^{2+} and Me^{3+}, then the structure is referred to as an *inverse* spinel, $(Me^{3+})[Me^{3+}Me^{2+}]$. In general, the cationic distribution in octahedral and tetrahedral sites is quantified by the "inversion degree" (γ), which is defined as the fraction of divalent ions in octahedral sites [117]:

$$\left(Me_{\gamma}^{3+}Me_{1-\gamma}^{2+}\right)^{Td}\left[Me_{2-\gamma}^{3+}Me_{\gamma}^{2+}\right]^{Oh}O_4^{2-}. \tag{51}$$

Properties of common spinels are listed in Table 2. Cobalt ferrite ($CoFe_2O_4$) is one of the most important representers of magnetic TMOs due to hard (semihard) magnetic properties. Moreover, it has one of the largest room temperature magnetostriction among the magnetic ferrites ($\lambda_{100} = -650\cdot10^{6}$, $\lambda_{111} = 120\cdot10^{6}$, $\lambda_{s,polycrystalline} = -110\cdot10^{6}$) [118], which allows a fine tuning of the physical properties by lattice strain. Cobalt ferrite is an inverted spinel with $\gamma \approx 0.8$–1. However, in the shape of nanoparticles, the inversion degree depends on the dimension and method of sample preparation. Other important representatives of the FiM inverted spinel family are nickel ferrite ($NiFe_2O_4$), magnetite (Fe_3O_4) and maghemite (γ-Fe_2O_3). Among normal spinels is the zinc ferrite ($ZnFe_2O_4$) and among mostly normal is manganese ferrite ($MnFe_2O_4$, $\gamma \approx 0.2$). Special attention is given to mixed ferrites reviled improved magnetic properties, such as the high value of magnetization saturation which will be discussed in the further paragraphs. All ferrites listed in Table 2 show FiM properties, except zinc and magnesium ferrites that are AFM or weak FiM depending on the inversion degree [119]. Magnetite and manganese ferrites show the highest values of saturation magnetization at 0 K owing to a combination of the highest magnetic moments of bivalent metal ions and inversion degree.

Table 2. Common spinel ferrites and their main properties: density, inversion degree (γ), magnetic Curie (Néel) temperature ($T_{C(N)}$), saturation magnetization (M_S) and magnetic anisotropy constant (K). *AFM*: antiferromagnetic, *PM*: paramagnetic.

Compound	**Density, *kg/m³***	***γ***	***T*$_{C(N)}$, K**	***M*$_S$*, Am²/kg* 0 K**	**300 K**	***K, ×10⁴* J/m³**
Fe_3O_4	5240	1	858	97	91	1.2
γ-Fe_2O_3	4900	1	948	81	73	0.46
$MnFe_2O_4$	5000	0.2	573	112	80	0.3
$CoFe_2O_4$	5290	0.8–1	793	90	80	20
$NiFe_2O_4$	5380	1	858	56	50	0.62
$ZnFe_2O_4$	5200	0	9	AFM	PM	—
$MgFe_2O_4$	5280	0.9	713	27	23	1.1*

Data are adapted from refs.[25,101,120]; * K value for $MgFe_2O_4$ is for a 110-nm thin film [121].

While magnetite contains both Fe^{2+} and Fe^{3+} ions, the maghemite is composed of Fe^{3+} with some vacancies of cations in spinel structure [122–124]. The maghemite is an oxidative product of magnetite because of the instability of Fe^{2+} under oxygen, which disturbs obtaining of the pure magnetite phase at the nanoscale by wet chemical methods in aqueous media [125]. Because of the similarity of the crystal structure and changing properties at the nanoscale, distinguishing these phases is still challenging using conversion technics such as laboratory X-Ray diffractometer (because of the bordering of diffraction peaks) or DC magnetometry (because of non-equilibrium cation distribution and uncompensated spins at surface affected saturation magnetization). Nerveless, both magnetic iron oxides are in the frame of interest for applications: magnetite because of the higher value of magnetization saturation and half-metallic properties for spintronics [126,127] and maghemite because of the absence of catalytically active Fe^{2+} inducing the formation of reactive oxygen spices in the biological medium for biomedical applications [124,128]. Magnetite is characterized by a metal/insulator transition occurring at the Verwey temperature (T_V = 120−125 K for bulk magnetite) [129]. Above T_V, the magnetite is a half-metal.

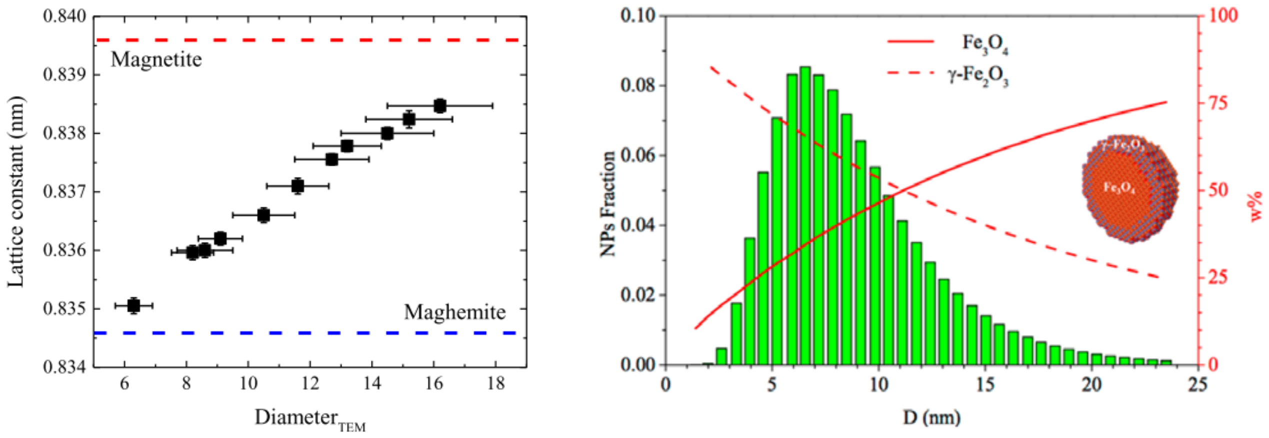

a) b)

Figure 24. a) Variation of lattice constant as a function of iron oxide particle size (reprinted from [130]) and b) magnetite/maghemite weight fractions beyond the particle size distribution (reprinted from [122]).

1.2.2 Magnetic properties of spinel ferrites

Super exchange interactions between atomic magnetic moments in A (A–O–A) and B (B–O–B) interstices lead to a ferromagnetic ordering between the ions located in the two sites giving rise to two magnetic sublattices [119]. On the other hand, interactions between magnetic ions in the A and B sites (A–O–B) induce antiferromagnetic order, and they are tenfold higher than the intra-lattice. Thus, spins will be oriented parallel inside each site but magnetization of two sublattices will be oriented antiparallel. Then, according to the Néel model of ferrimagnetism, the magnetic moment per formula unit (μ_S) arises from the superposition of moments of two sublattices [131]:

$$\mu_S = \mu_{SA} - \mu_{SB}, \tag{52}$$

where μ_{SA} and μ_{SB} are magnetic moments of A and B sites respectively. Since in the case of the inverted spinel, the Fe^{3+} ions are homogenously distributed among A and B sites, their contribution (5 μ_B) in the net magnetization is mutually compensated and the net magnetic moment is governed by the magnetic moment of the divalent cations Fe^{2+} (4 μ_B) occupied octahedral positions.

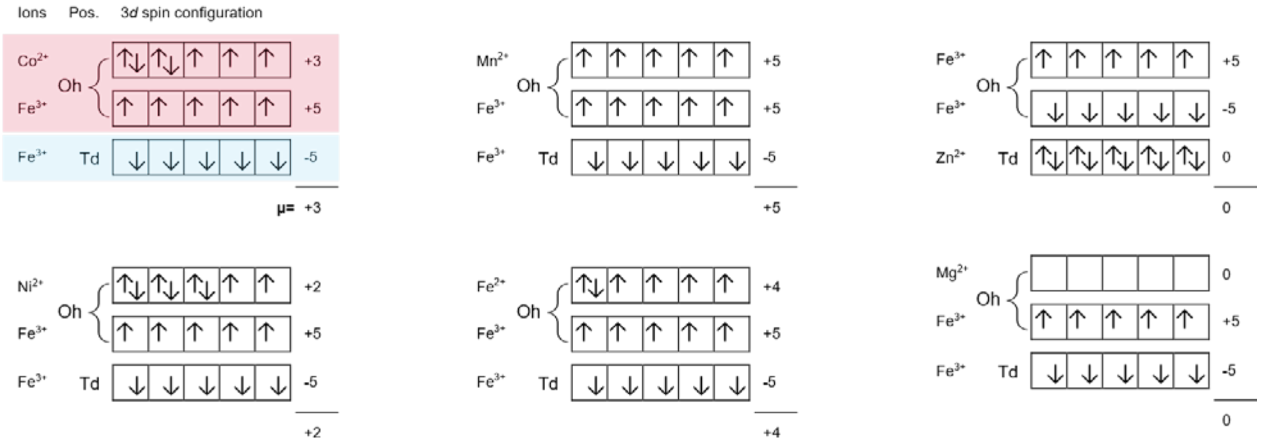

Figure 25. Scheme of the *3d* spin configurations of common ferrites with the spinel structure.

The magnetic moment per formula unit can be converted to the ferrite saturation magnetization [132]:

$$M_S = N_A \cdot \mu_B / M_w \, \mu, \tag{53}$$

where M_w is the molecular weight, N_A is the Avogadro constant (6.022×10^{23} mol^{-1}) and μ_B is the Bohr magneton (9.274×10^{-24} J/T).

Assuming the inversion degree strictly inverted ($\gamma = 1$) for nickel, cobalt and iron ferrites, one can estimate values of the saturation magnetization expressed in the Bohr magnetons per formula unit (μ_B/f.u.) of 2, 3 and 4, which are proportional to the number of unpaired electrons on *3d* orbital. In a similar way, saturation magnetization can be defined of the normal spinels or spinels with intermediate values of the inversion degree. While at 0 K the ground state for ideal ferrite is perfectly ordered inverted $\gamma = 1$ or normal $\gamma = 0$ spinels, in real material the inversion degree can vary from 1 to 0 due to a mixing of elemental species [133].

The behavior of saturation magnetization of many known oxides cannot be fully explained through the Néel model because weakening in interlattice interaction led to the spin canting into one of the sublattices [119,132,134]. According to the three-sublattice model suggested by Yafet and Kittel, the net magnetic moment can be expressed as

$$\mu_S = \mu_{SB} cos(\alpha_{YK}) - \mu_{SA}, \tag{54}$$

where α_{YK} is the Yafet–Kittel angle.

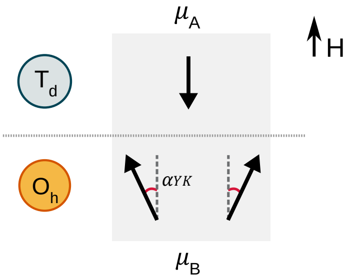

Figure 26. Scheme of spin orientation in non-collinear Yafet–Kittel model.

Besides saturation magnetization, the inversion degree affects anisotropy. The Co^{2+} ions in the octahedral sites have larger anisotropy (+850 × 10^{-24} J/ion) than Co^{2+} ions in a tetrahedral site (−79 × 10^{-24} J/ion) [135]. R. M. Freire et al. performed micromagnetic simulations supported by density functional theory (DFT) calculation of a system of cobalt ferrite MNPs with different values of inversion degrees [136]. The most stable atomic configurations of cobalt ferrite were defined by employing DFT at different levels of inversion. Defined in this way material parameters were used to reconstruct hysteresis cycles in micromagnetic simulations and compared with experimental results. The higher inversion leads to the higher coercivity of cobalt ferrite MNPs.

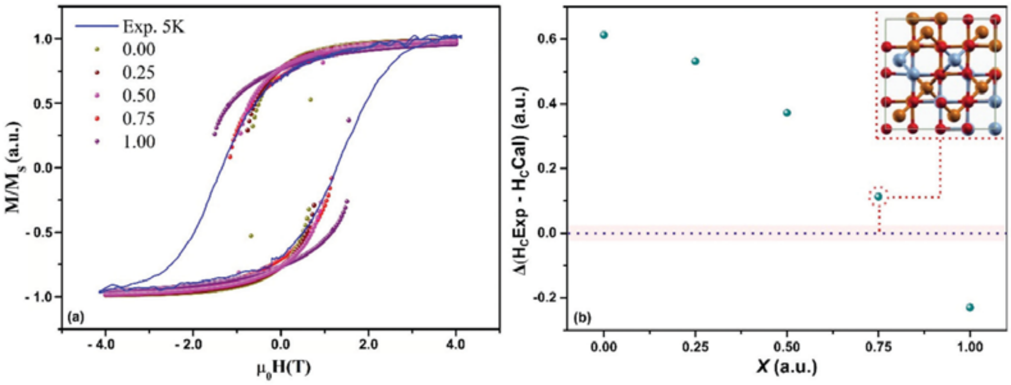

Figure 27. a) Normalized field-depended magnetization curves of ~7-nm solvothermaly synthesized cobalt ferrite MNPs measured at 5 K (blue line) and result of micromagnetic simulations obtained for different inversion degrees. The structural configuration and electronic properties of the spinel structure for micromagnetic simulations were taken from first-principles calculations based on density functional theory (DFT); b) difference of simulated and experimental of coercivity plotted versus inversion degree (*X*). Reprinted from [136].

Elias Ferreiro-Vila with colleagues [137] investigated thin films of cobalt ferrite prepared via a chemical solution and pulsed laser deposition methods. By variation of the deposition temperature and epitaxial stress, Co^{2+} cations migrate from octahedral to tetrahedral sites in strained layers. This leads to a drastic drop of anisotropy as confirmed by the appearance of two-phase-like M-H hysteresis loops or, in other words, in the appearance of a second peak (in the region $H \rightarrow 0$) in the susceptibility ($\chi = dM/dH$). Figure 28 shows the appearance of the magnetically soft cobalt ferrite phase with normal spinel structure characterized by the height of the peak close to zero field in dM/dH plots in cobalt ferrite thin films deposited at different temperatures.

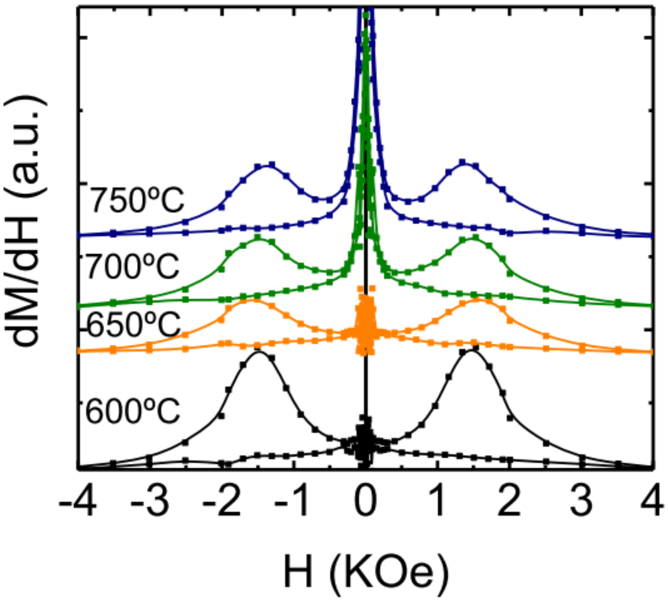

Figure 28. The first derivative of magnetization versus magnetic field of cobalt ferrite thin films deposited at different temperatures. Reprinted from [137].

While magnetic properties of spinel ferrites are well-known from the bulk materials, at the nanoscale these properties may vary significantly. This is related to the value of inversion degree which depends on crystal size and the method of synthesis [120]. Inversion degree in its turn drastically affects all magnetic properties of the material: saturation magnetization and magnetic anisotropy [136]. Even though in the bulk form, $CoFe_2O_4$ and $NiFe_2O_4$ are inverted spinel, nanoparticles with the chemical formula $Ni_{1-x}Co_xFe_2O_4$ ($0 \leq x \leq 1$) may show significant variation in inversion degree [120,138]. For example, Giuseppe Muscas et al. found the inversion degrees of

0.74, 0.78 and 0.44 for $CoFe_2O_4$, $Ni_{0.5}Co_{0.5}Fe_2O_4$ and $NiFe_2O_4$ nanoparticles prepared with the polyol method [138]. In properties of several spinel ferrite nanoparticle systems from literature are collected. One can see in this table that the magnetic properties of nanoparticles are significantly different as compared with bulk reported in Table 2, as well as with those for nanoparticles of approximately the same size and composition. Then, for nanostructured materials, the inversion degree differs drastically compared with the bulk and it can dramatically change with particle size (Figure 29).

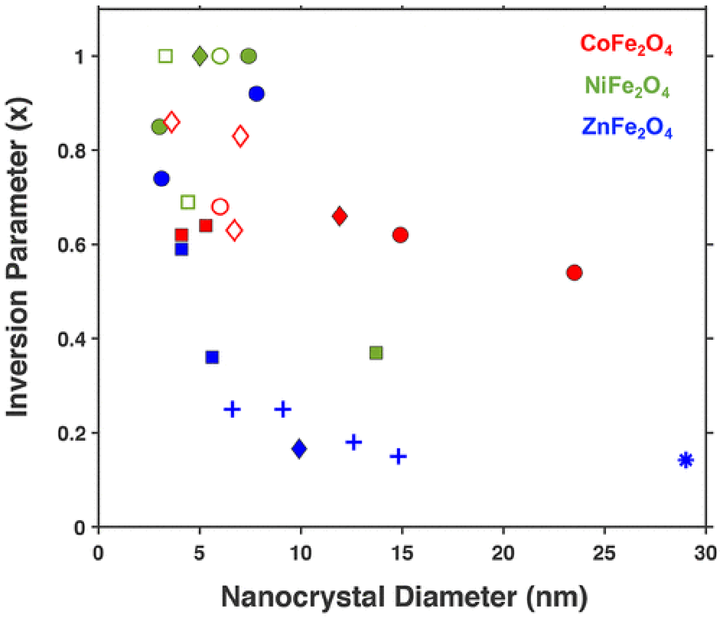

Figure 29. Dependence of inversion degree of common representatives of spinel ferrites $CoFe_2O_4$, $NiFe_2O_4$ and $ZnFe_2O_4$. Reprinted from [120].

Table 3. Case properties spinel ferrite MNPs.

Composition	***d*, nm**	***M_S*, Am^2/kg**		***$\mu_0 H_C$*, T**	***T_B*, K**	**Ref.**
		(5 K)	(300 K)	(5 K)		
$CoFe_2O_4$	7.5	109	92	1.2	—	[139]
$Zn_{0.30}Co_{0.70}Fe_{2.00}O_4$	7.1	142	94	0.46	—	
$Zn_{0.46}Co_{0.54}Fe_{2.02}O_4$	7.3	157	84	0.37	—	
$Zn_{0.53}Co_{0.47}Fe_{2.02}O_4$	8.0	140	70	0.44	—	
$CoFe_2O_4$ (HTD*)	4.6	70	—	1.29	120	[140]
$CoFe_2O_4$ (DM1)	4.8	54	—	1.17	154	
$CoFe_2O_4$ (DM2)	4.8	51	—	1.45	157	
		(15 K)	(300 K)	(15 K)		
$Mn_{0.11}Fe_{2.89}O_4$	6.4	78.2	68.7	0.006	~30	[141]
$Mn_{0.49}Fe_{2.54}O_4$	6.4	78.3	66.3	0.006	~30	
$Co_{0.12}Fe_{2.88}O_4$	5.9	81.3	74.7	~0.4	~120	
$Co_{0.55}Fe_{2.45}O_4$	6.4	85.4	80.5	~2.0	~220	
		(5 K)	(290 K)	(5 K)		
Fe_3O_4	12	79	69	0.028	—	[142]
$MnFe_2O_4$	12	81	74	0.0396	—	
$CoFe_2O_4$	12	54	50	1.7	—	
			(300 K)			
Fe_3O_4 (NaOH)	8.6	—	58.0	—	92	[143]
Fe_3O_4 (MIPA)	6.3	—	64.8	—	56	
Fe_3O_4 (DIPA)	4.9	—	60.4	—	34	

* some features of synthesis are reported in the parenthesis. More details are in the text.

The inversion degree is strongly related to the method of synthesis, size and surface properties of nanomaterial. In this way assuming, for instance, for cobalt ferrite the inversion degree of 0 (normal spinel), the value of net magnetization of 7 μ_B/f.u. ($[2\times5\ \mu_B]_{\text{B-site}} - [3\ \mu_B]_{\text{A-site}}$) is expected, which is higher than the expected value of 4 μ_B/f.u. for normal spinel. Thus, for nanosystems that are not in a thermodynamical equilibrium state, a higher value of saturation magnetization can be observed. Considering $\gamma = 0$ for cobalt ferrite, the inversion degree can be estimated from the value of saturation magnetization expressed in μ_B/f.u. [144]:

$$\gamma = (7 - \mu_S)/4 \tag{55}$$

where μ_S is expressed in Bohr magnetons and only the spin contribution is considered. Thus, inversion degree is one of determining factors of saturation magnetization.

Accordingly, by the variation of chemical composition and synthesis procedure, one can tune the saturation magnetization of those materials. For example, nanoparticles of Fe_3O_4 and $MnFe_2O_4$ doped by non-magnetic Zn^{2+} (0 μ_B) cation can exhibit enhanced saturation magnetization compared with undoped ferrites [145,146]. This enchantment can be achieved in artificially engineered nanoparticles through metastable states of spinel structure when a small amount of Zn^{2+} preferentially occupies tetrahedral sites pushing part of the Fe^{3+} cations to move into octahedral positions. A similar effect was observed in cobalt and nickel ferrites doped by zinc [139,147–149].

The high M_S values have been observed in Zn-doped spinel ferrites (i.e., $Zn_xFe_{1-x}Fe_2O_4$ [145,150–152], $Zn_xCo_{1-x}Fe_2O_4$ [132,139,147,153], $Zn_xNi_{1-x}Fe_2O_4$ [154], $Zn_xMn_{1-x}Fe_2O_4$ [145,153] MNPs where M_S increase while x (i.e., Zinc content) is less than ~0.5. For example, the research team of Jinwoo Cheon observed an extremely high M_S value of 161 and 175 Am^2/kg for $Zn_{0.4}Fe_{2.6}O_4$ and $Zn_{0.4}Mn_{0.6}Fe_2O_4$ respectively [145]. For $Zn^{2+}{}_xFe^{2+}{}_{(1-x)}Fe^{3+}{}_2O_4$ ferrites an increase in magnetic moment from 4.0 μ_B/f.u. to 8.3 μ_B/f.u. according to $(4 + 6x)$ μ_B/f.u. rule was confirmed through DFT calculations [152]. This rule was valid for Zn concentration $0 < x < 0.75$ where magnetization reached maximal value and start to decrease. That was explained by the replacement of Fe^{3+} with magnetic moment 5 μ_B/f.u. in A-sites by non-magnetic Zn^{2+} cations. The Co^{2+} in the structure of spinel ferrite makes material magnetically harder keeping the relatively high value of saturation magnetization [155–157]. Valentina Mameli and colleagues found that the M_S at 5 K reaches a value of 157 Am^2/kg for $Zn_{0.46}Co_{0.54}Fe_{2.02}O_4$ synthesized by the high-temperature decomposition method [139]. Gabriele Barrera et al. synthesized a set of $Zn_xCo_{1-x}Fe_2O_4$ MNPs with x in the range of 0.08–0.56 using a sol-gel autocombustion route (SGAC) [132]. In their work, authors observed that starting from inverse spinel at $x = 0.08$ future increase of zinc content to $x \approx 0.4$ leads to the formation of mixed ferrite where Zn^{2+} forces Co^{2+} migrate to A-site and Fe^{3+} to B-site. It was highlighted that non-equilibrium cation distribution is strongly related to the method of synthesis and, together with spin canting, leads to a non-monotonous change of saturation magnetization.

The increase in the concentration of non-magnetic zinc leads to a weakening of the super-exchange interaction between A and B sites, as result, the magnetization decreases due to a spin canting phenomenon. For example, for $Zn_{0.4}Co_{0.6}Fe_2O_4$ with a saturation magnetization of 5.8 μ_B the value α_{YK} = 29.3° was observed [147]. However, even with the significant influence of the spin canting value of saturation magnetization is higher undoped ferrite at low temperatures. A drawback of this approach is the significant reduction of Curie temperature and thus reduction of magnetization at room temperature.

The $CoFe_2O_4$ MNPs with the approximately same size of about 5 nm were prepared by different chemical methods and their magnetic properties were studied in ref. [140]. The sample $CoFe_2O_4$-HTD was synthesized by using high-temperature decomposition (HTD) method, in this case, MNPs were self-organization, which prevented their aggregation. The second method of synthesis, direct micelles (DM), was used to produce two samples: an unstructured organized system of particles $CoFe_2O_4$-DM1 and aggregated iso-oriented spherical arrangements of particles $CoFe_2O_4$-DM2. According to the ratio of remanent magnetization and saturation magnetization ($M_R/M_S \approx 0.68$), MNPs synthesized by the HTD method possess the dominant cubic magnetocrystalline anisotropy, while MNPs prepared by the DM showed a lower value of this ratio ($M_R/M_S \approx 0.39$ and 0.48), which indicates the dominant uniaxial anisotropy. Differences in remanent magnetization and coercivity in samples prepared by the DM method in different arrangements were attributed to the difference in the interparticle interactions. The highest values of coercivity and remanent magnetization of iso-oriented particles were observed. The increase in the remanent magnetization is related to the effect of the interaction between MNPs in the aggregates. Moreover, the MNPs prepared by the HTD method have a large value of saturation magnetization (Table 3).

1.2.3 Role of the synthesis conditions

In the previous paragraph, we already observed that MNPs prepared by different methods have very different magnetic properties. In this paragraph, we will deeply consider the effects of synthesis methods and the physical reasons behind their effect on structural properties and magnetic phenomena.

$MnFe_2O_4$, $CoFe_2O_4$, $NiFe_2O_4$, and $ZnFe_2O_4$ MNPs produced by solvothermal (T) and microwave-assisted (M) synthesis were compared in ref. [158]. Among studied materials, $NiFe_2O_4$ and $ZnFe_2O_4$ showed significantly different inversion degrees compared with the bulk (Table 4). This was especially noted in the case of Zn ferrite, between MNPs of the same composition and size prepared by the different methods. The magnetic moment individually for octahedral and tetrahedral sites was defined by neutron powder diffraction and Rietveld refinement. The magnetizations estimated from this measurement agreed with the macroscopic magnetic properties of samples measured with the SQUID magnetometer. The authors concluded that microwave-assisted methods allowed producing MNPs with similar structure and magnetic properties with a much shorter annealing time and lower temperature compared to those produced by the solvothermal method.

Table 4. Common spinel ferrite nanoparticles produced via solvothermal (T) and microwave-assisted (M) methods.

Composition	**Rout**	**d_{XRD}, nm**	**γ**	**μ_{SA}, μ_B/f.u.**	**μ_{SB}, μ_B/f.u.**
$MnFe_2O_4$	T	6.0	0.66	4.0	3.4
	M	7.2	068	4.8	1.7
$CoFe_2O_4$	T	5.7	0.64	4.4	3.0
	M	5.2	0.62	4.3	2.9
$NiFe_2O_4$	T	11.5	0.37	4.3	3.5
$ZnFe_2O_4$	T	5.6	0.36	1.0	2.1
	M	4.7	0.59	2.6	2.6

Gabriel Lavorato and colleagues studied $CoFe_2O_4$ MNPs produced by thermal decomposition (TD), solvothermal (SV), co-precipitation (CP), and autocombustion (AC) methods. Produced particles were in 7–10 nm size range. This study vividly shows the strong influence of synthesis conditions on the internal structure of particles and as consequence on the magnetic properties. XRD patterns of all samples (Figure 30 a) show pure spinel ferrite structure without any impurities. The lattice parameter (a_{CFO}) was close to the bulk value for samples produced with TD method, slightly higher for SV and lower for CP and AC methods (Figure 30 b). The d_{XRD} differs quite significantly for samples produced by different methods.

The level of crystallinity can be defined through the proximity of crystallite size d_{XRD} calculated from XRD data and particle size d_{TEM} defined by TEM image analysis (Figure 30 c). The difference between these parameters is due to the presence of a disordered amorphous shell. The higher d_{XRD}/d_{TEM} ratio was detected in samples prepared by TD and SV methods, and the lower in CP and AC methods. This agrees with the lower lattice parameters of CP and AC also ascribed to the crystalline disorder. Owing to the high crystal, higher values of saturation magnetization and coercivity were found in samples prepared via TD and SV methods. Also, M_R/M_S ratio was higher for samples prepared by TD method reaching a value of 0.77 which suggests dominating magnetocrystalline anisotropy with cubic symmetry while for particles prepared by CP method this value was 0.47 due to the local lattice strain and appearance of other sources of anisotropy (e.g., shape or strain) leading to the uniaxial anisotropy. It was concluded, in particular, that the surfactant in TD method promotes the formation of faceted nanocrystals characterized by the lower levels of local structural defects compared with MNPs produced in solvent-controlled SV synthesis with predominantly spherical particles.

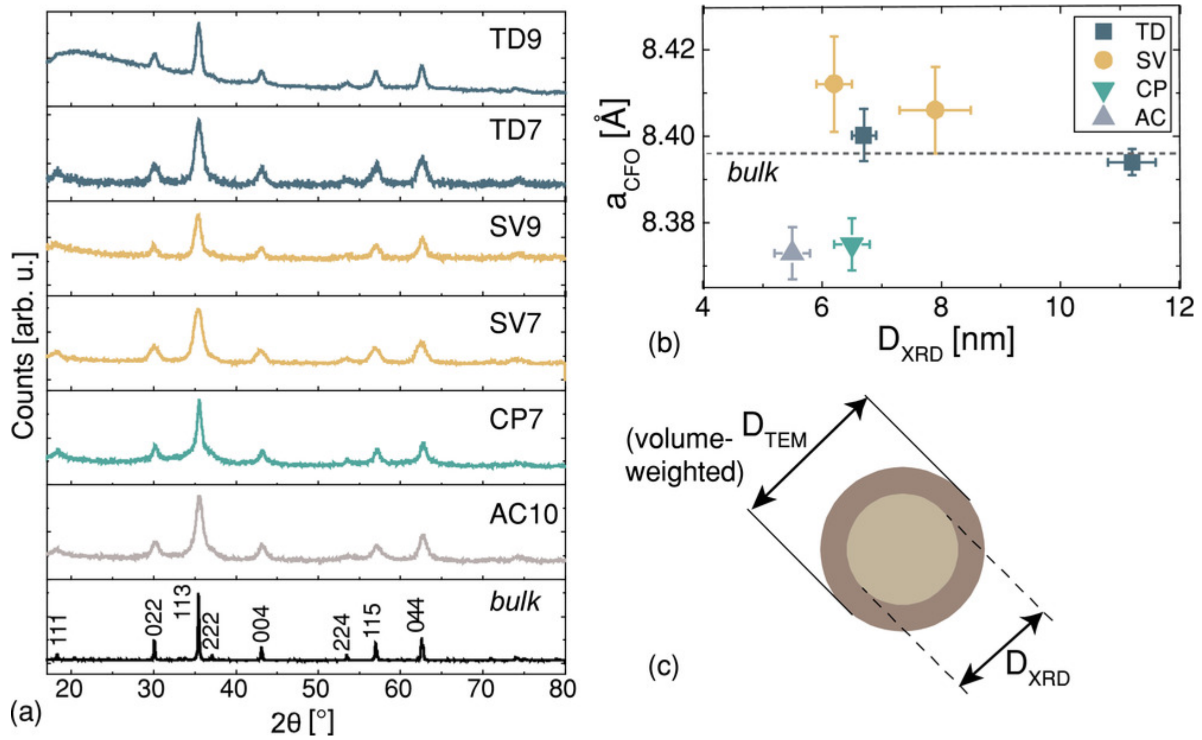

Figure 30. a) X-Ray diffractograms of $CoFe_2O_4$ MNPs synthesized via thermal decomposition (TD), solvothermal (SV), co-precipitation (CP), and autocombustion (AC); b) Cell parameter (a_{CFO}) and size of crystallite (d_{XRD}) were calculated from XRD data and c) schematical representation of particle size and crystallite size. Reprinted from [159].

Hence, even chemically homogeneous oxide MNPs can be considered *native* core/shell structures, where materials of core and shell are characterized by different structural and magnetic properties. The shell material is usually characterized by a higher structural disorder or amorphous state, the difference in spin canting and inversion degree compared with particle core [160]. Interesting, the high-field Mössbauer spectrum $NiFe_2O_4$ MNPs of about 8.6 nm prepared by mechanochemical synthesis indicates the presence of two magnetic phases each characterized by a superposition of two subspectra corresponding to A and B lattices. Two magnetic phases were attributed to the core and shell which formation was also confirmed by High-Resolution Transmission Electron Microscopy (HRTEM) image analysis. Magnetic phase with detected inversion degree of 1 and almost absent spin canting was considered to be the core material. While magnetic phase with a high level of spin canting and non-equilibrium cation distribution of 0.671 which is close to the random distribution of 2/3. Also interesting, is that the reduced saturation magnetization was because of spin canting that dominates over non-equilibrium inversion degree of the shell (reduced inversion degree in $NiFe_2O_4$ leads to the increase in M_S).

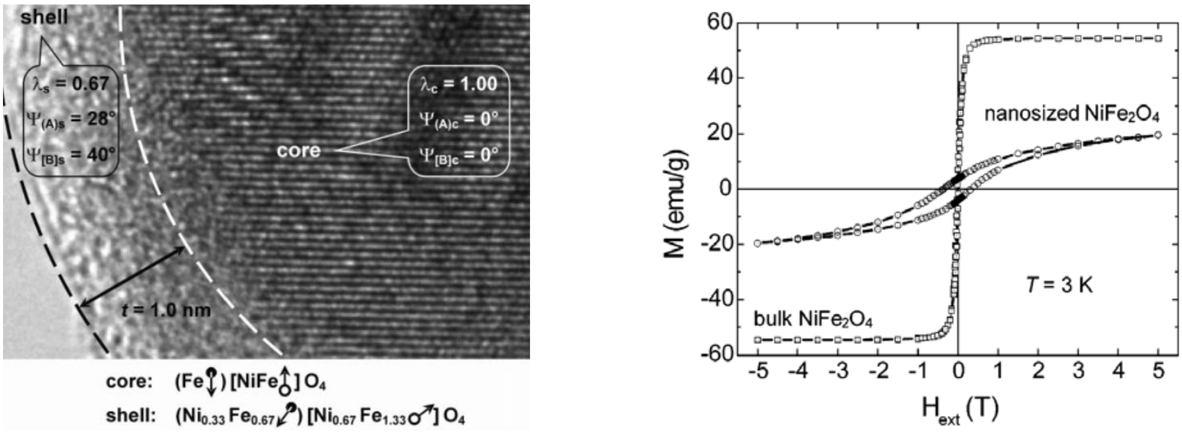

a) b)

Figure 31. a) HRTEM image of mechanosynthesized $NiFe_2O_4$ MNP: highly crystalline core (c) surrounded by an 1-nm shell (s). Inversion degree (λ) and average canting angle (Ψ) of Fe ions obtained from high-field Mössbauer spectra are indicated for each region. b) *M-H* hysteresis loops for bulk and nanosized $NiFe_2O_4$ measured at 3 K after cooling in field 5 T. Reproduced from [160].

As we already noticed, the synthesis procedure affects, in particular, the surface properties of MNPs and, ultimately, their magnetic properties. The different surfactants used in synthesis affect the ionic distributions of the particle surface and prevent particle growth. Clara Pereira et al. changed the NaOH alkaline agent with the alkanolamines isopropanolamine (MIPA) and diisopropanolamine (DIPA) to synthesize spinel ferrite MNPs by the aqueous coprecipitation method [143]. The alkanolamines additionally acted as complexing agents that reduced the particle size and improved the spin rearrangement at the surface (Figure 32). The MNPs produced with the use of novel alkaline agents were smaller in size compared with the classical approach and have a thinner dead layer and, as result, the smaller particles showed higher saturation magnetization (Table 3).

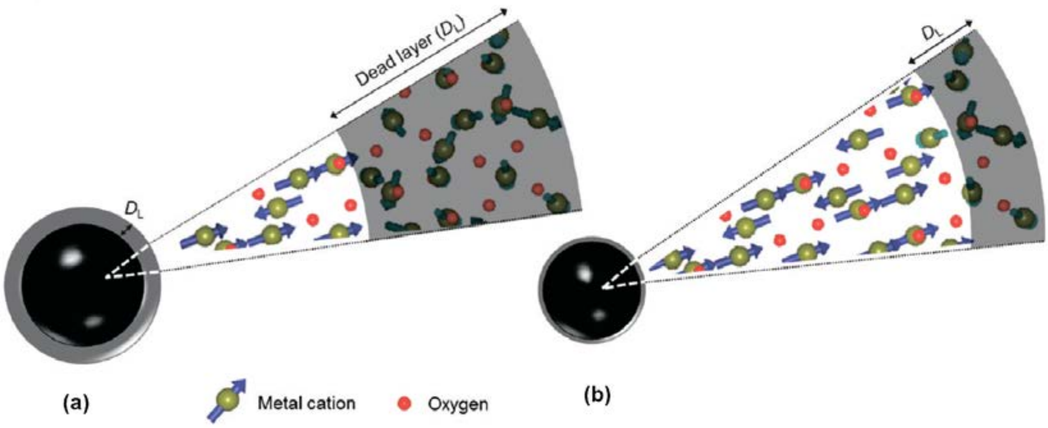

Figure 32. Schematic representation the surface spin structure of the MNPs prepared by coprecipitation in different types of bases: a) NaOH and b) MIPA and DIPA. Reprinted from [143].

1.2.4 Multiphase structures

MNPs composed of several magnetic phases with different properties, such as, for example, magnetically hard (h-) and soft (s-) F(i)M or AFM materials, are of considerable interest for both basic research and applications. Several magnetic phases hybridized in a single core/shell system are a unique platform to adjust and achieve enhanced magnetic properties, for example, enhanced magnetic anisotropy. We already discussed physical reasons and phenomena arising at the interface of two phases interacting via exchange coupling on page 28, here we will consider these effects applying to the real objects. Bi-magnetic exchange-coupled systems consisting of FM/AFM or h-FM/s-FM materials provide enhanced magnetic properties compared to their individual counterparts (i.e., single-phase systems) [68,161–164]. Hard/soft exchange-coupled MNPs have attracted significant attention owing to the great advantage of such structures for several applications (e.g., magnetic hyperthermia and permanent magnets). The manipulation of a bi-magnetic core/shell nanoarchitecture is a powerful tool for obtaining new functionalities in a single nanoscale object [153,161,163,165–169]. This high interest in multifunctional nanoscopic core/shell or multi-shell systems has triggered substantial synthetic advances that combine surface chemistry and nanoparticle synthesis [170–172].

1.2.4.1 Magnetic hard/soft and soft/hard systems

Depending on the size/thickness of h-FM and s-FM phases, the bi-magnetic system can act in a rigidly coupled regime if the s-FM phase is thinner than the double domain wall thickness of the h-FM [68]. This regime is characterized by a squared hysteresis loop of the soft phase being strongly exchange-coupled with the hard phase and the magnetization reversal process of the two phases occurring at the same field. In the case of the thicker s-FM phase, its reversal occurs at significantly lower fields than the switching of the h-FM. However, concerning nanoparticles, a wider phenomenology may be observed due to the large dispersion of magnetic properties arising from size distributions or divergences in the structural properties (i.e., stoichiometry and unit-cell parameters) of nanomaterials compared to bulk materials [173]. Special attention has been paid to the formation of the ultrathin shell of a few atomic layer thicknesses, exhibiting an enhanced spin canting (ESC) effect [84] which brings out a larger magnetic surface anisotropy, allowing exchange coupled systems to increase, for example, magnetic energy product $(BH)_{max}$ or specific loss power.

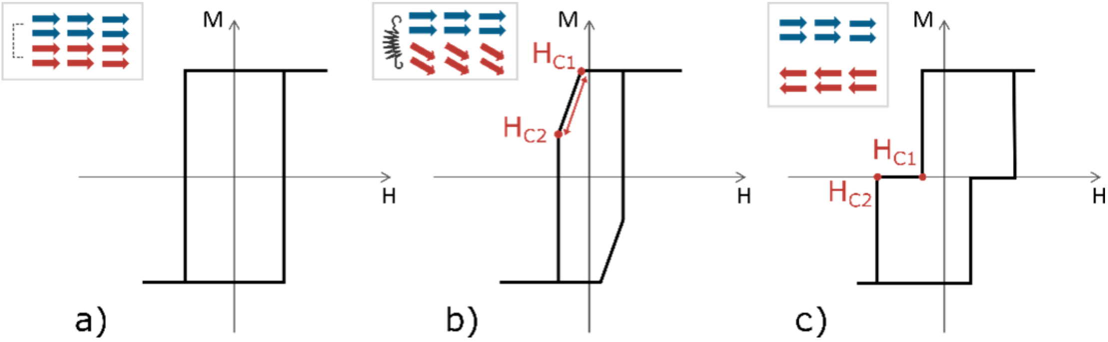

Figure 33. Schematic representation of the field-dependent magnetization loop of exchange-coupled hard/soft composites for different magnetic regimes. a) Rigid-coupling regime: the two phases reverse simultaneously at a critical field H_C.; b) Exchange-spring regime: the soft phase reverses first at H_{C1} in a reversible way (indicated by the red arrow) and supports the switching of the hard phase occurring at H_{C2}. c) Decoupled regime: the two phases reverse separately at H_{C1} and H_{C2}.

An illustrative example of these studies is represented by the work of G. Lavorato and co-authors [174], which clearly proved that the magnetic behavior of $Fe_3O_4/CoFe_2O_4$ spinel ferrite bilayers grown on $MgAl_2O_4$ (001) substrates can be finely modulated by changing the thickness of the softer Fe_3O_4 phase (Figure 34). A rigid-coupling regime can be indeed achieved for Fe_3O_4 thicknesses lower than the exchange length of the hard layer (8 nm), while two separated reversals are observed for larger Fe_3O_4 thicknesses indicating a partial decoupling of the two layers.

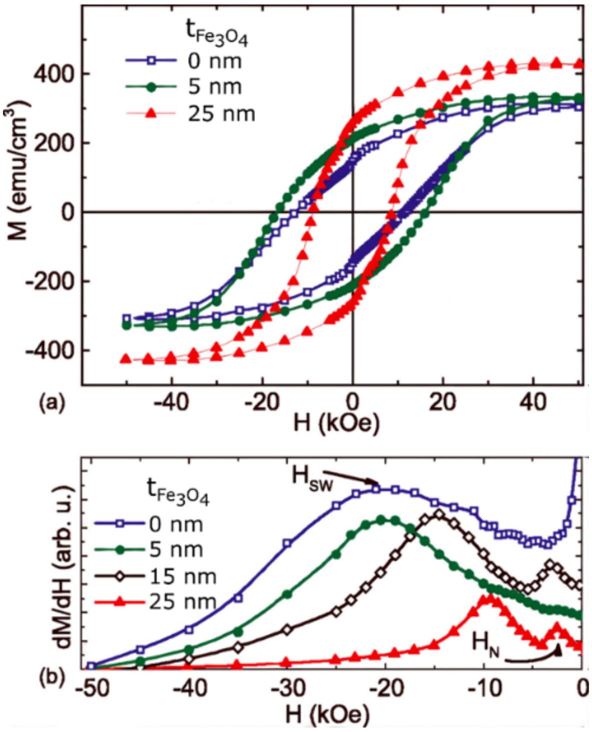

Figure 34. Low temperature (10 K) (a) field-dependent magnetization loops and (b) corresponding first-derivative curves of Fe_3O_4 (t nm)/$CoFe_2O_4$ (25 nm) bilayers as a function of the soft layer thickness. H_{sw} and H_N were associated with the irreversible switching field of the h-phase ($CoFe_2O_4$) and the nucleation field of the s-phase (Fe_3O_4), respectively. Reprinted from Ref. [174].

An example of hard/soft core/shell MNPs is reported in Figure 35**,** showing the microstructural features and the magnetic behavior of $CoFe_2O_4/MnFe_2O_4$ core/shell MNPs with a narrow size distribution. The smooth shape of the hysteresis loop of the core/shell MNPs indicates that the two phases are rigid-coupled giving rise to a material whose properties are averaged between the two phases [161]. The peculiar properties of these systems result in a great increment of the specific loss power (up to one order of magnitude) with respect to single-phase iron oxides MNPs, with implications for applications based on the magnetic hyperthermia [161].

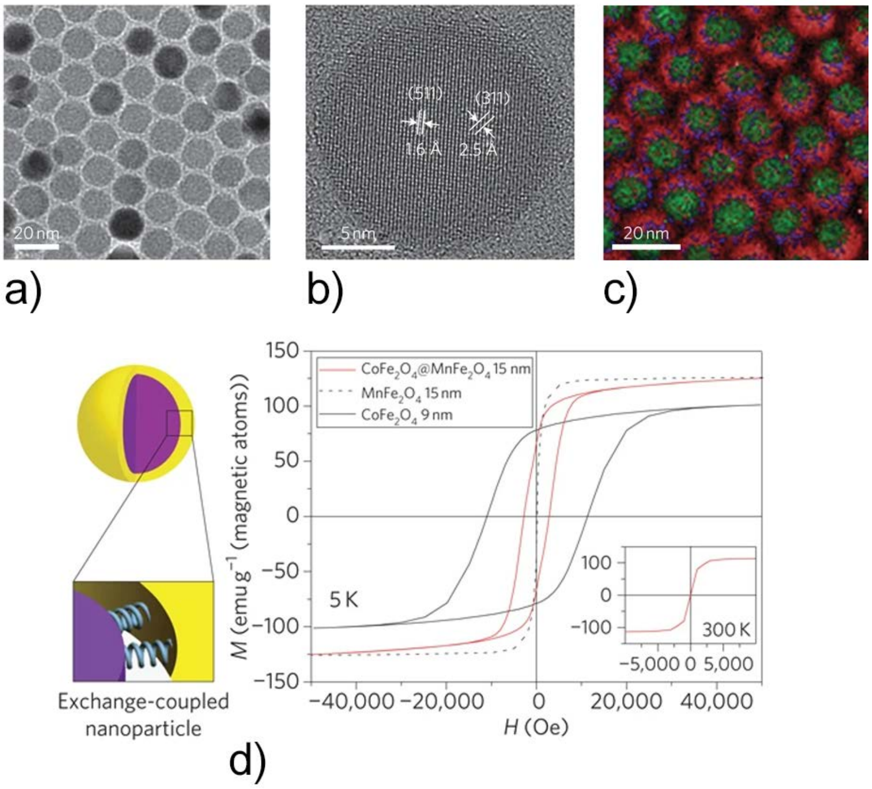

Figure 35. a) TEM and b) HRTEM images, c) electron energy loss spectroscopy elemental map (Co – green, Fe – red and Mn – blue) of 15 nm $CoFe_2O_4$/$MnFe_2O_4$; d) *M*-*H* curve of single-phase 15 nm $MnFe_2O_4$, 9 nm $CoFe_2O_4$ MNPs and exchange-coupled core/shell 15 nm $CoFe_2O_4$/$MnFe_2O_4$ MNPs. Reprinted from Ref. [161].

A complex study of tuning of magnetic properties of MNPs was carried out in the article of Seung-Hyun Noh et al. [175]. The effect of size, shape and core/shell structure of MNPs $Zn_{0.4}Fe_{2.6}O_4$ on magnetic properties were studied. The MNPs of an equal volume of sphere-shape show a lower saturation magnetization than cubic-shape particles. This phenomenon was studied by simulation by using OOMPH software and explained by the great volume of canted spins in the sphere-shaped particle. Also was studied method of tuning of the magnetic properties of the cubic-shape nanoparticles $Zn_{0.4}Fe_{2.6}O_4$ (core = 50 nm) by coating hard magnetic material $CoFe_2O_4$ (shell = 5 nm).

Interesting that for similar systems the opposed results may be obtained, for example, Liébana-Viñas et al. [155] observed stepped hysteresis attributed to spring magnets for core/shell $Fe_3O_4/CoFe_2O_4$ MNPs with the core of 9 nm and the size of core/shell system of 12 nm. At the same time, Lee et al. [161] observed a smoothed loop suggesting EC regime for the particles of a similar configuration. That can be attributed to hardly distinguished, at first glance, the difference in the structural properties: bordering of size distribution, diffusion of ions, quality of hard-soft interface, etc. Thus, to understand the magnetic structure, a detailed analysis of both structural and magnetic properties must be carried out, which will allow one to characterize the magnetic interparticle interactions and the distribution of magnetic anisotropies.

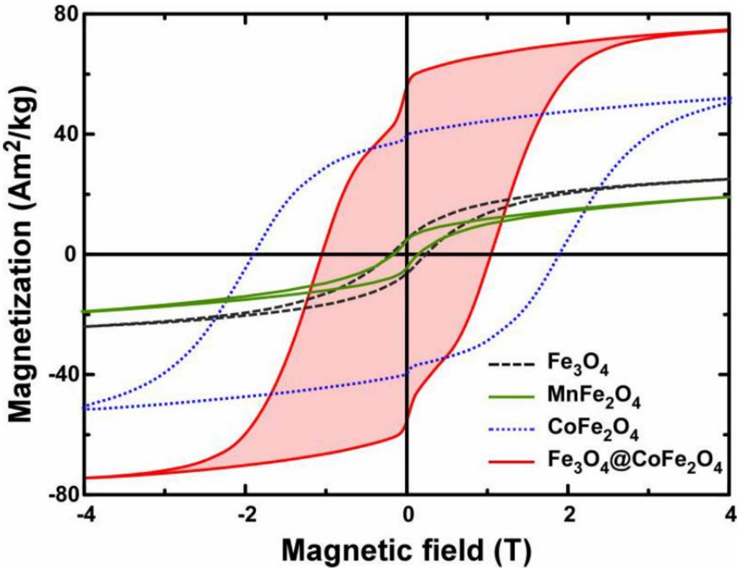

Figure 36. *M-H* hysteresis cycles for single-phase Fe_3O_4, $MnFe_2O_4$, $CoFe_2O_4$, and $Fe_3O_4/CoFe_2O_4$ core/shell MNPs at 5 K. Reprinted from [155].

Tuning of the core/shell chemical composition and the morphostructural features of the object (i.e. size of the core, thickness of the shell) add the necessary degrees of freedom for the precise tuning of magnetic properties for specific applications. The fine tuning of coercivity and blocking temperature have been achieved by modulation of shell thickness and order of soft and hard materials [153,164,175–178]. Despite the fact that a general trend of the simple linear dependence of the coercivity from the volume ratio of materials holds for the hard/soft system (eq.(19)), it was observed that it breaks when there is a transfer into inverted soft/hard [177]. As was reported by Song and Zhang [177], this linear trend is oversimplified and does not take into account magnetization reversal processes which are expected to be different when the order of shell and core materials changes. Moreover, it was demonstrated the significant effect of the surface spins on magnetic anisotropy in single magnetic phase nanoparticles [15]. For core/shell systems, a phenomenological model considering both surface and interface effects was developed by Trohidou et al. which estimated K_{eff} for two-phase exchange-coupled nanoparticle systems [179]:

$$K_{eff} = \frac{V^{Soft}}{V} K^{Soft} + \frac{V^{Hard}}{V} K^{Hard} + \frac{aS}{V} K_{inter} + \frac{a'S'}{V} K_{surf}, \qquad (56)$$

where K^{Hard} and K^{Soft} are the anisotropies of hard and soft phases, V^{Hard} and V^{Soft} are the volumes of the hard and soft phases, aS and $a'S'$ are the thickness and surface area of the interface and surface layers with anisotropy constants K_{inter} and K_{surf} respectively. It was found in this study that K_{inter} and K_{surf} were one order of magnitude higher than the bulk counterparts [179].

Varying the composition, the thickness of the shell and the sequence of layers allows adding further degrees of freedom to tune the magnetic properties and design multifunctional magnetic materials. Figure 37 shows linear dependence of coercivity versus the volume fraction of hard phase for hard/soft nanoparticles. However, this linear trend is oversimplified and does not take into account magnetization reversal processes which are expected to be different when the order of shell and core materials change.[177] For this reason, deviations are observed in inverted soft/hard systems (Figure 37) [177]. In this view, more efforts should be done to investigate comparatively normal (hard/soft) and inverted (soft/hard) core-shell systems [180].

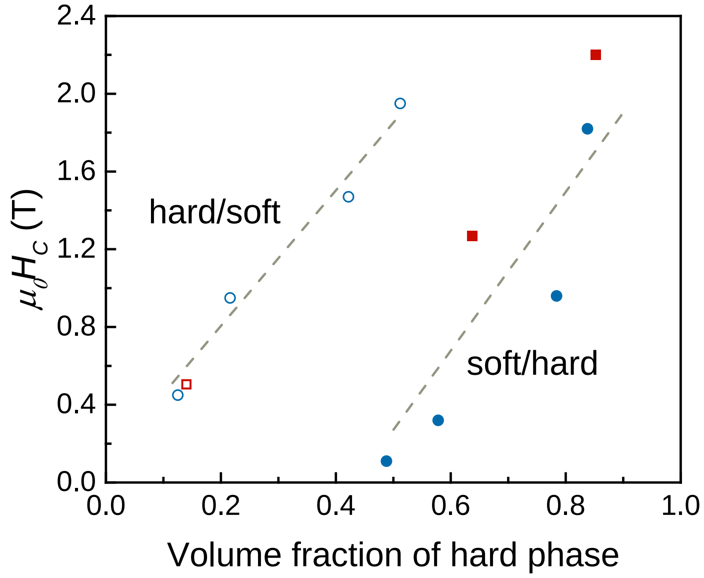

Figure 37. Dependence of coercivity on the volume fraction of the hard phase in $CoFe_2O_4/MnFe_2O_4$ and $MnFe_2O_4/CoFe_2O_4$ nanoparticles. Blue symbols are from ref. [177], red from ref. [178].

1.2.4.2 AFM/F(i)M systems

AFM/FM systems may cause an increase in magnetic anisotropy, which is exploited in different applications such as recording media, spintronics and permanent magnets [17,163,181,182]. Aside from the exchange bias (EB) phenomenon, resulting in unidirectional exchange anisotropy, an increase of the effective anisotropy energy of the FM phase has also been observed in AFM/FM systems [18,182]. On the other hand, bi-magnetic systems consisting of two FM or FiM interfaced phases, such as h-FM/s-FM core/shell MNPs, with tunable saturation magnetization, and magnetic anisotropy is beneficial to achieve, for example, contrast-enhanced magnetic resonance imaging or a high thermomagnetic effect [28,161,162,164,183,184]. Indeed, the magnetic properties of core/shell systems depend on the intrinsic parameters of h-FM and s-FM phases, as well as on the coupling strength and nanoparticle architecture which are controlled by the synthesis procedure (size of layers, quality of interface, shape, etc.) [164].

This shift is commonly accompanied by an increase in the coercivity of the F(i)M phase [17]. The high tuneability of the magnetic properties of complex TMO, which can manifest both FiM and AFM behaviors to changes in compositions, made them common building blocks for the realization of EB heterostructures.

Walid Baaziz et al., synthetized 11 nm-sized Fe_3O_4 MNPs using the TD of metal complexes method which were shelled with the 2 nm thick CoO layer in a seed-mediated growth process [185]. The AFM shell drastically increased coercivity up to ~1.5 T of s-FiM single-phase core (Figure 38). Moreover, core/shell system showed a large exchange bias of ~0.4 T at 5 K after cooling under the magnetic field of 7 T confirming the high quality of the core–shell interface. This confirms that the seed-mediated growth process is a promising method to produce MNPs with enhanced magnetocrystalline anisotropy for advanced applications.

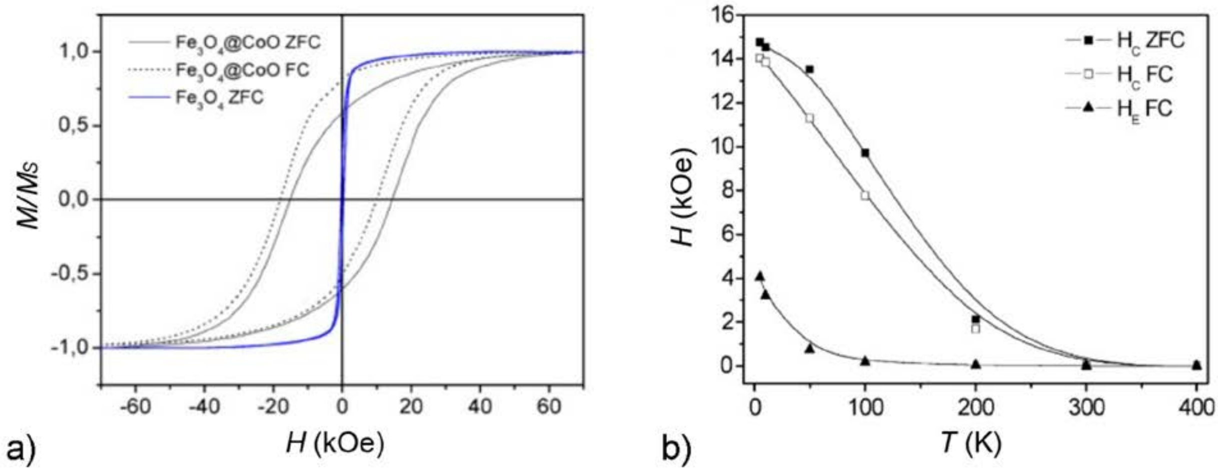

Figure 38. a) *M-H* hysteresis of 14 nm sized Fe_3O_4/CoO core/shell and 11 nm sized Fe_3O_4 single-phase MNPs; b) coercivity (H_C) and exchange bias field after cooling under 7 T (H_E) as functions of temperature of Fe_3O_4/CoO core/shell MNPs. Reprinted from [185].

Fabrication of nanocomposites containing TM monoxides as the AFM phase is particularly interesting owing to their relatively high magnetic anisotropy resulting in a large increase in coercivity and EB field [69]. Skumryev et al. observed a large EB field and a drastic increase of the blocking temperature from 10 to 290 K of 4 nm FM Co particles when they are embedded in an AFM CoO matrix [69]. It is worth mentioning that the EB effect does not always manifest with a shift of the hysteresis loop after field cooling; this generally happens in the case of very thin AFM layers or if the two phases have a similar magnetic anisotropy constant [186]. For example, the EB effect was not observed in $CoO/CoFe_2O_4$ MNPs in the size range 5–11 nm and with a core diameter ranging between 2.6–6.0 nm. Nevertheless, it was observed an increase in the coercivity from 2.2 T to 3.1 T at 5 K when the particle size is reduced.

The further enhancement of magnetic properties and be achieved by the design of multishell architectures. The scanning transmission electron microscopy (STEM) high-angle annular dark-field (HAADF) micrograph and electron energy loss spectroscopy (EELS) elemental maps showed $Fe_3O_4/CoO/Fe_3O_4$ core/shell/shell (CSS) MNPs prepared by a three-step seed-mediated growth based on the TD method. The Co is not homogeneously distributed because of the preferentially of CoO to grow on specific facets of the spinel structure. The thin shell of AFM CoO increases the coercivity of 10 nm core (C) Fe_3O_4 MNPs from 0.034 T up to 1.6 T at 300 K. The strong exchange coupling at the interface in Fe_3O_4/CoO core/shell (CS) MNPs was also manifested in the exchange bias field of 0.5 T observed after field cooling experiment. The second Fe_3O_4 shell reduces the coercivity until 1.5 T in $Fe_3O_4/CoO/Fe_3O_4$ CSS MNPs but increases saturation magnetization by more than at 50%. The resulted value of saturation magnetization was even higher than this value for bulk Fe_3O_4 which was explained by the transformation of the AFM CoO phase into FiM Co-doped ferrite.

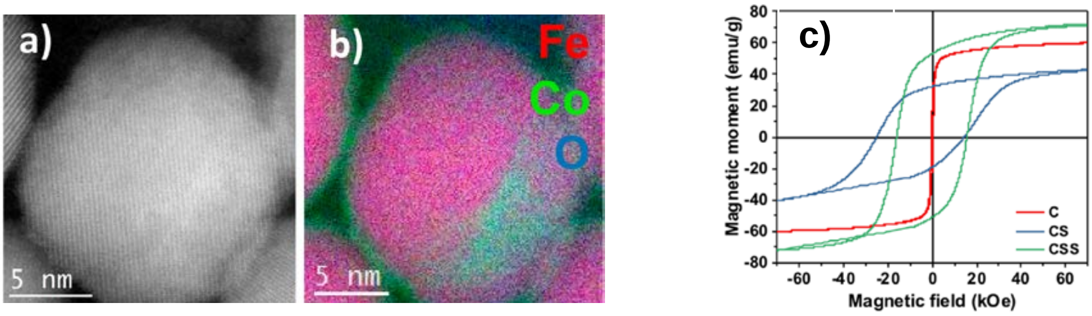

Figure 39. a) Dark field STEM-HAADF and b) STEM-EELS micrographs of $Fe_3O_4/CoO/Fe_3O_4$ core/shell/shell (CSS) MNPs. c) *M-H* hysteresis after field cooling under 7 T at 10 K for Fe_3O_4 (C), Fe_3O_4/CoO (CS) and CSS MNPs. Reprinted from [187].

The EB effect can be also observed at the interface between a F(i)M magnetic layer and a spin-glass system [80]. In very small MNPs with a high fraction of frustrated surface spins, at temperatures lower than the glassy temperature (T_g), this sort of spin became frozen and acts as a spin-glass. Such spin-glass-like frozen surface spins may act as a magnetically hard phase increasing anisotropy and leading to the intrinsic EB effect in chemically single-phase systems [81,82].

A very important but basically not explored issue is the interplay between intra- and interparticle interactions in core/shell MNPs and their influence on macroscopic magnetic properties. Ming Da Yang et al. [183], demonstrated that modulating interparticle interactions in core/shell systems allows for stabilisation of suspension properties, thus increasing the heat performance in hyperthermia as well as R2 relaxivity for contrast enhancement in MRI. Samuel D. Oberdick et al. employed theoretical calculations to describe the experimental data revealing that the DMI effect on the magnetic frustration of the shell spins, resulting in the canting of the net magnetic moment of bi-magnetic $Fe_3O_4/Mn_xFe_{1-x}O_4$ ($x > 0.8$) particles [71]. Moreover, interparticle interactions lead to the correlation of spin canting angle between neighbouring particles. Thus, the macroscopic magnetic properties of this system are determined by the strong interplay of mutually dependent intra- and interparticle interactions. Theoretical description of interacting bi-magnetic core/shell nanoparticles is a complex task due to the need to consider both long- and short-range interactions, to complete this task a mesoscopic model has been developed by M. Margaris et al. [188].

Conclusions:

1) Magnetic properties of oxide MNPs can be tuned by chemical composition affect the magnetocrystalline anisotropy;
2) The structure of particle core (inversion degree of spinel) and surface properties depend on the method of synthesis and also strongly affect magnetic properties;
3) Precise control of magnetic properties of particles can be achieved by the creation of complex nanohybrids but presented in literature data sometimes contradictive and more experimental data are needed.

Chapter 2. Materials and methods

2.1 Synthesis methods

Sol-gel autocombusion (SGAC)

In this method, the 1-molar aqueous solutions of metal salts in distilled water (DW) were prepared with different molar ratios. In all syntheses, the hydrous metal nitrates $Fe(NO_3)_3 \cdot 9H_2O$, $Co(NO_3)_2 \cdot 6H_2O$, $Ni(NO_3)_2 \cdot 6H_2O$ and $Zn(NO_3)_2 \cdot 6H_2O$ were used. The molar ratio was set to maintain the desired stoichiometry of resulted ferrite. Afterwards, the preliminary prepared 1-molar citric acid (CA, $C_6H_8O_7$) solution of the same volume was added to mixtures of metal salts under magnetic stirring. The pH level was adjusted to the value of 7 by dropwise adding 30% ammonia solution. The obtained sol was dried at the hotplate for about 60 min at 150 °C to form a gel. Then the temperature was increased up to 300 °C to induce the self-combustion reaction. Obtained powders were collected and ground with an agate mortar. Figure 40 shows the principal scheme of $CoFe_2O_4$ MNPs synthesis with SGAC method. The SGAC method was used to produce MNPs in [148,149].

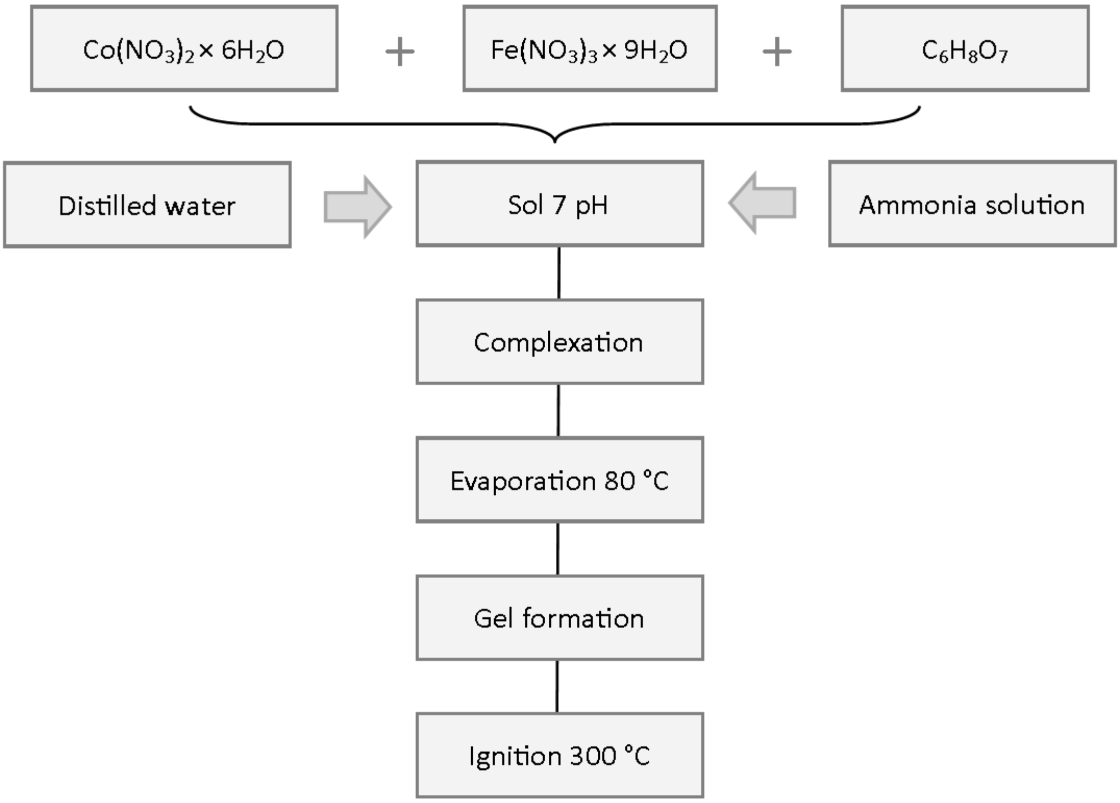

Figure 40. Schematic representation of $CoFe_2O_4$ MNPs preparation technique.

Co-precipitation (CP)

The modified Massart method of CP ([189]) was used. The modifications were concluded in the synthesis of MNPs in presence of ligands citric acid or glycine for *in situ* surface coating and particle growth control. The CP method was used to produce iron oxide MNPs in [190].

To synthesize CA covered iron oxide MNPs, 5 mM of $\mathrm{Fe(SO_4)\cdot 7H_2O}$ were dissolved with stirring in 50 ml of DW in a round bottom flask at room temperature. After that, 10 mM of $\mathrm{FeCl_3\cdot 6H_2O}$ were added to the flask with vigorous stirring, followed by the addition of CA concentration of 0.05 M. The solution was heated up to 80 °C and subsequently 20 ml of 3 M solution of NaOH, preheated up to 80 °C, was poured into the above solution and kept under the vigorous stirring for 2 h. The reaction can be written:

$$\begin{matrix}\mathrm{FeCl_3\cdot 6H_2O}\\ +\\ \mathrm{Fe}(SO_4)\ \cdot 7\mathrm{H_2O}\end{matrix} \xrightarrow[\mathrm{NaOH}]{\mathrm{H_2O}+ligand,\ 80^{\circ}\mathrm{C}} Fe_{3-\delta}O_4\,(MNPs) \tag{57}$$

The black precipitate obtained after the synthesis was washed several times with deionized water and ethanol. After drying at room temperature in the fume hood, the final powder was collected for further analysis. Following the same procedure, samples with 0.05, 0.1, 0.2 and 0.3 M of CA were synthesized and the concentration of CA was used as a sample name.

To produce samples in the presence of glycine ($\mathrm{NH_2–CH_2–COOH}$), 0.1 mol $\mathrm{FeSO_4\cdot 7H_2O}$ and 0.2 mol $\mathrm{FeCl_3\cdot 6H_2O}$ were dissolved in 50 ml DW and added into a 100 mL flask, which was immersed in a room temperature (~25 °C) water bath. Then the glycine was added to set the concentration of 0.06 mol/L in the reaction solution throughout the reaction. 3 mol of NaOH was dissolved in 20 mL DW. The reaction solution was mechanically stirred at 800 rpm while heating up to 80 °C. After reaching a temperature of 80 °C, NaOH was added dropwise to the mixture, stirring was continued for 2 h. This procedure was repeated with different glycine concentrations of 0.10, 0.15, 0.30 and 0.60 mol/L.

At the end of this reaction time, the solutions were decanted, allowing the particles to be washed with ethanol and centrifuged at 2900 rpm for 10 minutes. This procedure was repeated twice, then the particles were separated and dried overnight at 70 °C.

High-temperature decomposition (HTD)

For the synthesis of all core/shell and multishell structures, a seed-mediated growth and high-temperature decomposition of metal acetylacetonate salts approaches were applied. All the syntheses were conducted under oxygen-free conditions in a Schlenk line.

The core was synthesized using a modified procedure reported elsewhere [191]. For example, to obtain the $CoFe_2O_4$, $Fe(C_5H_7O_2)_3$ (2 mmol, 0.706 g), $Co(C_5H_7O_2)_2$ (1 mmol, 0.267 g), 1,2-hexadecanediol (10 mmol, 2.58 g), oleic acid (OA, 6 mmol, 1.69 g) and oleylamine (OLA, 6 mmol, 1.60 g), were dissolved in benzyl ether (20 mL) and magnetically stirred under a flow of nitrogen. The mixture was heated (5 °C/min) up to 200 °C for 100 min and then heated (5 °C/min) to reflux (~300 °C) for 60 min. The black-colored mixture was left to cool to room temperature (RT ~25 °C) and washed with toluene and isopropanol. Next, the precipitate was washed with ethanol and collected by centrifugation (4000 rpm, 10 min).

A seed-mediated growth at high temperature was used to achieve core/shell nanoparticles. For example, to produce $CoFe_2O_4/NiFe_2O_4$ MNPs, $CoFe_2O_4$ seeds were sonicated in 5 ml benzyl ether in the presence of OA (600 μl). Subsequently, the suspension was added to the flask containing $Ni(C_5H_7O_2)_2$ (0.33 mmol, 0.0848 g), $Fe(C_5H_7O_2)_3$ (0.67 mmol, 0.237 g) and OA (600 μl) were dissolved benzyl ether (15 ml). After 1 h under vacuum at RT, the solution was heated to reflux at 290 °C (5 °C/min) under argon atmosphere and kept at this temperature for 30 min. The reaction can be simplified as:

$$\underset{1^{\text{st}}\ \text{step}}{\underline{\begin{matrix}\text{Fe(acac)}_3\\ +\\ \text{Co(acac)}_2\end{matrix}\xrightarrow[300℃]{\text{AO,OLA}}}}\quad \underset{2^{\text{nd}}\ \text{step}}{\underline{\text{CoFe}_2\text{O}_4\text{(seeds)}+\begin{matrix}\text{Fe(acac)}_3\\ +\\ \text{Ni(acac)}_2\end{matrix}\xrightarrow[290℃]{\text{AO}}}}\quad \underset{\text{result}}{\underline{\text{CoFe}_2\text{O}_4/\text{NiFe}_2\text{O}_4}} \tag{58}$$

The HTD method was used to produce core/shell MNPs in [180,192].

2.2 Morphostructural characterization

X-Ray Diffraction (XRD) structural analysis

The crystalline properties of nanoparticles were carried out using an X-Ray diffractometer (XRD) with Bragg-Brentano 2θ geometry. X-Rays have wavelengths comparable to the distance between different crystallographic planes. The phenomenon of diffraction is described by the Bragg equation, where this effect is defined as the reflection of X-Rays on the lattice planes. Interference occurs if the path of the radiation differs from an integer multiple of the wavelength:

$$2d_{hkl}sin\theta = n\lambda, \tag{59}$$

where d_{hkl} is the distance between the grating planes determined by the Miller indices (hkl) characterizing the planes under consideration, θ is the angle of incidence, and λ is the wavelength of the incident radiation (for Cu Kα radiation λ = 1.54056 Å, for Co Kα source λ = 1.78919 Å). The lattice parameter of cubic structure (a) can be calculated by the equation

$$a = d_{hkl}\sqrt{h^2 + k^2 + l^2}. \tag{60}$$

The mean size of crystallites, d_{XRD}, was calculated by using Scherrer's equation [117,193,194]:

$$d_{XRD} = \psi\,\lambda\,/\,\beta cos\,\theta, \tag{61}$$

where ψ is a crystallite-shape factor (0.94 for spherical particles), β is the full width at half-maximum (FWHM) of peaks of the corresponding reflections at 2θ geometry.

Electron Microscopy

Transmission Electron Microscopy (TEM) is a technique based on the interaction of a high energy electron beam passing through a very thin sample. TEM images provide information about the internal structure of particles while scanning electron microscopy (SEM) scans a focused electron beam over a surface and provide information primarily about the external structure. Both electron microscopy methods are the most commonly used method for measuring particle sizes [195].

Statistic distributions of particle size were obtained elaborating STEM images with ImageJ software on more than 200 particles. A log-normal function was utilized to fit the particle size distribution [194]:

$$f(d) = \frac{1}{\sqrt{2\pi}\, d\, ln\, \sigma} exp\left[-\frac{ln^2\left(\frac{d}{d_{TEM}}\right)}{ln^2\, \sigma} \right], \tag{62}$$

where d_{TEM} is the median value of particle diameter and the standard deviation (SD) of the size distribution is $d_{TEM} \cdot e^{\sigma^2/2} \cdot \sqrt{e^{\sigma^2} - 1}$.

The additional data about internal structure can be obtained by high-resolution TEM-electron energy loss spectra (HRTEM-EELS) or energy-filtered TEM (EFTEM) maps. For example, compositional information regarding the structure of core/shell systems has been used.

2.3 Magnetic properties

Magnetometer instrumentations

The principle of operation of the vibrating-sample magnetometer (VSM) is based on the use of Faraday's law of electromagnetic induction [53]. If the sample under study, having magnetic moment μ makes harmonic oscillations with frequency ω and amplitude A, it is a magnetic dipole producing electromagnetic signals. The electromotive force (E) in the pickup coils depends on the magnitude of the magnetic moment of the sample and the direction of the sample velocity, as well as on the number (N) and location of pickup coils having the geometric factor $G(r)$:

$$E = \frac{1}{2} \mu G(r) N A cos(\omega t). \tag{63}$$

The VSM consists of four main blocks (Figure 41): electromagnet powered by direct current (DC) from the power supply, vibration unit, block of adjustments and measuring signals (electronics).

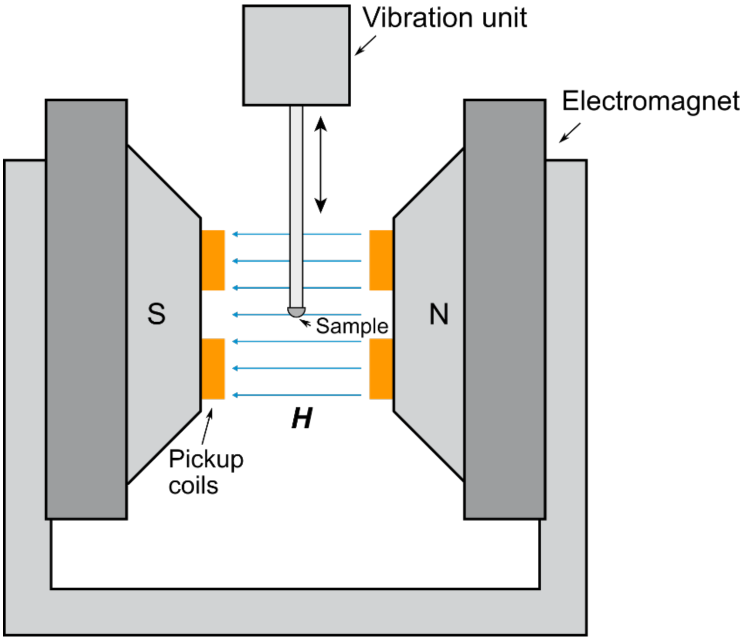

Figure 41. Schematic representation of a VSM.

The better sensitivity compared to VSM based on Faraday's induction can be provided by the superconducting quantum interferometer device (SQUID). SQUID as a magnetometer is formed by two superconductors separated by thin insulating layers that form two parallel Josephson junctions connected by conductive elements to an external circuit. The principle behind the transition of flux quantum into the current is the effect of electron tunneling through the insulating material. This leads to an ordered motion of electrons having a definite wave function described by Cooper pairs.

Analysis of the field dependences of magnetization

Field dependence of magnetization $M(H)$ typical for MNPs sample below the Curie and blocking temperatures shows classical M-H hysteresis cycle characterized by remanence (M_R) and coercivity (H_C) (Figure 42 a). The magnetization path starts from the initial magnetization collecting the magnetization values passing from zero field to the maximal field affordable by the magnetometer (in the case of MNPs, the high magnetic field are needed to saturate the sample). Then the descending branch of magnetization (M_{des}) is recorded up to the maximal negative field and, finally, the ascending (M_{asc}) branch is collected when the field increases up to the maximal positive field.

From measured *M-H* cycles, M_R and H_C values were determined as averaged values from $M_{des}(H)$ and $M_{asc}(H)$ branches:

$$H_C = \frac{H_{C+} - H_{C-}}{2}, \tag{64}$$

$$M_R = \frac{M_{R+} - M_{R-}}{2}. \tag{65}$$

The irreversibility field was defined as a field at which the difference between $M_{des}(H)$ and $M_{asc}(H)$ branches is 3%:

$$\frac{M_{des}(H_{irr}) - M_{asc}(H_{irr})}{M_{des}(0) - M_{asc}(0)} \times 100\% = 3\%. \tag{66}$$

If the sample of MNPs is below Curie temperature but above the blocking temperature (SPM regime), the *M-H* dependence is unhysteretic function described by the Langevin function (Figure 42 b). Analysis of such dependencies can be obtained by fitting the experimental data using the Langevin function, which considers the particle size distribution function.

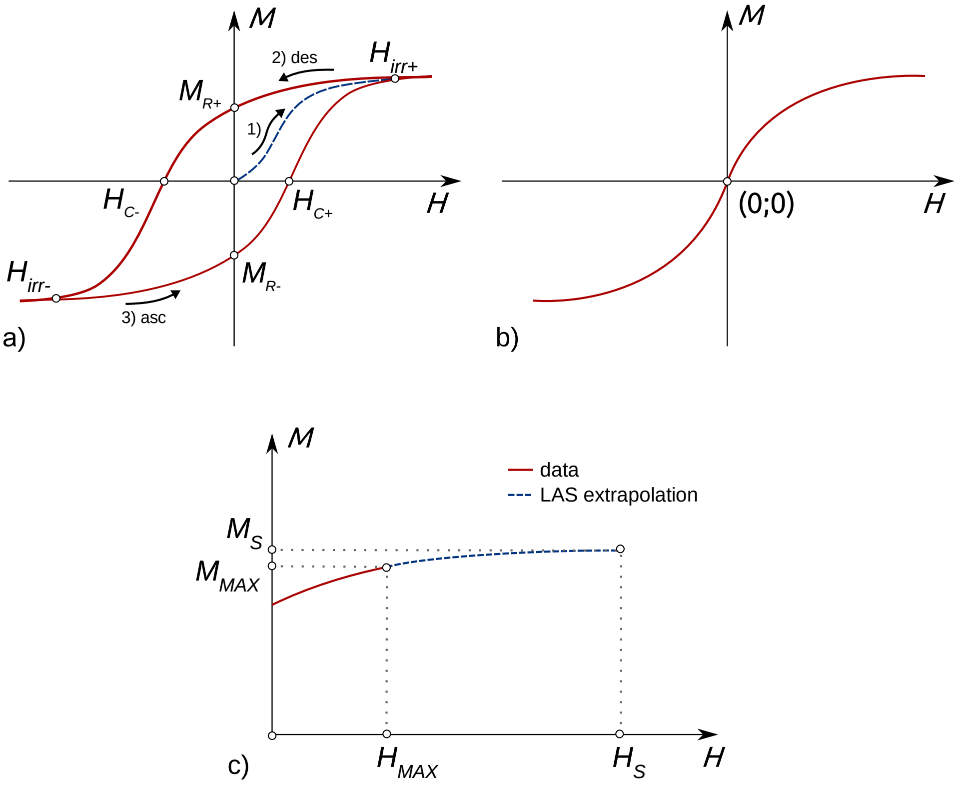

Figure 42. Schematic representation of typical *M-H* curve for a) blocked F(i)M and b) superparamagnetic systems; c) extrapolation of descending branch of high-field region of *M-H* curve.

As we already noted, to saturate the sample of MNPs the high saturation magnetic field (H_S) are needed. In some cases, those fields are above the maximal field (H_{MAX}) affordable by the laboratory magnetometer. In this case, the saturation magnetization (M_S) has been estimated by approximating the high-field region of the measured *M-H* curve by the Law of Approach to Saturation (LAS) [77,101,148,196]:

$$\lim_{H\to\infty}(M(H)) = M_S; \tag{67}$$

$$M(H) = M_S \cdot \left(1 - \frac{a}{H} - \frac{b}{H^2}\right), \tag{68}$$

where *a* and *b* are fitting parameters. The *a/H* term arises from the local stress caused by the crystalline defects according to Brown's theory [197]. In Akulov's theory, the b/H^2 term connects deviation of magnetization from saturation and magnetic crystallographic anisotropy of the material, which is a system of randomly oriented crystallites [52]:

$$b = \kappa\left(\frac{K}{\mu_0 M_S}\right)^2, \tag{69}$$

where κ is the dimensionless constant characterizing the dispersion of local easy axes magnetization (in the case of uniaxial anisotropy $\kappa=1/15$, in the case of cubic anisotropy $\kappa=2/105$ [198]). Iskhakov and Komogortsev extended the LAS for nanocrystalline and amorphous materials based on scaling in ferromagnets with random magnetic anisotropy [199].

In the case of two-phase systems, when one phase is dia- or paramagnetic the unsaturated magnetic susceptibility (χ_{SAT}) can be expected and it can be considered in the LAS as following [101]:

$$M(H) = M_S \cdot \left(1 - \frac{a}{H} - \frac{b}{H^2}\right) + H \cdot \chi_{SAT}. \tag{70}$$

The unsaturated magnetic susceptibility in or in a single-phase system of very small particles is closely related to the acting as a second magnetic phase, the noncollinear spin structure due to competing interactions between sublattices and symmetry breaking on the particle surface [82,200].

In order to estimate the nature and the intensity of the interparticle interactions, the remanence plot method based on SW model of hysteresis ([61,180,192,201]) was applied. In this method, the isothermal remanent magnetization (IRM) and direct current demagnetization (DCD) measurements were performed (Figure 43). The IRM magnetization curve was obtained starting from an initial state (the freshly prepared sample which was not subjected to magnetic field). The remanence $m_{IRM}(H_{app})$ was collected applying a gradually increasing positive magnetic field up to $\mu_0 H_{max}$, which was then removed. The $m_{DCD}(H_{app})$ curve was measured by saturating the sample in the negative field $-\mu_0 H_{max}$ and then measuring the remanence $m_{DCD}(H_{app})$ after applying reverse fields up to $\mu_0 H_{max}$.

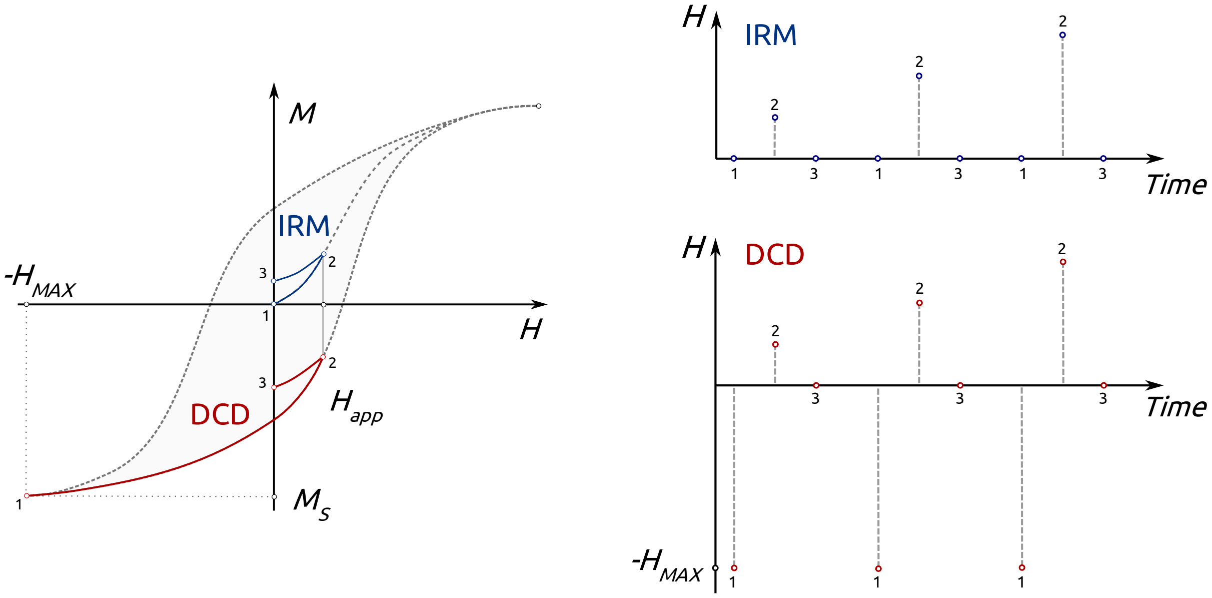

Figure 43. The procedure for measuring the residual IRM (blue) and DCD (red) magnetizations: (1) – initial state, (2) – magnetization at H_{app} and (3) – residual.

For an assembly of SD magnetic particles with uniaxial anisotropy is described by the Wohlfarth model [202]:

$$m_{DCD}(H_{app}) = 1 - 2 \cdot m_{IRM}(H_{app})\,. \tag{71}$$

The Henkel plot is m_{DCD} plotted versus the argument $1-2m_{IRM}$. The deviation from the linear relationship indicates the interparticle interactions. The downward concavity of the curve implies negative interparticle interactions stabilizing the demagnetized state. The upward concavity implies positive interparticle interactions promoting the magnetized state [203]. The Kelly plot can be implied to quantitatively analyze the interaction intensity [204]:

$$\delta m(H_{app}) = m_{DCD} - (1 - 2 \cdot m_{IRM}) . \tag{72}$$

where the $\delta \mathrm{m}(\mathrm{H}_{\mathrm{app}})$ can be considered as a quantitative parameter of interparticle interactions (in non-interacting case, $\delta m = 0$) [205].

The analysis of interparticle interactions can be performed by the calculation of the interaction field $\mu_0 H_{INT}$ defined as half the difference in the position of the maximum ($\mu_0 H_{Cr}$) of the derivatives $dm_{DCD}(H_{app})/dH_{app}$ and $dm_{IRM}(H_{app})/dH_{app}$:

$$H_{INT} = \frac{H_{Cr}^{DCD} - H_{Cr}^{IRM}}{2} . \tag{73}$$

The differentiated remanence curves represent the irreversible component of the susceptibility. This quantity can be considered as a measure of the energy barrier distribution, which, in a nanoparticle system, is associated with the switching field distribution (SFD) [206,207]. For a system of SW particles, SFD can be considered proportional to the distribution of particle's individual magnetic moment switching in an external magnetic field close to the anisotropy field. The H_{Cr}^{DCD} and H_{Cr}^{IRM}can be considered as remanence coercivity values.

Analysis of the temperature dependences of magnetization

The zero-field and field cooled magnetization (ZFC-FC) measurements are common way to characterize magnetic properties of MNPs, in particular, they provide information about the distribution of blocking temperature [15,96]. In section "1.1.6 Superparamagnetism", the theoretical background behind these measurement procedures is given. In the experiment, to record $M_{ZFC}(T)$, the samples were cooled down to a low temperature (4.2–5 K) in the absence of a magnetic field (Figure 44). Afterwards, the measuring magnetic field (10–25 mT) was applied, and the magnetization was recorded during heating from low temperature to 300 K. To record $M_{FC}(T)$, the samples were cooled in the magnetic field (10–25 mT) and then the magnetization was recorded during the heating in the same measuring field. The position of the maximum of the ZFC magnetization curve (T_{max}) was estimated by the fitting of $M_{ZFC}(T)$ with the Gaussian function in the region near the maximum. The irreversibility temperature (T_{irr}) was estimated as the temperature where

$$\frac{M_{ZFC}(T_{irr}) - M_{FC}(T_{irr})}{M_{ZFC}(T \to 0) - M_{FC}(T \to 0)} \times 100\% = 3\%. \tag{74}$$

To define, the blocking T_B, the first derivative of the difference $M_{ZFC}(T)-M_{FC}(T)$ versus the temperature was calculated. And average T_B was defined as the temperature at which the integral value (area under the $d(M_{ZFC}(T)-M_{FC}(T))/dT$)) after appropriate normalization is 50%. Alternatively, in some cases, instead of calculating the difference, the TRM magnetization was measured which is $M_{TRM}(T) \sim M_{FC}(T) - M_{ZFC}(T)$.

The memory effect was probed by the *stop&wait* ZFC protocol following refs. [208,209]. A set of ZFC *M-T* curves has been recorded after the prelaminar cooling of the sample with different waiting times order of several hrs. at a temperature of about half of the position of the peak of the reference ZFC curve.

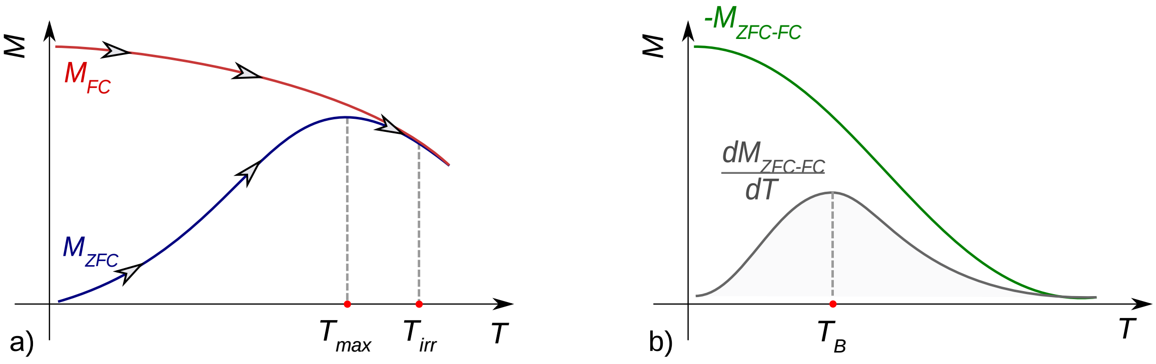

Figure 44. a) The procedure for measuring the ZFC (blue) and FC (red) magnetizations; b) the difference between ZFC and FC curves and its derivative.

Analysis of the time dependences of magnetization

Considering the Néel relaxation mechanism, the dependence of magnetization on logarithmic time is given by the following expression

$$M(t) = M_0 \pm S \, ln\left(\frac{t}{\tau_N}\right), \tag{75}$$

where S is the magnetic viscosity and t_0 is the reference time. According to Néel theory [192,210], the fluctuation field ($\mu_0 H_f$) can be used to describe the effect of temperature on the demagnetization process:

$$\mu_0 H_f = \frac{S}{\chi_{irr}}, \tag{76}$$

where χ_{irr} is irreversibility susceptibility defined as a peak value of the first derivative of the DCD remanence (dM_{DCD}/dH_{app}). This field describes the effect of the thermal fluctuations on magnetization reversal processes leading to an equilibrium thermodynamic state. Based on this concept, the magnetic activation volume (V_{act}) was defined as a volume of magnetic material simultaneously involved in the process of overcoming the energy barrier. For SD particles with uniaxial anisotropy, V_{act} is:

$$V_{act}^{uniaxial} = \frac{k_B T \chi_{irr}}{M_S S}, \tag{77}$$

In the case of the dominating cubic anisotropy, the MNPs have more easy axes and thus the energy barrier separating the minimums of the potential energy of magnetization states is lower. Thus, it was shown in the first approximation that [203]:

$$V_{act}^{cubic} = 4 \times V_{act}^{uniaxial}. \tag{78}$$

In the experiment, the S coefficient was found through relaxation measurements [78,203] in which the sample was cooled down to 5 K, afterwards saturated in the magnetic field of −5 T. Then the positive magnetic field ($\mu_0 H_{app}$) was applied and magnetization M^* as a function of time was recorded during 2 hrs. In this way, a set of $M(t)$ curves was recorded at different $\mu_0 H_{app}$ around the coercivity of the $M_{DCD}(H)$ [15,211]. The procedure of measuring a single relaxation curve is given in Figure 45.

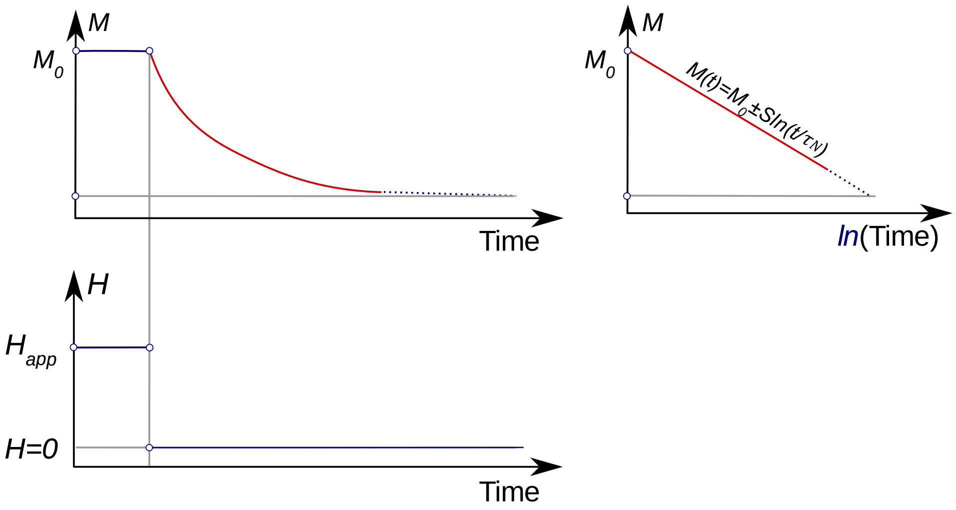

Figure 45. The procedure for relaxation measurements.

Chapter 3. Effect of chemical composition on the magnetic structure of spinel ferrite MNPs

One of the main sources of magnetic anisotropy in magnetic materials is the magnetocrystalline anisotropy occurring due to spin-lattice interaction. It is in strong dependence on the chemical and structural composition of magnetic material. Among magnetic TMO with spinel structure, the cobalt ferrite has the higher value of magnetic anisotropy constant at the nanoscale, which is about 1−2 orders of magnitude higher than in other spinel ferrites. This chapter is devoted to the study of the magnetic properties of spinel ferrite MNPs prepared by sol-gel autocombustion (SGAC) and hydrothermal coprecipitation (CP) methods. The cobalt ferrites doped with zinc and nickel are under investigation. The effect of the chemical composition of these materials on the magnetic, structural and magnetostructural properties of obtained MNPs is discovered.

On basis of the results reported in section 3.1.1 a paper was published in the Journal of Magnetism and Magnetic Materials [148], of section 3.1.2 in Materials [149].

3.1 Cobalt ferrites MNPs doped by zinc and nickel prepared by SGAC

3.1.1 Structural and magnetic properties of $Ni_xCo_{1-x}Fe_2O_4$ MNPs

The XRD patterns of $Ni_xCo_{1-x}Fe_2O_4$ nanoparticles with $x = 0, 0.25, 0.5, 0.75$ and 1 prepared via a SGAC method indicate the high crystallinity of nanoparticles without amorphous content (Figure 46). The main diffraction reflections were indexed to the inverted cubic spinel lattice for cobalt and nickel ferrites. The positions of the main peaks are almost equivalent for both ferrites (Table 2) since the Co and Ni ions preferentially occupy the same positions in spinel, a small deviation of about 0.5° is due to the difference in the sizes of Co^{2+} (0.74 Å) and Ni^{2+} (0.72 Å) ions [212].

The average size of crystallites d_{XRD} was calculated for (440) peak with Scherrer's formula (eq.(61)). Calculated d_{XRD} values of all samples of mixed ferrites are slightly higher than for pure cobalt and nickel ferrites. The increase of parties size with the increase of nickel content and the decrease of particle size for a pure nickel ferrite was observed earlier for Co-Ni ferrites prepared via a hydrothermal route [212]. The XRD patterns for samples with a content of nickel less than 0.75 suggest the presence of only a single phase of cubic spinel. With the increase of nickel content, the satellite peaks referred to the hexagonal hematite and to the cubic metallic nickel were observed [213].

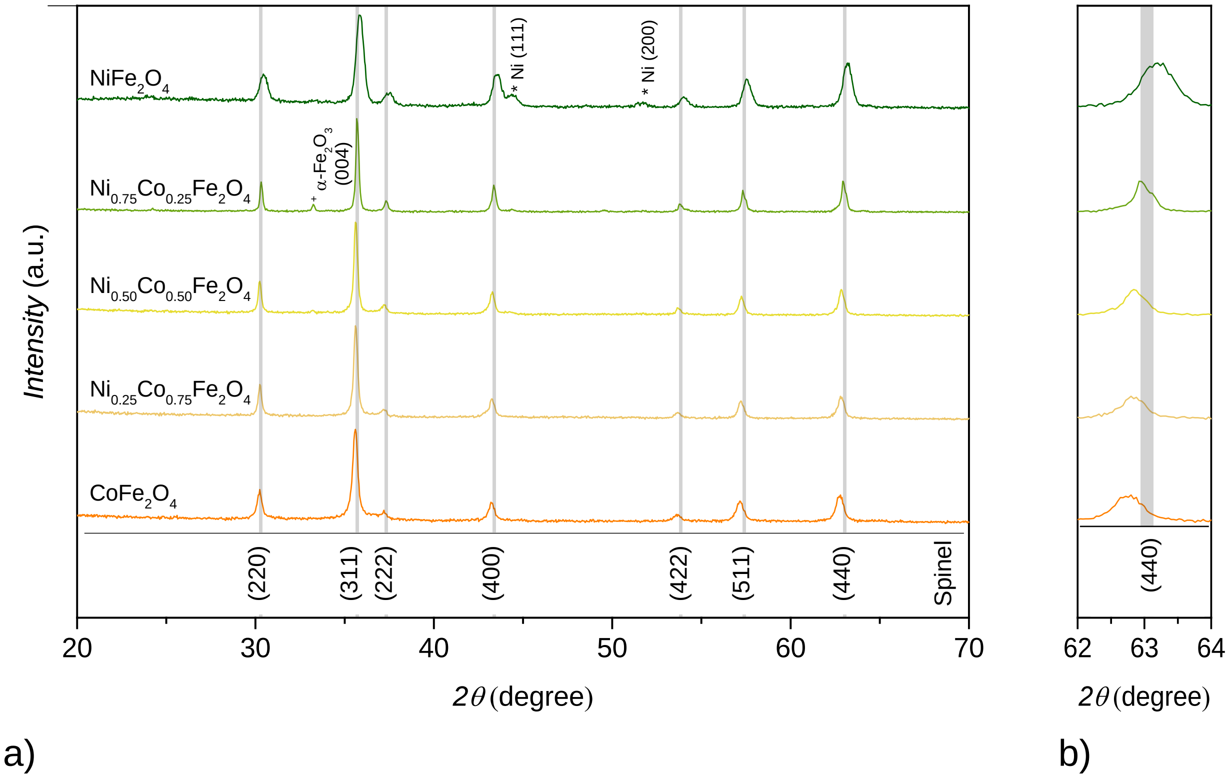

Figure 46. a) XRD spectra of Ni$_x$Co$_{1-x}$Fe$_2$O$_4$ MNPs (Cu Kα radiation); b) zoomed region of (440) reflection showing the shift of peak position [148].

Table 5. Chemical composition and microstructural properties of Ni$_x$Co$_{1-x}$Fe$_2$O$_4$ with x = 0, 0.25, 0.5, 0.75 and 1. Crystallite size (d_{XRD}) were calculated with Scherrer's equation on (440) peak. Uncertainties in last number are given in brackets.

x	**Composition**	**Peak position 2θ, degree**	**FWHM, degree**	**d_{XRD}, nm**
0	CoFe$_2$O$_4$	63.2±0.1	0.58±0.01	17±2
0.25	Ni$_{0.25}$Co$_{0.75}$Fe$_2$O$_4$	63.0±0.1	0.33±0.01	29±3
0.50	Ni$_{0.50}$Co$_{0.50}$Fe$_2$O$_4$	62.9±0.1	0.39±0.01	25±3
0.75	Ni$_{0.75}$Co$_{0.25}$Fe$_2$O$_4$	62.8±0.1	0.43±0.01	23±3
1	NiFe$_2$O$_4$	62.7±0.1	0.49±0.01	20±2

According to TEM and SEM images, the particles have a complex irregular shape with distinct cubic facets (Figure 47). The sharp shape confirms the fact that the particles have a high crystallinity caused by a high temperature during the particle growth process. The particles are strongly aggregated in particular because of the strong dipole-dipole interactions between particles.

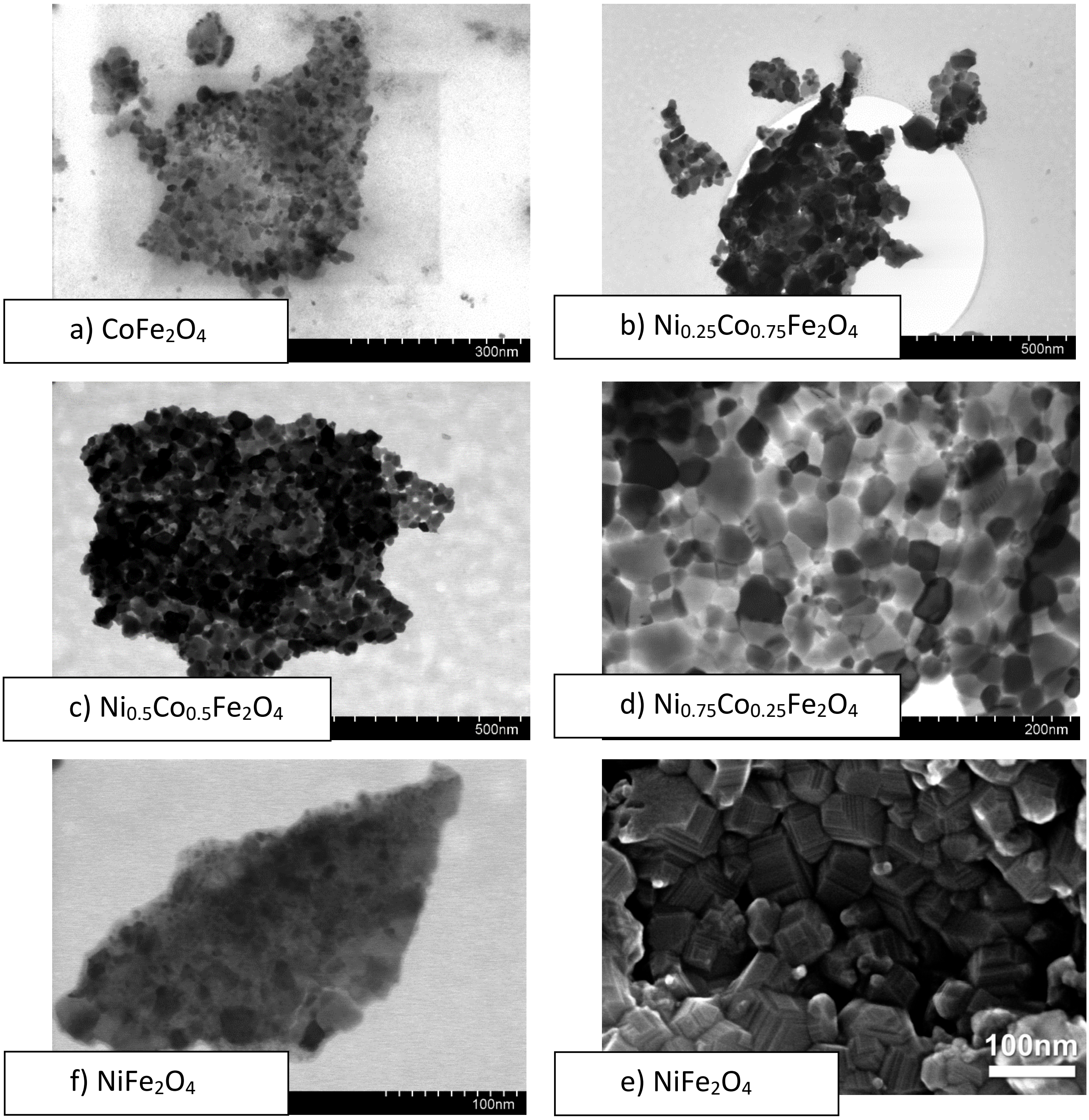

a) $CoFe_2O_4$

b) $Ni_{0.25}Co_{0.75}Fe_2O_4$

c) $Ni_{0.5}Co_{0.5}Fe_2O_4$

d) $Ni_{0.75}Co_{0.25}Fe_2O_4$

f) $NiFe_2O_4$

e) $NiFe_2O_4$

Figure 47. a-f) TEM microphotography images of Co-Ni ferrite MNPs; e) SEM image of $Ni_{0.75}Co_{0.25}Fe_2O_4$ powder [148].

The room temperature (295 K) hysteresis loops confirm a blocked ferrimagnetic behavior for all Co/Ni ferrite MNPs (Figure 48). The monotonic shape of hysteresis loops without any kinks proves the lack of separate Co- and Ni-rich phases confirming the structural properties by XRD [139]. The monotonical decrease of coercivity with the increase of nickel content from 132±1 mT to 20.5±0.3 mT for $CoFe_2O_4$ and $NiFe_2O_4$ samples respectively was observed (Table 6). The decrease in anisotropy is due to the strong single-ion anisotropy of Co^{2+} ions. Indeed, the $CoFe_2O_4$ is the (semi-)hard magnetic material with a bulk magnetic anisotropy constant of $\sim 30 \cdot 10^4$ J/m^3 while $NiFe_2O_4$ is soft with magnetic anisotropy constant of $\sim 0.7 \cdot 10^4$ J/m^3.

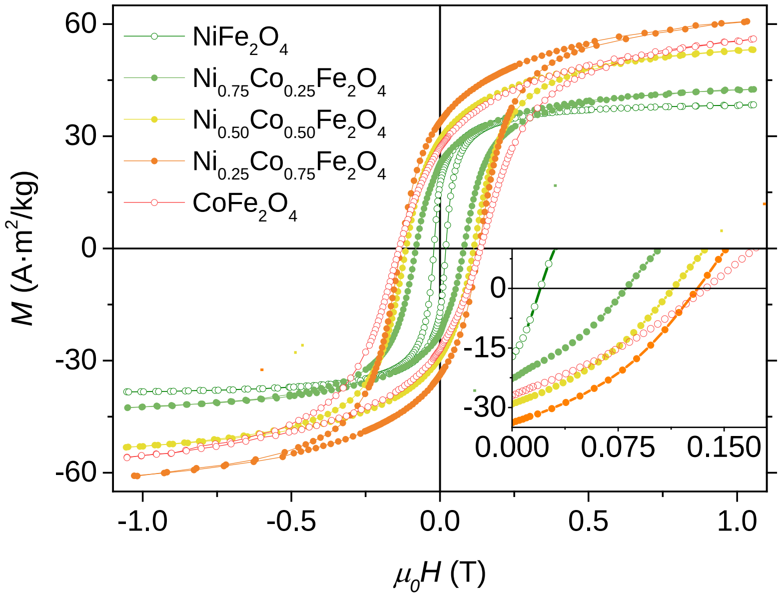

Figure 48. *M-H* loops of Co/Ni ferrite MNPs (~295 K) [148].

Table 6. Magnetic properties of $Ni_xCo_{1-x}Fe_2O_4$ MNPs (295 K).

x	$\mu_0 H_C$, mT	$\mu_0 H_{Cr}^{DCD}$, mT	M_S, $A \cdot m^2/kg$	M_R/M_S	K_{eff}, $\times 10^4$ J/m^3
0	132±1	175±5	65.8±0.6	0.44±0.04	14±1
0.25	131±2	149±5	69.1±0.3	0.49±0.02	13±1
0.50	113±2	132±5	59.5±0.3	0.49±0.02	15±1
0.75	80.6±0.6	91±4	46.9±0.4	0.54±0.05	17±1
1	20.5±0.3	21±1	40.3±0.5	0.43±0.05	5.8±0.7

Room temperature saturation magnetization of samples was estimated using LAS method explained in the experimental section (Table 6). The sample with the smallest nickel content $Ni_{0.25}Co_{0.75}Fe_2O_4$ ($x = 0.25$) shows a sufficiently high value of M_S

concerning the sample of pure cobalt ferrite $x = 1$. This phenomenon was observed earlier in mixed ferrites [214]. Deviation from linear behavior of M_S versus Co^{2+}/Ni^{2+} content attributed to non-equilibrium cation distribution.

The M_R/M_S ratio of around 0.5 implies that the particles have to dominate uniaxial anisotropy according to the SW model [61]. The SD state of particles is followed by the grain sizes calculated from XRD, and observed on SEM and TEM images, which are lower than the critical size. Interesting, the observed M_R/M_S values suggest the uniaxial symmetry of effective magnetic anisotropy despise the cubic magnetocrystalline anisotropy of bulk cobalt ferrite which predict this value of about ~0.8 [215]. This can be explained by the effects of magnetic interparticle interactions or demagnetization induced caused by particles` shapes [156,193].

For MNPs with uniaxial anisotropy, the values of the effective anisotropy constant can be estimated from the anisotropy field $\mu_0 H_K$ (eq.(16)). Calculated values of K_{eff} are reported in Table 6. The anisotropy constant for samples with Co content in the range of 0.25–1.0 is similarly showing the low dependence on the chemical composition; only pure $NiFe_2O_4$ powder shows a significantly lower value. Thus, the magnetocrystalline contribution on effective anisotropy can be considered important but not determining and other factors such as interparticle interactions, shape and internal magnetic structure affect the effective anisotropy.

The SFD (calculated from DCD) correlates with the distribution of particle coercivity reflecting only irreversible magnetization processes (Figure 49). The set of dm_{DCD}/dH_{app} curves clearly renders the adjustable by the chemical composition the anisotropy for mixed Ni/Co ferrites. The peak positions of SFD, $\mu_0 H_{Cr}^{DCD}$, is in good proximity with the coercivity $\mu_0 H_C$ for pure $NiFe_2O_4$ sample, however with the decrease of nickel content the difference increases.

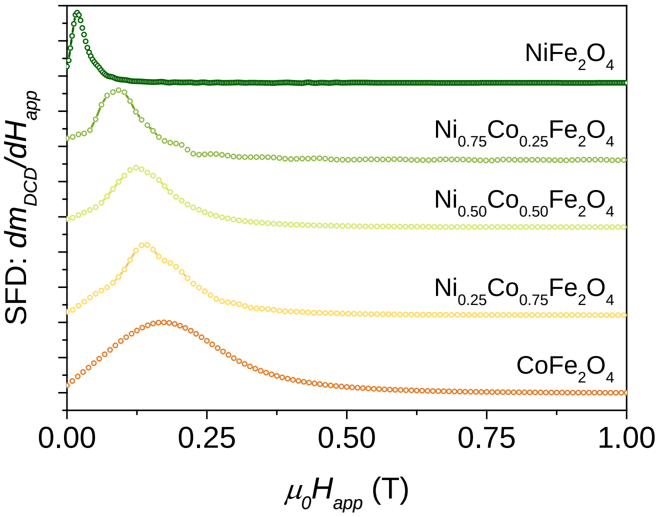

Figure 49. Switching field distribution of Co/Ni ferrite MNPs (~295 K) [148].

3.1.2 Structural and magnetic properties of $Zn_xCo_{1–x}Fe_2O_4$ MNPs

Samples of $Zn_xCo_{1–x}Fe_2O_4$ with x = 0, 0.15, 0.25, 0,35, 0.5, 0.75 and 1 were prepared by the same SGAC method as the set of Ni/Co ferrite MNPs. The structure was confirmed by XRD (Figure 50) showing for all the samples the cubic spinel structure. No other phases have been detected in contrast to Ni/Co ferrites where metallic nickel and hematite (α-Fe_2O_3) satellites were formed in the samples with high Ni content. The d_{XRD} value decreases with the increase of Zn content (Table 7).

Table 7. Structural and magnetic properties (~300 K) of $Zn_xCo_{1–x}Fe_2O_4$ MNPs.

Sample composition	**d_{XRD}, nm**	**M_S, Am^2/kg**	**M_R/M_S, a.u.**	**μ_0H_C, mT**	**K_{eff}, ×10^4 J/m^3**
$CoFe_2O_4$	18±2	69±2	0.42±0.02	140±4	14±2
$Zn_{0.15}Co_{0.85}Fe_2O_4$	15±2	71±2	0.35±0.01	76±3	12±2
$Zn_{0.25}Co_{0.75}Fe_2O_4$	16±2	74±2	0.34±0.01	54±2	9.5±0.04
$Zn_{0.35}Co_{0.65}Fe_2O_4$	14±1	65±2	0.27±0.01	37±2	7.5±0.3
$Zn_{0.50}Co_{0.50}Fe_2O_4$	15±2	52±2	0.22±0.01	21±1	3.3±0.1
$Zn_{0.75}Co_{0.25}Fe_2O_4$	15±1	32±1	0.09±0.01	5.5±0.2	0.72±0.04
$ZnFe_2O_4$	14±1	10±1	0.08±0.01	4.8±0.2	0.064(4)

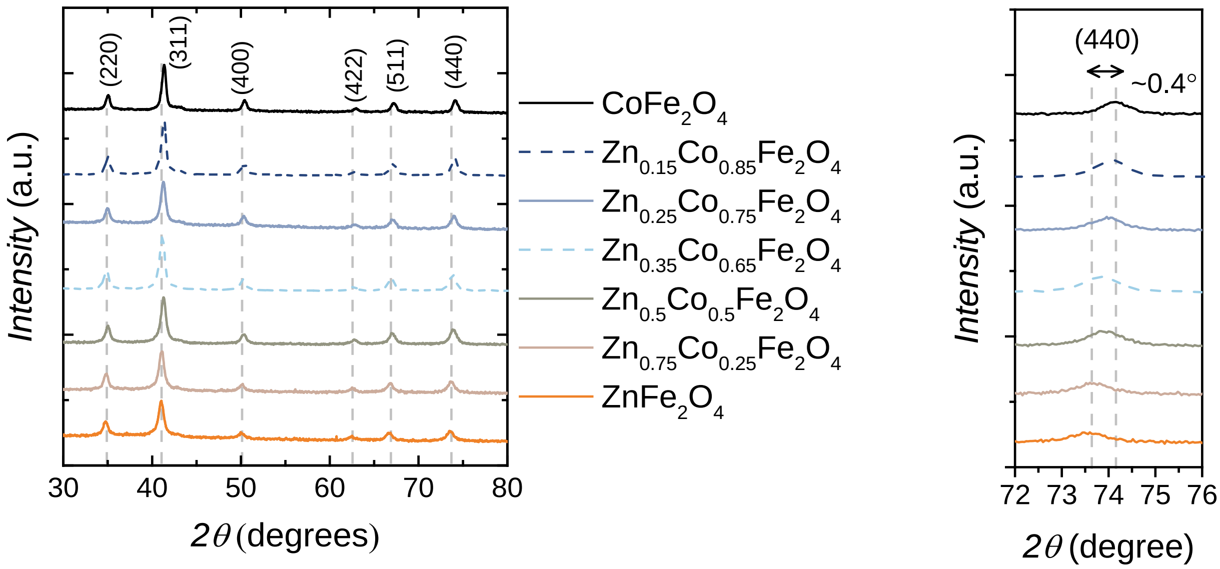

a) b)

Figure 50. a) XRD patterns of $Zn_xCo_{1-x}Fe_2O_4$ MNPs (Co Kα radiation), b) zoomed region of (440) reflection showing the shift of peak position [149].

All $Zn_xCo_{1-x}Fe_2O_4$ samples exhibited ferrimagnetic nature at 300 K (Figure 51) with the values of M_S, M_R/M_S and μ_0H_C reported in Table 1. The M_S value increases with the increase of Zn-content up to x = 0.25, then it decreases. This behavior agrees with the literature data and may be explained by the cation distribution [132,139,147,153]. The maximal value of M_S of 74±2 Am^2/kg was for $x = 0.25$, which is higher than reported for samples prepared with a similar SGAC method, probably because we used the higher reaction temperature promoting better crystallinity of particles. For $Ni_{0.25}Co_{0.75}Fe_2O_4$ MNPs prepared by the same method, earlier we observed a maximal M_S value of 69 Am^2/kg. The μ_0H_C and M_R/M_S decrease with the increase in the zinc content.

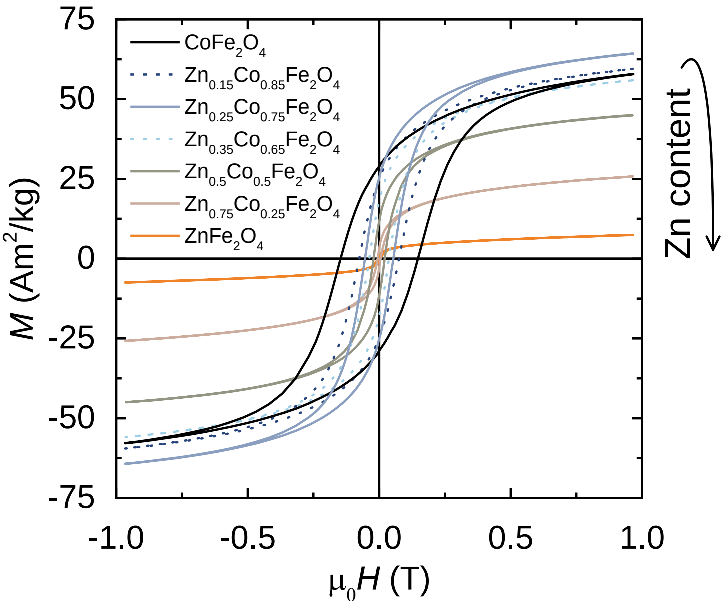

Figure 51. *M-H* hysteresis cycles recorded at 300 K of $Zn_xCo_{1-x}Fe_2O_4$ MNPs. The arrow indicates the trend of M_S [149].

The M_S values were converted to the magnetic moment per formula unit in Bohr magnetons (eq.(53)) to better understand processes associated with the cation distribution and spin canting. Figure 52 shows the values of M_S in μ_B units evaluated from *M-H* hysteresis loops (300 K).

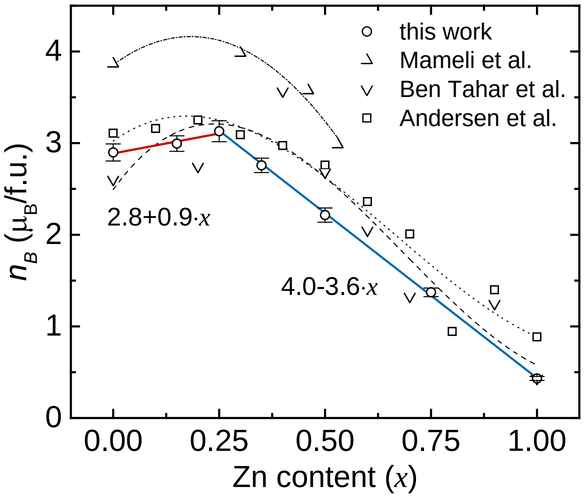

Figure 52. Dependence of net magnetic moment per formula unit (300 K) for $Zn_xCo_{1-x}Fe_2O_4$ MNPs compared with literature data from refs. [139,216,217];

For $0 < x < 0.25$ in $Zn_xCo_{1-x}Fe_2O_4$, the increase in M_S is due to the partial migration of Fe^{3+} cations to B-sites. For the samples with low Zn content, Zn^{2+} cations push Fe^{3+} cations from A to B site (Figure 53). Hence, the uncompensated magnetic moment of Co^{2+} ($3\mu_B$) became replaced by 2 uncompensated Fe^{3+} ($5\mu_B$) moments in the octahedral position [144,145,218] The net magnetization may be expressed as $(3 + 7x)\times\mu_B$, if exchange interactions between two different sites, described by exchange integral J_{AB}, are stronger than intra-lattice interactions J_{AA} and J_{BB}. The intralattice A-B interaction weakens with the increasing zinc content. In the extremal case $x = 1$, J_{AB} and J_{AA} are equal to 0 since the tetrahedral positions are filled with non-magnetic Zn^{2+} ions and B-B interaction leads to the establishment of AFM order of spins in the octahedrally coordinated lattice. On basis of this simple model, a general rule of zinc dependence of magnetization can be ascribed as $m = (\mu_I + \delta\mu`x)\times\mu_B$, where $\delta$ is delta equal to 1 if $J_{AB} >> J_{AA} + J_{BB}$ and equal to $-1$ if $J_{AB} << J_{AA} + J_{BB}$, $\mu_I$ is the initial magnetic moment of undoped ferrite and $\mu`$ is a concentration-depended magnetic moment resulting from the recombination of cations between lattices and disruption of ideal FiM order.

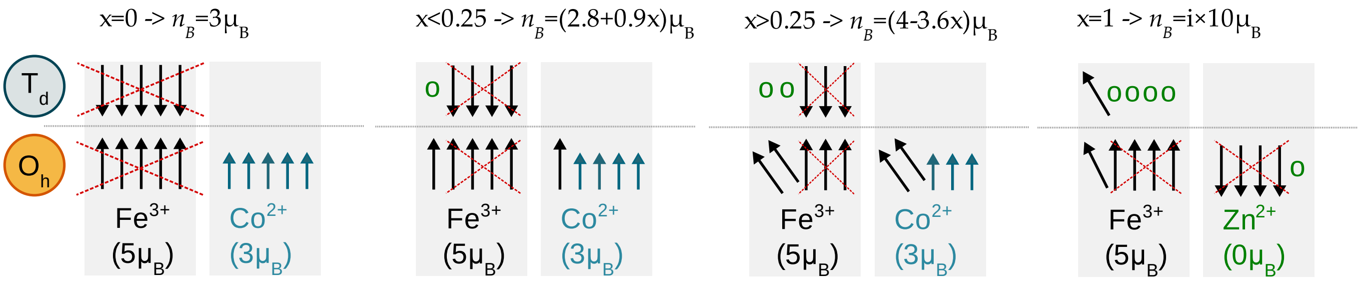

Figure 53. Schematic representation of the magnetic structure of $Zn_xCo_{1-x}Fe_2O_4$ synthetized via SGAC rout.

The linear fitting of region $0 < x < 0.25$ gives $(2.8 + 0.9x)\times\mu_B$. The value of magnetization per formula unit in the case of pure $CoFe_2O_4$, is close to the theoretical value of $3\mu_B$ for the inverted spinel (only spin contribution to the magnetic moment it is considered). In our case, the coefficient before x is much lower than the estimated one. This indicates that the Zn^{2+} occupy only partially T_d sites while some amount of Zn^{2+} cations occupies O_h sites. This value is also affected due to the AFM order between magnetic cations in B sites since the B–B superexchange interactions become dominating because of the breaking of the A–B interactions. Spin canting arises when in B-sites, the concertation of non-magnetic ions becomes too high and can be explained in the frame of the Yafet−Kittel model eq.(54) [132]. Gómez-Polo et al. found the divergence in the inversion degree between the calculated and measured by neutron diffraction [134]. In our case, the trend becomes more pronounced in the region of $0.25 < x < 1$ due to the change in the slope of the linear function $(4 - 3.6x)\times\mu_B$. This non-monotonical trend of magnetization suggests that the filling of the spinel positions is non-monotonical.

The observed trend well agrees with literature data (Figure 52). Valentina Mameli et al. observed the maximal M_S value for 7-nm MNPs prepared by HTD method for the zinc content $x = 0.46$ at 5 K; however at 300 K, the maxim of M_S shifts to the lower x values [139]. Ben Tahar et al. observed the maximum of M_S at $x = 0.4$ in ~5-nm MNPs prepared via the polyol method [217]. Andersen et al. observed the maximal M_S at $x = 0.2$ in ~14-nm MNPs prepared with the hydrothermal method [216]. The difference in the absolute value of M_S and the position of its maxima is due to the fact, that MNPs were prepared with different methods thus having different sizes, cation distribution, etc.

3.1.3 Comparison of Zn/Co and Ni/Co nanoparticle systems synthetized by SGAC method

Structural properties

The size of crystallites depends on chemical composition. In the case of Co/Ni ferrite MNPs obtained with the SGAC method, a higher size of crystallites was observed in mixed Ni/Co ferrites (Figure 54 a). While in Zn/Co ferrites, it gradually decreases with the increase of Zn.

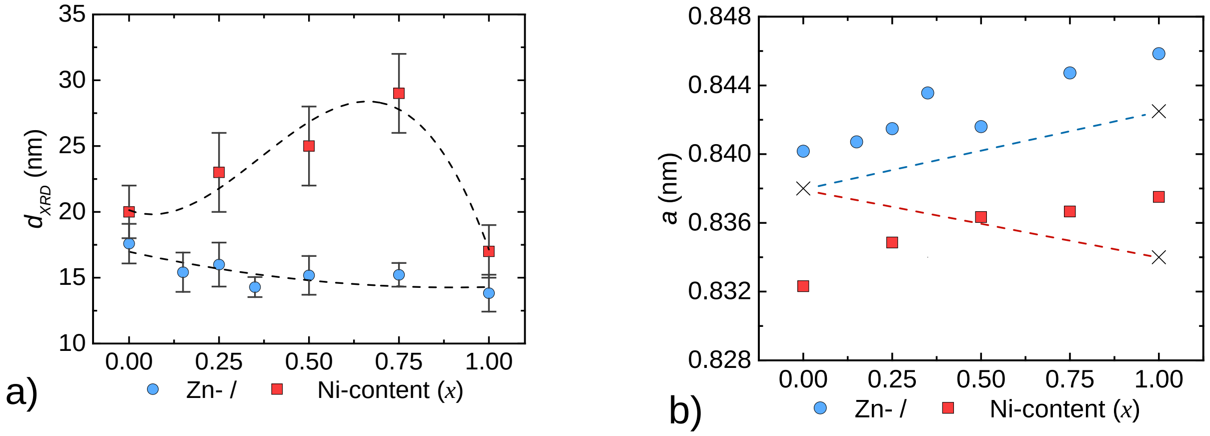

Figure 54. a) Size of crystallites and b) lattice constant of $Me_xCo_{1-x}Fe_2O_4$ (Me = Zn or Ni) MNPs synthetized via SGAC route, the dashed lines represent Vegard`s law for bulk materials (data from refs. [148] and [149]).

According to Vegard's law, the lattice parameter should increase linearly in $Ni_xCo_{1-x}Fe_2O_4$ with the increase of *x* (Figure 54 b). The lattice constant for $CoFe_2O_4$ is 0.838 nm and for $NiFe_2O_4$ is 0.834 nm [101]. However, it is only correct considering the same inversion degree for both Co and Ni ferrites. The fact, that the lattice constant has a nonlinear behavior can be explained by the variation of inversion degree, namely the overall decrease of the lattice constant with the replacement of bigger Co^{2+} (0.82 Å) ions by smaller Ni^{2+} (0.72 Å) ones in octahedral sites are suppressed by migration Co^{2+} and Ni^{2+} into smaller tetrahedral sites replacing Fe^{3+} (0.67 Å) and thus inducing overall expansion of the unit cell. For the $CoFe_2O_4$ sample, the initial value of inversion degree was probably higher than the bulk value about 0.8, thus for this sample, the lattice parameter is lower than the bulk value. With further increase of *x*, lattice constant increases that can be explained for example by a rapid decrease of the inversion degree till $x = 0.5$, after this value the lattice parameter is only slowly increasing.

The position of main reflexes is continuously increasing with the increase of zinc content despite the similar ionic radii of Zn^{2+} (0.82 Å [41]) and Co^{2+} (0.82 Å [41]) ions: this can be ascribed to the migration of the smaller Fe^{3+} (0.67 Å [41]) ions to octahedral sites since zinc ions prefer to occupy the tetrahedral position [20]. The fact that bigger Zn^{2+} occupies the smaller tetrahedral sites is confirmed by the expansion of the lattice parameter *a*. This behavior agrees with Vegard's law prediction that the lattice parameter of the chemically homogenous mixture will be approximately the weighted mean of two constituents [42]. Some difference in the value of lattice constant for pure $CoFe_2O_4$ is probably due to the difference in used XRD equipment, for Ni/Co set the Cu Kα radiation $\lambda = 1.54056$ Å was used, while for Zn/Co it was Co Kα source $\lambda = 1.78919$ Å.

Magnetic properties

For both sets of samples, magnetic properties are gradually depending on chemical composition. The coercivity decreases continuously with the increase in Zn content (Figure 55 a). The difference with the Ni/Co MNPs is the coercivity decreases much faster with the downward trend, while for Ni/Co ferrite MNPs, the upward trend was observed.

To better understand the role of magnetic anisotropy the constant of effective magnetic anisotropy (K_{eff}) was calculated by eq.(17). The maximal K_{eff} of 14×10^4 J/m^3 for pure $CoFe_2O_4$ fast dropdown with the increase in Zn content. The obtained M_R/M_S and K_{eff} values are lower than for cubic anisotropy. The magnetocrystalline anisotropy of $CoFe_2O_4$ has the cubic symmetry, in the case of MNPs, the effective magnetic anisotropy frequently turns on the uniaxial one due to the arising of additional sources of magnetic anisotropy, such as shape, surface, and magnetic interparticle interactions [196]. The divergence in the behavior of coercivity and closure field was noted: the H_{irr}/H_C increases in two times for Zn/Co ferrites compared with the pure $CoFe_2O_4$. These facts confirm the important role of magnetocrystalline anisotropy for Zn/Co ferrites and arising a stronger surface anisotropy with the increase of Zn content. The role of chemical composition in the Zn/Co systems can be considered stronger than in the Ni/Co systems. Moreover, it is known to form literature that the Zn^{2+} cations significantly decrease the T_N of $CoFe_2O_4$. For Zn-dopped cobalt ferrite MNPs was shown that the T_N decreased from 713 to 453 K when the *x* increases from 0 to 0.5 [219]. Thus, Zn-substituted $CoFe_2O_4$ MNPs is the potentially interesting system with gradually tunable magnetization, anisotropy and T_N, which is appliable in, for example, the self-controlled hyperthermia [153,220].

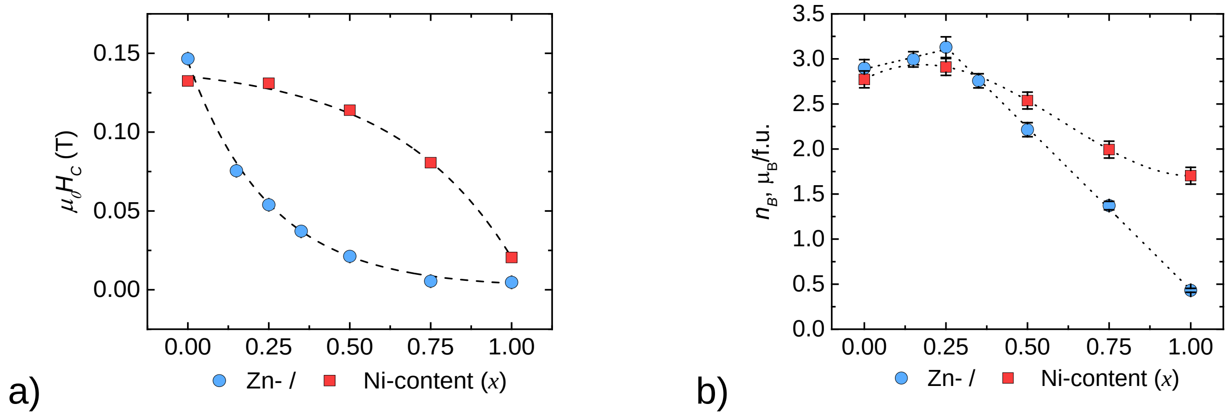

Figure 55. a) Coercivity and b) magnetization per formula unit of Me$_x$Co$_{1-x}$Fe$_2$O$_4$ MNPs (Me = Zn or Ni) synthetized via SGAC rout (295–300 K) (data from refs. [148] and [149]).

Besides anisotropy, saturation magnetization varies significantly for both systems. The introduction of Zn or Ni first slightly increases the magnetization reaching a maximum at $x \approx 0.25$, then it starts to decrease (Figure 55 b). These observations render sharp changes in the electronic structure of magnetic ions in Ni$_x$Co$_{1-x}$Fe$_2$O$_4$ nanoparticles caused by features of spinel structure formation during the nanoparticle synthesis.

3.2 $Zn_xCo_{1-x}Fe_2O_4$ MNPs synthetized via hydrothermal method

The set of $Zn_xCo_{1-x}Fe_2O_4$ MNPs synthesized following the hydrothermal CP method was provided by Dr Sonja Jovanović (Vinca Institute of Nuclear Sciences, University of Belgrade). The method of sample preparation is described in refs. [196,221]. Briefly, sodium hydroxide (10 mmol) was dissolved in 2ml of distilled water, then 10 ml of 1-pentanol and 3.8 ml of oleic acid were added to the solution with vigorous stirring. The second solution of 18 ml of distilled water with 2 mmol of iron nitrate and 1 mmol of cobalt nitrate and zinc nitrate was poured into the first solution and stirred for 1 h at room temperature, after which the autoclave was closed and placed at 180 °C for 8 h. After the synthesis, the samples were washed five times with n-hexane and ethanol and dried in air. Properly adjusting the amount of precursors, cobalt ferrite $CoFe_2O_4$ (CFO_Zn_0) and three samples of cobalt-zinc ferrites with different stoichiometry $Co_{0.9}Zn_{0.1}Fe_2O_4$ (CFO_Zn_0.1), $Co_{0.7}Zn_{0.3}Fe_2O_4$ (CFO_Zn_0.3) and $Co_{0.5}Zn_{0.5}Fe_2O_4$ (CFO_Zn_0.5) have been prepared. For some experiments the sample with smaller Zn concentration $Co_{0.95}Zn_{0.05}Fe_2O_4$. The stoichiometry of the final products has been confirmed by inductively coupled plasma atomic emission spectroscopy (ICP-AES) analysis (Table 8).

Table 8. Chemical composition, crystallite size d_{XRD}, lattice constant a, particle size d_{TEM} of $Zn_xCo_{1-x}Fe_2O_4$ MNPs synthetized via hydrothermal method.

Sample	**Composition (ICP-AES)**	**d_{XRD}, nm**	**a, Å**	**d_{TEM}, nm**
CFO_Zn_0	$Co_{1.04}Fe_{1.96}O_4$	3.6	8.400(2)	5.2±0.7
CFO_Zn_0.1	$Zn_{0.13}Co_{0.92}Fe_{1.95}O_4$	3.1	8.401(0)	5.1±0.8
CFO_Zn_0.3	$Zn_{0.34}Co_{0.71}Fe_{1.95}O_4$	3.0	8.407(0)	5.2±0.8
CFO_Zn_0.5	$Zn_{0.55}Co_{0.52}Fe_{1.93}O_4$	3.2	8.418(0)	5.4±0.9

The XRD patterns of the zinc-substituted cobalt ferrite MNPs (CFO_Zn_*x*; *x*=0; 0.1; 0.3 and 0.5) are presented in Figure 56. It can be noticed that all diffraction maxima, both of pure as well as zinc substituted cobalt ferrite, correspond to the cubic spinel structure. The average crystallite size and lattice parameters have been assessed from

XRD patterns by using the Rietveld refinement method (Table 8). The results show that the increase of the zinc content in the spinel structure does not influence the average crystallite size. However, the zinc substitution leads to an increase in the lattice parameters. In their study, Mameli et al. [139] investigated the influence of zinc substitution on the structural properties of cobalt ferrite nanoparticles prepared by the HTD method. Their results also showed that average crystallite size remained unchanged both for pure CFO nanoparticles and for substituted ones; however, the lattice parameter increased with the increase of zinc content within the spinel structure.

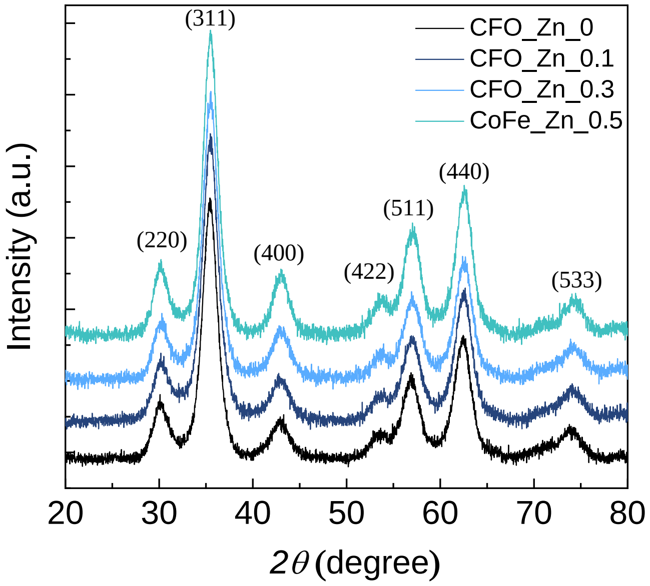

Figure 56. XRD patterns of $Zn_xCo_{1-x}Fe_2O_4$ MNPs synthetized via hydrothermal method.

TEM image analysis of shows the sphere-like particles whose size follows the log-normal distribution with an average diameter of around 5 nm for all samples (Figure 57). It can be observed that the average particle size is slightly larger than the average crystallite size (Table 8). It can be noticed that the nanoparticles are well-dispersed and that the Zn-substitution has no influence on particles morphology. This can be ascribed to oleic acid *i.e.* its beneficial effects of steric stabilization acting against attractive magnetic attractive and Van der Waals interactions [222]. At the same time, the oleic acid inhibits the growth of nanoparticles by serving as a barrier to mass transfer which hinders the Oswald ripening process [223].

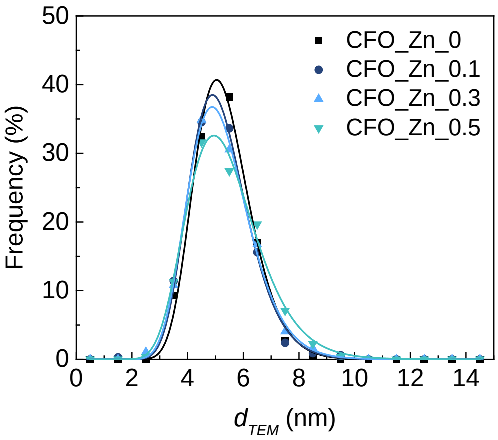

Figure 57. Particle size distribution of CFO_Zn_*x* (x=0; 0.1; 0.3 and 0.5) MNPs.

Magnetic properties

M-H hysteresis cycles for samples CFO_Zn_*x* (x=0; 0.1; 0.3 and 0.5) measured at 5 K and 300 K are shown in Figure 58. The saturation magnetization M_S of unsubstituted cobalt ferrite is 95±3 Am^2/kg at 5 K and it is close to the value usually reported for bulk CFO (80–90 Am^2/kg [101]). The M_S value slowly increases when Zn^{2+} enters the structure and reaches a value of 103±4 Am^2/kg for the sample with the highest zinc concentration among studied (Table 9). The coercivity $\mu_0 H_C$ gradually decreased with the increase in Zn content from 1.13 to 0.6 T. A similar trend shows the irreversible field $\mu_0 H_{irr}$ defined as a field value at which both branches of hysteresis merge (difference reaches 3%). At the same time, the remanence $M_R/M_S \approx 0.5$ was almost constant for all samples.

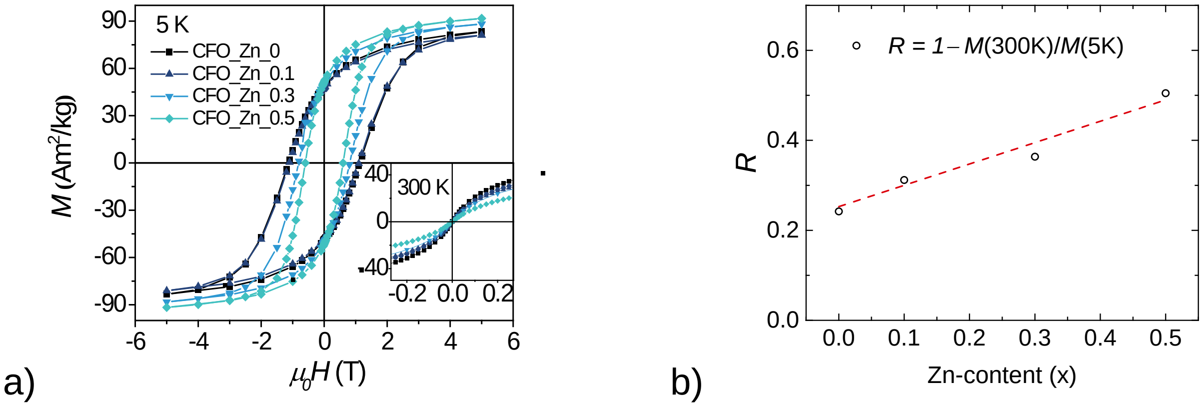

Figure 58. a) *M-H* hysteresis cycles recorded at 5 K, inset shows zoomed low-field region of *M-H* curves at 300 K; b) rate of temperature reduction of magnetization (R) for samples CFO_Zn_*x* (x=0; 0.1; 0.3 and 0.5).

At 300 K measured *M-H* cycles demonstrated an unhysteretic behavior expected for SPM nanoparticles (Figure 59). Besides transformation to the SPM regime and vanishing of remanence, the reduction of the saturation magnetization at 300 K was observed. This reduction can be quantitated as [147]

$$R = (1 - M_S^{300K}/M_S^{5K}). \tag{79}$$

The *R* factor increases (Figure 58) with the increase of the Zn content due to the effect of the diamagnetic Zn^{2+} ions disturbing a FiM order.

Table 9. The saturation magnetization (M_S), irreversibility ($\mu_0 H_{irr}$), coercivity ($\mu_0 H_C$) and reduced remanent magnetization (M_R/M_S) measured at 5 K for samples CFO_Zn_*x* (*x*=0; 0.1; 0.3 and 0.5).

Sample	**M_S, Am^2/kg**	**$\mu_0 H_C$, T**	**$\mu_0 H_{irr}$, T**	**M_R/M_S**
CFO_Zn_0	95 ± 3	1.13 ± 0.01	3.5 ± 0.1	0.52 ± 0.01
CFO_Zn_0.1	93 ± 3	1.11 ± 0.01	3.6 ± 0.1	0.53 ± 0.01
CFO_Zn_0.3	99 ± 3	0.81 ± 0.01	2.6 ± 0.1	0.52 ± 0.01
CFO_Zn_0.5	103 ± 4	0.60 ± 0.01	1.9 ± 0.1	0.52 ± 0.01

According to ZFC-FC measurements (Figure 59), $M_{ZFC}(T)$ and $M_{FC}(T)$ curves merge at temperatures below room temperature, confirming transition from blocked to the SPM regime [54]. The temperature where $M_{ZFC}(T)$ and $M_{FC}(T)$ curves merge is called irreversibility temperature, T_{irr}, indicating the temperature at which the magnetic moments of the biggest particles in the assembly are in the blocked state [224]. The maximum of $M_{ZFC}(T)$, T_{max}, for noninteracting particles is directly proportional to the average blocking temperature (T_B). Blocking temperature T_B was defined as a temperature at which the integral value of $\Delta E_a(T) \sim dM_{FC\text{-}ZFC}(T)/dT$ reaches 50%. The characteristic temperatures are listed in Table 10. Those values are decreasing with the increase of zinc concentration, which is attributed to the decrease in magnetocrystalline anisotropy therm.

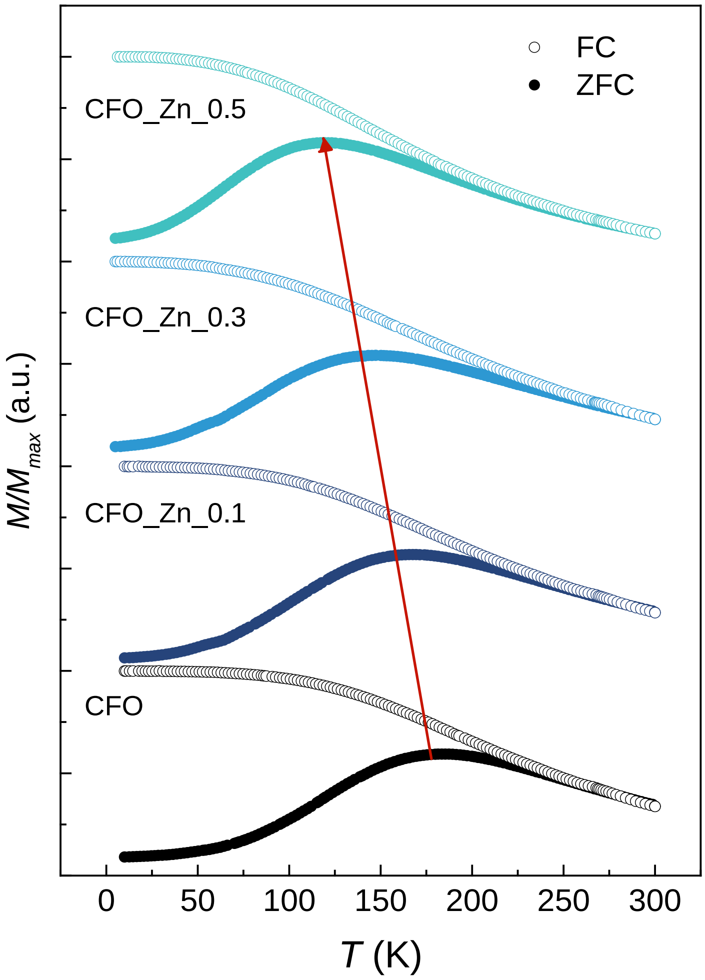

Figure 59. ZFC and FC magnetization curves recorded at 2.5 mT for samples CFO_Zn_*x* (*x*=0; 0.1; 0.3 and 0.5).

Table 10. The peak (T_{max}), irreversibility (T_{irr}) and blocking (T_B) temperature estimated from ZFC-FC curves at a measuring field of 2.5 mT for samples CFO_Zn_*x* (*x*=0; 0.1; 0.3 and 0.5).

Sample	**T_{max}, K**	**T_{irr}, K**	**T_B, K**
CFO_Zn_0	184±4	234±8	132±5
CFO_Zn_0.1	168±4	232±8	111±4
CFO_Zn_0.3	148±4	246±8	97±4
CFO_Zn_0.5	120±4	209±6	78±4

Mössbauer spectroscopy measurements have been performed in Institut des Molécules et Matériaux du Mans, Université du Maine & CNRS by Dr Nader Yaacoub (Figure 60). The ^{57}Fe Mössbauer spectra were measured in the transmission mode with ^{57}Co diffused into a Rh matrix as the source moving with constant acceleration. The spectrometer (Wissel) was calibrated utilizing a standard α–Fe foil. The isomer shift was expressed concerning this standard. The samples were measured at 11 K under 8 T magnetic field in the perpendicular arrangement of the magnetic field vector for the γ-beam. The fitting of the spectra was performed with the help of the NORMOS program using Lorentzian profiles.

All spectra were fitted with two sextets, due to different isomer shifts related to Fe^{3+} ions in different anionic surroundings, namely to the Fe^{3+} located in the tetrahedral (FeO_4) and octahedral (FeO_6) positions of the cubic spinel structure [224,225]. The results of this fit are in Table 11. The fact that the effective field associated with tetrahedrally located Fe^{3+} ions is higher than the hyperfine field ($H_{eff}>H_{hyp}$) and, in opposite for octahedral sites ($H_{eff}<H_{hyp}$) confirms that ions in both sites are oriented antiparallelly [224]. Thus, exchange interactions between octahedral and tetrahedral lattice (J_{AB}) are stronger than intralattice interactions (J_{AA} and J_{BB}). While the shifts and hyperfine fields of the A and B sites remained almost the same when Zn content was increased, the Fe^{3+} occupancy of spinel sites showed a remarkable trend of increase of Fe^{3+} subpopulation in octahedral site from 1.22 to 1.35 atom per formula unit (f.u.) (that accompanied with an iron decrease in tetrahedral site).

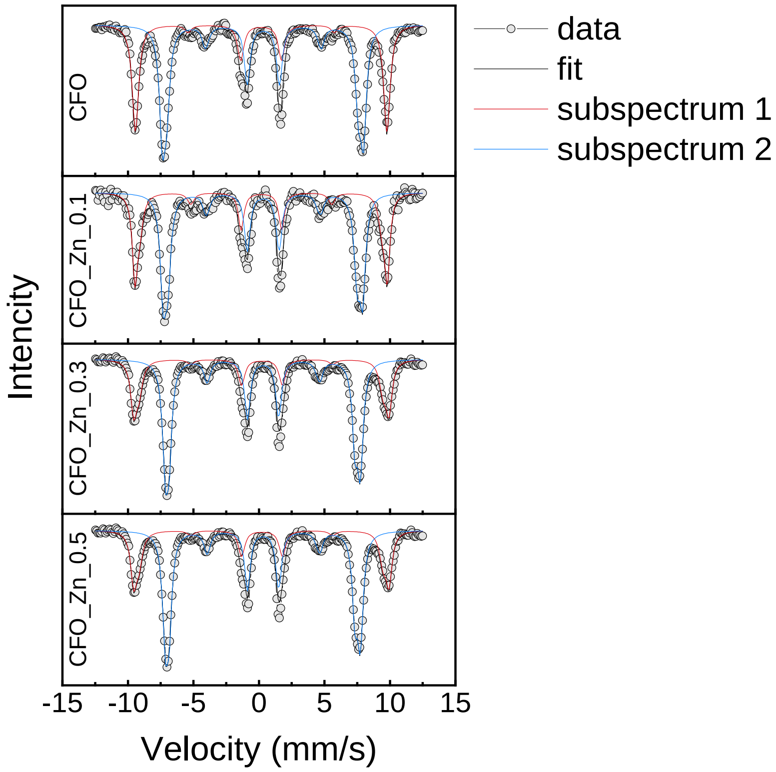

Figure 60. Mössbauer spectra of the for of samples CFO_Zn_*x* (*x*=0; 0.1; 0.3 and 0.5) at 11 K under magnetic field of 8 T.

Table 11. Results of Mössbauer spectra fit: position of iron cations in spinel (Pos.), values of isomer shift (δ), effective magnetic field ($\mu_0 H_{eff}$), hyperfine field ($\mu_0 H_{hyp}$), spin canting angle in each spinel`s position (θ), its mean value (θ_{mean}) and the last column is the distribution of Fe^{3+} cations.

Sample	**Pos.**	**δ, mm/s**	**$\mu_0 H_{eff}$, T**	**$\mu_0 H_{hyp}$, T**	**θ, °**	**θ_{mean},°**	**Fe^{3+} distr., %**
CFO_Zn_0	A	0.35	59.3	51.8	18	22.88	39
	B	0.48	46.5	53.8	26		61
CFO_Zn_0.1	A	0.35	58.6	51.4	24	25.24	38
	B	0.48	45.9	53.2	26		62
CFO_Zn_0.3	A	0.37	59.0	51.7	22	24.6	35
	B	0.47	45.5	52.8	26		65
CFO_Zn_0.5	A	0.37	59.0	51.2	12	20.78	32.5
	B	0.47	45.1	52.5	25		67.5

The results of morpho-structural investigations show that all samples are sphere-like nanoparticles with the same particle size distribution and amount of organic phase. Therefore, any difference in magnetic properties can be attributed to the effect of chemical composition on the magnetic structure (i.e., cationic distribution and spin canting) of Zn substituted $CoFe_2O_4$ nanoparticles.

The blocking temperature as well as characteristic temperatures proportional to blocking temperature (T_{irr} and T_{max} [54,89,224]) decrease following the trend of increase in Zn content. Since the T_B for static magnetic measurements is equal to $K_{eff}V/25k_B$, then, for the case of equisized particles, it is expected to be proportional to the magnetic anisotropy constant. The linear dependence K_{eff} versus Zn-content x (Figure 61) suggests that Zn ions reduce the effective anisotropy of nanoparticle systems.

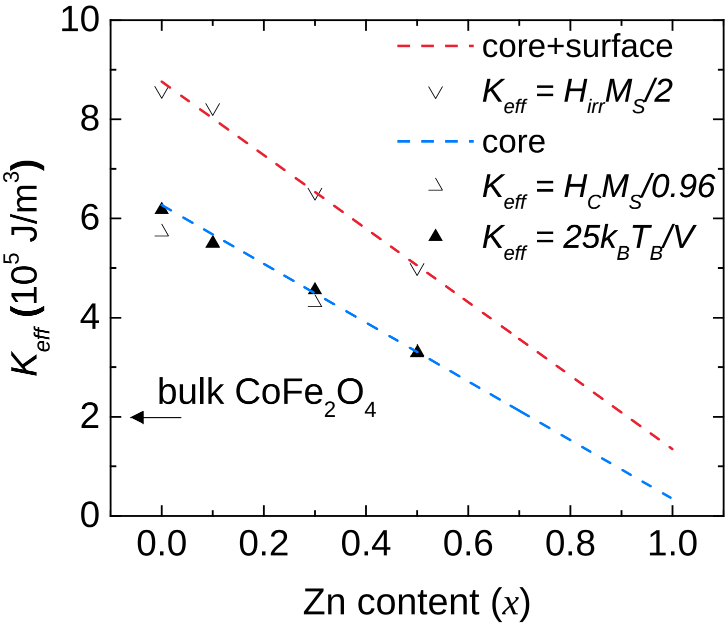

Figure 61. Magnetic anisotropy constants calculated after *M-H* and *M-T* measurements for samples CFO_Zn_*x* (*x*=0; 0.1; 0.3 and 0.5).

Interesting that the reduced remanence (M_R/M_S) was observed almost constant beyond the chemical composition of the sample, and it was nearly a value of 0.5 (Figure 62). The M_R/M_S value of 0.5 is very close to the theoretically predicted value for a system of non-interacting particles with uniaxial anisotropy although bulk cobalt ferrite has strongly pronounced cubic magnetocrystalline anisotropy and thus expected M_R/M_S value is around 0.8 [203,226].

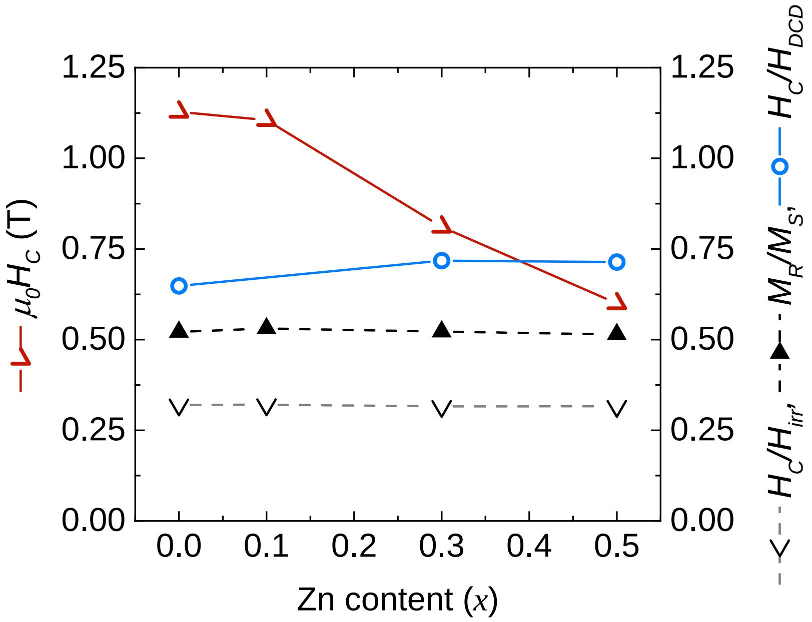

Figure 62. Coercivity (left axis) and H_C/H_{irr}, M_R/M_S and H_C/H_{DCD} rations (right axis) measured at 5K for samples CFO_Zn_x (x=0; 0.1; 0.3 and 0.5).

It is worth noting the difference between our results with literature data, wherein in most of the cases, a reduction of M_R/M_S was observed when Zn content in cobalt ferrite nanoparticles is increasing [139,227]. Possible reasons for the reduction in M_R/M_S are thermal fluctuations of the smallest particles in distribution, magnetic interparticle interactions, and the appearance of surface sources of anisotropy. In most of the cases in the literature, the M_R/M_S reduction was attributed to the switching from domination cubic magnetocrystalline anisotropy to mixed cubic/uniaxial or uniaxial surface anisotropy. The residual thermal fluctuation in the presented case can be eliminated from consideration because T_B is relatively far from 5K and H_C/H_{Cr}^{DCD} ratio (Figure 62) shows almost constant value over chemical composition ($\mu_0 H_{Cr}^{DCD}$ is sensitive only to irreversible switching of magnetisation of blocked particles and thus the H_C/H_{Cr}^{DCD} ratio for particles with the same size distribution is expected to fast decrease with the decrease of anisotropy). Magnetic interparticle interactions for some of the presented samples were investigated with Henkel plot and random anisotropy model (RAM) methods [196]. The dip of δm was about −0.1 and the correlation length of 8–9 nm (slightly more than the size of a single 5-nm particle with a 2-nm oleic acid shell) indicates the presence of moderate dipolar interaction effects which apparently can not invoke so strong deviation of the remanent state. Thus, effective anisotropy is strongly affected by the surface.

This trend was also confirmed by the calculation of the anisotropy constant with equation (16), where anisotropy field $\mu_0 H_K$ was approximated with irreversibility field $\mu_0 H_{irr}$ (Figure 61) [64,65,203]. At first glance, the fact of reduction in $\mu_0 K_{eff}$ is quite expected Zn-doped cobalt ferrites due to reducing magnetocrystalline term K_V, however, in the studied case, the effective anisotropy of the cobalt ferrite sample ($x = 0$) was much higher than K_V of bulk $CoFe_2O_4$ in about 3 times and it has uniaxial but not cubic symmetry ($M_R/M_S \approx 0.5$). Increased effective anisotropy of nanoparticle systems was frequently observed, and it was referred to as the surface effects ($K_{eff} = K_V + 6K_S/d$) [15,54,228]. Thus, the Zn-doping affects not only the magnetocrystalline term of the effective anisotropy (K_V) but, despite the equal surface area of particles, also the surface term giving rise to a simultaneous change of both anisotropy`s terms. This trend is also confirmed in comparison of K_{eff} calculated with two approaches of estimation of anisotropy field: $H_K = H_{irr}$ and $H_K = H_C/0.48$ (for SD non-interacting magnetic nanoparticles with uniaxial anisotropy) (Figure 61) [65]. Since $\mu_0 H_{irr}$ is affected by the influence of highly anisotropy surface spins, $\mu_0 H_K$ value is usually observed to be higher than the $\mu_0 H_C/0.48$ one mainly attributed to the volumetric term of magnetic anisotropy. As result, the K_{eff} values calculated with those two approaches were different by absolute value but in both cases, the linear trend is confirmed.

Considering the cobalt ferrite to be an invert spinel ($i = 1$) and zinc ferrite is a normal spinel ($i = 0$), M_S value will linearly increase according to the Néel model with an increase in Zn content till the interlattice exchange interactions are dominating [101]. In the Néel model, the net magnetic moment of spinel can be expressed as a simple superposition of individual magnetization of sublattices ($\mu = \mu_{A\text{-}site} - \mu_{B\text{-}site}$). In the case of Zn doping of $CoFe_2O_4$, considering the magnetic moment of Fe^{3+} is 5 μ_B, Co^{2+} is 3 μ_B and Zn^{2+} is 0 μ_B (where μ_B is the Bohr magneton), it is expected that the Zn^{2+} ions preferring A sites will push Fe^{3+} ions from A to B sites increasing the net magnetic moment per formula unit according to the following rule: $\mu=(3+7x)\times\mu_B$, where x is the zinc content [101].

This rule good describes some experimental data [227], however, it does not take into account such facts as the partially non-equilibrium ion distribution among sublattices and spin canting. It is known, for example, that even in bulk material for cobalt ferrite inversion degree is usually lower than the ideal value of 1, which leads to the increased value of magnetization Figure 63 [101]. Thus, if one will consider the spin canting and intermediate inversion degree values, the magnetic moment can be expressed as

$$\begin{gathered}\mu(x) = \cos(\alpha`) \times 3j(1-x) + \cos(\alpha``) \times 5(2-i) - \\ \left(\cos(\alpha`) \times 3\left(1-x-j(1-x)\right) + \cos(\alpha``) \times 5i\right),\end{gathered} \tag{80}$$

where $i(x)$ is the inversion degree of Fe^{3+} and $j(x)$ of Co^{2+} ions, $\alpha`(x)$ and $\alpha``(x)$ are spin canting angles for cobalt and iron ions, respectively. All the mentioned parameters are functions of Zn-content x. If all parameters are defined, resolving eq.3 makes it possible to determine both inversion degrees thus fully reconstructing the magnetic structure of spinel.

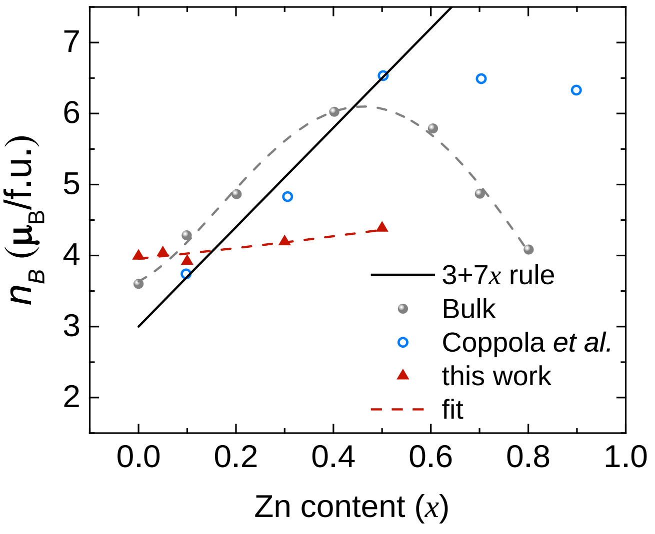

Figure 63. Net magnetic moment in Bohr magnetons at 5 K for $Zn_xCo_{1-x}Fe_2O_4$ MNPs compared with literate data and theoretical estimations.

To define the magnetic structure of our system, we applied the described classical rule and combined it with information obtained from ^{57}Fe Mössbauer spectroscopy.

Namely, the nominal magnetic moment of Fe^{3+} can be replaced with effective moment $\cos(\alpha``)\times5\mu_B$ and the distribution of Fe^{3+} in two sites was taken as two linear functions of x parameter. Spin canting for Co^{2+} was neglected due to a strong single-ion anisotropy of cobalt ions related to the manifestation of a strong orbital magnetic moment. Considering the abovementioned approximation and information obtained from Mössbauer spectroscopy, in eq.(3) only $j(x)$ is still incognito that can be defined through the fitting. To fulfil this fitting, it is necessary to guess a general shape of the $j(x)$ function, which was taken to be linear ($j(x)=ax+b$, where a and b are fitting parameters) in the first approximation, analogous to the $i(x)$ determined experimentally. Note that the linear approximation is not applied to every system because the cation distribution is strongly dependent on the synthesis method. Among the literature data we have revised, a good result of fitting at low Zn-content region was achieved with nanoparticles also synthesized with the hydrothermal method [227]. Implementation of this fitting allowed us to define $j(x)$ and thus define the entire magnetic structure of samples (add to known distribution Fe^{3+} from Mössbauer distribution of Co^{2+} and Zn^{2+}). A Python 3.5 script was used to analyse magnetic data via the Anaconda environment for scientific computing [229].

Literature data on the behaviour of spin canting for cobalt ferrite doped with zinc is very contradictive and probably it is in the strong correlation with the method of synthesis and morphostructural properties of particles rather than their chemical composition. For example, in 7–8 nm nanoparticles prepared with HTD method almost no spin canting was observed [139]. For 20–35 nm particles prepared with the SGAC method, spin canting angle showed a strong and non-monotonous dependence on chemical composition [132]. The spin canting dependence on Zn content in 8–15 nm particles prepared with hydrothermal method demonstrated a monotonous increase from 0 to 82° when x increased from 0 to 1 [230]. In the studied system, the spin-canting demonstrated non-regular behavior (Figure 64): spin-canting angle of Fe^{3+} in the tetrahedral site was almost constant (~26°), although spin-canting angle Fe^{3+} in octahedral site first increase from ~18° at $x = 0$ to then decrease to ~12° passing maximum of 24° at x of about 0.1.

The stronger spin canting in B sites than it is in A sites has been observed earlier and attributed to the preferential spin canting of Fe^{3+} spins at the surface [231]. Since particles have the same size and the fact that Zn ions are slowly entering in B site, the spin canting is just slowly decreeing with the increase of Zn concentration. The B sites have a double population concerning A sites and thus the mean value of spin canting varies slowly [232]. Interesting, that the spin canting in A sites has non-monotonous behaviour, first increasing with the increase of zinc then decreasing. A possible explanation of this phenomenon is that at a small concentration of zinc, it almost does not enter in B sites (considering that most of neighboring cations for Fe^{3+}_A are cations in B sites, Figure 65) but reduces the magnetocrystalline anisotropy. The result of reduced anisotropy and decreased interlattice A–O–B exchange interaction is the increased spin canting angle for the sample with the concentration of zinc $x = 0.1$ [134,217,230]. Then, the overall increase of diamagnetic Zn ions disturbs dominating interlattice A–O–B exchange interaction reinforcing intralattice A–O–A and B–O–B interactions, primary B–O–B interaction because B sites are less filled with Zn as result spin canting of cations in opposite sites is reduced.

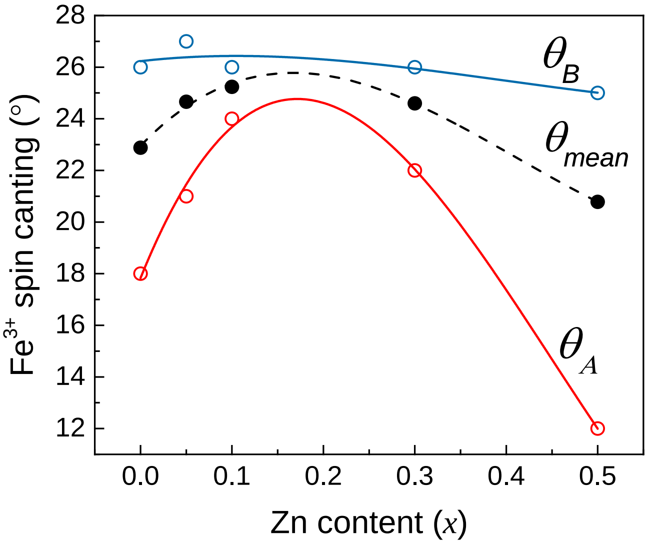

Figure 64. Spin canting angle of Fe cations in A (red) and B (blue) sites of spinel, and averaged value (black) as functions of zinc content.

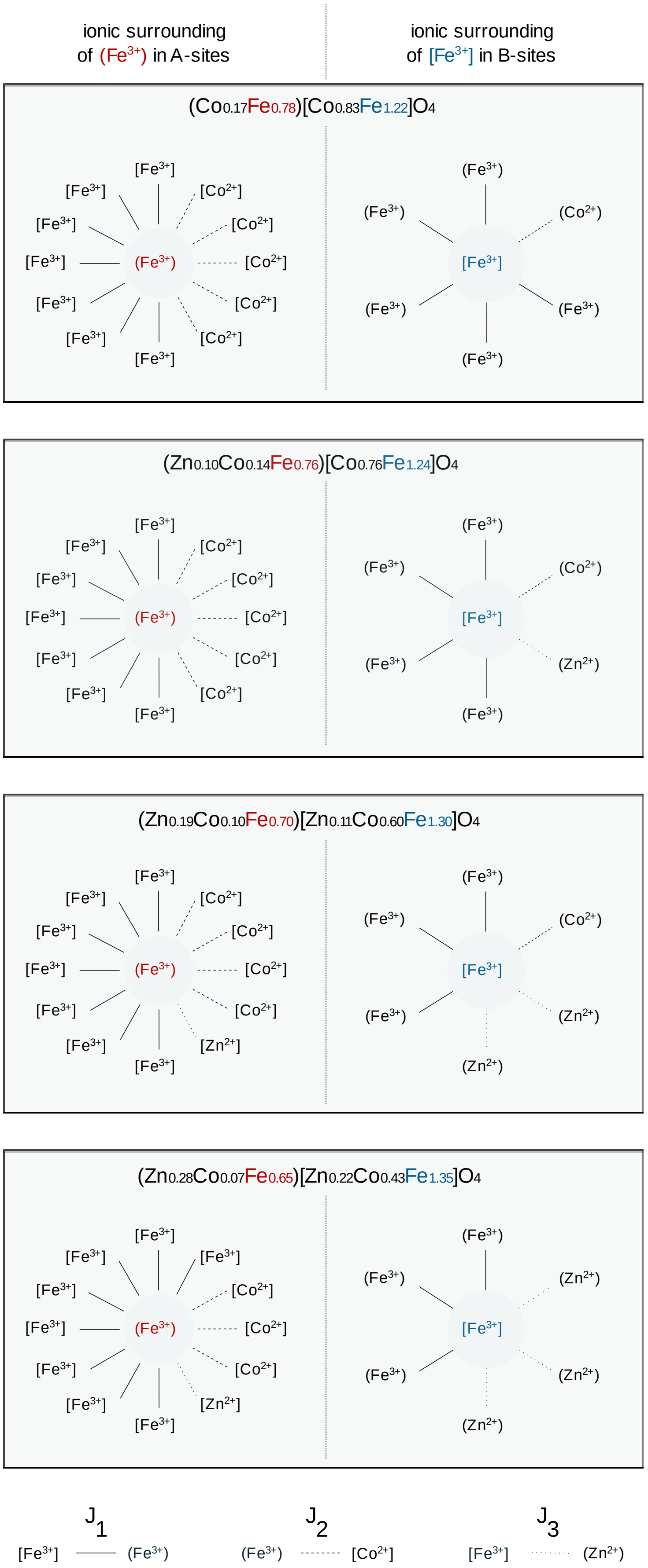

Figure 65. Schematic representation of the magnetic environment of Fe^{3+} cations located in A (red) and B (blue) sites of zinc substituted cobalt ferrite nanoparticles.

3.3 Conclusions

1) SGAC method allows producing cobalt ferrite nanocrystals ($d \approx 20$ nm) dopped with Zn and Ni. However, at the high atomic percentage of Ni (≥75% of Co), the satellite phases are forming during the synthesis;

2) The introduction of Ni and Zn cations into cobalt ferrite structure in SGAC method modifies its magnetic properties: the coercivity gradually decreases starting from the value of 175 Am^2/kg while the saturation magnetization has a non-monotonic behavior with the maximum at about 25% of the atomic percentage of dopped ions (69 and 74 Am^2/kg for $Ni_{0.25}Co_{0.75}Fe_2O_4$ and $Zn_{0.25}Co_{0.75}Fe_2O_4$ compositions, respectively);

3) The Ni ions replacing Co keeps the inverted structure of the spinel and ferrimagnetic order. However, the inversion degree has changed when variating the Ni content. The Zn turns the inverted spinel into normal simultaneously leading to the formation of antiferromagnetic/weak ferrimagnetic order;

4) The magnetic properties of small cobalt ferrite nanoparticles ($d \approx 5$ nm) doped with zinc produced by the hydrothermal coprecipitation differ drastically from those produced by SGAC and other systems from literature, including theoretical. The reason for this difference is the different size and shape of particles as well as the kinetics of the particle growth resulting in the different magnetic structures of spinel and the surface properties;

5) The magnetic structure of investigated nanoparticles was recovered by a combination of SQUID magnetometry and Mössbauer spectroscopy methods. The spin canting and distribution of cations among spinel sublattices was experimentally obtained for particles produced by the hydrothermal coprecipitation method.

Chapter 4. Size, surface, and interparticle interactions effects on magnetic properties of ultrasmall MNPs

As is known from the literature, the magnetic properties of MNPs of the same chemical composition strongly depend on their size, the magnetic interactions between the particles, and their surface properties. Thus, in order to experimentally establish the size dependences of magnetic parameters, it is necessary to find a synthesis method that allows one to controllably change the particle size without affecting the other properties. This chapter is devoted to the study of iron oxides MNPs made by CP in the presence of various organic ligands and cobalt ferrite made by the SGAC method in a silicon dioxide matrix. The organic ligands and silicon precursors allow controlling the particle size.

The synthesis of nanoparticle samples by CP method (sections 4.1) was carried out by Ivan Kozenkov under the supervision of Dr Sonja Jovanović (Vinča Institute of Nuclear Sciences) at IKBFU, with the direct participation of the author of this dissertation. Samples of cobalt ferrite in a silicon dioxide matrix (sections 4.2) were obtained by Prof. Davide Peddis. The magnetic properties were investigated by means of SQUID magnetometry at the University of Brasilia (Dr Franciscarlos Gomes da Silva and colleagues), the Kirensky Institute of Physics, Federal Research Center KSC SB RAS (Prof. Alexey Sokolov and colleagues) and the Institute of Structure of Matter ISM-CNR (Prof. Davide Peddis with the direct participation of the author of this dissertation). The structural properties were investigated at the CNR-ICM, and at the MISiS University (Prof. Tatiana Sviridova). Prof. Alexander Kamzin from the Ioffe Institute of Russian Academy of Science is acknowledged for Mössbauer spectroscopy measurements of samples from section 4.1.1 (data are not shown). The analysis and processing of the results of the morphostructural and magnetic studies were carried out by the author of the dissertation. In addition to the supervisors, the author of the dissertation is grateful to Prof. Dino Fiorani (ISM-CNR) for fruitful discussions and advice about the magnetic properties of samples studied in sections 4.1.2 and 4.2.

4.1 Iron oxide MNPs below 10 nm prepared by coprecipitation method

In Chapter 3, we investigated several examples of MNPs with different chemical compositions, and study the effect of chemical composition on their magnetic properties. Another important parameter allowing to control the magnetic properties is the particle size. To study the effect of the particle size of magnetic properties the method of synthesis must be modified but this modification should not add additional factors of the dispersion of properties of studied systems. In this section, we will use the method of coprecipitation in the presence of two organic ligands of different concentrations to obtain MNPs with controllable size.

Based on the results reported in section 4.1.2, a paper was published in the Journal of Alloys and Compounds [190], on results reported in section 4.2 in Nanomaterials [15].

4.1.1 MNPs obtained via glycine-assisted coprecipitation

This study describes a modified one-step method of CP in the presence of glycine allowing the production of MNPs with controllable size and *in situ* surface decoration. Five samples of iron oxide MNPs (Fe_3O_4/γ-Fe_2O_3) were prepared by CP in the presence of different concentrations of glycine (0.06, 0.10, 0.15, 0.30 and 0.60 mol/L). All samples of MNPs were labelled according to the glycine content used in synthesis (G0.06, G0.10, G0.15, G0.30 and G0.60).

XRD data of all prepared samples present a typical pattern of a cubic spinel ferrite with no impurities (Figure 66). Phase distinguishing between γ-Fe_2O_3 and Fe_3O_4, for nanostructured materials is a complicated task due to similar spinel. The typical value of lattice constant (a) for maghemite is $a \approx 0.834$ nm and for magnetite is $a \approx 0.839$ nm [233]. The observed value of lattice constant $a \approx 0.836$ nm lays between both and it slightly increases for the sample prepared with the minimal concentration (0.06 mol) of glycine (Table 12). The d_{XRD} for samples G0.06–0.15 are $d_{XRD} \approx 9$ nm and equivalent within the frame of experimental error. For samples G0.30 and G0.60, the d_{XRD} gradually decreases to 8.3±0.5 and 6.8±0.5 nm respectively.

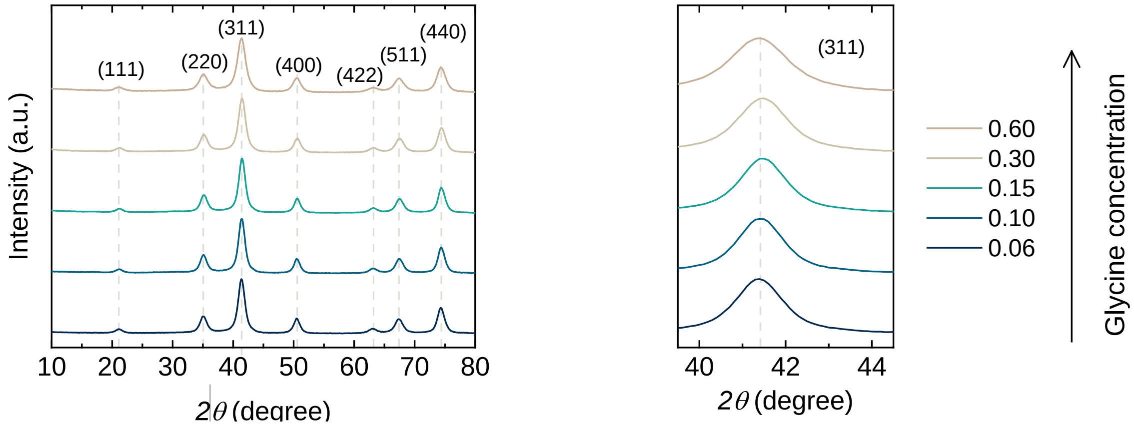

a) b)

Figure 66. a) XRD patterns of iron oxide MNPs prepared in the presence of different concentrations of glycine; b) enlargement of the strongest (311) reflection: one can observe a slight peak broadening and preserving its position with an increase in glycine concentration. The X-Ray source is Cu Kα $\lambda = 1.54177$ Å.

Table 12. The results of XRD and TEM analyses of MNP samples prepared at different glycine concentrations: lattice parameter (a), the crystallite size (d_{XRD}), median particle size (d_{TEM}) and standard deviation of the log of the distribution (σ).

Sample	**Glycine concentration, mol/L**	**a, nm**	**d_{XRD}, nm**	**d_{TEM}, nm**	**σ**
G0.06	0.06	0.8368	8.8±0.5	10.2±0.3	0.31±0.03
G0.10	0.10	0.8360	9.4±0.5	10.1±0.2	0.20±0.02
G0.15	0.15	0.8361	9.3±0.5	9.7±0.2	0.23±0.02
G0.30	0.30	0.8361	8.3±0.5	8.1±0.3	0.33±0.03
G0.60	0.60	0.8362	6.8±0.5	7.2±0.5	0.35±0.07

According to the TEM investigation, particles have nonhomogeneous rectangular/spherical shapes (Figure 67 a). Resultant size distributions fitted with the lognormal function are shown in Figure 67 b). Average particle sizes (d_{TEM}) decrease with the increase of glycine concentration in agreement with decreased size of crystallites d_{XRD} (Table 12). The d_{TEM} was slightly larger than the d_{XRD} for bigger particles and almost equal for smaller ones, which confirms the good crystal nature of particles.

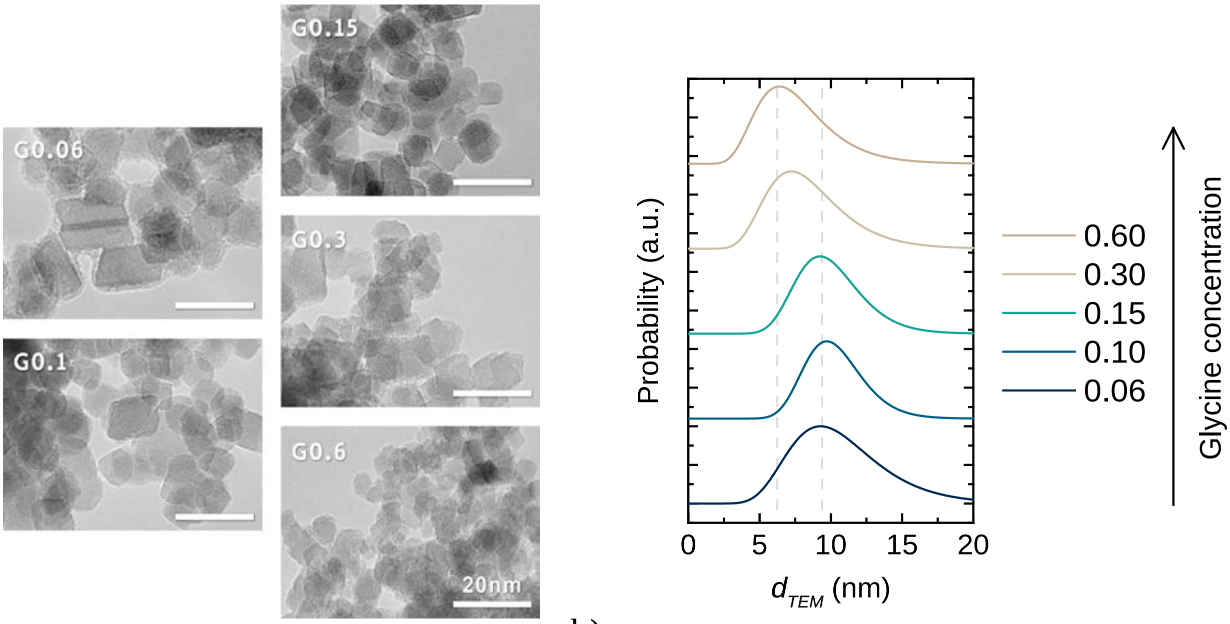

a)

b)

Figure 67. a) TEM images of G0.06–G0.60 samples (scale bar of 20 nm is the same for all images); b) results of log-normal fit of particle size distribution.

Magnetic properties

The magnetic properties of all samples were studied with the VSM of a Quantum Design Physical Property Measurement System (PPMS 9T) (Figure 68). In all cases, the M_S at 4.2 K (Table 13) is smaller than that of bulk Fe_3O_4 ($M_S \approx 92$ Am^2/kg) or γ-Fe_2O_3 ($M_S \approx 83$ Am^2/kg) [122,228]. The reduction in M_S for small crystals is expected, due to the surface spin disorder [234,235]. The lowest M_S value (~64 Am^2/kg at 4.2 K) was found in the sample G0.60, while for the rest of the samples, this value is almost equal within the confidence interval. The coercivity is also almost unaltered for the whole set of samples, except for the sample G0.60. Obtained M_S and μ_0H_C values are the following literature data for magnetic iron oxide nanoparticles in the studied size range [123,130,236]. At 300 K, all M-H curves exhibit SPM character with no observable coercivity (Figure 68 b).

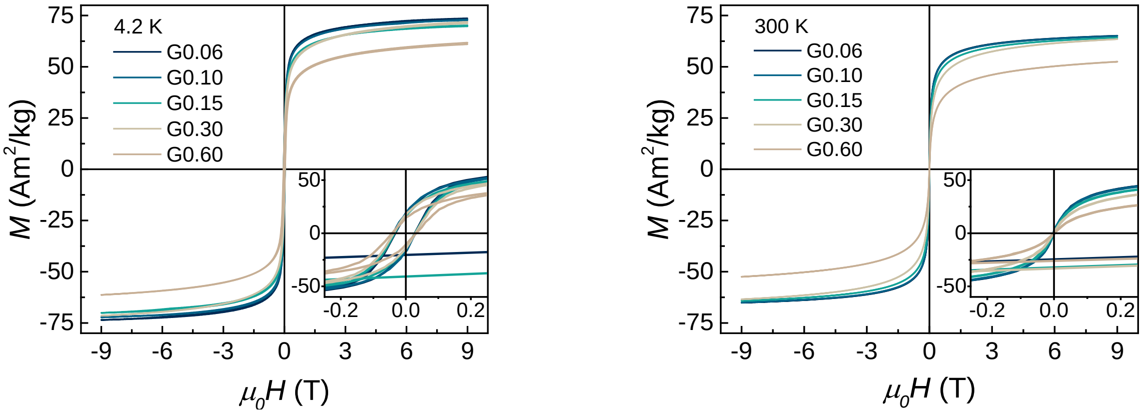

a) b)

Figure 68. *M-H* curves of G0.06–G0.60 samples measured at a) 4.2 K and b) 300 K. Insets: enlargement of a low-field region.

Table 13. Magnetic properties of G0.06–G0.60 samples: the saturation magnetization (M_S), the coercive field (μ_0H_C), the maximum of M_{ZFC} (T_{max}) and the blocking temperature (T_B).

Sample	**M_S, Am^2/kg**		**μ_0H_C, mT**	**T_{max}, K**	**T_B, K**	**β**
	(4.2 K)	**(300 K)**	**(4.2 K)**			**(T_{max}/T_B)**
G0.06	73±4	69±4	30±1	227±2	77±2	3.0
G0.10	75±4	69±4	34±1	220±2	76±2	2.9
G0.15	70±4	68±4	31±1	199±2	71±2	2.8
G0.30	74±4	69±4	34±1	169±2	63±2	2.7
G0.60	64±3	59±3	37±1	142±2	58±2	2.4

The temperature dependence of magnetization measured for ZFC and FC samples represents a typical bifurcating curve for SPM particles (Figure 69 a). The peak value of the ZFC curve (T_{max}) shifts toward the lower temperatures for samples prepared in the presence of the higher glycine content. Although $d(M_{ZFC} – M_{FC})/dT$ does not reach zero at low temperatures (probably due to interparticle interactions or surface spin freezing), the trend of T_B agrees with the trend of T_{max}. Both T_{max} and T_B values decrease with the decrease in particle size (or increase in glycine content). Linear dependence of T_B versus particle volume ($V \sim d_{TEM}^3$) in Figure 69c can be expected since $T_B \sim KV$, where K is the anisotropy constant. Thus, T_B is proportional to the particle size if K does not depend on it. T_{max} is related to T_B according to equation $\beta = T_{max}/T_B$ [224]. The shift of T_{max} from T_B and, as the consequence, the value of the β coefficient, is due to particle size distribution.

In our case, the value of β gradually decreases from the value of 3.0 for the G0.06 sample to 2.4 for the G0.60 sample.

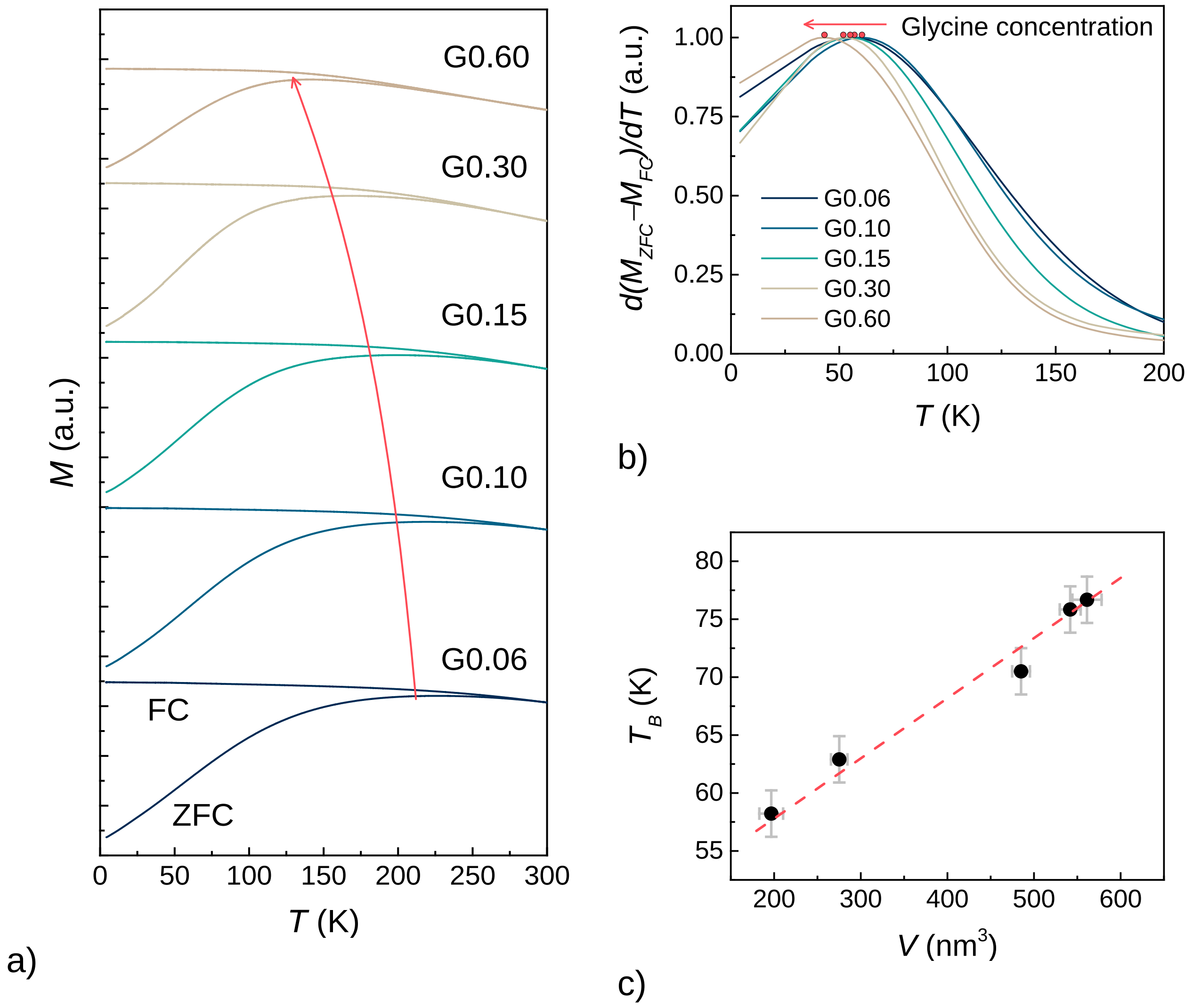

Figure 69. a) ZFC and FC curves measured in a measuring field of 10 mT (arrow indicates the temperature of the maximum of the ZFC curve); b) energy barrier distribution $d(M_{ZFC} – M_{FC})/dT$ plotted versus temperature (dots indicate its maximum); c) blocking temperature as a function of particle volume for G0.06–G0.60 samples.

4.1.2 MNPs obtained via citric acid-assisted coprecipitation

Analogously with the CP in the presence of glycine in the previous subchapter, the iron oxide MNPs were obtained by the precipitation of iron ions in the presence of different amounts of CA (citric acid). The CA acts as a capping agent and provides control of the particle size to be obtained. MNPs were synthesized in presence of 0.05, 0.1, 0.2 and 0.3 M of CA and the concentrations of CA was used as sample names (Table 14).

Structural properties

The XRD patterns (Figure 70) of iron oxide MNPs synthesized in different CA concentrations were indexed to the cubic spinel structure of magnetite (Fe_3O_4) or maghemite (γ-Fe_2O_3). For iron oxide particles prepared by this method, a core/shell-like structure is expected with an oxidized layer of γ-Fe_2O_3 and core Fe_3O_4 [122,130]. The thickness of the oxidized layer (1–2 nm) is independent on the size of particles. Thus, the smallest particles are expected to be fully oxidized maghemite. The broadening of reflections confirms that the particles are very small and/or in the partially amorphous state.

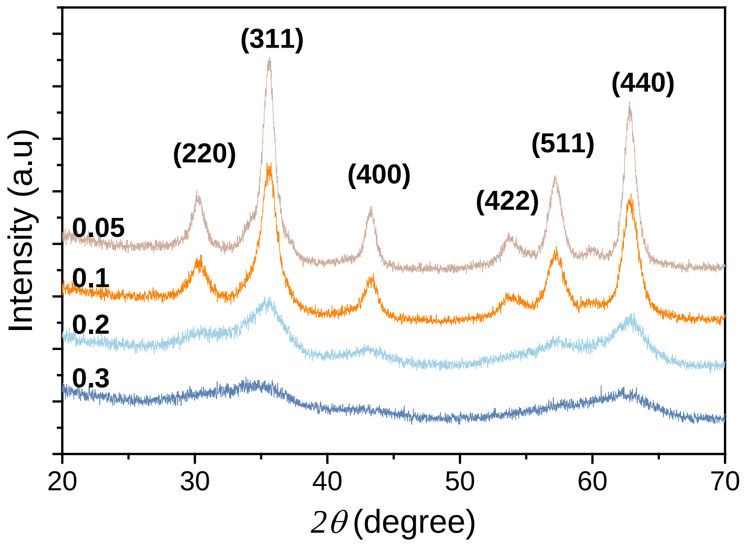

Figure 70. XRD patterns of iron oxide MNPs prepared by CP method in the presence of 0.05, 0.1, 0.2 and 0.3 M of CA [190].

Table 14. The structural properties of iron oxide MNPs prepared by CP method in the presence of different concentrations of CA: d_{XRD} is the average crystalline diameter; d_{TEM} is the average particle size from TEM; d_{mag} is the average magnetic size and t_s is the thickness of the magnetically death surface layer.

CA, M	**d_{XRD}, nm**	**d_{TEM}, nm**	**d_{mag}, nm**	**t_s, nm**
0.05	8.9±2.0	8.2±0.2	6.4±0.8	0.9
0.1	6.8±1.8	6.5±0.1	5.0±0.5	0.8
0.2	3.2±1.8	4.4±0.1	2.2±0.3	1.1
0.3	<2*	2.0±0.1	0.3±0.1	0.9

*the exact calculation of d_{XRD} for this sample with Scherrer`s equation is difficult due to a high broadening of all reflections.

Produce in the presence of CA particles have irregular shapes with sharp edges for the biggest particles and rounded edges for the smaller ones (Figure 71). The particle size decreases from about 8 to 2 nm when CA content increases from 0.05 to 0.3 M. Physical particle size estimated from TEM analysis follows the same trend of particle size reduction as observed in the reduction of crystallite size from XRD diffraction.

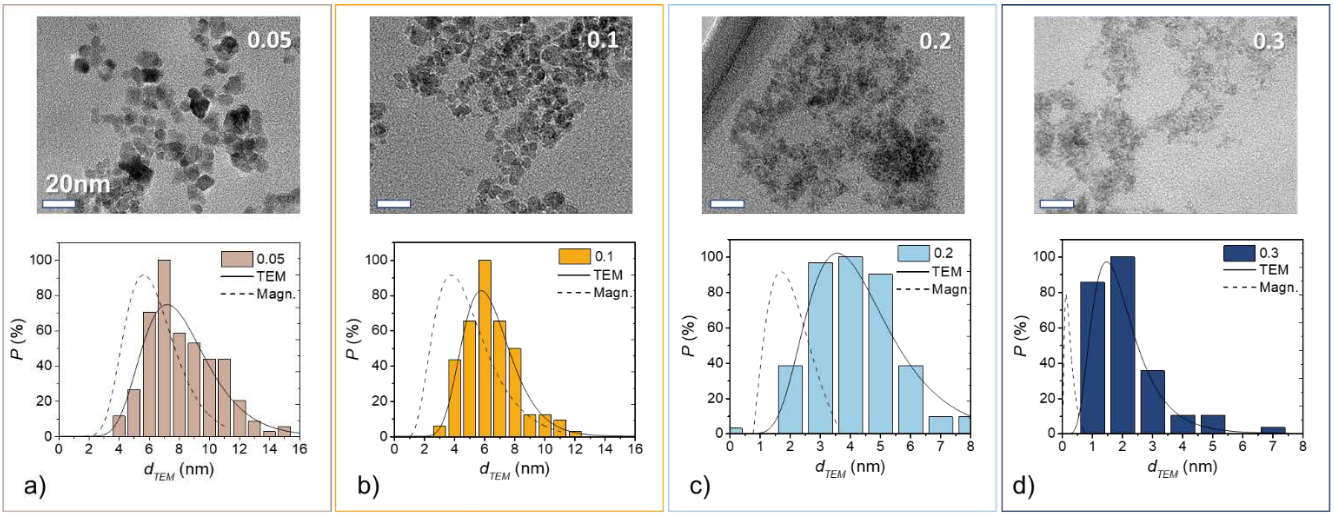

Figure 71. Upper panel: TEM images of iron oxide MNPs prepared by CP method in the presence of different concentrations of CA. Bottom panel: Particle size distribution (histograms) and their fit (solid lines), the estimated distribution of the magnetic size (dashed lines). The scale bar 20 nm is the same for all TEM images. Reprinted from [190].

Particle volume ($V \sim d_{TEM}^3$) with the increase of CA content decreases rapidly in comparison to a similar system, where instead of CA, different concentrations of glycine were added before precipitation of iron oxide MNPs (Figure 72).

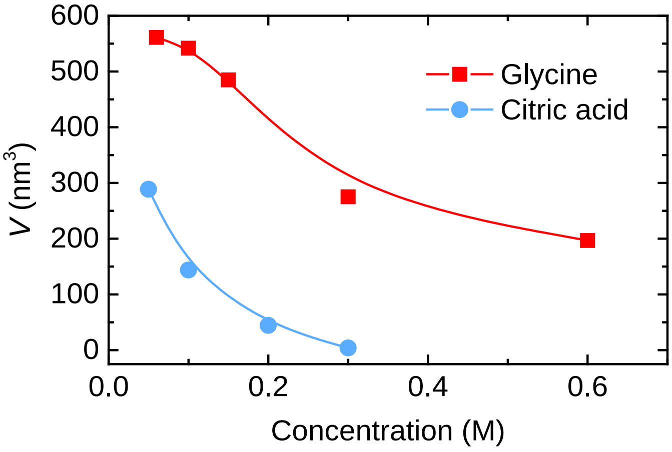

Figure 72. Dependence of particle volume on the concentration of glycine and CA added before precipitation (data for MNPs prepared in the presence of citric acid adapted from ref. [190]).

Magnetic properties

M-H curves measured at 300 K (Figure 73) exhibits non-hysteretic character suggesting the SPM state of particles [54]. *M-H* curves were fitted to the Langevin–Chantrell method with the following equation (30). Considering the lognormal distribution of the particle sizes and the spherical shape of particles. The magnetic moment μ of a single particle is $\rho M_S^{bulk} \times \pi d_m^3/6$, ρ is the density of magnetite and d_m is the “magnetic diameter” of the particle.

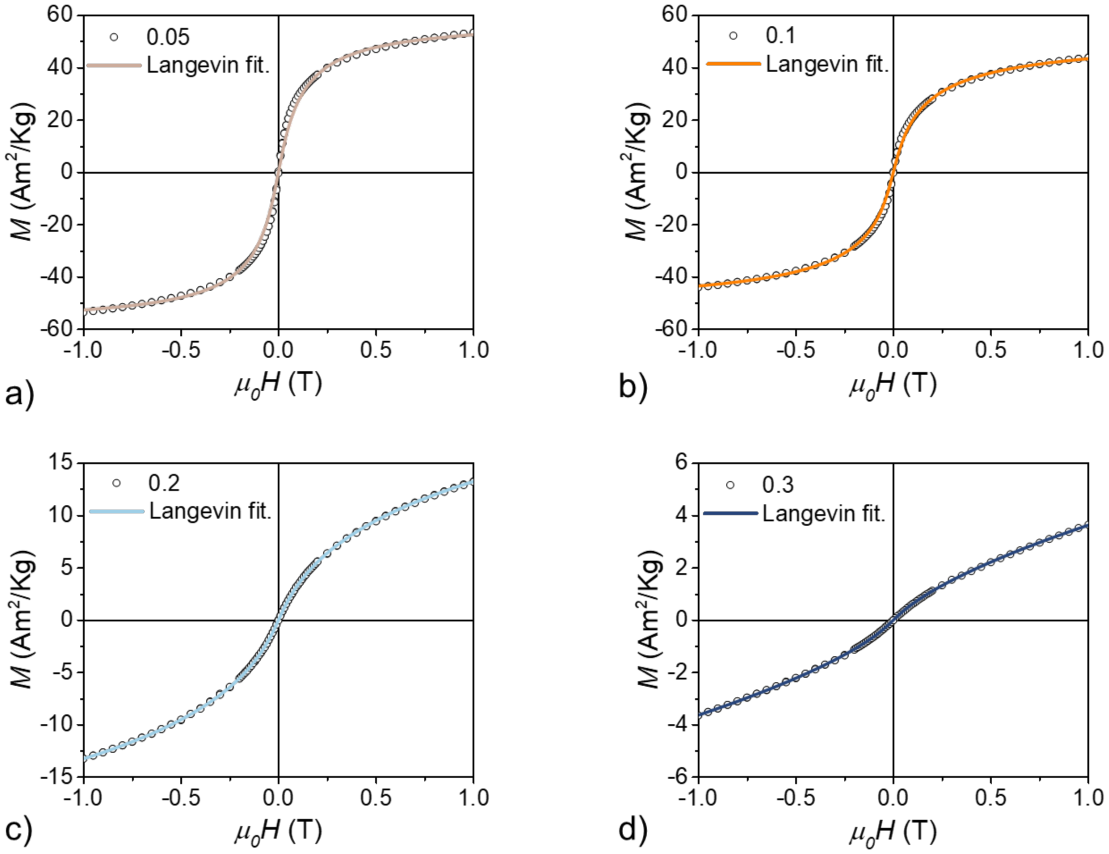

Figure 73. *M-H* curves recorded at 300 K (dots) and Langevin–Chantrell fit (lines) for iron oxide MNPs prepared by CP method in the presence of a) 0.05 , b) 0.1, c) 0.2 and d) 0.3 M of CA [190].

In the Langevin–Chantrell model, it is assumed that the distribution of particle magnetic moments $f(\mu)$ can be described by a log-normal function with average magnetic size (d_m) and its dispersion (σ_m) as free parameters. Magnetic and physical sizes decrease monotonically with the increase in the CA amount: the d_m is lower than d_{TEM}. Assuming that such reduction is due to the disordered spins on the surface (surface dead layer) with thickness t_s, the particle diameter is $d = d_m + 2\times t_s$. The calculated values for t_s of about 0.9 nm (Table 14). This is close to literature data for similar systems [237]. The relative difference of d_m and d_{TEM} increases with the size decrease, since the surface/volume ratio is higher for smaller particles.

The M_S was normalized to the mass of iron oxide. The presence of CA in the powders was quantitatively identified by TG analysis (Figure 74). The mass loss was attributed to the burning of the organic phase, which increases from 3 to 24% when CA concentration increases from 0.05 to 0.3 M. This also confirms that the added CA remains at particle surface.

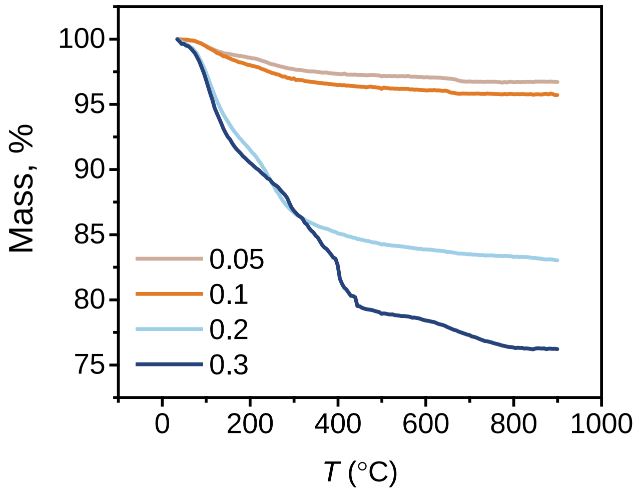

Figure 74. TG of iron oxide MNPs prepared by CP method in the presence of different concentrations of CA (argon/air (80/20) atmosphere) [190].

The *M-H* curves at 5 K (Figure 75) indicate that at low temperatures, MNPs are in a blocked FiM state with significant remanence and coercivity. The size dependences of M_S at 5 K and 300 K are reported in Table 15. In all cases, the M_S values at 5 K are smaller comparing the values for bulk magnetite (92 Am^2/kg) and close to that of maghemite bulk (83 Am^2/kg) [122,228]. The reduced M_S values for iron oxide MNPs with respect to the bulk value are due to surface disorder [122,228,238].

It is also worth noting that the magnetization decreasing rate, evaluated as eq.(79) [147], increases with decreasing size. This may be due to a lower Curie temperature (T_C) in these particles or to macrospin thermal fluctuations, which cannot be equalized even at 7 T. Moreover, for these small particles, the magnetization values are far from saturation even at a higher magnetic field (7 T). Figure 75 c) shows the parameter *R* as a function of particle size. While *R* is 94% for the largest particles, it decreases to 78% and 57% for particles of size 4 and 2 nm, respectively.

Table 15. Magnetic properties of iron oxide MNPs after precipitation in different concentrations of CA.

CA, M	**M_S, Am²/kg (5 K)**	**(300 K)**	**μ_0H_C, mT**	**μ_0H_{irr}, T (5 K)**
0.05	84±3	72±3	32±2	0.75±0.04
0.1	73±2	61±2	31±2	0.90±0.08
0.2	45±2	34±2	91±3	3.4±0.1
0.3	33±2	24±2	99±3	3.9±0.1

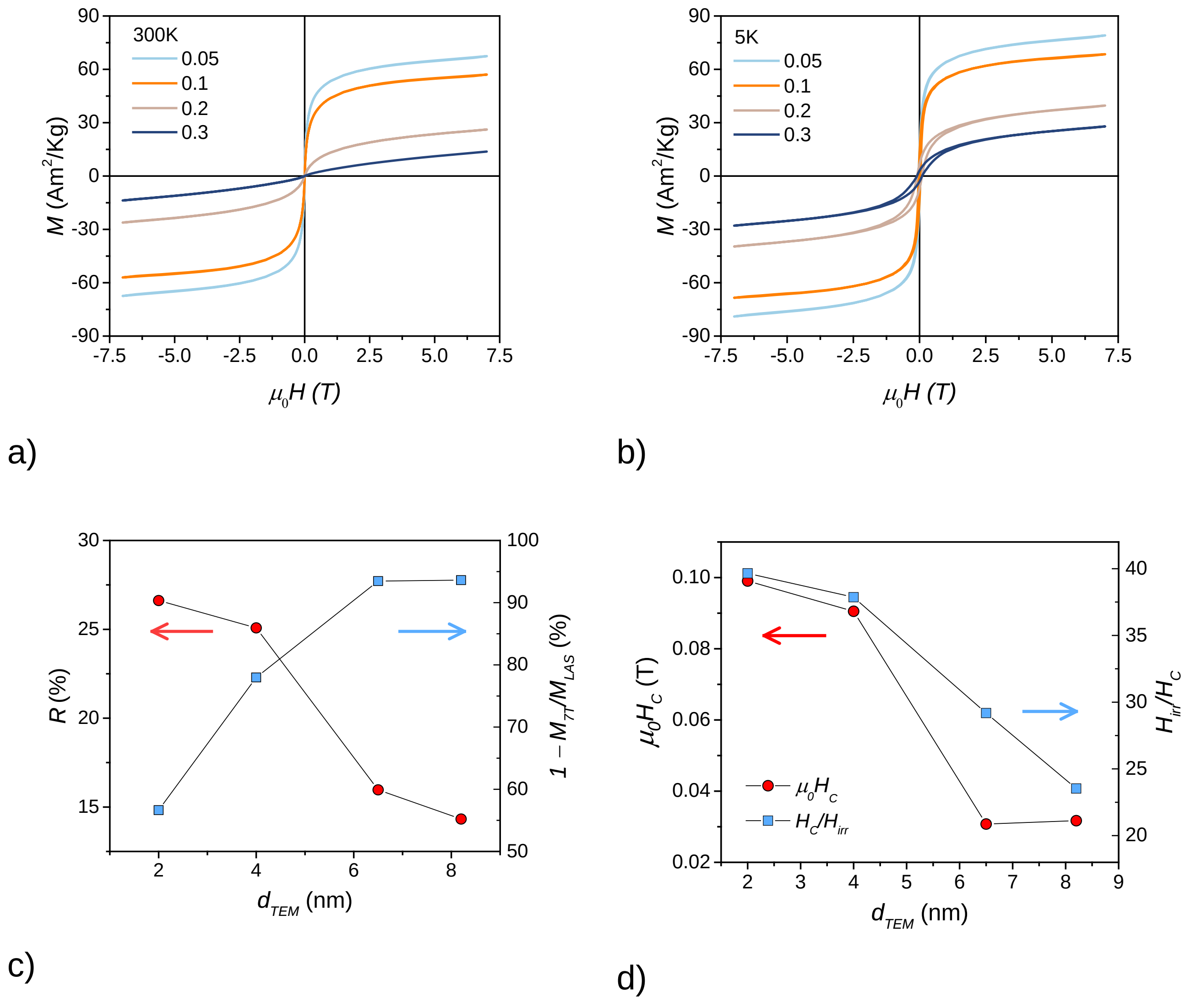

Figure 75. *M-H* curves of iron oxide MNPs prepared by CP method in the presence of 0.05 , 0.1, 0.2 and 0.3 M of CA measured at a) 300 K and b) 5 K; c) the parameter *R* and field-delay coefficient of saturation as functions of d_{TEM}; d) the size dependence of μ_0H_C and H_C/H_{irr} ratio measured at 5 K [190].

M-H hysteresis loops at 5 K show values of high coercivity ($\mu_0 H_C$) and irreversibility field ($\mu_0 H_{irr}$) (Figure 75 d). Both $\mu_0 H_C$ and $\mu_0 H_{irr}$ increase with the decrease in d_{TEM}, in accordance with previous results for ultrasmall iron oxide MNPs, due to the surface contribution to the effective magnetic anisotropy [239]. H_{irr}/H_C ratio increases with the decrease in particle size, also confirming the strong effect of surface anisotropy: $\mu_0 H_{irr}$ is about 24 and 40 times higher than $\mu_0 H_C$ for the biggest and smallest particles respectively (Figure 75d). This with literature data for $MnFe_2O_4/\gamma\text{-}Fe_2O_3$ core/shell MNPs of 3 nm prepared by the CP method [65].

The intensity of interparticle magnetic interactions was estimated from the method proposed by Thamm and Hesse [240]. In this method, the mean value of the left and right branches of the hysteresis loop minus the initial magnetization curve is analyzed (reduced values of magnetization are taken):

$$\varDelta M(H) = \ m_{initial}(H) - \frac{m_{des}(H) - m_{asc}(H)}{2}. \tag{81}$$

Such a curve is similar to δm-plot (Kelly plot) but does not require any additional measurements to be performed. In Figure 76, the $\varDelta M(H)$ functions multiplied by 2 are plotted to make easier the comparison with the Kelly plots. As evident in the $2\times\varDelta M$ plots (Figure 76), the more intense value of the negative dip for 8-nm particles (CA = 0.05) is about 0.2. The magnitude of the negative slope $\varDelta M(H)$ decreases with increasing CA concentration (decreasing particle size) and decreasing M_S. The value $\varDelta M \approx 0.2$ is close to the value of the negative slope δm obtained for highly diluted 8-nm maghemite MNPs [241]. Thus, the intensity of magnetic interparticle interactions is moderate. The energy of magnetic dipole-dipole interactions for an ensemble of randomly distributed MNPs with magnetic moments $\mu = M_S \times V$ at distances l calculated from center-to-center of neighboring particles eq.(49). With the increase of l (the higher concentration of CA) and reduction of μ (both M_S and V). Thus, the observed decrease in intensity of magnetic interparticle interactions with the decrease in particle size is reasonable.

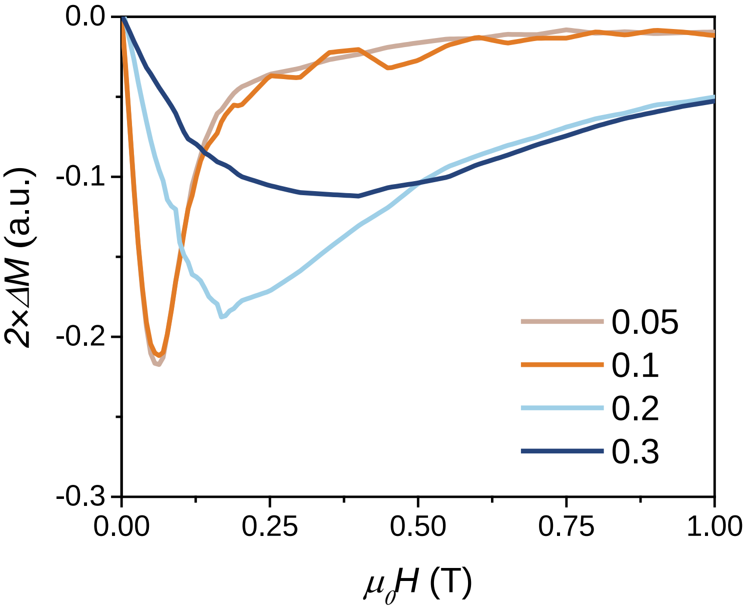

Figure 76. *ΔM*-plot obtained from Thamm–Hesse method at 5 K for iron oxide MNPs prepared by CP method in the presence of different amounts of CA [190].

The ZFC/FC curves (Figure 77) are strongly dependent on the particle size. For the samples of 2 and 4 nm MNPs, the behavior of the ZFC and FC curves with decreasing temperature is characterized by the sharp maximum of the ZFC curve and the temperature independence of FC curve below T_{max} [242–244]. While the splitting between FC and ZFC curves occurring at T_{max} is the fingerprint of a transition from the SPM (paramagnetic) regime to the superspin-glass (spin-glass) state. The superspin-glass state caused by long-range dipolar interactions between MNPs [242–244]. For larger particle sizes (CA = 0.1, 0.05) the maximum becomes broader, indicating a classical blocking process of particle moments due to the distribution of anisotropy energies. The T_{irr} associated with the blocking of the magnetic moments of the particles with the highest effective anisotropy of the assembly was found to be 30±5, 66 ±5, 95±6 and 70±7 K, for CA = 0.3, 0.2, 0.1, 0.05 [245].

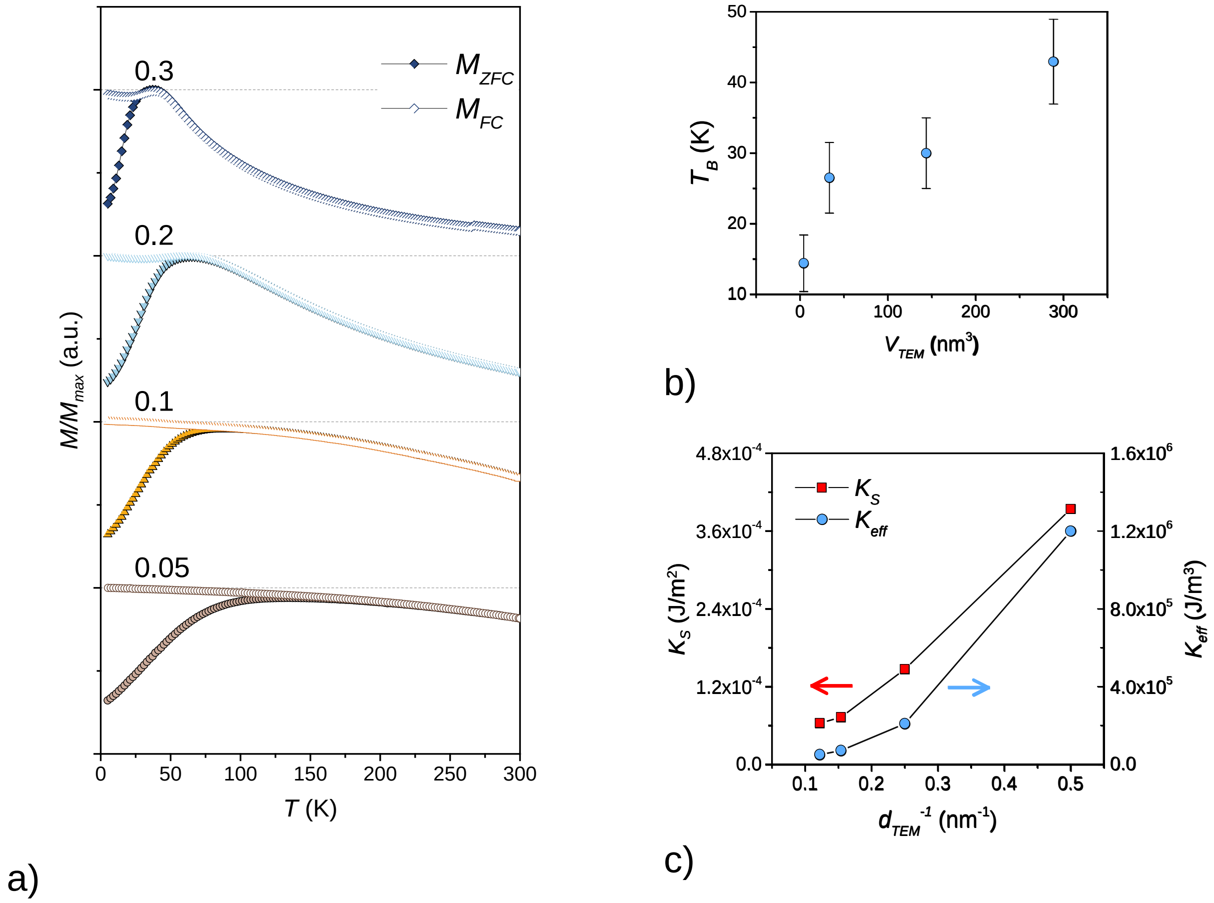

Figure 77. a) ZFC (full symbols) and FC (empty symbols) magnetizations for iron oxide MNPs prepared by CP method in the presence of 0.05 , 0.1, 0.2 and 0.3 M of CA ([190]); b) the blocking temperature versus particle volume and c) the surface anisotropy constant as a function of reciprocal size. The ZFC/FC curves were measured with an applied magnetic field of 25 mT.

Due to the fact, that particles were covered by CA and observed a low value of ΔM, we can expect that dipolar interactions are moderated. Since interparticle interactions are moderated and are not differ among samples, we can neglect them in a first approximation. However, those interactions may affect absolute values of calculated effective anisotropy.

The values of T_B and T_{irr} are reported in Table 3. They decrease with decreasing the particle size. For non-interacting particles, the effective anisotropy constant K_{eff} can be derived from eq.(29), considering the $Ln(\tau_m/\tau) = 25$ for DC magnetometry. Thus, K_{eff} can be calculated using the values of T_B and V. The obtained value increases with decreasing the particle size from 5.1×10^4 to 1.2×10^6 J/m^3 for 4- and 2-nm particles, respectively. These values are much higher than the magnetite (1.2×10^4 J/m^3) and maghemite (0.46×10^4 J/m^3) bulk values [101,122], due to the contribution of surface anisotropy. Such contribution (K_S) can be estimated, by the expression below, assuming the same value of the bulk anisotropy, due to magnetocrystalline anisotropy, for magnetite eq.(18). The K_S increases with decreasing size, the values being 1.5×10^{-4} and 3.9×10^{-4} for 4 and 2 nm, respectively and those values are one order of magnitude higher than for bigger particles.

However, this dependence has deviated from the linear trend suggesting that the surface anisotropy constant depended not only on the quantitative value of surface area but on the qualitative properties of surface and interface between spines of core and frustrated shell. In this case, surface anisotropy constant K_S is not *constant* versus size, but it is a function that reflects the change of particle structure and morphology induced by the change of synthesis parameters (CA concentration) as well as its temperature dependence. Moreover, in the case of a strong contribution of the surface on anisotropy a strong temperature dependence of anisotropy is expected, because of the change in the regime from unfrozen paramagnetic to the randomly

The low temperature glassy magnetic phase observed for the samples, consisting of 2- and 4-nm particles, can have two origins:

i) strong dipolar interparticle interaction, leading to a superspin-glass state [244]);

ii) disordered freezing, spin-glass type, of surface spins.

The second one implies an interface exchange coupling between the magnetically ordered core and surface spin-glass phase [78]). Experimentally it is difficult to distinguish the effect of the two states on the macroscopic magnetic properties.

Aging and exchange bias experiments

The magnetic memory effect at temperatures below a glassy temperature (T_G) in MNPs systems is the unequivocal evidence of non-equilibrium magnetization dynamics [208,241]. The magnetic memory effect in the sample consisting of the smallest particles (2 nm) for which the behavior of ZFC/FC curves clearly indicates glassy freezing below 44±4 K was exanimated. The peak temperature in ZFC curves can be considered as T_G. Magnetic memory effects in classical spin-glasses or superspin-glasses are manifested in ZFC magnetization curves recorded after a *stop&wait* procedure. Unlike the standard ZFC protocol, the measurements were performed with interrupting the cooling at a certain temperature below T_G for a certain time (t_{wait}). The four ZFC-memory curves following *stop&wait* protocols at different waiting times t_{wait} = 0.5 h, 3 h, 12 h and 24 h at temperature 20 K which is about half of T_g (Figure 78) were collected. The downward deviations of the memory curve from the reference ZFC were observed. The dip increases with the increase of t_{wait}. The dip magnitude increases as a logarithm with of t_{wait}. This behavior is a typical manifestation of slow dynamics [246]. Clear logarithmic behavior of the memory dip depth was observed in superspin-glass MNPs systems [208,247].

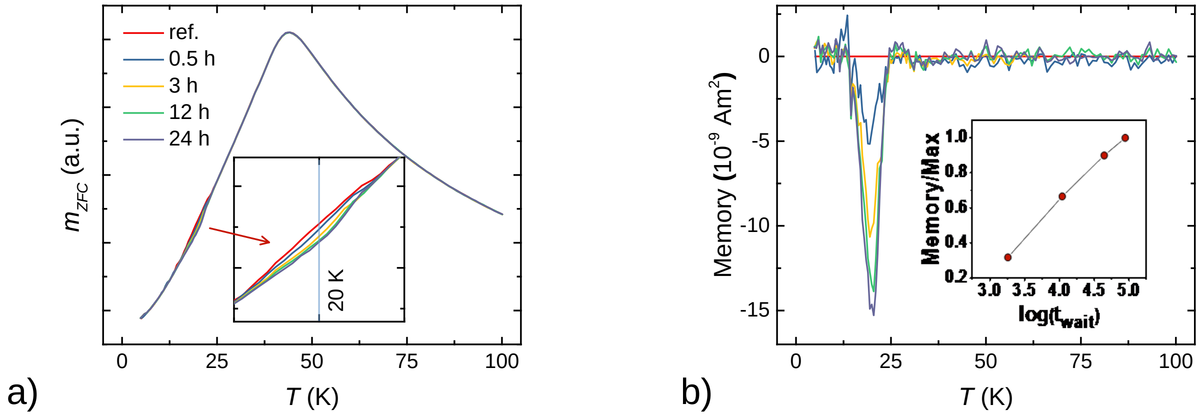

Figure 78. a) ZFC reference curve (red line) and ZFC-memory curves after stop-and-wait for 0.5, 3 h, 12 h and 24 h at 20 K; b) Difference between ZFC-reference and ZFC-memory curves for 2-nm iron oxide MNPs prepared in CA concentration of 0.3 M. ZFC curves were measured in the field of 10 mT. The inset is the normalized dip magnitude in the logarithmic scale [190].

The random surface anisotropy of the frozen frustrated spins makes the spin-glass surface phase highly anisotropic [241,244], capable to pin the spins of the core through interface exchange coupling. Such pinning invokes the EB phenomenon accompanied by an increase in the magnetic anisotropy [81,248]. The EB phenomenon was observed by comparing the hysteresis loops measured at 5 K after ZFC with those measured at the same temperature after cooling the sample from 300 K by applying a magnetic field $\mu_0 H_{FC}$

of 3 T. In Figure 79, the region of the FC and ZFC hysteresis is plotted for 2-nm particles sample. The shift of the hysteresis curve measured after field cooling concerning that measured after ZFC indicates the presence of the EB effect. The exchange bias field was calculated following eq.(21). The $\mu_0 H_E$ is 9±1 mT and it was also observed for the 4.4 nm particles sample ($\mu_0 H_E = 8.5 \pm 1.0$ mT), whereas it was not observed for the bigger particles.

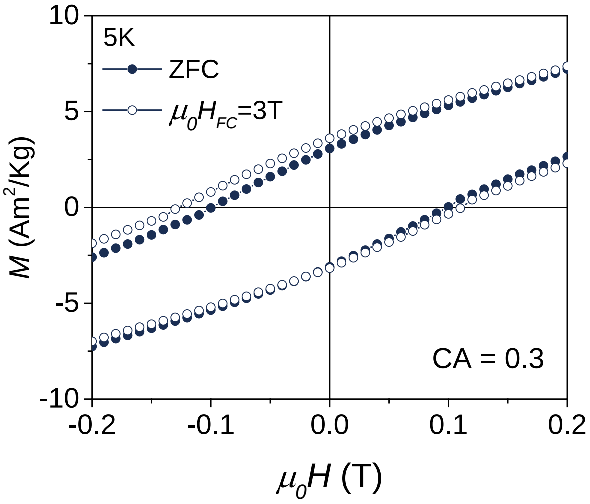

Figure 79. The ZFC and FC *M-H* loops measured at 5 K for 2-nm iron oxide MNPs prepared in CA concentration of 0.3 M [190].

This observation confirms that the smallest particles have a core/shell magnetic structure where the FiM core and the spin-glass type shell which are exchange-coupled at the interface [81]. Recently M. Vasilakaki et al. provided evidence, by magnetization measurements and Monte Carlo simulations, of the EB phenomenon in 2-nm $MnFe_2O_4$ MNPs [244]. The EB field and the increase in coercivity were attributed to the intraparticle interactions through the core/shell interface. The observation of EB provides evidence of the significant role of the surface spins in the low-temperature magnetic behavior, characterized by slow non-equilibrium dynamics.

The EB effect depends on the magnetic anisotropy of the core and surface phases, their relative size and the quality of the interface. Since the estimated thickness of the magnetically frustrated region (known from the comparison of physical and magnetic sizes) is almost the same in all samples, the size-dependent behavior of EB can be explained in terms of the relative volume fraction of the surface spins. Namely, the critical particle size (d_c) for the observation of EB was defined as the size at which the FiM core (d_m) is lower than the double thickness of the spin-glass surface layer, $d_m < 2\times t_s$ (Figure 80). We should highlight here, there this model considers average values of particle sizes and frustrated region thickness, thus in the case of the smallest particles in assembly can be presented very small particles with the almost totally frustrated core as well as relatively big particles giving a major contribution to the magnetic properties of the whole system.

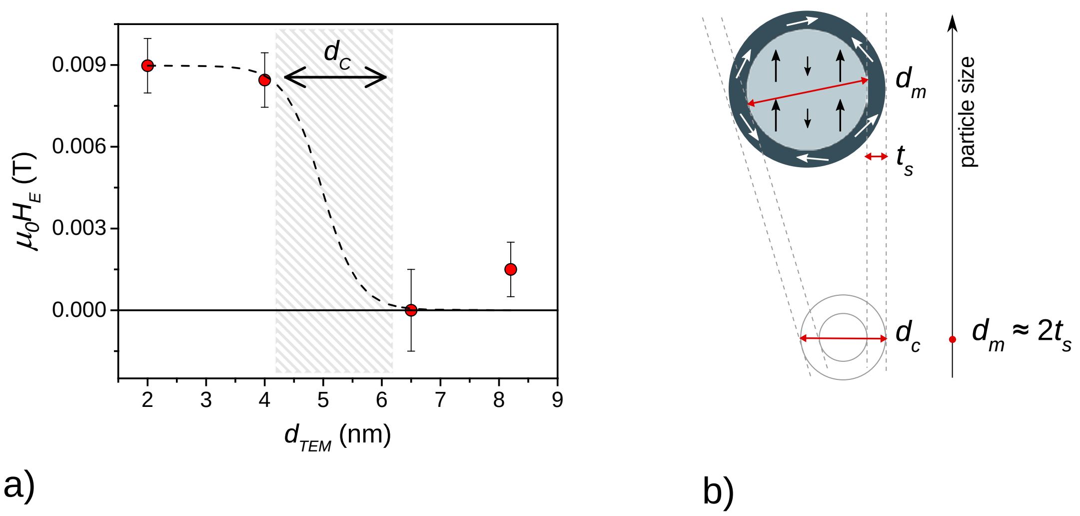

Figure 80. a) Dependence of the exchange bias field (μ_0H_E) at 5 K for iron oxide MNPs of different size (the field of cooling was 3 T; b) the schematic representation of the model of critical size to observe EB in MNPs with spin-glass shell. Data adapted from ref. [190].

Our finding agrees with the results reported in [249], where the EB phenomenon was observed in systems with the spin-glass region corresponding to 50% of the particle volume. In the case of the AFM shell, it was demonstrated that only two monolayers of the AFM shell were enough to induce EB in ultrasmall Fe/Cr nanoparticles [250]. Our results are consistent with those of ref. [249], as exchange bias was observed only for the smaller particles samples where the fraction of surface spins represents the majority of spins in the particle volume. The requirement of the critical size, i.e. $d_m < 2t_s$, is satisfied for the 2 nm particles sample, showing EB. For 4.4 nm particles sample, showing EB,

$d_m \approx 2t_s$, identifying the critical size for our nanoparticle system. For 6.5 nm and 8.2 nm particles samples, not showing EB, d_m is well above $2t_s$ (d_m and t_s values in Tab.1).

4.1.2 Cobalt ferrite MNPs in Si_2O matrix

A set of $CoFe_2O_4$ MNPs in diamagnetic SiO_2 matrix with a certain concentration of FiM phase (5–15%) was synthesized by SGAC method and treated at three different annealing temperatures (700, 800 and 900 °C). This set of samples was provided by prof. Davide Peddis. Briefly, for nanoparticle synthesis, aqueous solutions of iron and cobalt nitrate in a molar ratio of 2:1 and CA with a molar ratio of metals to CA in a ratio of 1:1 were mixed. Then the pH was adjusted to the value of 2 by adding ammonia solution. Tetraethoxysilane (TEOS) dissolved in ethanol was used as a silica precursor. After stirring intensively for 30 min all the reagents, the resulting sols were placed in a furnace for gelling in air at 40 °C for 24 h. The gels were successively subjected to heat treatment in a muffle furnace at 300 °C for 15 min, where the autocombustion reaction took place. The temperature was then increased for 1 h to T_{ann} = 700, 800, or 900 °C for each sample (hereafter referred to as CFO_700, CFO_800, and CFO_900). The particle size distribution was obtained by TEM images analysis (Table 16). An increase in particle size with the increase in annealing temperature was observed (Figure 81).

Table 16. Structural and magnetic properties of $CoFe_2O_4$ MNPs in SiO_2 matrix.

Sample	**d_{TEM}, nm**	**T_{max}, K**	**T_{irr}, K**	**$T_B^{CH.}$, K**	**$PD^{CH.}$, %**	**$T_B^{H.M.}$, K**	**$PD_{H.M.}$, %**
CFO_700	2.5±0.2	29±1	57±5	18±1	3.26	16±1	4.56
CFO_800	5.3±0.5	43±1	70±5	22±2	2.86	25±2	2.44
CFO_900	6.6±0.5	53±1	82±3	29±1	2.41	31±2	2.45

*Average blocking temperatures from TRM ($T_B^{CH.}$), and Hansen and Mørup ($T_B^{H.M.}$).

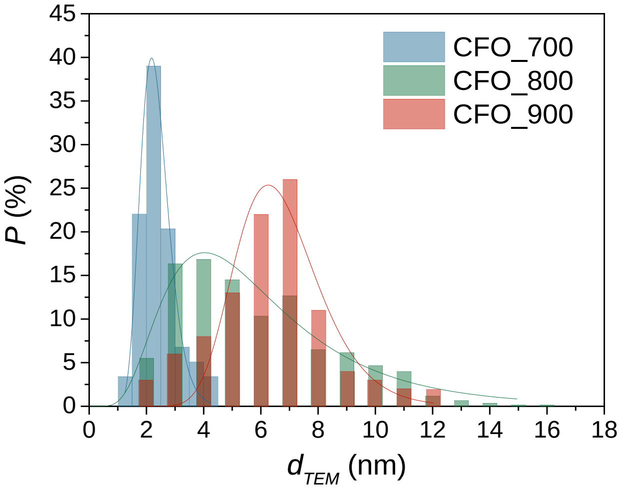

Figure 81. Lognormal particle size distribution of $CoFe_2O_4$ MNPs in diamagnetic SiO_2 matrix annealed at 700, 800, and 900 °C.

The ZFC/FC magnetizations are shown in Figure 82. The shape of the FC curves implies that interparticle interactions are negligible [54,205,251]. The temperatures T_{irr} and T_{max} increase with the annealing temperature. According to Gittleman et al. [99], T_{max} is related to the average blocking temperature T_B through the equation $T_{\mathrm{max}} = \beta T_B$. The difference between T_{irr} and T_{max} reflects the broadening in the blocking temperature distribution in the absence of magnetic interparticle interactions and it is correlated to the distribution of particle sizes. In our samples, such difference is weakly dependent on the annealing temperature, indicating that the thermal treatment does not significantly affect the distribution of $f(T_B)$. Indeed, the shape of the $f(E_a)$ is similar for the three samples, confirming that the sources of anisotropy are basically the same. Following Chantrell and co-workers [106], the $f(E_a)$ was fitted by a log-normal function to determine the mean value of the blocking temperature (T_B^{CH}) Table 1 [252–254]. Hansen and Mørup proposed a phenomenological approach to calculate the average blocking temperature ($T_B^{\mathrm{H.M.}}$) and its standard deviation ($\sigma_{\mathrm{H.M.}}$) [88]. They found that $T_B^{\mathrm{H.M.}}$ and $\sigma_{\mathrm{H.M}}$ can be expressed with known values of T_{irr} and T_{max} from

$$T_B^{\mathrm{H.M.}} = T_{max}\left[1.792 + 0.186 \cdot \ln\left(\frac{T_{\mathrm{irr}}}{T_{max}} - 0.918\right)\right] - 1 + 0.0039 \cdot T_{\mathrm{irr}}\ ; \tag{82}$$

$$\sigma_B^{H.M.} = 0.624 + 0.397\, ln(T_{irr}/T_{max} - 0.665). \tag{83}$$

$T_B^{\text{H.M.}}$ values are 16±1, 25±2 and 31±2 K and their standard deviation values are 0.73, 0.61, and 0.57 for samples CFO_700, CFO_800 and CFO_900, respectively. The values of the average blocking temperatures extracted by both models are equal within the experimental errors (Table 16). To estimate the polydispersity of the sample properties with respect to the average, a polydispersity index (*PD*) has been defined as:

$$PD = 100\% \times \frac{\sigma}{T}. \tag{84}$$

The *PD* values obtained by Chantrell ($PD^{\text{CH.}}$) and Hansen–Mørup models ($PD^{\text{H.M.}}$) decrease with increasing particle size, although this trend is more evident for the Chantrell model.

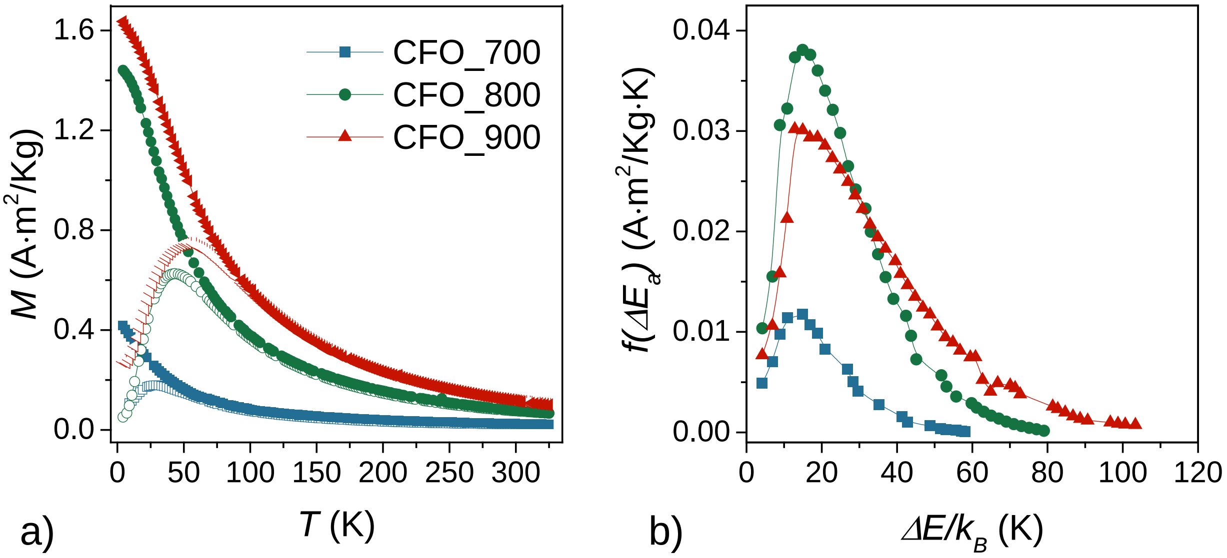

Figure 82. a) ZFC (empty symbols) and FC (solid symbols) magnetization curves; b) magnetic anisotropy energy distribution obtained from the first derivative of the TRM magnetization $M_{\text{TRM}}(T)$ versus temperature for CFO_700, CFO_800 and CFO_900 samples [15].

Figure 83 a) shows the AC-susceptibility measurements performed using a susceptometer (Model ACS 7000, Lake Shore Cryotronics) in a field of 2.5 mT at frequencies υ from 5 Hz to 10 kHz, in the temperature range of 18–310 K. According to the Néel–Arrhenius model, the relaxation process of the particle moments due to thermal activations in the absence of interparticle interactions can be derived from eq.(26):

$$ln\;(\tau_m) = ln\;(\tau_0) + \frac{K_{\mathrm{eff}}V}{k_B T_B}. \tag{4}$$

For the sample CFO_700, the τ_0 value 1.9×10^{-9} s confirms that the interparticle interactions are small. For CFO_800 and CFO_900 samples, the τ_0 is unphysically small (Table 17). This fact indicates that the magnetic interparticle interactions are not negligible for these samples and Néel–Arrhenius model is not appropriate to describe the dynamical behavior of magnetic moments. In this case, the Vogel–Fulcher law considering the weak interparticle interactions by a temperature term T_0 can be applied [87,255,256]. The eq. (28) was then rewritten in the following form:

$$ln\;(\tau_m) = ln\;(\tau_0) + \frac{K_{eff}V}{k_B(T_B + T_0)}. \tag{5}$$

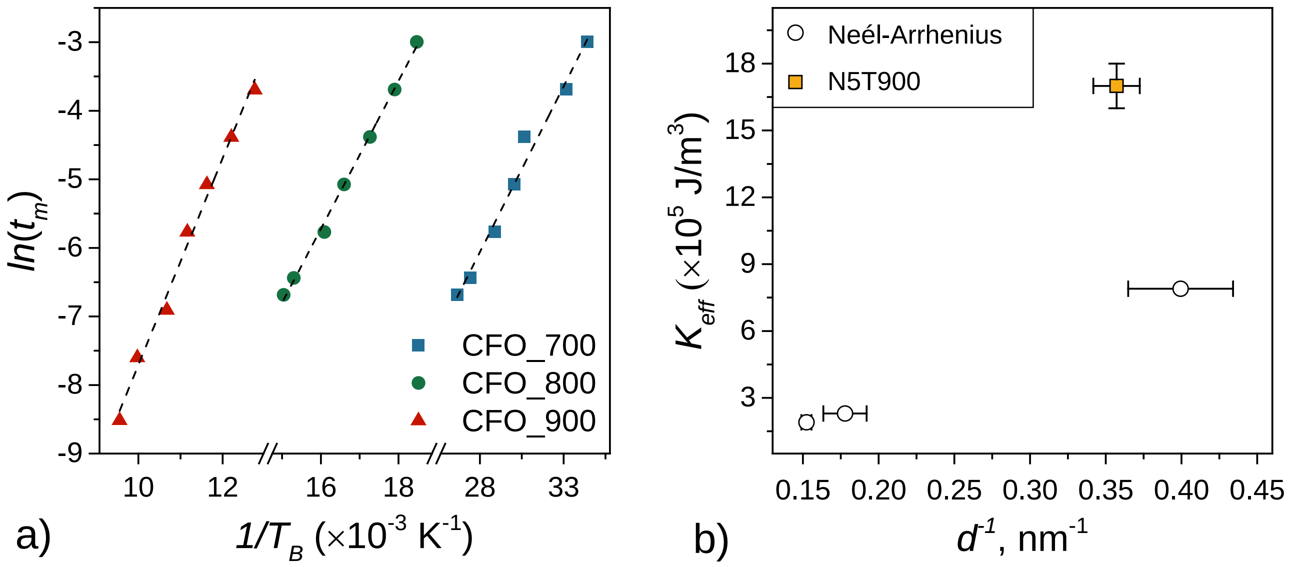

Figure 83. a) $ln(\tau_m)$ versus $1/T_B$ and its linear fit (dashed line); b) effective anisotropy constant K_{eff} of CFO_700, CFO_800 and CFO_900 obtained from fitting $\ln\,(\tau_m)$ versus $1/T_B$ by Neél–Arrhenius model (empty circles) [15]. N5T900 is the reference sample from [107].

Table 17. Magnetic parameters obtained from AC magnetic susceptibility measurements for CFO_700, CFO_800 and CFO_900 samples.

Sample	**Néel−Arrhenius** [1]		**Vogel−Fulcher** [2]	
	$\boldsymbol{K_{eff}}$, **J m**$^{-3}$	$\boldsymbol{\tau_0}$, **s**	$\boldsymbol{K_{eff}}$, **J m**$^{-3}$	$\boldsymbol{T_0}$, **K**
N15T700	$7.9\pm0.4\times10^5$	1.9×10^{-9}	$11\pm1\times10^5$	-1 ± 3
N15T800	$2.3\pm0.2\times10^5$	8.2×10^{-14}	$1.3\pm0.1\times10^5$	14 ± 2
N15T900	$1.9\pm0.2\times10^5$	1.5×10^{-14}	$0.92\pm0.01\times10^5$	32 ± 3

The values of T_0 and K_{eff} (Table 17) have been obtained with the fixed specific relaxation time τ_0 equal to 10^{-10} s for all the samples [107,254]. From this fit for the sample CFO_700, T_0 is almost zero additionally confirming that interparticle interactions are negligible in this sample. In samples annealed at higher temperatures, T_0 indicates an increase in the dipolar interactions. The values of K_{eff} obtained by Néel–Arrhenius and Vogel–Fulcher models are almost equal for sample CFO_700 but the difference is observed for CFO_800 and CFO_900 due to magnetic interactions.

In both models, K_{eff} decrease with the increasing particle size. The K_{eff} decreases by ~30% comparing 6.6 nm (CFO_900) to 5.6 nm (CFO_800) MNPs, while a much higher growth of ~70% was observed comparing 6.6 nm (CFO_800) to 2.5 nm (CFO_700) MNPs. Hence, the surface anisotropy increases with a decrease in the particle size, and it becomes dominant in the smallest particle CFO_700. The smaller anisotropy in $CoFe_2O_4$ MNPs compared to the bulk value can be related to a change in the inversion degree. This agrees with reported data for $CoFe_2O_4$ MNPs [107,257] and it was explained by a change in the cation distribution inducing the decrease of the magnetocrystalline anisotropy determined by the distribution of the Co^{2+} cations between O_h and T_d sites [135].

Figure 83 b) shows the K_{eff} value of a reference sample of $CoFe_2O_4$ MNPs embedded in a SiO_2 matrix with a 5% w/w concentration of FiM phase annealed at 900 °C (N5T900 [107]). For this sample, the $d_{TEM} = 2.8 \pm 0.3$ nm is close to that of the CFO_700 ($d_{TEM} = 2.5 \pm 0.5$ nm), and they have the *PD* index (Table 18). It is important to underline that the interparticle interactions in both N5T900 and N15T700 samples are negligible, as indicated by their ZFC/FC magnetizations and δm-plots (Figure 84). The K_{eff} is higher for N5T900 sample despite both samples have the same morphological features. This can be explained by the cation distribution change caused by the annealing. The highest temperature induces a larger occupancy of O_h sites by the Co^{2+} cations in N5T900 sample [107].

Table 18. The particle size d_{TEM}, the standard deviation σ, the percentual polydispersity of N5T900 and CFO_700 samples.

Sample	d_{TEM}**, nm**	σ	***PD*, %**
CFO_700	2.3±0.1	0.19±0.01	8.3
N15T900	2.8±0.1	0.22±0.01	7.9

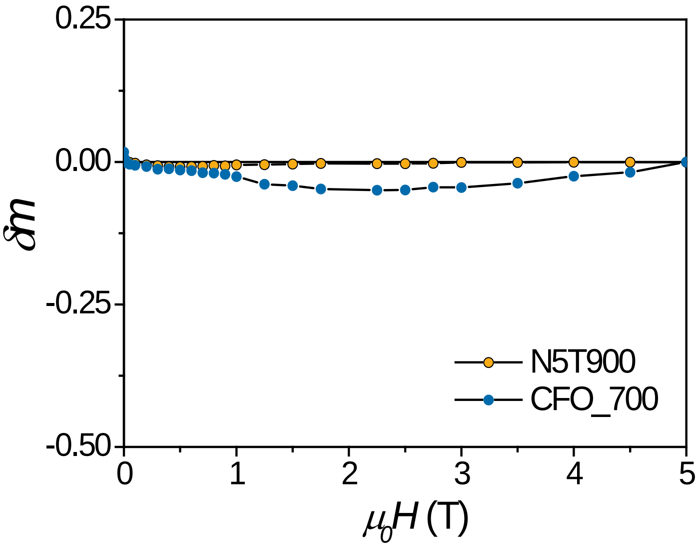

Figure 84. δm plots for sample CFO_700 [15] and sample N5T900 from ref. [258]. The temperature is 5 K.

Figure 85 shows low-temperature *M-H* loops of the samples CFO_700 and N5T900. Both hysteresis loops are not saturated due to high anisotropy of samples. The M_S and χ_{SAT} were found employing the LAS (eq.(70)). The latter is strongly related to the non-collinear spin structure due to competing interactions between sublattices, and to the symmetry breaking at the particle surface [82,200].

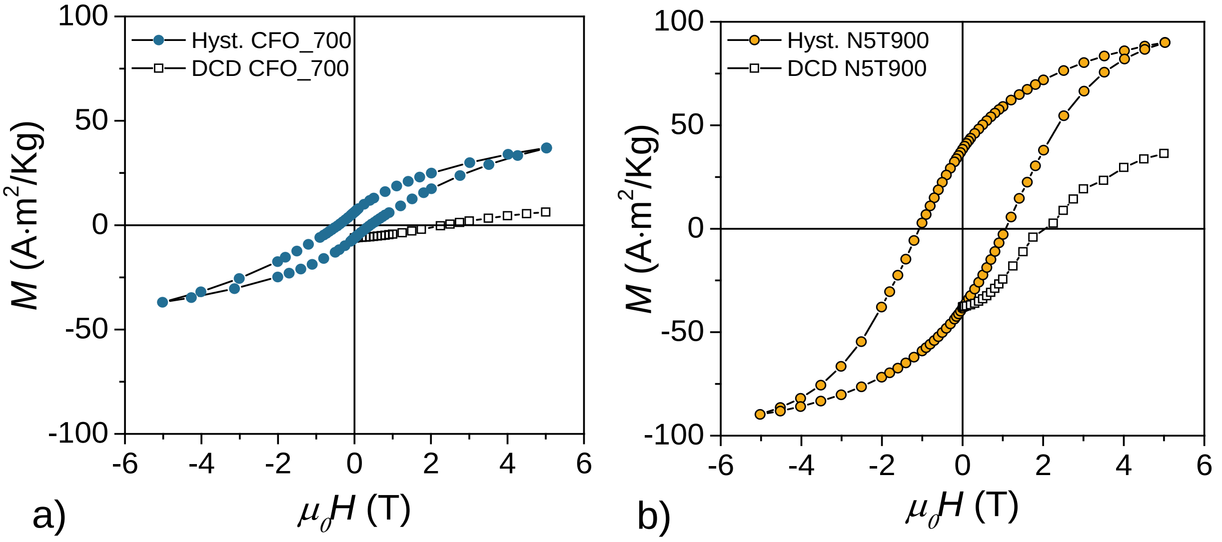

Figure 85. M-H and DCD curves measured at 5 K for a) sample CFO_700 [15] and b) reference sample N5T900 with the same particle size [107].

The M_S increases with particle size growth, i.e., with annealing temperature (Figure 86). Despite reference sample N5T900 (2.8 ± 0.3 nm particle size) and CFO_700 having the same d_{TEM}, M_S for N5T900 is almost twice that for CFO_700. This difference can be ascribed to the combined effect of cation distribution, spin-canting, and surface anisotropy [107,259]. The χ_{SAT} increases with decreasing particle size. The trend of χ_{SAT} indicates the stronger contribution of the surface magnetic anisotropy for smaller particles. It is worth emphasizing that CFO_700 has a higher value of χ_{SAT}, indicating that the surface contribution to the effective magnetic anisotropy is higher in CFO_700 than in CFO_900. The energy barrier distribution can confirm this. In fact, despite N5T900 and CFO_700 having the same *PD* of the d_{TEM}, the *PD* for T_B calculated by H.M. model is much higher for CFO_700 (*PD* of $T_B^{\mathrm{H.M.}}$ is 4.6) than for N5T900 (*PD* of $T_B^{\mathrm{H.M.}}$ is 2.5). Labarta and co-workers have shown that, for spinel ferrite MNPs, even when the size distribution is narrow, the surface anisotropy can produce a substantial broadening of the anisotropy energy distribution [260]. This effect is an obvious consequence of the different size dependence of the energy contributions from the core and the surface. Because the volume content of the surface spin layer increases with a decrease in size, and it becomes more significant for ultrasmall particles (<10 nm).

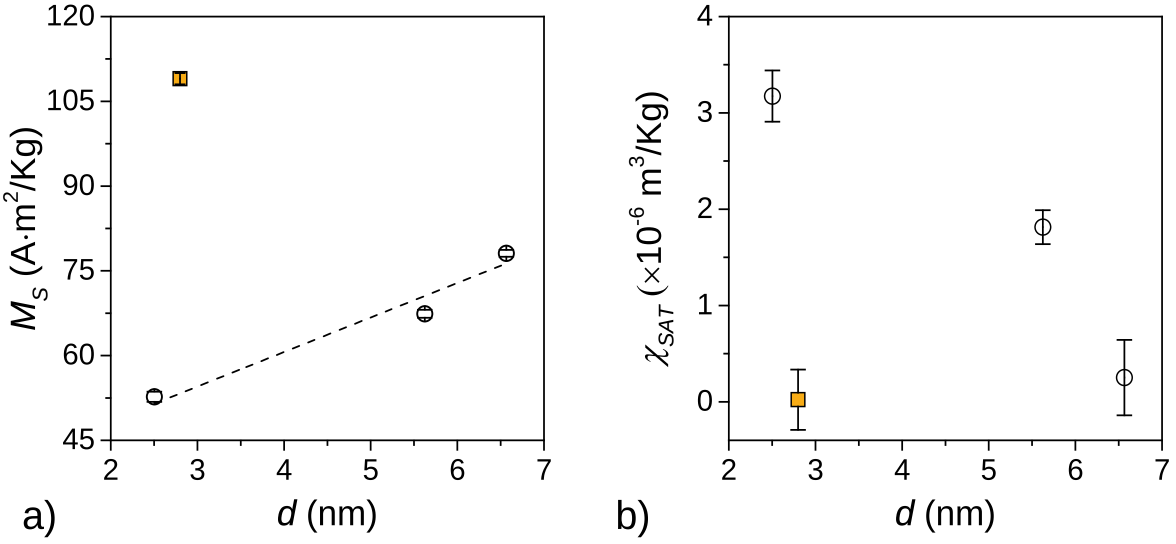

Figure 86. a) Saturation magnetization, M_S, and b) non-saturated susceptibility, χ_{SAT} of $CoFe_2O_4$ MNPs of different size in diamagnetic SiO_2 matrix [15]. The square in both graphs corresponds to the reference sample N5T900 [107].

The squares in Figure 85 represent $M_{DCD}(H)$ curves measured at 5 K. M_{DCD} is only sensitive to the irreversible component of the magnetization and only the blocked particles contribute to the remanent magnetization. The curve shape approximates the SFD related to the energy barrier distribution. The value of the field at which the M_{DCD} is equal to zero ($\mu_0 H_{Cr}^{DCD}$) corresponds to the average switching field. Notwithstanding, that both samples with the different $\mu_0 H_C$ have close the $\mu_0 H_{Cr}^{DCD}$ (for CFO_700 $\mu_0 H_{Cr}^{DCD}$ = 2.4 T, for N5T900 $\mu_0 H_{Cr}^{DCD}$ = 2.1 T). This result is in line with the similar anisotropy fields $\mu_0 H_K$ (for CFO_700 5.8±0.5 T, for N5T900 5.9±0.6 T) estimated by the SW model (eq.(17).

Even though $\mu_0 H_{Cr}^{DCD}$ and $\mu_0 H_K$ are equal within the experimental error, the coercivities of the two samples are different. Such differences can be associated with a larger fraction of disordered spins correlating with the cation distribution, also confirmed by the lower value of the remanent and saturation magnetizations [261].

4.3 Conclusions

1. The size of iron oxide MNPs can be gradually modulated in the coprecipitation route by adding the capping agent (oleic acid or glycine) preventing particle growth;
2. Produced by this method MNPs have relatively high saturation magnetization which reduces from 84±3 Am^2/kg to 33±2 Am^2/kg with the reduction of average particle size from 9 nm to 2 nm due to the high contribution of canted magnetic moments of atoms at the surface;
3. The layer of magnetically frustrated spins can be considered as the second magnetic phase in a chemically homogenous system;
4. At low temperatures, due to surface disorder, the canted surface can be frozen in spin-glass-like manner and collect attributes of both surface and interface, namely slow dynamics typical for magnetically frustrated materials and exchange bias;
5. The thickness of the canted region of atomic magnetic moments was experimentally found to be about 1 nm and it was shown that the critical to observe exchange bias in quasi-spherical iron oxide MNPs produced by the described method is about 4 nm (in other words, when the radius of the core is equal to the thickness of frustrated region because of the correlation length of exchange interactions);
6. In ultra-small cobalt ferrite MNPs prepared by the SGAC method despite the strong contribution of the surface, magnetocrystalline anisotropy plays an important role and for those particles the constant of effective anisotropy exceeded the bulk value up to 4 times;
7. Magnetocrystalline anisotropy of ferrites at the nanoscale changes due to variation of structural parameters, such as inversion degree, which is a function of synthesis condition.

Chapter 5. Magnetic anisotropy of nanohybrid systems

According to the literature review of recent publications on the topic of magnetic nanoparticles, the development of novel synthesis methods and advanced techniques of structural analysis of nanoscale objects invoke interest in producing complex nanohybrids composed of several magnetic phases, for example, core/shell architectures. Considering the strong exchange-coupling between the two phases and the relatively thin layer of the soft phase, the saturation magnetization and the effective anisotropy contestant are expected as $M_S = f_{soft}M_{soft} + f_{hard}M_{hard}$ and $K_{eff} = f_{soft}K_{soft} + f_{hard}K_{hard}$, where f is the mass fraction. For SD MNPs with uniaxial anisotropy, the value of coercivity for can be expressed as $\mu_0H_{C(SW)} = 2(f_{soft}K_{soft} + f_{hard}M_{hard})/(f_{soft}M_{soft} + f_{hard}M_{hard})$. Nevertheless, such a simplified model does not consider many size features, surface phenomena, and the effects of magnetic interactions between MNPs. The object of this section is MNPs with the core/shell structure of various configurations and their magnetic properties will be experimentally investigated and discussed. In addition, the AFM/FiM and hollow nanoparticle systems will be studied.

Sample of MNPs studied in this chapter were produced by the HTD method at the University of Genova by Dr Silvia Villa, Prof. Fabio Canepa and Prof. Davide Peddis. XRD and STEM investigations were performed by Dr Gurvinder Singh (department of Biomedical Engineering and Sydney Nano Institute, The University of Sydney). EFTEM and HAADF-STEM investigation was done in Istituto di Scienze e Tecnologie Chimiche “Giulio Natta” by (Prof. Alessandro Ponti and Prof. Anna M. Ferreti). The author of the dissertation is grateful to Prof. Kalliopi Trohidou from Institute of Nanoscience and Nanotechnology (National Center for Scientific Research Demokritos) for the discussion of magnetic properties and the development of a theoretical model allowing a deeper understanding of the magnetic properties reported in sections 5.1 and 5.2. Results of the application of the theoretical model compared with experimental results reported in section 5.1 are published in Nanoscale Advanced [180]. On basis of the results reported in section 5.3, a paper was published Magnetochemistry [192] and results of section 5.4 in Nanotechnology [16].

5.1 Soft/hard and hard/soft MNPs

In this section, a study of the physical properties of two systems of nanoparticles with a core/shell structure is presented: one system is hard/soft MNPs with a core consisting of magnetically hard cobalt ferrite coated with a magnetically soft nickel ferrite shell, and the second system has the opposite configuration: a magnetically soft shell and a magnetically hard core with almost the same size and shape. The synthesis of core/shell MNPs was carried out according to a two-step procedure in which preformed cobalt or nickel ferrite MNPs were used as "seeds" (core) for the subsequent growth of a shell consisting of cobalt or nickel ferrite different from the core material.

Among spinel ferrites, the cobalt ferrite has a higher value of magnetic anisotropy constant of 0.1−10 J/m^3, which is about 1−2 orders of magnitude higher than in other spinel ferrites [262]. Because of this reason, the cobalt ferrite acts as a hard phase in most core/shell MNPs and its counterpart is another soft magnetic material with high saturation magnetizations [68]. The nickel ferrite was chosen because of the significant difference in magnetocrystalline anisotropy $K^{NFO} = -6.2\times10^3$ J/m^3 and $K^{CFO} = 2\times10^5$ J/m^3 as well as the relatively high saturation magnetization value [262].

Samples

STEM images show the size and morphology of the synthesized single-phase $CoFe_2O_4$ and $NiFe_2O_4$ nanoparticles (labeled as CFO and NFO, respectively) and core/shell nanoparticles (labeled as CFO/NFO and NFO/CFO). Figure 87 a,b) and d,f) show that the prepared MNPs were approximately spherical in shape. The result of the approximately two hundred particle size calculation for each sample is shown in Figure 87 c) and e). STEM studies confirm the uniform core/shell size distribution of the nanoparticles and approximately equal sizes of the original single-phase nanoparticles. Regarding the average size obtained from STEM images, all core/shell samples are characterized by a larger diameter than the original nanoparticles, confirming that the shell growth is 2 nm thick (Table 19).

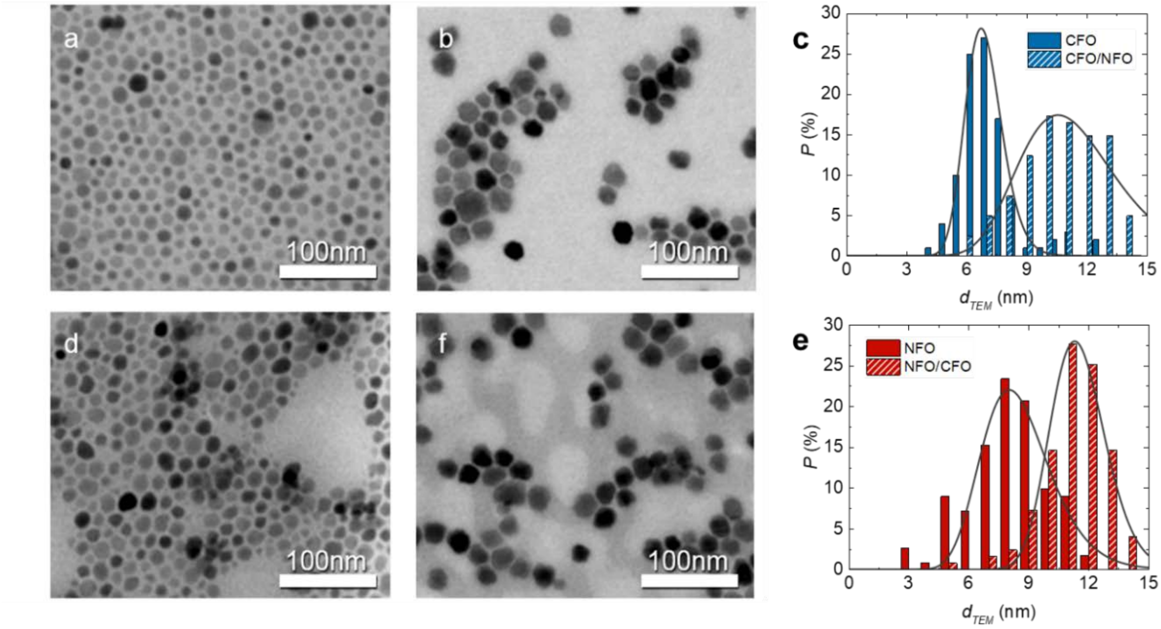

Figure 87. TEM images of a) CFO core and b) CFO/NFO core/shell, d) NFO core and f) NFO/CFO core/shell MNPs; c,e,) histograms of particle size distributions [180].

XRD patterns of the samples (Figure 88) confirmed the spinel structure of cobalt and nickel ferrite without any impurity phases. Crystallite sizes were calculated using the Scherrer formula from the [311] reflections. The fact that the core/shell samples possess a higher structural correlation length supports the idea that the shell grows epitaxially continuing the crystal sites of the core. This confirms the results of electron microscopy.

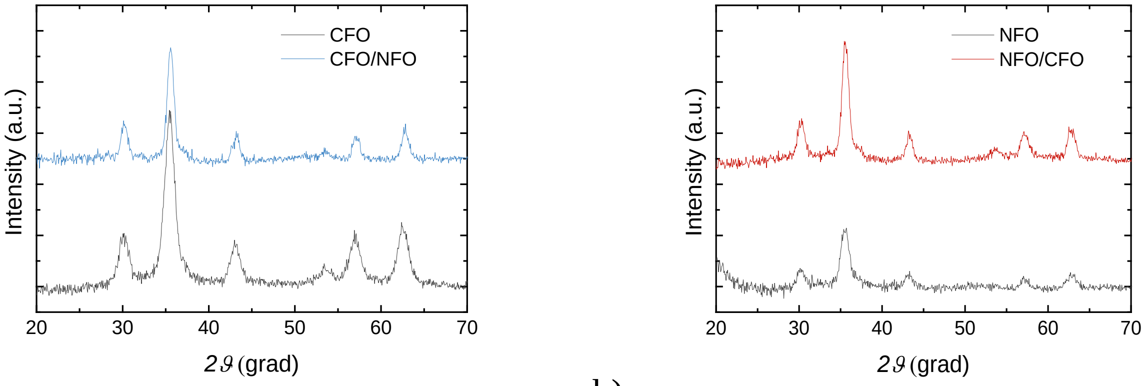

a) b)

Figure 88. XRD patterns of a) CFO core and CFO/NFO core/shell, b) NFO core and NFO/CFO core/shell MNPs [180]. The source is Cu Kα (λ = 1.54056 Å).

Table 19. Morphostructural parameters of the CFO and NFO core, CFO/NFO and NFO/CFO core/shell MNPs.

Sample	**Composition**	d_{TEM}**, nm**	**SD**	d_{XRD}**, nm**	***a*, nm**	V^{Hard}/V
CFO	$CoFe_2O_4$	6.9±0.1	0.9	6.2±0.2	0.840(1)	1
CFO/NFO	$CoFe_2O_4/NiFe_2O_4$	11	3	9.2±0.4	0.838(1)	0.3
NFO	$NiFe_2O_4$	8.4±0.2	1.8	6.2±0.4	0.838(1)	0
NFO/CFO	$NiFe_2O_4/CoFe_2O_4$	12	2	9.0±0.2	0.837(1)	0.6

Comparing the elemental maps Figure 89 with the panel a), one can see that, within each MNP, the intensity of the Fe map (b) is uniform throughout the entire nanoparticle volume, as expected on the basis of the chemical composition of the core/shell MNPs, while the intensity of the Co (c) and Ni (d) maps evidence the Co-rich core and Ni-rich shell of the core/shell MNPs. The EFTEM data are thus clear proof of the core/shell structure of CFO/NFO samples.

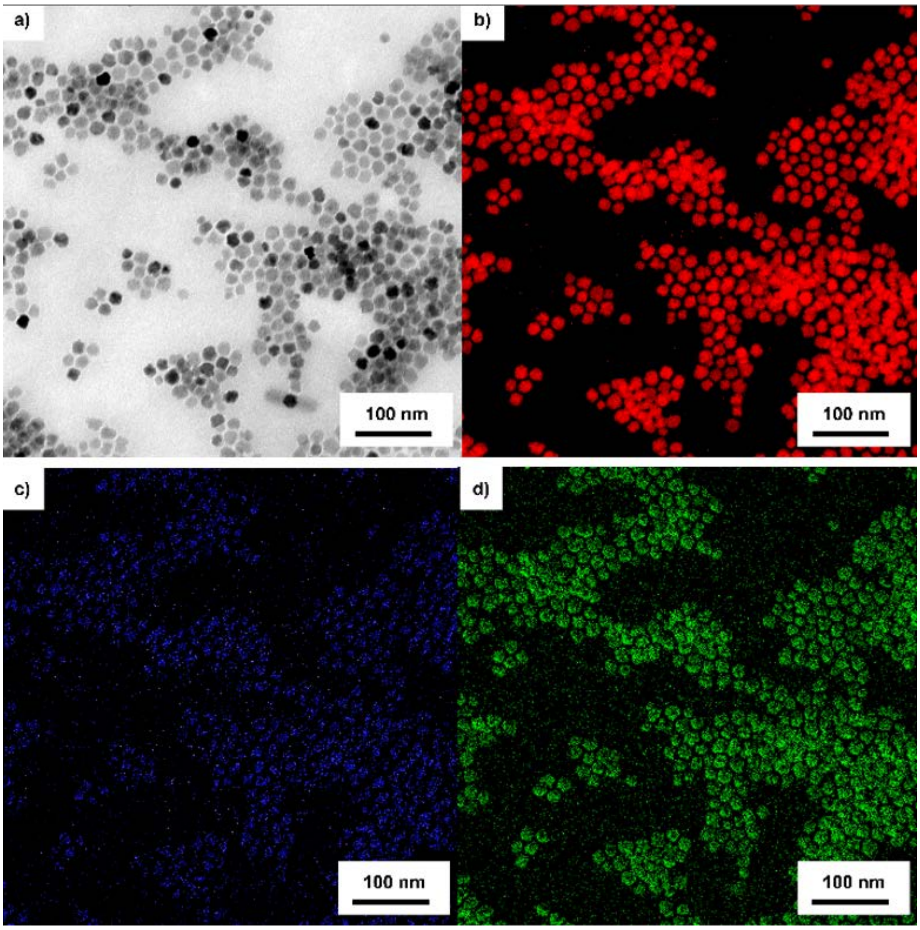

Figure 89. a) TEM image of CFO/NFO sample, b-d) EFTEM (Energy Filtered TEM) images showing the elemental maps of the metals b) Fe (red), c) Co (blue) and d) Ni (green) [180].

Magnetic properties

The *M-H* and *M-T* measurements were performed by a SQUID magnetometer. The magnetization value was normalised by considering the mass of the remaining organics (oleic acid, oleylamine) at the surface of the particle. The mass of the inorganic component of the samples was measured by TG analysis.

The *M-H* curves at 5 K (Figure 90) show the hysteretic behaviour of all samples. All the extracted magnetic parameters are reported in Table 20. The observed M_S values of 98±5 and 75±3 $A{\cdot}m^2/kg$ for CFO and NFO are higher than the bulk values of 88 and 55 $A{\cdot}m^2/kg$ for bulk CFO and NFO, respectively. This is due to some differences in the cationic distribution of ferrite structure (inversion degree). For both core/shell samples, the M_S values are close to the average of the M_S of the two materials. The monotonic shape of the hysteresis loops of the core/shell MNPs suggests a strong coupling between the hard core and the soft shell phases [177].

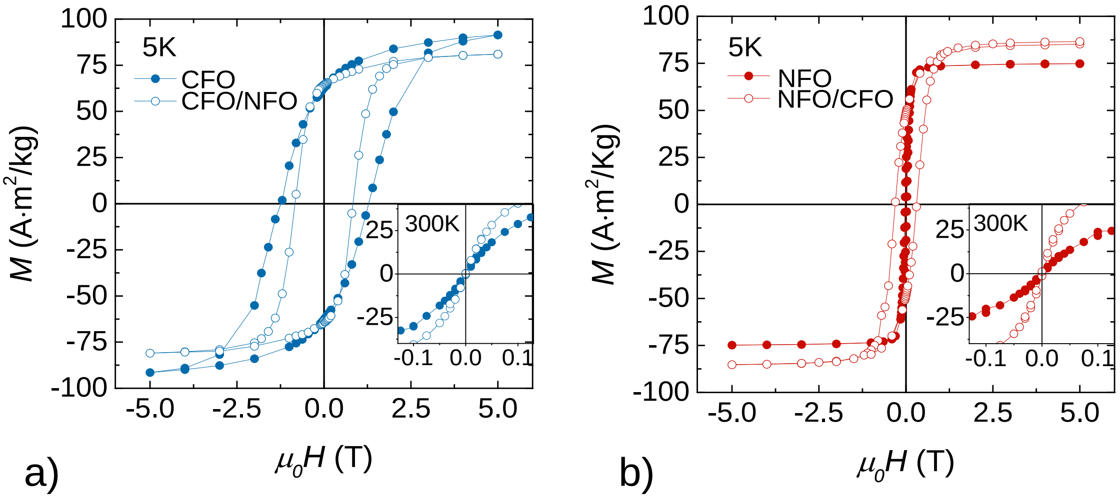

Figure 90. *M-H* curves measured at 5 K for a) CFO core and CFO/NFO core/shell, b) NFO core and NFO/CFO core/shell MNPs [180].

In all samples, the reduced remanent magnetisation increases going from the single-phase to the core/shell systems. CFO show $M_R/M_S \approx 0.47$ and an evident increase is observed in CFO/NFO system ($M_R/M_S \approx 0.61$) approaching the theoretical value (~0.8) expected for SD non-interacting MNPs with cubic magnetic anisotropy [201]. The lower, than the theoretical value for uniaxial particles according to SW model value of M_R/M_S, was found for NFO sample (~0.21). This can be ascribed to the fraction of SPM MNPs which are still unblocked at 5 K or to the presence of inter-particle interactions or some effects due to a demagnetising field [263]. A significant increase in M_R/M_S is observed in NFO/CFO core/shell systems. The largest M_R/M_S has been observed for sample CFO/NFO (i.e., the tendency to cubic anisotropy), besides this sample is expected to have the lower magnetocrystalline anisotropy compared to the NFO/CFO sample, where the fraction of CFO is higher. This can be explained by the proximity effects that increase anisotropy in NFO when it grows on magnetically harder CFO seeds due to the induced strong pinning of interfacial spins [182,264]. In contrast, a smaller M_R/M_S was observed in the system with the predominant CFO volume.

A decrease in μ_0H_C and μ_0H_{irr} of the CFO sample was observed in the CFO/NFO sample. In contrast, μ_0H_C and μ_0H_{irr} of the NFO/CFO sample increased compared to the NFO seeds (Table 20). Thus, the design of the core/shell structure (i.e., the mutual arrangement of soft and hard materials) plays a crucial role in their effective magnetic anisotropy. Indeed, the anisotropy calculated from eq.(56) without taking into account surface and interface effects predicts a different trend.

Room temperature (300 K) *M-H* curves show the reversible behaviour with zero remanences and coercivity suggesting that all the samples are in the SPM regime. To further disclose the magnetic behaviur of all systems, their *M-T* magnetizations have been also investigated by employing the ZFC and FC protocols measured under the magnetic field of 2.5 mT (Figure 91). The ZFC and FC magnetisation curves for all samples showed typical behaviour of interacting SD MNPs. For the samples CFO, CFO/NFO and NFO/CFO, the T_{irr} is close to 300 K.

Table 20. The summary of magnetic properties of CFO core, CFO/NFO core/shell, NFO core and NFO/CFO core/shell MNPs.

Sample	**M_S, A·m^2/kg**	**μ_0H_C, T**	**μ_0H_{irr}, T**	**M_R/M_S**	**K_{eff}, ×10^5 J/m^3**
CFO	98±5	1.3±0.2	3.2±0.2	0.47	8.3±0.2
CFO/NFO	83±3	0.83±0.1	1.8±0.1	0.61	3.9±0.2
NFO	75±3	0.025±0.01	0.3±0.1	0.21	0.6±0.1
NFO/CFO	86±3	0.30±0.01	1.3±0.1	0.45	2.9±0.1

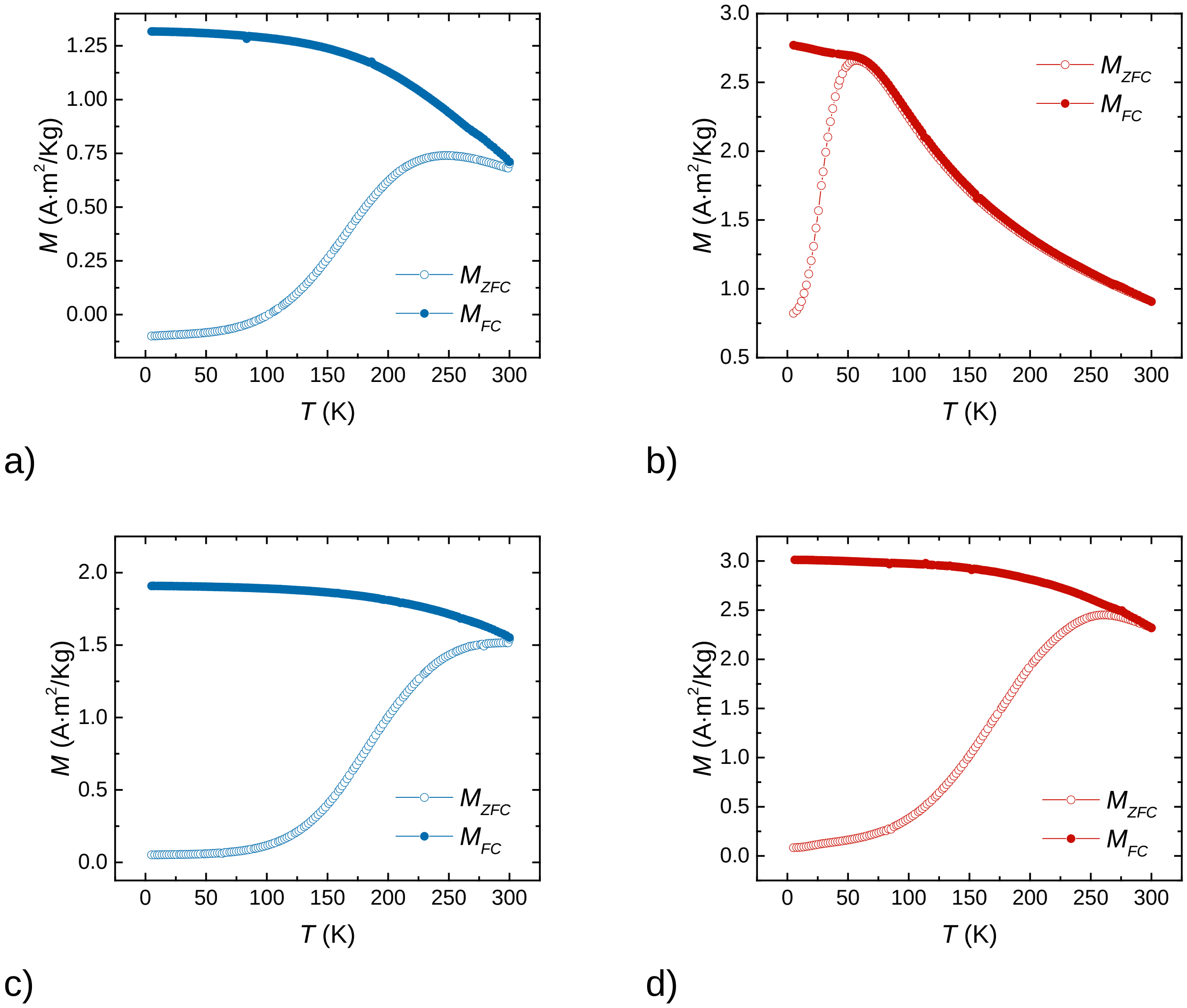

Figure 91. ZFC (empty symbols) and FC (solid symbols) magnetization curves recorded in a measuring field of 2.5 mT: a) CFO and b) NFO seeds; c) CFO/NFO and d) NFO/CFO core/shell MNPs [180].

Figure 92 shows the derivatives of the ZFC and FC magnetizations differences ($dM_{ZFC-FC}(T)/dT$). The filled areas under the curve $dM_{ZFC-FC}(T)/dT$ are visual representations of the integral value proportional to the magnetic anisotropy energy. In this case, the average T_B is insufficient to describe the difference in the magnetic anisotropy between the systems. Indeed, the average T_B value for the CFO sample (Table 21) is almost equal with CFO/NFO and NFO/CFO samples (the same is true for T_{max}), but they have different $\mu_0 H_C$. For the single-phase NFO and CFO MNPs, the different values of the blocking temperature (28±3 and 175±3 K, respectively) is mainly due to the different magnetocrystalline anisotropy of the $NiFe_2O_4$ and $CoFe_2O_4$. The distribution function $f(T_B) \sim dM_{ZFC-FC}(T)/dT$ represents the anisotropy distribution function. The shape of this function (its broadening) is directly related to the core/shell structure: the magnetically hard shell likely causes a stronger broadening of the $f(T_B)$, since the shell material occupies a larger volume and it strongly depends on d_{TEM}. The magnetically soft shell almost does not broaden $f(T_B)$, because the main source of anisotropy, in this case, is the magnetically hard core domination in the magnetic anisotropy of the whole system.

Table 21. Blocking temperature, normalised energy of dipolar interactions and interaction field of CFO, NFO, CFO/NFO and NFO/CFO samples.

Sample	**T_B, K**	**E_{dip}/k_B, K**	**$\lvert H_{INT}\rvert/H_C\times 100\%$**
CFO	175±5	44	6%
CFO/NFO	174±4	198	2%
NFO	28±3	57	33%
NFO/CFO	173±4	295	2%

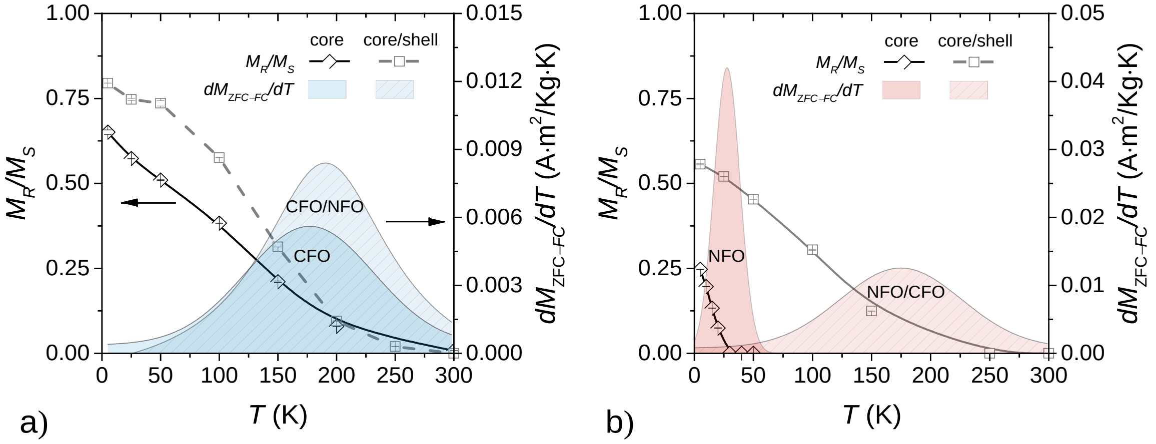

Figure 92. The diamond and square symbols are the M_R/M_S, the filled areas are the $dM_{ZFC\text{-}FC}(T)/dT$ curves calculated from the ZFC and FC magnetizations: a) CFO and CFO/NFO; b) NFO and NFO/CFO samples [180].

Figure 92 shows the temperature dependence of the M_R/M_S estimated from M-H loops recorded at different temperatures in the range of 5–300 K. The M_R/M_S trend for all the samples substantially confirms the landscape of distribution of anisotropy energy. The $M_R/M_S(T)$ curves vanish at the upper limit of the distribution of anisotropy energy ~T_{irr}. The exception is the single-phase NFO sample where the M_R/M_S vanishes at lower temperatures, closer to T_B.

The anisotropy constant was defined by eq.(16), where $\mu_0 H_K \approx \mu_0 H_{irr}$, an approximation first suggested by Kodama et al. The K_{eff} behaves in the qualitatively agreement with the coercive and irreversibility fields (Table 20), confirming the efficiency of interface coupling in tuning the anisotropy.

The differentiated remanence curve $dM_{IRM}(H)/dH$ (Figure 93a) represents the irreversible component of the susceptibility representing the measure of the energy barriers distribution associated with the SFD [206,207]. The $\mu_0 H_{Cr}^{IRM}$ represents the coercive field of the blocked particles, which are responsible for the irreversible magnetization processes. For a system of SW particles, the SFD can be considered as the distribution of the particle magnetic anisotropy energy compared with the energy of the external magnetic field. Thus, considering the equivalent distributions of particle volumes, deviations in the shape of SFD will reflect in the difference in the distribution of M_S or K (their size dependences) in addition to the effect of particle size distribution and interparticle interactions. The SFD normalized in x-axis by $\mu_0 H_{Cr}^{IRM}$ and in Y-axis to the maximum (Figure 93 b), shows that the seed-mediated shell growth process does not induce new factors of broadening the distribution of magnetic properties. Furthermore, the soft NFO MNPs and NFO/CFO core/shell MNPs have a higher dispersion than that of the CFO sample. This is consistent with the observed higher SD from TEM measurements and the expected stronger influence of the surface effects in magnetically soft particles. Comparing NFO/CFO and CFO/NFO systems, one can note that the SFD is broader in the NFO/CFO sample than in the CFO/NFO sample, while the SD from the TEM analysis has the opposite trend. This behavior can be explained by the dominant role of the magnetically hard CFO core, governing the magnetization processes in the CFO/NFO system.

A negative contribution to the Kelly plot (δm-plot) indicates the dominant demagnetizing character of dipolar interactions between particles in all samples (Figure 93). For NFO/CFO and CFO/NFO systems, the absolute magnitude of the $|\delta m|$ dip is in the range of 0.2–0.3 while for NFO samples this value is almost twice as large reaching 0.45. Hence, in NFO samples interparticle interactions are stronger. The interaction field $\mu_0 H_{INT}$ (eq.(73)) can provide a quantitative characterization of magnetic interparticle interactions. The ratio H_{INT}/H_C (normalization of interaction field to coercivity field) is relatively low for magnetically hard samples. While in the case of the single-phase NFO MNPs for which the intrinsic anisotropy is small, the interparticle interactions have a stronger effect.

The value of dipolar interaction energy (Table 21) was roughly estimated using eq.(49) where l is the average distance, which is the particle diameter plus the thickness of two monolayers ~4 nm of oleic acid residual at particle surfaces after synthesis) [57]. The calculated E_{dip} does not agree with the δm-plot. We attribute the observed magnetic behavior to the complex interplay between intraparticle and interparticle interactions. This is further confirmed by the calculated SFD and δm-plots, showing very good qualitative agreement with the experimental results [180].

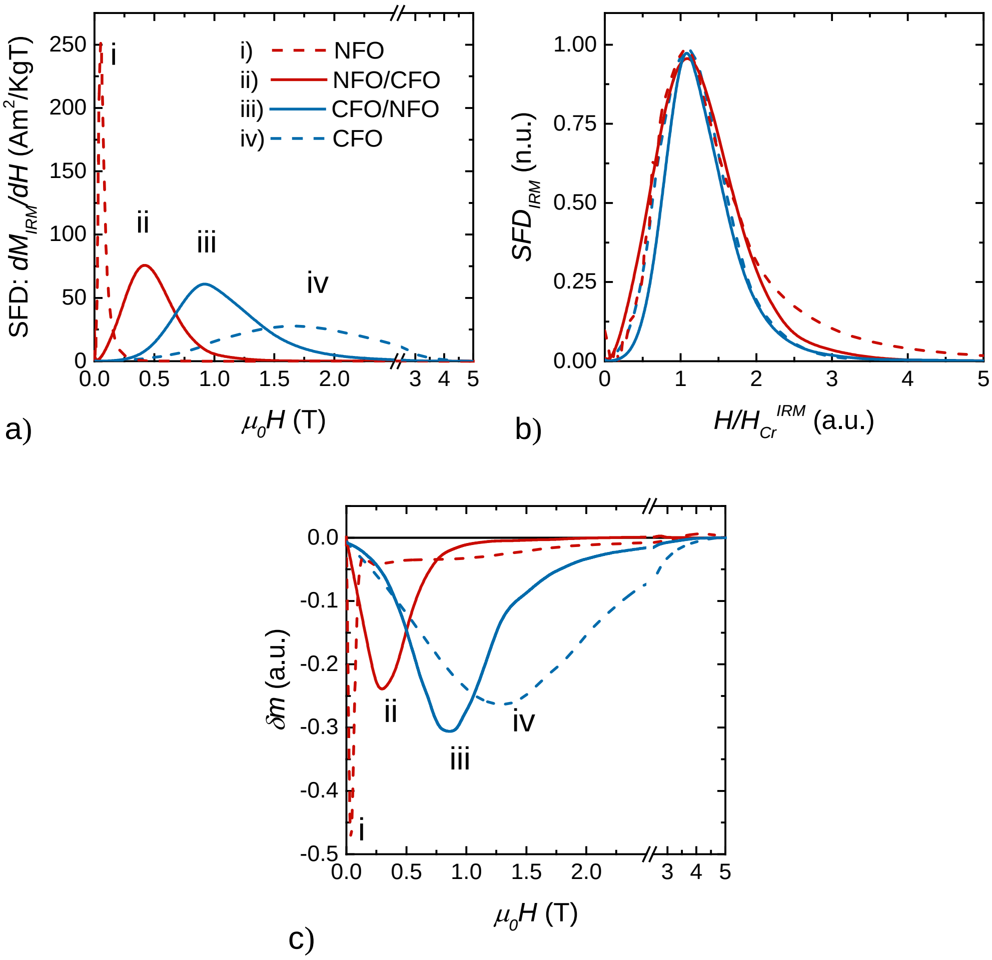

Figure 93. a) Switching field distribution $dM_{IRM}(H)/dH$, b) normalized and centered switching field distribution and δm-plot measured at 5 K for NFO and CFO seeds, NFO/CFO and CFO/NFO core/shell MNPs [180].

Conclusions

The interfacial exchange coupling in core/shell MNPs is s manifested in the dramatic changes of the magnetic properties, such as the M_R/M_S and the $\mu_0 H_C$, and the smooth hysteresis loops observed after shell growth. The growth of a soft nickel ferrite magnetic shell affects the hard properties of the cobalt ferrite seeds with a decrease of $\mu_0 H_C$ from ~1.3 to 0.8 T. On the contrary, the magnetically harder cobalt ferrite shell increases the coercivity of the soft seeds from ~0.025 to 0.3 T. But the core of magnetically hard material stronger affects the magnetic anisotropy of the whole system. This has been explained by the proximity effect related to the epitaxial growth of the shell material, in which cobalt ferrite induces an increase in nickel ferrite anisotropy. The experimental results in this section are in qualitative agreement with the results of computer simulations reported in ref. [180].

5.2 $CoFe_2O_4/NiFe_2O_4$ hard/soft MNPs with the various thicknesses of shell

In section 5.1, we have shown the efficiency of the exchange coupling mechanism to tune magnetic anisotropy of soft/hard bi-magnetic core/shell systems. It was, in particular, noted that the magnetically hard core governs the magnetization reversal processes of the core/shell system even though the volume of shell fraction exceeds the core volume. This chapter aims to study how the thickness of the magnetically soft shell influence the magnetic properties of core/shell MNPs.

Samples

Multishell MNPs were obtained by the multistep procedure of HTD explained in methodological sections, the cobalt ferrite MNPs of similar size to those studied in section 5.1 were used as seeds for the subsequent growth of several nickel ferrite shells. STEM size analysis indicates that particles are monodisperse with narrow size distributions. Histograms of the particle size distribution provide an excellent illustration of the progressive increase of d_{TEM} when new magnetic shells are added (Figure 94).

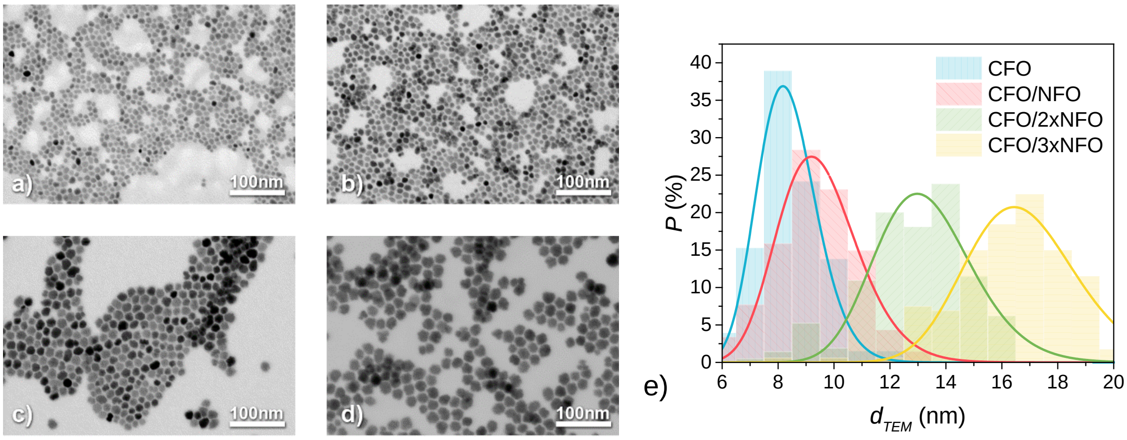

Figure 94. STEM images of a) bare $CoFe_2O_4$ MNPs, b) core/shell MNPs with 1st, c) 2nd and d) 3rd $NiFe_2O_4$ shell; e) histograms of size distribution. The scale bar on all TEM images is 100 nm.

Notable that the addition of the shells does not change the standard deviation (σ) of lognormal size distribution suggesting monotonically growth of shells on the surface of the seeds (Table 22). The thickness of the shell (t_{sh}) was estimated from the difference in the size of the core (d_c) and core/shell particles $d_{TEM}=d_c+2t_{sh}$. The volume fraction of the shell`s material, f_{NFO}, was estimated with the same geometrical approach assuming that particles have a spherical shape.

Table 22. Composition and size of bare $CoFe_2O_4$ MNPs, core/shell MNPs with 1st, 2nd and 3rd $NiFe_2O_4$ shell.

Sample	**Composition**	**d_{XRD}, nm**	**d_{TEM}, nm**	**σ,**	**t_{sh}, nm**	**f_{NFO}, %**
CFO	$CoFe_2O_4$	9±1	8.3±0.1	0.13±0.01	—	—
1° shell	$CoFe_2O_4/1\times NiFe_2O_4$	12±1	9.4±0.1	0.15±0.01	0.55	31
2° shell	$CoFe_2O_4/2\times NiFe_2O_4$	14±2	13.3±0.2	0.14±0.02	2.5	76
3° shell	$CoFe_2O_4/3\times NiFe_2O_4$	17±2	16.8±0.2	0.12±0.01	4.3	88

Notwithstanding that the time of reaction and concentration of precursors are the same for steps, the first deposition of $NiFe_2O_4$ on the $CoFe_2O_4$ core has a slower growth rate, achieving only a 0.55 nm thickness with respect to more than 2 nm of the other shells. The difference in the shell thickness between the first and the following ones can be related to different kinetics of deposition of the $NiFe_2O_4$ phase.

Figure 95 shows the XRD patterns of the samples. Observed peaks are indexed to a cubic spinel structure of cobalt and nickel ferrites. Although, the position of peaks is very close for both materials and the difference is hardly distinguished because of identical crystalline structure, a small shift of about 0.2° was observed due to the slight difference in Co^{2+} and Ni^{2+} ions radii. Broadening of the peak is attributed to the small size of crystallite which size was calculated using the Scherer formula. The calculated structural correlation lengths (d_{XRD}) are presented in Table 1. We observed monotonical behaviour in good agreement with the TEM particles size distribution that confirms the high crystalline nature of the sample and the fact that growth of the shells occurs in a stacking layer-by-layer way following the seed without forming polycrystallinity of the shells.

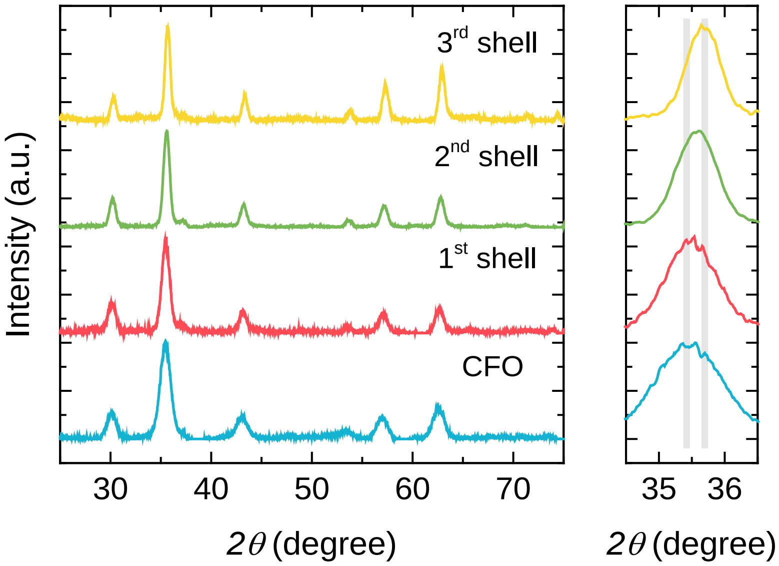

Figure 95. XRD patterns of CFO core and CFO/NFO multishell MNPs with one, two and three layers of NFO. The source is Cu Kα (λ = 1.54056 Å).

The core/shell nature of the particles is demonstrated by EDX analysis. Figure 96 a)-e) show the high-angle annular dark field (HAADF) STEM image of the sample "1°shell" and the corresponding EDX maps associated to Fe, Co, Ni and the integrated map with the total distribution of the previous elements, respectively. A color code was used for the easily identifiable of Fe (blue), Co (green) and Ni (red) distribution in the particles. Comparing these images, the uniform distribution of Ni atoms around the cobalt core of the particles is evident, and the Fe atoms are present in all the particles extensions as expected. The same core/shell structure is clearly demonstrated for the sample "3°shell" by the images shown in Figure 96 f)-l). In this case, the distribution and uniformity of the Ni shell is still more evident due to its larger thickness with respect the sample "1°shell". The thickness of the Ni shells estimated by EDX maps is in very good agreement with those reported in Table 1.

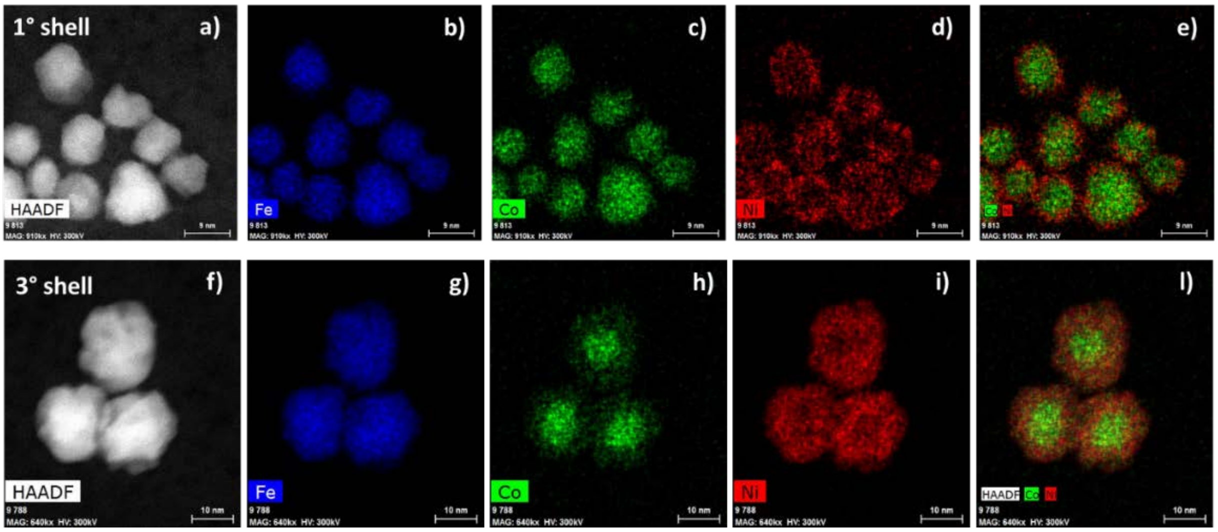

Figure 96. HAADF-STEM images and corresponding EDX maps of sample «1° shell» (a-e) and «3° shell» (f-l). A color code was used for identifying Fe (blue), Co (green) and Ni (red) distribution in the particles. Images shown in e and l are the composition of previous images for «1° shell» and «3° shell», respectively, showing the core/shell nature of the particles.

To deeper investigate the growth of the $NiFe_2O_4$ shell on the $CoFe_2O_4$ core, high-resolution HAADF-STEM analyses were performed (Figure 97). The atomic planes inside the oriented particles are clearly visible and extend until the edges suggesting that both Ni and Co ferrites are well crystalized, without the presence of an amorphous phase. The continuity and regularity of the atomic distribution inside the whole particle (core and shell) do not allow to distinguish the two phases, even performing a Fast Fourier Transform (FFT) of the images. This result indicates a perfect oriented growth of one phase on the other. In more detail, the $CoFe_2O_4$ core lattice acts as a template for the growth of the $NiFe_2O_4$ as in the epitaxial growths. Looking at Figure 97 c), it is possible to observe that the atomic planes of different particles tend to merge suggesting a great correlation among particles

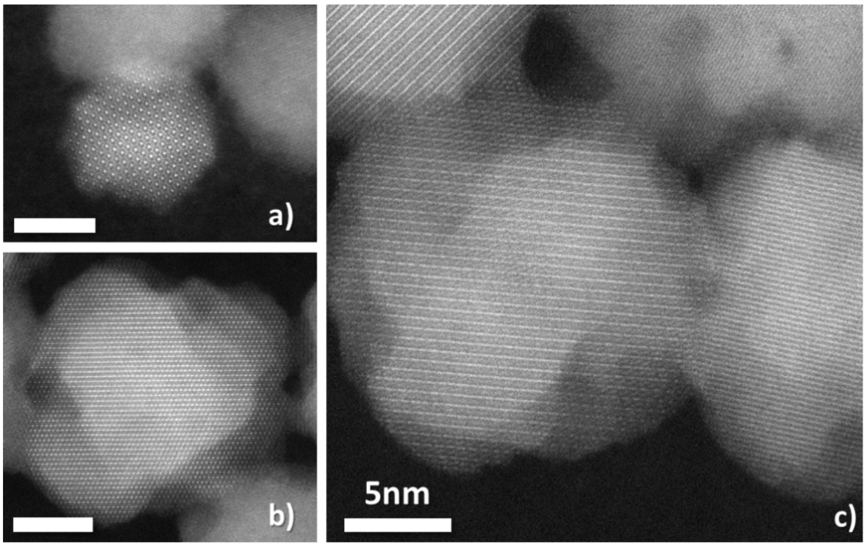

Figure 97. High resolution HADDF-STEM images of sample «1° shell» (a) and «3° shell» (b and c).

Magnetic properties

For soft-hard exchange coupled systems the hard phase prevails on anisotropic characteristics of the material, namely the linear dependence of coercivity on volume content of hard phase was predicted (Figure 98) [68]. Clear that this law is not considering any interfaces as well as geometric features. For example, it was observed earlier the change of position of soft and hard phases in $CoFe_2O_4/MnFe_2O_4$ and $MnFe_2O_4/CoFe_2O_4$ MNPs the superposition law is not respected [177]. In the case of the multishell structure $MnFe_2O_4/CoFe_2O_4/NiFe_2O_4$, it was observed that this law predicts the only qualitative trend [265]. For the «1°shell» sample a high value of coercivity was observed; which may be explained by the exchange spin coupling (ESP) phenomenon expected for an ultrathin shell regime in hard/soft nanoparticles systems since the thickness of the shell of 0.55 nm is less than 1 nm (approximately the size of a crystalline unit-cell) [84,177]. Similar behaviour was observed earlier for $CoFe_2O_4/MnFe_2O_4$ MNPs with different thicknesses of the shell when a thin layer of the soft phase increased μ_0H_C but the thicker decrease [177]. For the 2nd and 3rd shells, the value of μ_0H_C decreased qualitatively following the trend of superposition however those values are higher than predicted (Figure 98 b), Table 23).

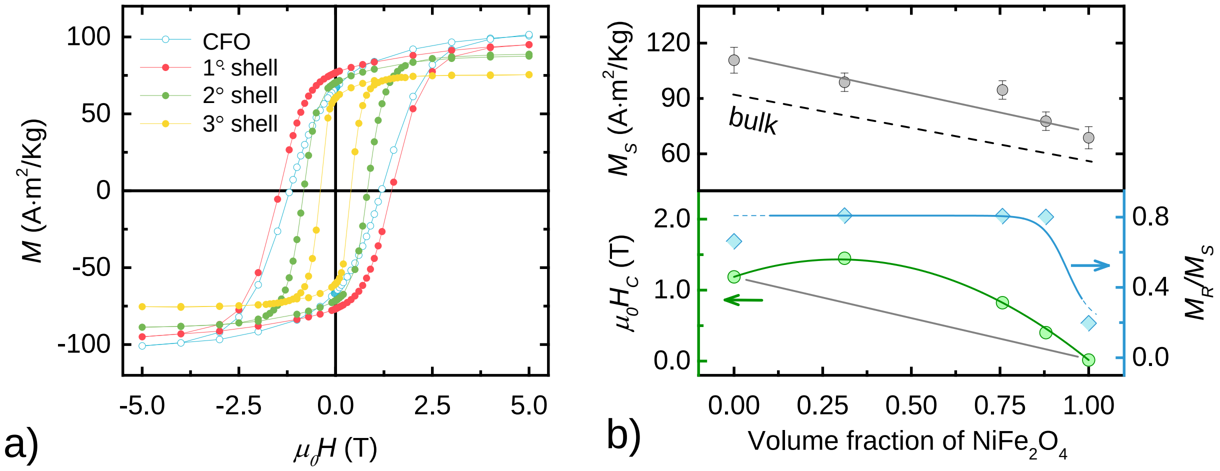

Figure 98. a) *M-H* measurements at 5K and b) comparative plot of M_S, μ_0H_C and M_R/M_S as a function of nickel ferrite content (f_{NFO}) for CFO core and CFO/NFO multishell MNPs with one, two and three layers of NFO.

Table 23. Magnetic properties of CFO core and CFO/NFO multishell MNPs measured at 5K.

Sample	**μ_0H_C, T**	**μ_0H_{irr}, T**	**$\mu_0H_{Cr}^{DCD}$, T**	**M_S, A·m²/kg**	**M_R/M_S**	**ξ**
CFO	1.19±0.01	3.3±0.1	1.44±0.01	111±7	0.66	0.36
1° shell	1.45±0.01	3.0±0.1	1.52±0.01	99±5	0.81	0.48
2° shell	0.82±0.01	1.7±0.2	0.84±0.02	95±5	0.81	0.47
3° shell	0.40±0.01	0.98±0.02	0.41±0.01	78±5	0.80	0.41

Surprisingly, it was observed the strong manifestation of the cubic type of anisotropy on the remanent state of samples with higher nickel ferrite content (Figure 98, Table 23). For cobalt ferrite MNPs due to high magnetocrystalline anisotropy, the value of the remanence of 0.8 is expected but for softer materials, the shape or surface anisotropy component results in the uniaxial type of anisotropy with the expected M_R/M_S of 0.5 [61,140,241]. The small deviation of the reduced remanent magnetization for CFO seeds is probably due to thermal fluctuations tended to misalign magnetic moments of MNPs from easy axis directions of mixed uniaxial/cubic type of anisotropy for the smallest particles. Nonetheless, the blue line shows the tendency to be lower than the limit value of 0.5 for nickel ferrite MNPs (a reference sample of the sample size as CFO core) that is predicted in soft MNPs because of finite temperature, stronger demagnetizing field and interparticle interactions in respect to magnetocrystalline anisotropy [266,267].

Interesting that M_R/M_S points to the cubic type of anisotropy whereas the coordination of coercivity and irreversible field refers to the uniaxial one. The $\mu_0 H_{irr}$ can be considered as an anisotropy field $\mu_0 H_K$, as first suggested by Kodama et al. for $NiFe_2O_4$ MNPs [268]. Indeed, according to Stoner–Wohlfarth model, the coercivity field is proportional to the anisotropy field $\mu_0 H_C = \xi \cdot \mu_0 H_K$ where ξ is a constant dependent on the type of anisotropy and equal to ~0.48 for the case of uniaxial and ~0.32 ($K>0$) and ~0.19 ($K<0$) for cubic [226,269]. The obtained values for core/shell systems (Table 2) are in good agreement with the theoretical one for the uniaxial anisotropy. Notably, the M_R/M_S values on the contrary indicated the cubic anisotropy type. Therefore, we can suggest the following scenario: i) under a magnetic field, the magnetically soft shell having the higher energy (due to its higher volume) governs the net magnetic moment of the whole particle; ii) when the magnetic field is off, the remanent state is mainly governed by a magnetically hard core which keeps the net magnetic of the particle along magnetocrystalline easy axes. This interplay of two counterparts of bi-magnetic particles, in general, can be considered as an effect of intaparticle interactions.

Effective anisotropy constant (Table 24), $K_{eff} = \mu_0 H_K \cdot M_S/2$, was calculated in two ways of determination of anisotropy field: 1) calculated from coercivity $\mu_0 H_K = \mu_0 H_C/\xi$, and 2) measured $\mu_0 H_K = \mu_0 H_{irr}$. For this calculation, ξ=0.48 was taken considering uniaxial type anisotropy for all core/shell samples. Calculated in both manners K_{eff} are close and decreases with the increase of shell thickness. The proximity of these values indicates the minor influence of canted surface spins of undercoordinated atoms which significantly affect the irreversible processes in the smaller particles, therefore, increasing in $\mu_0 H_{irr}$ [65]. In smaller CFO core particles, the anisotropy type was mixed thus the theoretical value of ξ is undefined and only K_{eff} from $\mu_0 H_{irr}$ can be determined. The effective anisotropy constant was higher than the bulk magnetocrystalline anisotropy constant (2×10^5 J/m^3 [262]) which agrees with previous studies where the increase in anisotropy was attributed to surface effects and cation distribution within spinel structure [15,65].

Table 24. Effective anisotropy constant calculated from coercivity and irreversibility fields for CFO core and CFO/NFO multishell MNPs.

Sample	***K_{eff} (from H_C)***	***K_{eff} (from H_{irr})***
	$\times 10^5$ J/m^3	
CFO	—	9.8
1° shell	7.9	7.9
2° shell	4.3	4.4
3° shell	1.7	2.0

Following the described in the experimental part protocol, the M_{IRM} and M_{DCD} curves were recorded and plotted versus the reversal field (Figure 99). The coercivity of DCD remanence ($\mu_0 H_{Cr}^{DCD}$) for all samples is in Table 2. The value of $\mu_0 H_{Cr}^{DCD}$ increases for "1°shell" sample, then it decreases with the increase of volume fraction of the magnetically soft shell of $NiFe_2O_4$. The proximity of $\mu_0 H_{Cr}^{DCD}$ and $\mu_0 H_C$ indicates the magnetization processes in the systems are mostly irreversible excepting the CFO sample where the thermal fluctuation affects the magnetization that agrees with reduced M_R/M_S value. The M_{DCD} and M_{IRM} are only sensitive to the irreversible component of magnetization and thus the first derivative of the remanent magnetization curve shows the SFD in the samples [15]. The first derivative of M_{DCD} is plotted in Figure 99 b). Normalized SFD indicate that the shell growth makes the width of the distribution narrower. It can be due to the thermal stabilization of the particles when the size is increasing. As well as one can conclude that the process of the growth of soft shell does not add new factors of distribution of magnetic properties since mostly the irreversible processes are governed by magnetically hard CFO cores which remain the same (this is agreed with results discovered in section 5.1).

According to δm-plots, the absolute value of the height of maxima is proportional to the intensity of the dipolar interactions [270]. For all samples, the strong dipolar interactions are dominated over exchange intraparticle interactions and exchange interparticle interactions between particles' shell-shell contact. Since δm-plot originates from magnetic remanences it is not only a matter of interparticle interactions but more generally reflects the magnetic irreversible processes. We observe the increase of the δm magnitude with the increase in the number of shells.

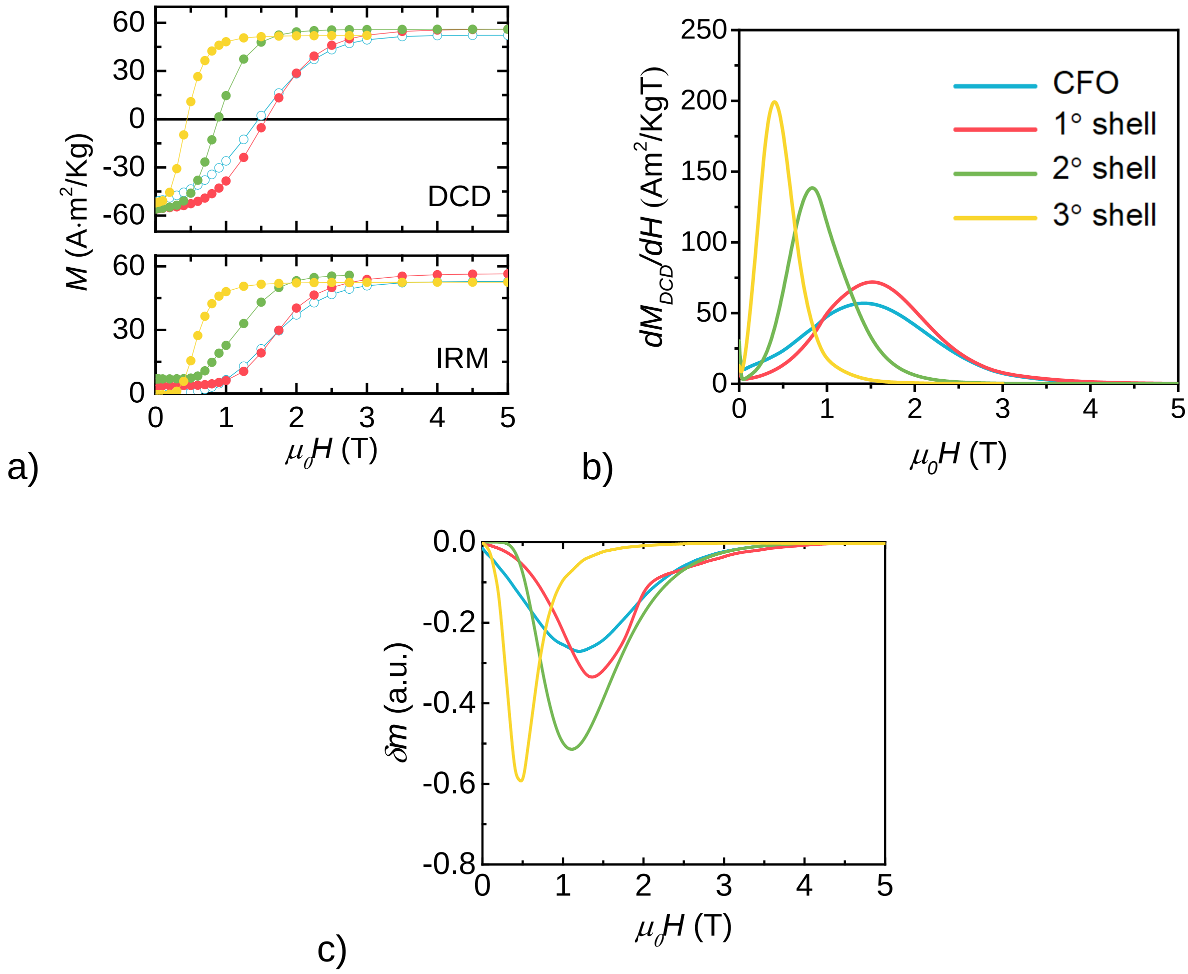

Figure 99. a) M_{DCD} and M_{IRM}, b) the derivative of the M_{DCD} and c) δm-plot measured at 5K for CFO core and CFO/NFO multishell MNPs with one, two and three layers of NFO

Conclusion

A non-monotonic change in the coercivity was observed in the core/shell CFO/NFO MNPs with variable shell thickness. The effective magnetic anisotropy constant decreases from 9.8×10^5 J/m^3 for single-phase cobalt ferrite with an average size of about 9 nm to 2×10^5 J/m^3 for them coated with an nickel ferrite shell about 4 nm thick. This was explained by competition of different contributions of the magnetic counterparts in the total energy of the system. The thin layer of magnetically soft material can increase the anisotropy of core/shell MNPs increasing the canting of magnetic moments of atoms at the surface. As the thickness of the NFO shell increases, the magnetic moments of the particles become higher, which also leads to an increase in the intensity of dipole interparticle interactions.

5.3 $CoFe_2O_4/NiFe_2O_4$ and $CoFe_2O_4/NiO$ nanoparticles

The previous section reveals that the thin layer of soft FiM material on magnetically hard cobalt ferrite seed increases its anisotropy due to enchasing the spin disorder of the surface. In this section, the CFO/NFO sample similar to the sample with the thinner shell from the previous section will be compared with core/shell FiM/AFM CFO/NiO MNPs with almost the same thickness of the shell.

Samples

The XRD patterns suggest the presence of only cubic spinel and rock salt phases in the core/shell MNPs (Figure 100). STEM images show a nearly spherical shape of core and core/shell MNPs (Figure 101). The crystal sizes d_{XRD} have been calculated using eq.(61) and averaging 5 for the most intense reflections. In agreement with the previously studied systems, the d_{XRD} and d_{TEM} sizes increase after the deposition of shells confirming the formation of core/shell structures. The increase of the d_{XRD} in the CFO/NiO sample is less than the d_{XRD} in the CFO/NFO sample. This is due to the partial mismatch of the rock salt structure of the NiO phase spinel with those of planes of the $CoFe_2O_4$. However, the d_{TEM} confirms the growth of the shell with a thickness of less than 1 nm in both core/shell systems. The physical size for both core/shell systems was almost the same (Table 25).

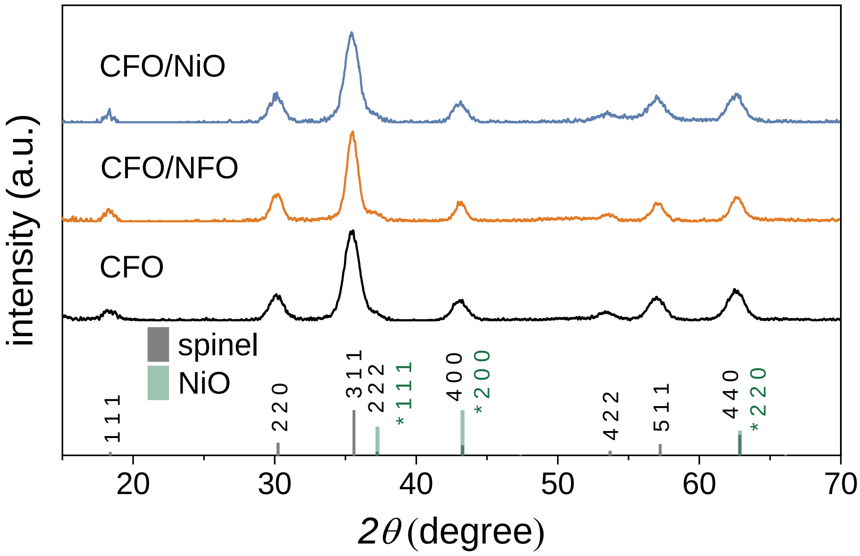

Figure 100. XRD patterns of CFO core, CFO/NFO and CFO/NiO core/shell MNPs. The source is Cu Kα (λ = 1.54056 Å) [192].

Table 25. Morphostructural properties of CFO core, CFO/NFO and CFO/NiO core/shell MNPs.

Sample	**d_{XRD}, nm**	**d_{TEM}, nm**	**σ_{TEM}**
CFO	7.2±0.4	8.3±0.1	0.13±0.02
CFO/NFO	8.9±0.9	9.5±0.1	0.15±0.02
CFO/NiO	7.8±0.7	9.6±0.2	0.19±0.02

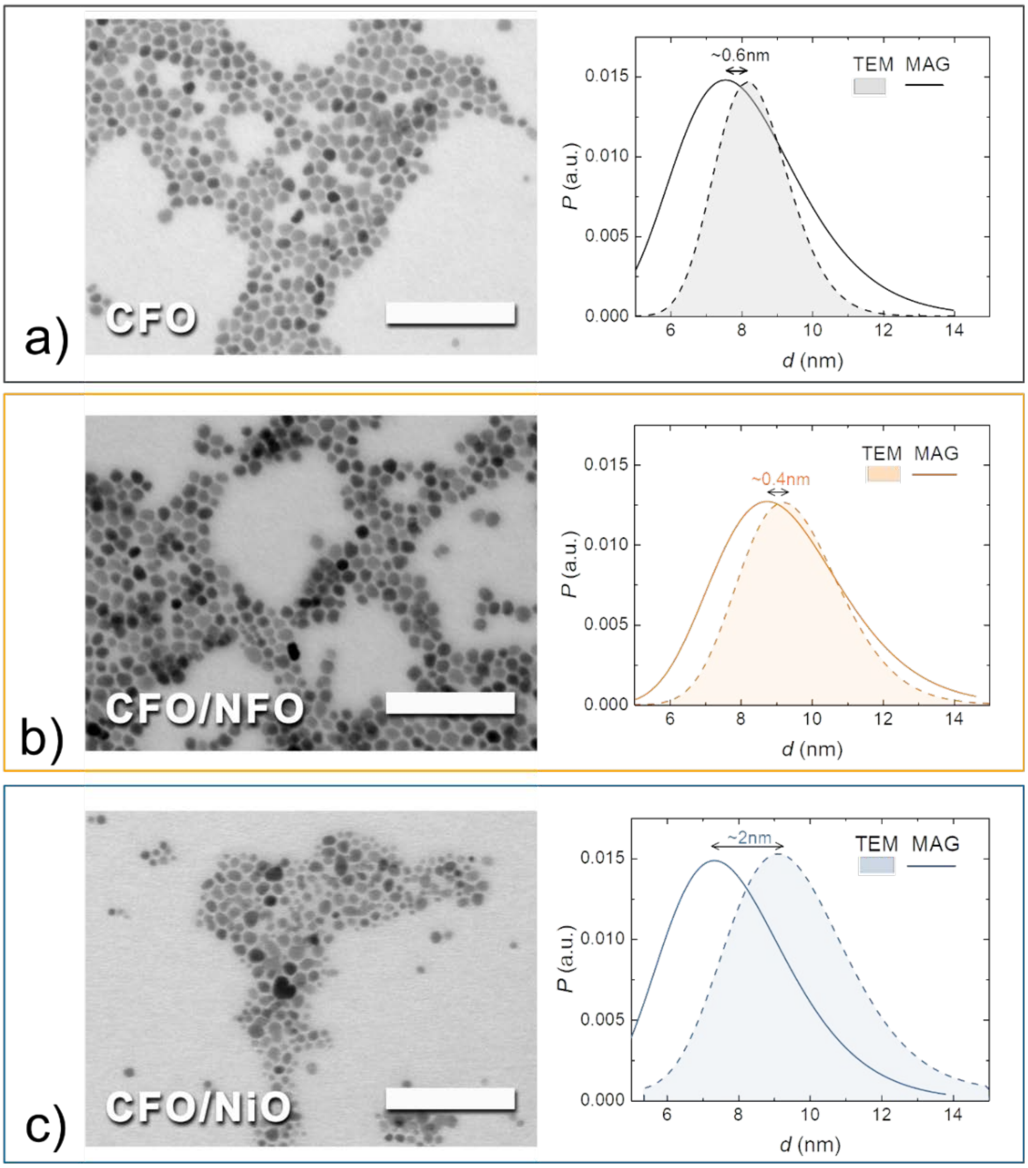

Figure 101. STEM images (left) and lognormal distribution of particle size obtained by the fit of histograms of size distribution after TEM and lognormal function of particle magnetic moment calculated after the fit of superpamagnetic curves for a) CFO core, b) CFO/NFO and c) CFO/NiO core/shell MNPs [192].

Magnetic properties

The M-T dependencies investigated by the ZFC and FC protocols show irreversibility in the temperature range 5–300 K for core/shell MNPs (Figure 102). The blocking temperatures for all samples are below 300 K. The T_B was found to be around 200 K for the single-phase CFO and core/shell CFO/NiO samples (Table 26). For the CFO/NFO sample, T_B is significantly higher (259±10 K). At temperatures above T_B, all samples exhibit non-hysteretic behavior. M-H curves recorded at 5 K show typical magnetic hysteresis loops with a high value of μ_0H_C and M_R/M_S for all samples (Figure 3 and Table 2). The larger value of saturation magnetization M_S = 84±4 Am^2/kg was found in the CFO sample, then the M_S reduces for CFO/NFO and CFO/NiO core/shell samples.

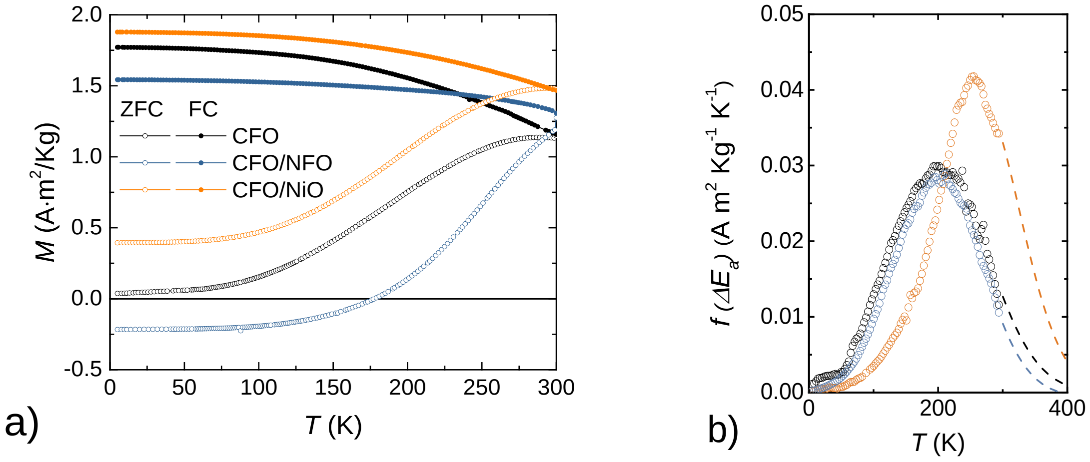

Figure 102. a) ZFC/FC magnetizations measured in 2.5 mT magnetic field; b) distribution of anisotropy energy: data (dots) and extrapolation with the normal function (dashed lines) for CFO core, CFO/NFO and CFO/NiO core/shell MNPs [192].

Table 26. Magnetic properties of CFO core, CFO/NFO and CFO/NiO core/shell MNPs. The saturation magnetization (M_S), reduced remanent magnetization (M_R/M_S) and coercivity field (μ_0H_C) are measured at 5 K.aa

Sample	**T_B, K**	**M_S, Am^{2}kg^{-1}**	**M_R/M_S**	**μ_0H_C, T**
CFO	201±8	84±4	0.61±0.01	1.2*
CFO/NFO	259±10	75±4	0.76±0.01	1.5±0.1
CFO/NiO	200±8	80±4	0.74±0.01	2.0±0.1

Isothermal magnetic hysteresises, measured at 5 K, are shown in Figure 103. Both CFO/NFO and CFO/NiO core/shell samples showed increased μ_0H_C values compared to the CFO sample $\mu_0H_C = 1.2$ T, namely the μ_0H_C is 1.5±0.1 T for CFO/NFO sample and 2.0±0.1 for CFO/NiO sample. The increase in μ_0H_C had already been observed in exchange-coupled nanostructures consisting of AFM NiO and hard FM CoPt [182] and hard FiM $CoFe_2O_4$ [31] counterparts. This was attributed to the interface exchange interaction. Moon et al. showed an increase of the anisotropy of hard FiM CFO covered with the thin layers of $NiFe_2O_4$, $MnFe_2O_4$ and Fe_3O_4 soft FiM with the volume fraction of the magnetically soft shells ($f_{shell} = V_{shell}/V_{total}$) lower than 0.25 [84]. This effect has been attributed to the enhanced spin canting (ESC) mode on the surface spins. The cobalt ions with high anisotropy are less prone to canting, while in softer ferrites spin canting can be stronger [64,82]. *M-H* cycles measured at 5 K after cooling from 300 K in a μ_0H_{app} of 3 T do not show any exchange bias. This can be explained both by the result of the extremely thin AFM shell ($t_{shell} \approx 0.6$ nm), which is not capable of maintaining the AFM order or carrying the FiM volume, and by a possible discrepancy in the stoichiometry of the shell material [173]. However, the core/shell exchange coupling of CFO/NiO nanoparticles leads to an evident increase of the effective anisotropy at 5 K.

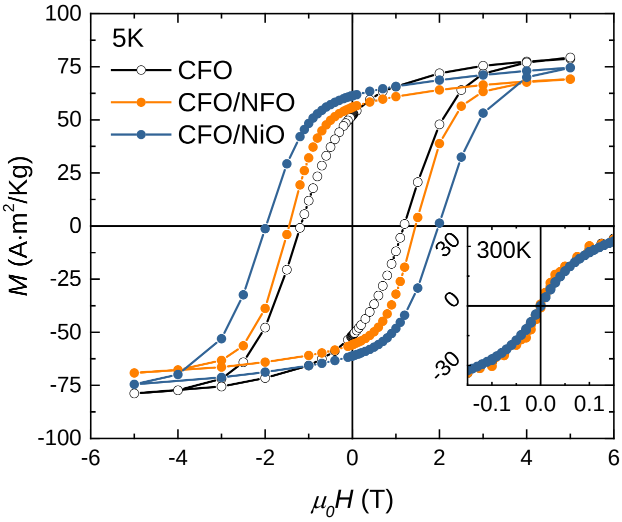

Figure 103. *M-H* hysteresis loop at 5 K for CFO core, CFO/NFO and CFO/NiO core/shell MNPs. Inset shows low field region of *M-H* curves at 300 K [192].

The negative value of δm indicating the dominant dipolar interactions was observed in all samples (Figure 104). The highest magnitude of $|\delta m|$ was observed in CFO/NFO core/shell MNPs. This is due to the higher size and magnetization of these particles. For CFO/NiO MNPs the value of $|\delta m|$ dip was the lowest because the AFM shell prevents the magnetic interactions between the FiM cores. This agrees with the previously observed decrease of $|\delta m|$ dip in the nanocomposite of the $CoFe_2O_4$ and NiO MNPs [31].

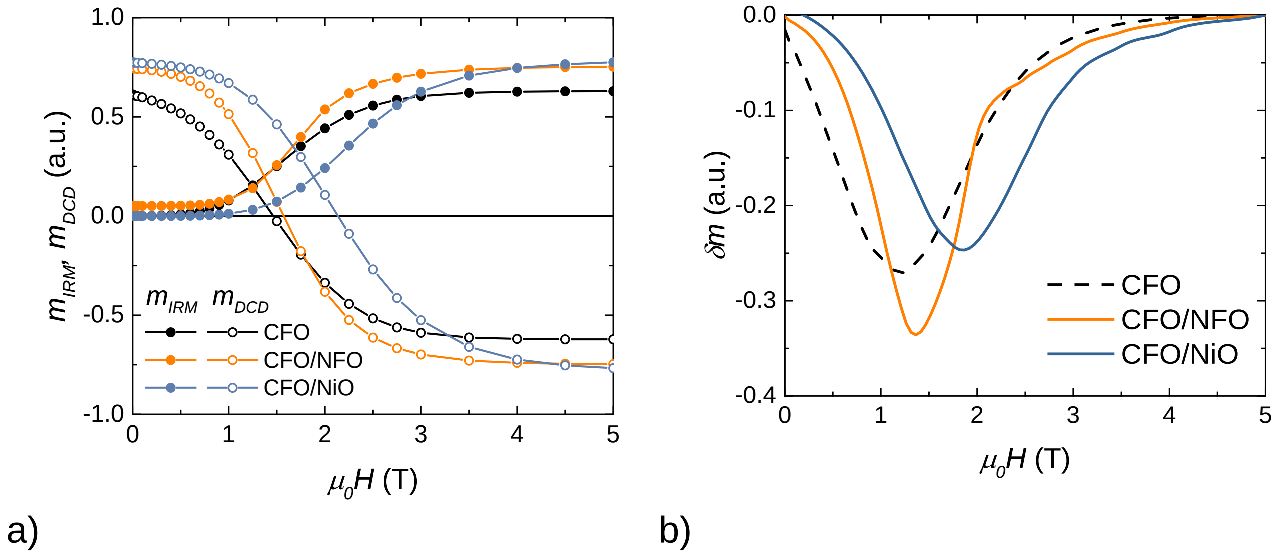

Figure 104. a) m_{IRM} and m_{DDC} remanent magnetizations and b) δm-plots for CFO, CFO/NiO and CFO/NFO core/shell MNPs measured at 5 K [192].

The “magnetic size” of the particles was studied using three approaches (Table 27):

1. Magnetic viscosity coefficient measurements at 5 K [184,203,272];
2. *M-H* curve (300 K) fits with Langevin–Chantrell method [90];
3. *M-H* curve (300 K) fits with the numerical inversion method [93,94].

The magnetic viscosity (S) was found through the relaxation measurements at 5K (Figure 105). The magnetization as a function of time was recorded for 120 min at a positive applied field (μ_0H_{app}) 5 K after the previous saturation of the sample in the magnetic field of −5 T. The obtained $M(t)$ curves were fitted using eq. (75). The magnetic activation volume (V_{act}) for SD MNPs with uniaxial anisotropy was found through the eq.(77) considering irreversibility susceptibility χ_{irr} as the values of dM_{DCD}/dH_{app} at fields $\mu_0 H_{Cr}^{DCD}$ of 1.5, 1.6 and 2.1 T for CFO core, CFO/NFO and CFO/NiO core/shell MNPs, respectively. Considering the dominant cubic anisotropy $V_{act}^{cubic} = 4 \times V_{act}^{uniaxial}$ [46], the V_{act} was calculated and converted into a "magnetic size" d_m^a as the diameter of the sphere with this volume. For a weakly interacting particles system without canted spins at the surface, the magnetic size is expected to be equal to the physical size of the particles as estimated by the TEM analysis. The small reduction of magnetic size with respect to the physical one was ascribed to the presence of a thin layer of the magnetically dead surface.

Table 27. Particle size obtained after TEM image analysis (d_{TEM}^{log}), the magnetic size evaluated from the magnetic viscosity (d_m^a), Langevin–Chantrell fit (d_m^b) and MINORIM software (d_m^c) of CFO core, CFO/NFO and CFO/NiO core/shell MNPs.

Sample	**d_{TEM}^{log}, nm**	**d_m^a, nm**	**d_m^b, nm**	**d_m^c, nm**
CFO	8.3±0.1	6.9±0.2	5.5±0.2	6.9
CFO/NFO	9.5±0.1	7.3±0.2	6.0±0.2	7.7
CFO/NiO	9.6±0.2	6.5±0.5	5.4±0.2	6.9

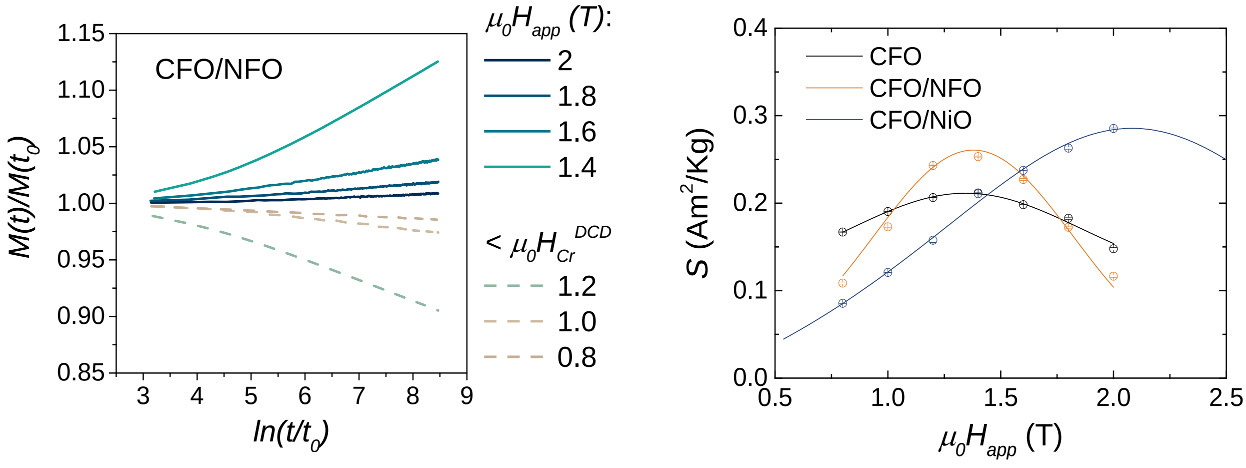

a) b)

Figure 105. a) Normalized $M(t)$ measured at different values of $\mu_0 H_{app}$ after saturation at −5 T for CFO/NFO sample; b) magnetic viscosity S as a function of the applied field $\mu_0 H_{app}$ for CFO, CFO/NiO and CFO/NFO core/shell MNPs [192].

Another approach to determine the magnetic size is the fit of the SPM *M-H* curves (Figure 106) the Langevin–Chantrell method (eq.(30), considering the lognormal distribution of particle sizes) [47].

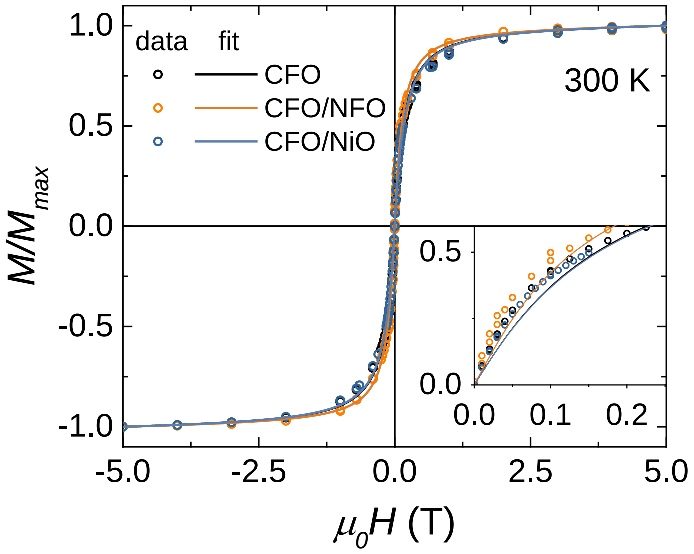

Figure 106. Measured at 300 K (dots) and fitted with the Langevin–Chantrell method (lines) *M-H* curves for CFO, CFO/NiO and CFO/NFO core/shell MNPs [192].

The fit of *M-H* curves measured at 300 K, provides the magnetic size d_m^b with its standard deviation σ_m^b. The corresponding to fitted parameter, the lognormal distributions of magnetic sizes were plotted together with the lognormal distribution of physical sizes (Figure 101). This method additionally confirms the reduction of magnetic size concerning the physical one. Another approach to fit SPM *M-H* curves is based on the numerical inversion method. This method is also based on the Langevin function fit but does not assume a particular shape of the particle size distribution. To perform the fit for the core/shell samples, an averaged M_S over the fraction content of the bulk magnetization values was taken. The fit has been performed with the MINORIM software [94]. Comparing the results of the three different methods of magnetic size estimation, a qualitative agreement between the three methods can be observed. The magnetic size increases when the hard FiM CFO grains are covered by the soft FiM NFO layer, while it remains unchanged in the case of the AFM NiO shell (Figure 107). Moreover, the magnetic size determined by magnetic viscosity was in better quantitative agreement with the result obtained by the numerical inversion method. This fact can be explained by the non-lognormal distribution of the magnetic properties of the studied samples. All magnetic dimensions are slightly smaller than the physical dimensions of the particles, which may be due to the following surface effects: disordered spins on the surface form a nonmagnetic shell with a thickness in the range of 0.5–1 nm or some internal spin canting.

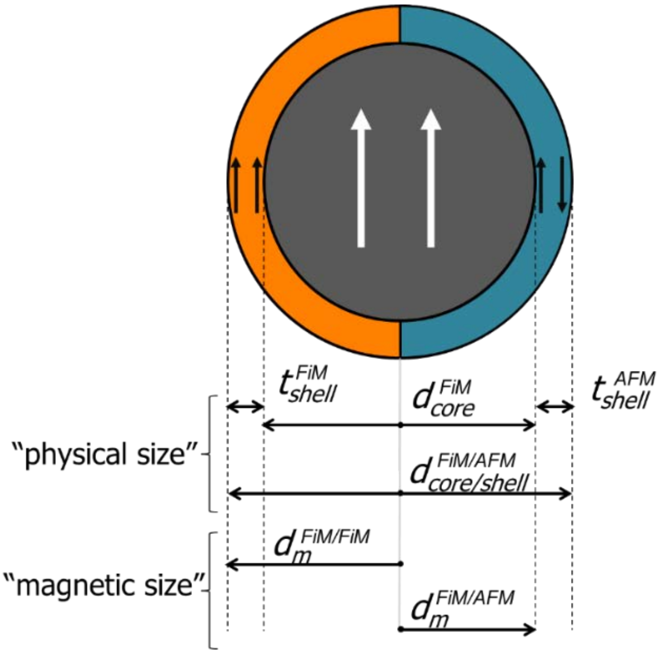

Figure 107. Schematic representation of the magnetic structure of CFO/NFO and CFO/NiO core/shell MNPs [192].

Conclusions

The thin shell of about 0.6 nm soft FiM NFO or AFM NiO on 8 nm hard FiM CFO seed particles strongly affected the magnetic reversal process of core/shell MNPs. The soft FiM NFO and AFM NiO shells increased the magnetic anisotropy and prevented reversible processes (residual thermal fluctuations) at low temperatures of core/shell MNPs: the increased anisotropy results from the interface exchange interaction between the FiM core and AFM shell (CFO/NiO) or the disordered spins in the ESC regime (CFO/NFO).

5.4 Mn_3O_4/MnO core/shell and hollow Mn_3O_4 nanoparticles

In section 5.3, we observed that the AFM shell strongly increases the anisotropy of the system of exchange coupled AFM and FiM layers. At the nanoscale, the surface plays an important role in the formation of magnetic properties. In fact, even a chemically single-phase system, as we observed in chapter 4, at the nanoscale can turn into a bi-magnetic system, where frustrated spins at the surface act as spin-glass at low temperatures. Thus, a single-phase nanosystem can emerge the typical for interfacial exchange-coupled systems the enhanced magnetic anisotropy and exchange bias. This chapter will provide a vivid example of the manifestation of interface and surface effects by comparing FiM/AFM core/shell and single-phase hollow FiM MNPs.

The samples were synthesised by the HTD method by Prof. Davide Peddis. XRD and STEM investigations were performed by Dr Gurvinder Singh (Department of Biomedical Engineering and Sydney Nano Institute, The University of Sydney). The author of the dissertation is grateful to Prof. Dino Fiorani and Dr Sara Laureti for the fruitful discussion of the magnetic properties of the studied system.

Samples

The Mn_3O_4/MnO core/shell MNPs were synthesized by using the HTD of manganese oleate and then functionalized by ʟ-3,4-dihydroxyphenylalanine (ʟ-DOPA). The details of the synthesis are reported in ref [273]. Morphostructural characterization of the Mn_3O_4/MnO core/shell MNPs (Figure 108) gives evidence of a two-phase system where 15±3 nm MNPs consist of a FiM Mn_3O_4 core, surrounded by an AFM MnO shell (2 nm). The formation of core/shell structure is native due to the oxidation process of manganese. The hollow Mn_3O_4 MNPs can be obtained from as-prepared Mn_3O_4/MnO core/shell MNPs by the degradation process occurring in the aqueous medium (Kirkendall effect [274–276]). After a few hours in the water, the diameter of Mn_3O_4/MnO core/shell MNPs decreases gradually up to the complete dissolution. The intermediate state is the hollow nanoparticles [273]. In this study, as-prepared Mn_3O_4/MnO core/shell and aged for 1 hour in water MNPs were compared. The diameter of the hollow Mn_3O_4 MNPs was 13±2 nm.

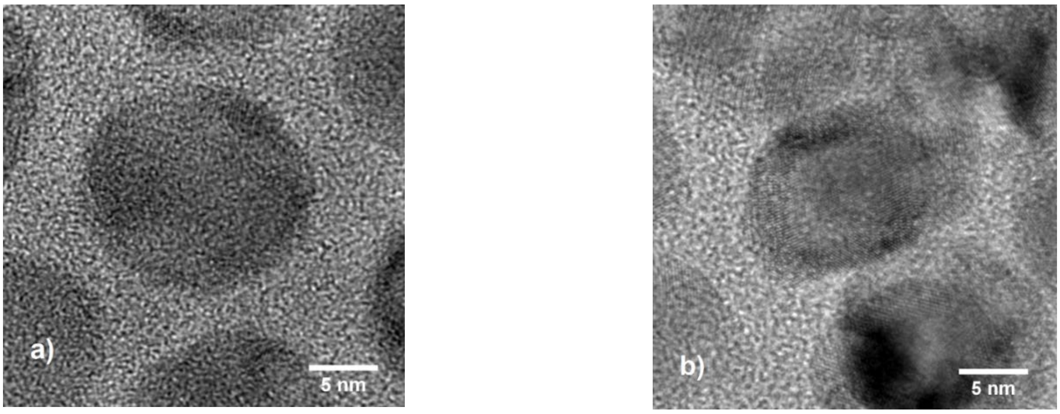

Figure 108. HRTEM micrographs of a) Mn_3O_4/MnO core/shell and b) hollow Mn_3O_4 MNPs [16].

Magnetic properties

As we already noticed, Mn_3O_4/MnO core/shell MNPs are a FiM/AFM system. The manganese oxides core/shell MNPs are considered inverted exchange bias systems because the T_N of the AFM phase (118 K) is above the T_C of FiM one (43 K). The temperature dependence of magnetization measured by the ZFC and FC protocols (Figure 109) confirms the FiM nature of the samples at temperatures below the ~43 K. At higher temperatures, the magnetic properties of the sample are paramagnetic or antiferromagnetic with weakly temperature-dependent magnetic susceptibility.

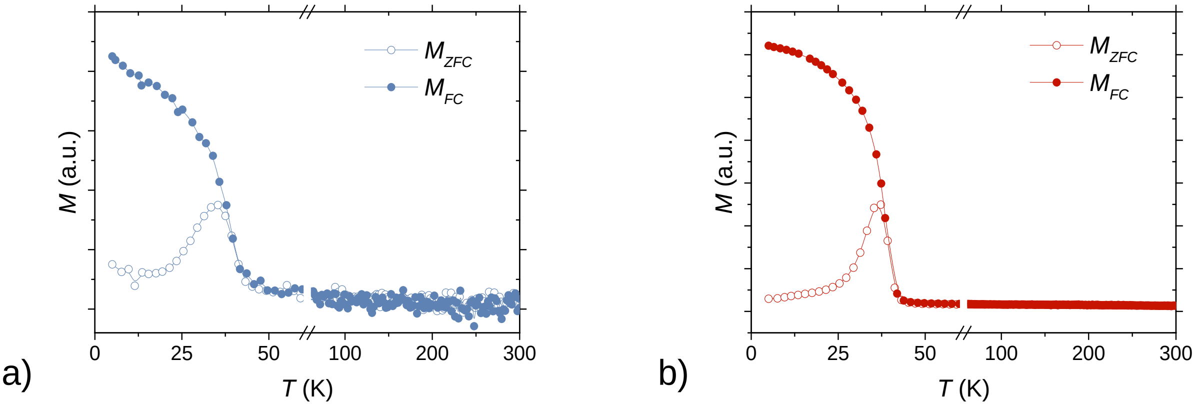

Figure 109. ZFC and FC magnetization in magnetic field of 50 mT as function of temperature for a) Mn_3O_4/MnO core/shell [16] and b) hollow Mn_3O_4 MNPs.

Comparing *M-H* loops of both systems measured at 5 K after FC and ZFC (Figure 110), one can note that Mn_3O_4/MnO core/shell MNPs show magnetic hysteresis with a coercivity of 0.31 T and significantly high exchange bias field (0.12 T), while the hollow MNPs possess higher coercivity of 0.65 T and almost no exchange bias. Such a significant change in the magnetic behavior suggests a strong modification of the spin configuration, which can be explained by structural and chemical changes in the system. Indeed, the TEM results clearly indicate the formation of a hollow structure as a consequence of the Kinkerdall effect, which breaks up the nanoparticle structure as a result of further oxidation that occurs in an aqueous solution. The magnetic behavior of the system after being in the water is characterized by a single ferromagnetic contribution with a strongly anisotropic character, which is caused by the huge number of surface spins of the hollow structure. Indeed, in the case of hollow particles, they have two surfaces—external and internal—giving rise to topological magnetic frustration of the spin of the surface ions.

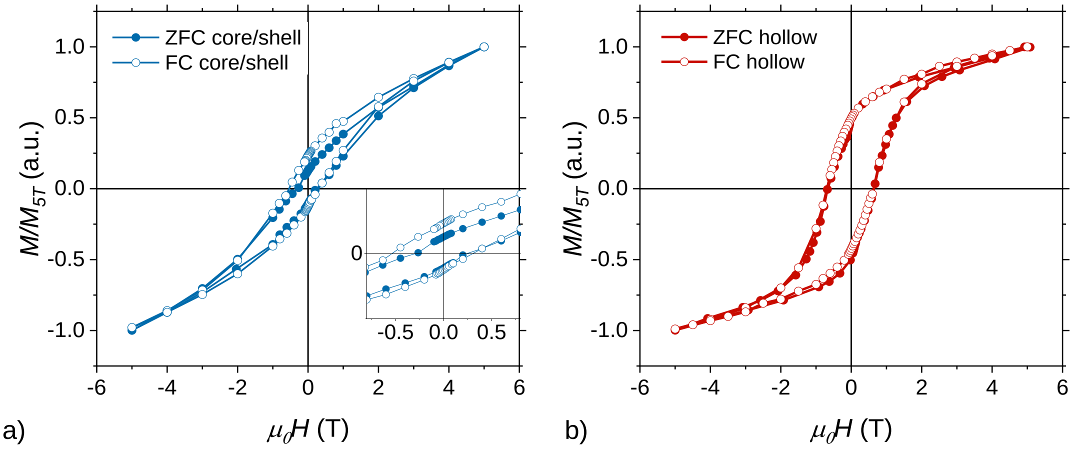

Figure 110. Isothermal *M-H* cycles recorded at 5 K after ZFC and for a) Mn_3O_4/MnO core/shell and b) hollow Mn_3O_4 MNPs [16].

By measuring the *M-H* cycles at different temperatures after FC, one can observe a decrease in magnetization and coercivity, which is typical for FM and FiM materials (Figure 111). The coercivity vanishes at a temperature close to the Curie temperature of Mn_3O_4. At the same time, *M-H* cycles recorded after FC, possess higher coercivity and exchange bias which are rapidly decrease with temperature. A small $\mu_0 H_E$ in the ZFC loop is due to the high anisotropy of spins at the surface and interface: the system is not completely saturated even in the field of 5 T, thus the hysteresis cycle is minor.

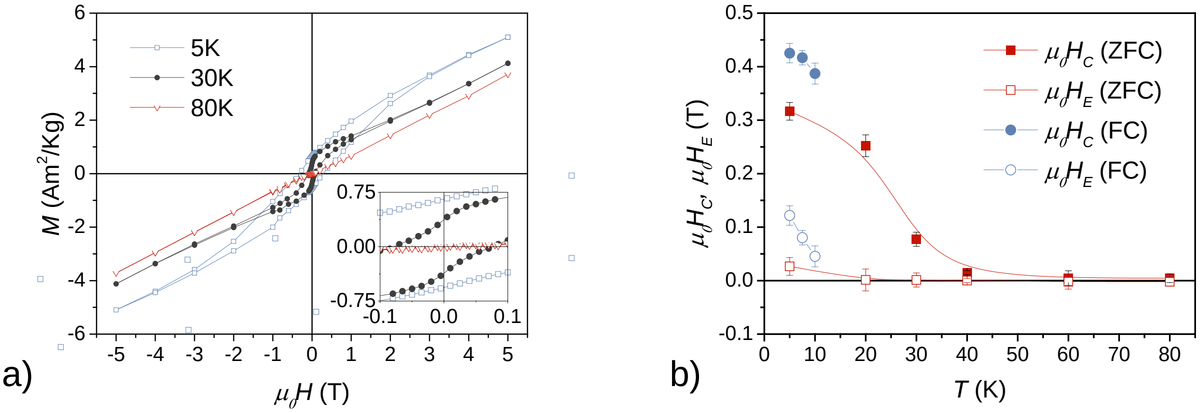

Figure 111. a) *M-H* cycles recorded at 5, 30 and 80 K after ZFC; b) the temperature dependences of coercivity and exchange bias field after FC and ZFC processes for Mn_3O_4/MnO core/shell MNPs [16].

A requirement for observing the EB phenomenon is that the T_C of the FM phase (or FiM) is higher than the T_N of the AFM phase to establish unidirectional anisotropy during FC through T_N. In the case of inverted systems, such as Mn_3O_4/MnO, where $T_C < T_N$, the mechanism of how unidirectional anisotropy can be established during field cooling is still controversial, although loop displacement has been observed up to T_C. In the Mn_3O_4/MnO core/shell MNPs, the interface can be represented as a region of strongly anisotropic frustrated spins that freeze at the glass temperature T_G below T_N (Figure 112). During cooling, the AFM shell is expected to reach a spin configuration at the T_N ordering temperature that is mainly determined by local magnetocrystalline anisotropy. In other words, a shell of randomly oriented domains is expected after both FC and ZFC processes. As the temperature gradually decreases, the uncompensated AFM spins in the interfacial region are expected to reach a frustrating configuration resulting from competition between different energy conditions, including the Zeeman contribution due to interaction with the externally applied field. The hysteresis loops after ZFC and after FC reflect the presence of two contributions to magnetization, with different strength and thermal evolution of magnetic anisotropy, suggesting the presence of a disordered anisotropic region at the interface that behaves differently from the core. From this point of view, the loop displacement can be assumed to be a consequence of a minor loop, rather than an effect of unidirectional anisotropy induced by the AFM/FM interface.

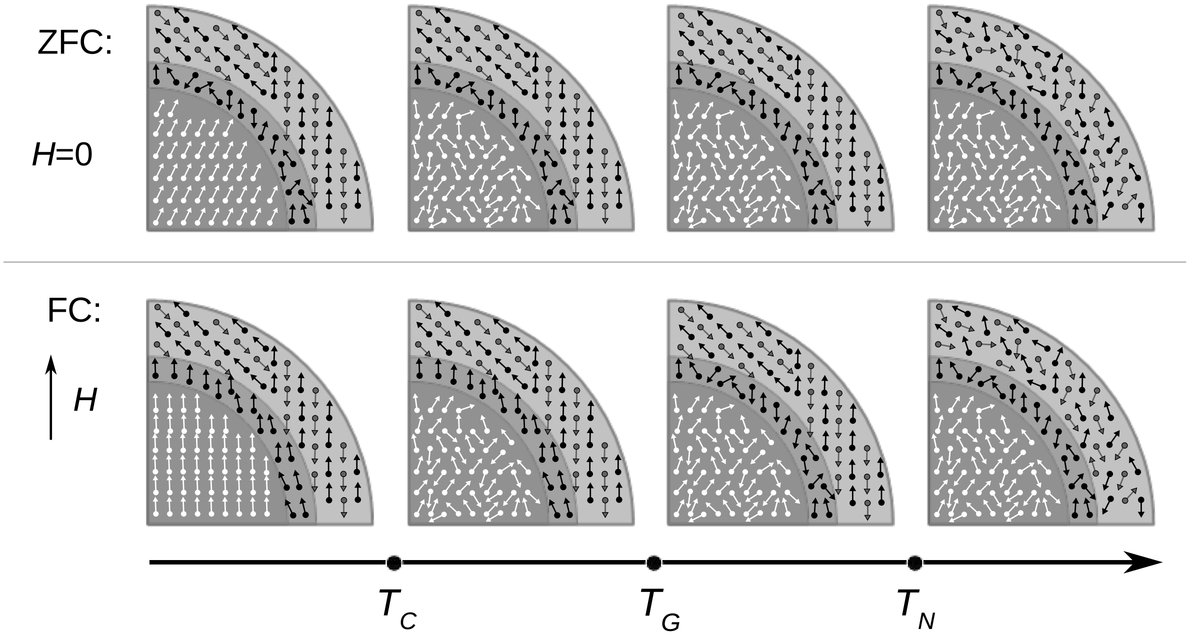

Figure 112. Schematical representation of the proposed magnetic structure evolution of Mn_3O_4/MnO core/shell MNPs during FC and ZFC.

Conclusions

The Mn_3O_4/MnO core/shell MNPs is an inverted system of classical systems where exchange bias is observed because the Néel temperature of the AFM lies above the ordering temperature of the FiM. However, the observed exchange bias of 0.12 T at 5 K confirmed the determining role of frozen magnetic moments of atoms at the AFM/FiM interface in unidirectional anisotropy. Interestingly, after dilution of the MNPs in water, the exchange bias was no longer observed, but the hollow system possessed an increased coercive force from 0.31 T up to 0.65 T, which was explained by the contribution of the increased effective surface and particle shape.

5.5 Conclusions

The system with a magnetically soft shell NFO has an effective magnetic anisotropy constant of 4×10^5 J/m^3, while for the inverted system with a magnetically hard shell CFO it is 3×10^5 J/m^3. This has been explained by the proximity effect associated with the epitaxial growth of the shell material, in which CFO induces an increase in NFO anisotropy. Thus, with the given volume content of phases, the CFO core contributes more to the magnetic anisotropy of the whole CFO/NFO system, comparing with the inverted NFO/CFO system. This has been attributed to the proximity effect associated with epitaxial growth of the shell material, in which CFO induces an increase in NFO anisotropy. The coating of the CFO core with a thin (less than 1 nm) NFO increases its coercivity at low temperatures by enhancing the degree of canted atomic magnetic moments at surface. An AFM shell of the same thickness increases the coercivity of a cobalt ferrite core measured at 5 K from 1.2 T to 2 T. For thicker soft shells, the effective magnetic anisotropy constant decreases from 9.8×10^5 J/m^3 for single-phase CFO with an average size of about 9 nm to 2×10^5 J/m^3 for the same CFO phase coated with an NFO shell of about 4 nm thick.

The last section of this chapter presents the results of the core/shell Mn_3O_4/MnO and hollow Mn_3O_4 nanoparticles studies. For such particles, an exchange bias of 0.12 T at 5 K confirmed the determining role of the frozen magnetic moments of the atoms at the antiferromagnetic/ferrimagnetic interface in unidirectional anisotropy. Interestingly, the exchange bias was no longer observed after the particles was diluted in water, but the hollow system possessed an increased coercive force.

Main results and conclusions

1. Cobalt ferrite nanoparticles with crystallite sizes of about 20 nm with gradually replaced cobalt ions with nickel and zinc were produced by the sol-gel autocombustion method. Their structural and magnetic properties were investigated. The dependences of the main parameters of magnetic hysteresis on the chemical composition were determined and, as a consequence, the compositions with the maximum values of coercive force (175±5 mT for pure cobalt ferrite at 300 K) and saturation magnetization (69.1±0.3 and 74±2 Am^2/kg for $Ni_{0.25}Co_{0.75}Fe_2O_4$ and $Zn_{0.25}Co_{0.75}Fe_2O_4$, respectively) were determined. The nonmonotonical dependence of the saturation magnetization on the chemical composition was explained by a complex change in the magnetic structure such as degree of spinel inversion with a decrease in cobalt content.
2. The magnetic properties and magnetic structure of small cobalt ferrite nanoparticles (5±1 nm) doped with zinc produced by the hydrothermal coprecipitation method were investigated. It was found that the coercivity decreases from 1.1 T down to 0.6 T with increasing zinc concentration from 0 up to 50%. The change in the saturation magnetization was different compared with the particles produced by the sol-gel autocombustion method: it slowly depends on the chemical composition and its value for pure cobalt ferrite of about 95±3Am^2/kg was higher than this for bulk. The saturation magnetization behavior is determined by the magnetic structure, which in turn is determined by the synthesis method. The magnetic structure of a series of obtained nanoparticles was reconstructed by combined SQUID magnetometry and Mössbauer spectroscopy. In particular, the nonmonotonic behavior of the canting of atomic magnetic moments, which depends in a complex way on the distribution of cations over spinel sublattices and the formation of corresponding exchange interactions, was found.

3. The magnetic properties of iron oxide nanoparticles synthesized by coprecipitation in the presence of citric acid and glycine were investigated. The used capping agents allowed controlling the particle size in the range from 10 to 2 nm. It was shown that at cryogenic temperatures in the smallest particles, 2–4 nm in average dimeter, the magnetically disordered layer of surface atom magnetic moments of freezes and acts as a spin-glass. This was confirmed by the presence of magnetic memory effects and the horizontal shift of the hysteresis loop (9±1 mT). It was shown that in nanoparticles fabricated by this method, the thickness of the surface layer is about 1 nm, i.e., the condition for observing the hysteresis loop shift and the magnetic memory effect is the commensurability of the thickness of the magnetofrustrated layer and the radius of the ferrimagnetic core. This is due to the correlation length of the exchange interaction.
4. The magnetic properties of cobalt ferrite nanoparticles obtained by the sol-gel autocombustion method with average diameters in the range of 2.5–6.6 nm, embedded in a diamagnetic matrix of mesoporous silicon dioxide, were investigated. In such a system the particles are isolated from each other, the influence of interparticle interactions is negligible and magnetic properties are defined primarily by the magnetocrystalline and surface magnetic anisotropy. Comparing nanoparticles of the same size but with different temperatures of annealing, it was shown that even in ultra-small (<3 nm) cobalt ferrite nanoparticles, despite the significant surface contribution, the greatest contribution to the effective anisotropy is magnetocrystalline. The annealing of the cobalt ferrite nanoparticles could lead to the migration of cobalt 2+ ions to tetragonal from octahedral positions, where cobalt ions have a significantly higher impact on the magnetocrystalline anisotropy. The maximum value of the effective magnetic anisotropy constant of about 8×10^5 J/m^3 was found in nanoparticles of 2.5±0.2 nm.

5. Magnetic properties of nanoparticles with the core/shell structure with different structural features (material deposition sequences, core composition and shell thickness) were investigated. The systems of cobalt ferrite nanoparticles with an antiferromagnetic nickel monoxide shell were also investigated. The antiferromagnetic shell increases the coercivity measured at 5 K of cobalt ferrite core from 1.2 T up to 2 T. A phenomenological model for the formation of magnetic properties of such particles was constructed, including the fact that the choice of magnetically hard material as the core leads to increased magnetic anisotropy compared to the anisotropy of the inverted system. The hard/soft system possesses magnetic anisotropy constant of about 4×10^5 J/m^3, while for the inverted system with the magnetically hard shell it is 3×10^5 J/m^3. Besides the exchange interaction between two magnetic phases, the magnetic structure of the shell is also important: the covering of the magnetically hard core with thin (less than 1 nm) soft material increases its anisotropy by enhancing the canting of magnetic moments of atoms at particle surface.
6. The magnetic properties of Mn_3O_4/MnO core/shell nanoparticles and their degradation product in the aqueous medium, hollow Mn_3O_4 nanoparticles, were investigated. The formation of the magnetic properties of the core/shell nanoparticles is influenced by the exchange interaction at the interface between the ferrimagnetic and antiferromagnetic material, which, in particular, was confirmed by the presence of the hysteresis loop shift of 0.12 T at 5 K after cooling in the magnetic field of 5 T. On the other hand, the peculiarities of the magnetic properties of hollow nanoparticles were explained by the large specific surface area, which is the source of the increased magnetic anisotropy resulting in the increase of coercivity from 0.31 T up to 0.65 T.

Acknowledgements

I would like to express my gratitude to my supervisors, Valeria Rodionova and Davide Peddis, for their support, encouragement and patience. As well I would like to thank Sara Laureti, Gaspare Varvaro, Dino Fiorani, Fabio Canepa, Pietro Manfrinetti, and other people who supervised and advised me during my work on dissertation. I would also like to show my deep appreciation to my colleagues and friends, current and former members of REC «Smart Materials and Biomedical Applications» (former Laboratory of Novel Magnetic Materials) and Nanostructured Magnetic Materials Lab «*nM*^{2}*-Lab*», without whom I would not have been able to complete this research. I would like to thank all colleagues, co-authors and collaborators from around the world involved in this research. During these years, I met a lot of people at IKBFU as well as during my internships and visits in University of Genova, ISM-CNR and, especially with who I stayed at guesthouse in Piana Bella Di Montelibretti, who have become very important parts of my life, which I am very happy about.

To conclude, I cannot forget to thank my family and friends for all the unconditional support in this very intense and long academic years.

List of symbols and acronyms

AC = Alternating Current
AFM = Antiferromagnetism(-ic)
CA = Citric Acid
CFO = $CoFe_2O_4$
CP = Co-Precipitation
DC = Direct Current
DCD = DC Demagnetization
DMI = Dzyaloshinskii–Moriya Interaction
EB = Exchange Bias
EDX = Energy-Dispersive X-ray spectroscopy
EELS = Electron Energy Loss Spectroscopy
EFTEM = Energy-Filtered Transmission Electron Microscopy
ESC = Enhanced Spin Canting
F(i)M = Ferrimagnetism(-ic) or ferromagnetism(-ic)
FC = Field Cooling
FiM = Ferrimagnetism(-ic)
FM = Ferromagnetism(-ic)
HAADF = High-Angle Annular Dark-Field
HRTEM = High-Resolution Transmission Electron Microscopy
HTD = High-Temperature Decomposition
IRM = Isothermal Remanence Magnetization
LAS = Law of Approach to Saturation
MD = Multi-Domain
MNHs = Magnetic Nanohybrids
MNPs = Magnetic Nanoparticles
MRI = Magnetic Resonance Imaging
NFO = $NiFe_2O_4$
OA = Oleic Acid
RAM = Random Anisotropy Model
SD = Single-Domain
SEM = Scanning Electron Microscopy
SFD = Switching Field Distribution
SGAC = Sol-Gel Autocombustion
SPM = Superparamagnetism(-ic)
SQUID = Superconducting Quantum Interference Device
SSG = Superspin-Glass
STEM = Scanning Transmission Electron Microscopy
SW = Stoner–Wohlfarth
TEM = Transmission Electron Microscopy
TG = Thermogravimetry
TMO = Transition Metal Oxide
TRM = Thermoremanent Magnetization

VSM = Vibrating-Sample Magnetometer
XRD = X-Ray Diffraction
ZFC = Zero Field Cooling
T_d = Tetrahedral, A site
O_h = Octahedral, B site
μ = Magnetic moment
μ_0 = Vacuum magnetic permeability ($4\pi \cdot 10^{-7}$ T m A^{-1})
μ_B = Bohr magneton (9,274 · 10-24 J T^{-1})
γ = Inversion degree
k_B = Boltzmann constant ($1.381 \cdot 10^{-23}$ J K^{-1})
T_B = Superparamagnetic blocking temperature
T_C = Curie temperature
T_g = Spin glass transition temperature
T_{irr} = Irreversibility temperature
T_{max} = Temperature of the maximum of $M_{ZFC}(T)$ curve
T_N = Verwey transition temperature
M_S = Saturation magnetization
M_R = Remanent magnetization
K = Magnetic anisotropy constant
K_S = Surface anisotropy
K_{eff} = Effective anisotropy
E_a = Magnetic anisotropy energy
χ = Magnetic susceptibility
X_{SAT} = Magnetic susceptibility after saturation
χ_{irr} = Irreversibility susceptibility (peak value of (dM_{DCD}/dH_{app}))
$\mu_0 H_E$ = Exchange bias field
$\mu_0 H_C$ = Coercivity
$\mu_0 H_{irr}$ = Irreversibility field
$\mu_0 H_{Cr}^{DCD}$ = Coercivity of remanence cure after DCD
$\mu_0 H_{Cr}^{IRM}$ = Coercivity of remanence cure after IRM
$\mu_0 H_{INT}$ = Interaction field
$\mu_0 H_K$ = Anisotropy field
$\mu_0 H_f$ = Fluctuation field
ξ = Reduced coercivity (H_C/H_K)
d_{TEM} = Average particle diameter after TEM analysis
d_{XRD} = Average size of crystallites
d_m = Magnetic particle size
V_{act} = Activation volume
t_s = Shell thickness
R = Parameter of magnetization reduction
S = Magnetic viscosity
δm = Kelly plot
a = Lattice constant

Reference List

1. Gu H., Liu C., Zhu J., Gu J., Wujcik E.K., Shao L., Wang N., Wei H., Scaffaro R., Zhang J., Guo Z. Introducing advanced composites and hybrid materials // Adv. Compos. Hybrid Mater. Advanced Composites and Hybrid Materials, 2018. Vol. 1, № 1. P. 1–5 DOI:10.1007/s42114-017-0017-y.
2. Efremova M. V., Naumenko V.A., Spasova M., Garanina A.S., Abakumov M.A., Blokhina A.D., Melnikov P.A., Prelovskaya A.O., Heidelmann M., Li Z.-A., Ma Z., Shchetinin I. V., Golovin Y.I., Kireev I.I., Savchenko A.G., Chekhonin V.P., Klyachko N.L., Farle M., Majouga A.G., Wiedwald U. Magnetite-Gold nanohybrids as ideal all-in-one platforms for theranostics // Sci. Rep. 2018. Vol. 8, № 1. P. 11295 DOI:10.1038/s41598-018-29618-w.
3. Pineider F., de Julián Fernández C., Videtta V., Carlino E., al Hourani A., Wilhelm F., Rogalev A., Cozzoli P.D., Ghigna P., Sangregorio C. Spin-Polarization Transfer in Colloidal Magnetic-Plasmonic Au/Iron Oxide Hetero-nanocrystals // ACS Nano. 2013. Vol. 7, № 1. P. 857–866 DOI:10.1021/nn305459m.
4. Psimadas D., Baldi G., Ravagli C., Comes Franchini M., Locatelli E., Innocenti C., Sangregorio C., Loudos G. Comparison of the magnetic, radiolabeling, hyperthermic and biodistribution properties of hybrid nanoparticles bearing CoFe2O4 and Fe3O4 metal cores. // Nanotechnology. 2014. Vol. 25, № February 2016. P. 025101 DOI:10.1088/0957-4484/25/2/025101.
5. Katz E., Willner I. Integrated nanoparticle-biomolecule hybrid systems: Synthesis, properties, and applications // Angew. Chemie - Int. Ed. 2004. Vol. 43, № 45. P. 6042–6108 DOI:10.1002/anie.200400651.
6. Vinayan B.P., Ramaprabhu S. Platinum–TM (TM = Fe, Co) alloy nanoparticles dispersed nitrogen doped (reduced graphene oxide-multiwalled carbon nanotube) hybrid structure cathode electrocatalysts for high performance PEMFC applications // Nanoscale. 2013. Vol. 5, № 11. P. 5109 DOI:10.1039/c3nr00585b.

7. Bavio M.A., Lista A.G. Synthesis and characterization of hybrid-magnetic nanoparticles and their application for removal of arsenic from groundwater // Sci. World J. 2013. Vol. 2013 DOI:10.1155/2013/387458.
8. Baeza A., Guisasola E., Ruiz-Hernández E., Vallet-Regí M. Magnetically triggered multidrug release by hybrid mesoporous silica nanoparticles // Chem. Mater. 2012. Vol. 24, № 3. P. 517–524 DOI:10.1021/cm203000u.
9. Liu R., Duay J., Lee S.B. Heterogeneous nanostructured electrode materials for electrochemical energy storage // Chem. Commun. 2011 DOI:10.1039/c0cc03158e.
10. Manjunatha R., Karajić A., Liu M., Zhai Z., Dong L., Yan W., Wilkinson D.P., Zhang J. A Review of Composite/Hybrid Electrocatalysts and Photocatalysts for Nitrogen Reduction Reactions: Advanced Materials, Mechanisms, Challenges and Perspectives // Electrochemical Energy Reviews. Springer Singapore, 2020 DOI:10.1007/s41918-020-00069-0.
11. Fullerton E.E., Jiang J.S., Bader S.D. Hard/soft magnetic heterostructures: model exchange-spring magnets // J. Magn. Magn. Mater. 1999. Vol. 200, № 1–3. P. 392–404 DOI:10.1016/S0304-8853(99)00376-5.
12. Salvador M., Moyano A., Martínez-García J.C., Blanco-López M.C., Rivas M. Synthesis of Superparamagnetic Iron Oxide Nanoparticles: SWOT Analysis Towards Their Conjugation to Biomolecules for Molecular Recognition Applications // J. Nanosci. Nanotechnol. 2019. Vol. 19, № 8. P. 4839–4856 DOI:10.1166/jnn.2019.16931.
13. Roca A.G., Gutiérrez L., Gavilán H., Fortes Brollo M.E., Veintemillas-Verdaguer S., Morales M. del P. Design strategies for shape-controlled magnetic iron oxide nanoparticles // Adv. Drug Deliv. Rev. Elsevier B.V., 2019. Vol. 138, № xxxx. P. 68–104 DOI:10.1016/j.addr.2018.12.008.
14. Vázquez-Vázquez C., López-Quintela M.A., Buján-Núñez M.C., Rivas J., Lo M.A., Va C., Rivas J., Buja M.C. Finite size and surface effects on the magnetic properties of cobalt ferrite nanoparticles // J. Nanoparticle Res. 2011. Vol. 13, № 4. P. 1663–1676 DOI:10.1007/s11051-010-9920-7.

15. Omelyanchik A., Salvador M., D’orazio F., Mameli V., Cannas C., Fiorani D., Musinu A., Rivas M., Rodionova V., Varvaro G., Peddis D. Magnetocrystalline and surface anisotropy in CoFe2o4 nanoparticles // Nanomaterials. Multidisciplinary Digital Publishing Institute, 2020. Vol. 10, № 7. P. 1–11 DOI:10.3390/nano10071288.
16. Omelianchik A., Singh G., McDonagh B.H., Rodionova V., Fiorani D., Peddis D., Laureti S. From Mn 3 O 4 /MnO core–shell nanoparticles to hollow MnO: evolution of magnetic properties // Nanotechnology. IOP Publishing, 2018. Vol. 29, № 5. P. 055703 DOI:10.1088/1361-6528/aa9e59.
17. Nogués J., Schuller I.K. Exchange bias // J. Magn. Magn. Mater. 1999. Vol. 192, № 2. P. 203–232 DOI:10.1016/S0304-8853(98)00266-2.
18. Meiklejohn W.H., Bean C.P. New magnetic anisotropy // Phys. Rev. 1957. Vol. 105, № 3. P. 904–913 DOI:10.1103/PhysRev.105.904.
19. Ong Q.K., Wei A., Lin X.-M. Exchange bias in Fe/Fe3O4 core-shell magnetic nanoparticles mediated by frozen interfacial spins // Phys. Rev. B. 2009. Vol. 80, № 13. P. 134418 DOI:10.1103/PhysRevB.80.134418.
20. Ong Q.K., Lin X.-M., Wei A. Role of Frozen Spins in the Exchange Anisotropy of Core−Shell Fe@Fe 3 O 4 Nanoparticles // J. Phys. Chem. C. 2011. Vol. 115, № 6. P. 2665–2672 DOI:10.1021/jp110716g.
21. Manna P.K., Yusuf S.M., Shukla R., Tyagi A.K. Exchange bias in BiFe0.8Mn0.2O3 nanoparticles with an antiferromagnetic core and a diluted antiferromagnetic shell // Phys. Rev. B. 2011. Vol. 83, № 18. P. 184412 DOI:10.1103/PhysRevB.83.184412.
22. Li Z.-A., Fontaíña-Troitiño N., Kovács a, Liébana-Viñas S., Spasova M., Dunin-Borkowski R.E., Müller M., Doennig D., Pentcheva R., Farle M., Salgueiriño V. Electrostatic doping as a source for robust ferromagnetism at the interface between antiferromagnetic cobalt oxides. // Sci. Rep. 2015. Vol. 5. P. 7997 DOI:10.1038/srep07997.
23. Bader S.D., Parkin S.S.P. Spintronics // Annu. Rev. Condens. Matter Phys. 2010. Vol. 1, № 1. P. 71–88 DOI:10.1146/annurev-conmatphys-070909-104123.

24. Coey J.M.D., Venkatesan M., Xu H. Introduction to Magnetic Oxides // Functional Metal Oxides. Weinheim, Germany: Wiley-VCH Verlag GmbH & Co. KGaA, 2013. P. 1–49 DOI:10.1002/9783527654864.ch1.
25. Dionne G.F. Magnetic Oxides // Journal of Chemical Information and Modeling. Boston, MA: Springer US, 2009. Vol. 8, № 9. 1–58 p. DOI:10.1007/978-1-4419-0054-8.
26. Cardoso V.F., Francesko A., Ribeiro C., Bañobre-López M., Martins P., Lanceros-Mendez S. Advances in Magnetic Nanoparticles for Biomedical Applications // Adv. Healthc. Mater. 2018. Vol. 7, № 5. P. 1–35 DOI:10.1002/adhm.201700845.
27. Song G., Kenney M., Chen Y.-S., Zheng X., Deng Y., Chen Z., Wang S.X., Gambhir S.S., Dai H., Rao J. Carbon-coated FeCo nanoparticles as sensitive magnetic-particle-imaging tracers with photothermal and magnetothermal properties // Nat. Biomed. Eng. Springer US, 2020. Vol. 4, № 3. P. 325–334 DOI:10.1038/s41551-019-0506-0.
28. Socoliuc V., Peddis D., Petrenko V.I., Avdeev M. V, Susan-resiga D., Szabó T., Turcu R., Tombácz E., Vékás L. Magnetic Nanoparticle Systems for Nanomedicine — A Materials Science Perspective // Magetochemistry. 2019. Vol. 6, № 2. P. 1–36 DOI:10.3390/magnetochemistry6010002.
29. Farooq M.U., Novosad V., Rozhkova E.A., Wali H., Ali A., Fateh A.A., Neogi P.B., Neogi A., Wang Z. Gold Nanoparticles-enabled Efficient Dual Delivery of Anticancer Therapeutics to HeLa Cells // Sci. Rep. Springer US, 2018. Vol. 8, № 1. P. 2907 DOI:10.1038/s41598-018-21331-y.
30. Martins P.M., Lima A.C., Ribeiro S., Lanceros-Mendez S., Martins P. Magnetic Nanoparticles for Biomedical Applications: From the Soul of the Earth to the Deep History of Ourselves // ACS Appl. Bio Mater. 2021. Vol. 4, № 8. P. 5839–5870 DOI:10.1021/acsabm.1c00440.
31. Maldonado-Camargo L., Unni M., Rinaldi C. Magnetic Characterization of Iron Oxide Nanoparticles for Biomedical Applications. 2017. P. 47–71 DOI:10.1007/978-1-4939-6840-4_4.

32. Tkachenko M. V., Kamzin A.S. Synthesis and properties of hybrid hydroxyapatite–ferrite (Fe3O4) particles for hyperthermia applications // Phys. Solid State. 2016. Vol. 58, № 4. P. 763–770 DOI:10.1134/S1063783416040260.

33. Kamzin A.S., Valiullin A.A., Khurshid H., Nemati Z., Srikanth H., Phan M.H. Mössbauer Studies of Core-Shell FeO/Fe3O4 Nanoparticles // Phys. Solid State. 2018. Vol. 60, № 2. P. 382–389 DOI:10.1134/S1063783418020129.

34. Du Y., Liu X., Liang Q., Liang X.J., Tian J. Optimization and Design of Magnetic Ferrite Nanoparticles with Uniform Tumor Distribution for Highly Sensitive MRI/MPI Performance and Improved Magnetic Hyperthermia Therapy // Nano Lett. 2019. Vol. 19, № 6. P. 3618–3626 DOI:10.1021/acs.nanolett.9b00630.

35. Liang Y., Xie J., Yu J., Zheng Z., Liu F., Yang A. Recent advances of high performance magnetic iron oxide nanoparticles: Controlled synthesis, properties tuning and cancer theranostics // Nano Sel. 2021. Vol. 2, № 2. P. 216–250 DOI:10.1002/nano.202000169.

36. Вонсовский С.В. Магнетизм. Магнитные свойства диа-, пара, ферро-, антиферро-, и ферримагнетико. Москва: Наука, гл. ред. физ. -матем. лит., 1971. 1032 p.

37. Мейлихов Е.З. Магнетизм. Основы теории. Учебное пособие. Москва: ИД Интеллект, 2014. 184 p.

38. Koch E. Exchange Mechanisms // Correlated Electrons: From Models to Materials Modeling and Simulation Vol. 2. Julich: Forschungszentrum, 2012. Vol. 2. P. 743–765 DOI:10.1007/978-3-319-24094-7_30.

39. Peddis D., Jönsson P.E., Laureti S., Varvaro G. Magnetic Interactions // Frontiers of Nanoscience. 2014. Vol. 6. P. 129–188 DOI:10.1016/B978-0-08-098353-0.00004-X.

40. Dzyaloshinsky I. Thermodynamic Theory of “Weak” Ferromagnetism In Antiferromagnetic Substances // Sov. Phys. JETP. 1957. Vol. 5, № 6. P. 1259–1272.

41. Chen G., Mascaraque A., Jia H., Zimmermann B., Robertson M., Conte R. Lo,

Hoffmann M., Barrio M.A.G., Ding H., Wiesendanger R., Michel E.G., Blügel S., Schmid A.K., Liu K. Large Dzyaloshinskii-Moriya interaction induced by chemisorbed oxygen on a ferromagnet surface // Sci. Adv. 2020. Vol. 6, № 33. P. 1–8 DOI:10.1126/sciadv.aba4924.

42. Hellman F., Division M.S., Berkeley L., Hoffmann A., Beach G.S.D., Fullerton E.E., Macdonald A.H., Ralph D.C. Interface-Induced Phenomena in Magnetism // Rev. Mod. Phys. 2017. Vol. 89, № June. P. 025006.
43. Enders A., Skomski R., Honolka J. Magnetic surface nanostructures // J. Phys. Condens. Matter. 2010. Vol. 22, № 43 DOI:10.1088/0953-8984/22/43/433001.
44. Kovalev A.A., Sandhoefner S. Skyrmions and antiskyrmions in quasi-two-dimensional magnets // Front. Phys. 2018. Vol. 6, № SEP. P. 1–8 DOI:10.3389/fphy.2018.00098.
45. Oberdick S.D., Abdelgawad A., Moya C., Mesbahi-Vasey S., Kepaptsoglou D., Lazarov V.K., Evans R.F.L., Meilak D., Skoropata E., van Lierop J., Hunt-Isaak I., Pan H., Ijiri Y., Krycka K.L., Borchers J.A., Majetich S.A. Spin canting across core/shell Fe3O4/MnxFe3−xO4 nanoparticles // Sci. Rep. 2018. Vol. 8, № 1. P. 3425 DOI:10.1038/s41598-018-21626-0.
46. Lak A., Disch S., Bender P. Embracing Defects and Disorder in Magnetic Nanoparticles // Adv. Sci. 2021. Vol. 8, № 7. P. 2002682 DOI:10.1002/advs.202002682.
47. Fiebig M., Lottermoser T., Meier D., Trassin M. The evolution of multiferroics // Nat. Rev. Mater. 2016. Vol. 1, № 8. P. 16046 DOI:10.1038/natrevmats.2016.46.
48. Pankhurst Q.A., Ucko D.H., Fernández Barquín L., García Calderón R. Non-dipolar magnetic coupling in a strongly interacting superparamagnet: Nanogranular Fe26Cu8Ag66 // J. Magn. Magn. Mater. 2003. Vol. 266, № 1–2. P. 131–141 DOI:10.1016/S0304-8853(03)00464-5.
49. De Toro J.A., Andres J.P., González J.A., Goff J.P., Barbero A.J., Riveiro J.M. Improved giant magnetoresistance in nanogranular Co/Ag: The role of interparticle RKKY interactions // Phys. Rev. B - Condens. Matter Mater. Phys.

2004. Vol. 70, № 22 DOI:10.1103/PhysRevB.70.224412.

50. Herzer G. The Random Anisotropy Model: Properties and Applications of Nanocrystalline Alloys from Amorphous Precursors. 2005. Vol. 184, № 1. P. 15–34.

51. Herzer G. Soft-magnetic nanocrystalline materials // Scr. Metall. Mater. 1995. Vol. 33, № 10–11. P. 1741–1756 DOI:10.1016/0956-716x(95)00397-e.

52. Akulov N.S. Uber den Verlauf der Magnetisierungskurve in starken Feldern // Zeitschrift fur Phys. 1931. Vol. 69, № 11–12. P. 822–831 DOI:10.1007/BF01339465.

53. О.А. Котельникова, Н.С. Перов, А.А. Радковская, Н.И. Шпиньков. Вибрационный анизометр. Спецпрактикум кафедры магнетизма. Москва, 2014. 18 p.

54. Knobel M., Nunes W.C., Socolovsky L.M., De Biasi E., Vargas J.M., Denardin J.C. Superparamagnetism and other magnetic features in granular materials: A review on ideal and real systems // J. Nanosci. Nanotechnol. 2008. Vol. 8, № 6. P. 2836–2857 DOI:https://doi.org/10.1166/jnn.2008.017.

55. Bødker F., Mørup S., Linderoth S. Surface effects in metallic iron nanoparticles // Phys. Rev. Lett. 1994. Vol. 72, № 2. P. 282–285 DOI:10.1103/PhysRevLett.72.282.

56. Ionescu A., Llandro J., Ziebeck K.R.A. Magnetism, magnetic materials, and nanoparticles // Magnetic Nanoparticles in Biosensing and Medicine. 2019. 1–51 p. DOI:10.1017/9781139381222.002.

57. Moreno R., Poyser S., Meilak D., Meo A., Jenkins S., Lazarov V.K., Vallejo-Fernandez G., Majetich S., Evans R.F.L. The role of faceting and elongation on the magnetic anisotropy of magnetite Fe3O4 nanocrystals // Sci. Rep. Springer US, 2019. P. 1–14 DOI:10.1038/s41598-020-58976-7.

58. Oyarzún S., Tamion A., Tournus F., Dupuis V., Hillenkamp M. Size effects in the magnetic anisotropy of embedded cobalt nanoparticles: from shape to surface // Sci. Rep. Nature Publishing Group, 2015. Vol. 5, № August. P. 14749 DOI:10.1038/srep14749.

59. Frenkel J., Dorfman J. Spontaneous and Induced Magnetisation in Ferromagnetic Bodies // Nature. 1930. Vol. 126, № 3173. P. 274–275 DOI:10.1038/126274a0.
60. Chikazumi S. Physics of Magnetism // Oxford University Press. New York, 2009.
61. Stoner E.C., Wohlfarth E.P., Stoner A.E.C., Wohlfarth E.P. A Mechanism of Magnetic Hysteresis in Heterogeneous Alloys // Philos. Trans. R. Soc. A Math. Phys. Eng. Sci. 1948. Vol. 240, № 826. P. 599–642 DOI:10.1098/rsta.1948.0007.
62. Gubin S.P., Koksharov Y.A., Khomutov G.B., Yurkov G.Y. Magnetic nanoparticles: preparation, structure and properties // Russ. Chem. Rev. 2005. Vol. 74, № 6. P. 489–520 DOI:10.1070/RC2005v074n06ABEH000897.
63. Peschany S.E., Usov N.A. Theoretical hysteresis loops for single-domain particles with cubic anisotropy // J. Magn. Magn. Mater. 1997. Vol. 174, № 3. P. 247–260 DOI:10.1016/S0304-8853(97)00180-7.
64. Kodama R.H., Berkowitz A.E., McNiff E.J., Foner S. Surface spin disorder in NiFe2O4 nanoparticles // Phys. Rev. Lett. 1996. Vol. 77, № 2. P. 394–397 DOI:10.1103/PhysRevLett.77.394.
65. Cabreira Gomes R., G da Silva F., Silva T.-Q., Gomide G., Pilati V., Aquino R., Geshev J., Perzynski R., Depeyrot J. Magnetic irreversibility and saturation criteria in ultrasmall bi-magnetic nanoparticles // J. Alloys Compd. Elsevier B.V., 2020. Vol. 824. P. 153646 DOI:10.1016/j.jallcom.2020.153646.
66. Salazar-Alvarez G., Qin J., Šepelák V., Bergmann I., Vasilakaki M., Trohidou K.N., Ardisson J.D., Macedo W.A.A., Mikhaylova M., Muhammed M., Baró M.D., Nogués J. Cubic versus spherical magnetic nanoparticles: The role of surface anisotropy // J. Am. Chem. Soc. 2008. Vol. 130, № 40. P. 13234–13239 DOI:10.1021/ja0768744.
67. Skomski R., Coey J.M.D.D. Giant energy product in nanostructured two-phase magnets // Phys. Rev. B. 1993. Vol. 48, № 21. P. 15812–15816 DOI:10.1103/PhysRevB.48.15812.
68. López-Ortega A., Estrader M., Salazar-Alvarez G., Roca A.G., Nogués J. Applications of exchange coupled bi-magnetic hard/soft and soft/hard magnetic

core/shell nanoparticles // Phys. Rep. Elsevier B.V., 2015. Vol. 553. P. 1–32 DOI:10.1016/j.physrep.2014.09.007.

69. Skumryev V., Stoyanov S., Zhang Y., Hadjipanayis G., Givord D., Nogués J. Beating the superparamagnetic limit with exchange bias // Nature. 2003. Vol. 423, № 6942. P. 850–853 DOI:10.1038/nature01687.
70. Hasz K., Ijiri Y., Krycka K.L., Borchers J.A., Booth R.A., Oberdick S., Majetich S.A. Particle moment canting in CoFe2 O4 nanoparticles // Phys. Rev. B - Condens. Matter Mater. Phys. 2014. Vol. 90, № 18. P. 1–5 DOI:10.1103/PhysRevB.90.180405.
71. Oberdick S.D., Abdelgawad A., Moya C., Mesbahi-Vasey S., Kepaptsoglou D., Lazarov V.K., Evans R.F.L., Meilak D., Skoropata E., Van Lierop J., Hunt-Isaak I., Pan H., Ijiri Y., Krycka K.L., Borchers J.A., Majetich S.A. Spin canting across core/shell Fe3O4/MnxFe3-xO4 nanoparticles // Sci. Rep. 2018. Vol. 8, № 1. P. 3425 DOI:10.1038/s41598-018-21626-0.
72. Dutta P., Pal S., Seehra M.S., Shah N., Huffman G.P. Size dependence of magnetic parameters and surface disorder in magnetite nanoparticles // J. Appl. Phys. 2009. Vol. 105, № 7. P. 10–13 DOI:10.1063/1.3055272.
73. Krycka K.L., Booth R.A., Hogg C.R., Ijiri Y., Borchers J.A., Chen W.C., Watson S.M., Laver M., Gentile T.R., Dedon L.R., Harris S., Rhyne J.J., Majetich S.A. Core-shell magnetic morphology of structurally uniform magnetite nanoparticles // Phys. Rev. Lett. 2010. Vol. 104, № 20. P. 2–5 DOI:10.1103/PhysRevLett.104.207203.
74. Chen J.P., Sorensen C.M., Klabunde K.J., Hadjipanayis G.C., Devlin E., Kostikas A. Size-dependent magnetic properties of MnFe2O4 fine particles synthesized by coprecipitation // Phys. Rev. B. 1996. Vol. 54, № 13. P. 9288–9296 DOI:10.1103/PhysRevB.54.9288.
75. Köhler T., Feoktystov A., Petracic O., Kentzinger E., Bhatnagar-Schöffmann T., Feygenson M., Nandakumaran N., Landers J., Wende H., Cervellino A., Rücker U., Kovács A., Dunin-Borkowski R.E., Brückel T. Mechanism of magnetization reduction in iron oxide nanoparticles // Nanoscale. 2021. Vol. 13, № 14. P. 6965–

6976 DOI:10.1039/d0nr08615k.

76. Unni M., Uhl A.M., Savliwala S., Savitzky B.H., Dhavalikar R., Garraud N., Arnold D.P., Kourkoutis L.F., Andrew J.S., Rinaldi C. Thermal Decomposition Synthesis of Iron Oxide Nanoparticles with Diminished Magnetic Dead Layer by Controlled Addition of Oxygen // ACS Nano. 2017. Vol. 11, № 2. P. 2284–2303 DOI:10.1021/acsnano.7b00609.
77. Morrish A.H. The Physical Principles of Magnetism // Wiley-IEEE Press. Piscataway: IEEE Press, 1965. Vol. 1, № 1. 1–700 p. DOI:10.1002/9780470546581.
78. Peddis D., Cannas C., Piccaluga G., Agostinelli E., Fiorani D. Spin-glass-like freezing and enhanced magnetization in ultra-small CoFe 2 O 4 nanoparticles // Nanotechnology. 2010. Vol. 21, № 12. P. 125705 DOI:10.1088/0957-4484/21/12/125705.
79. Zákutná D., NiŽňanský D., Barnsley L.C., Babcock E., Salhi Z., Feoktystov A., Honecker D., Disch S. Field Dependence of Magnetic Disorder in Nanoparticles // Phys. Rev. X. 2020. Vol. 10, № 3 DOI:10.1103/PhysRevX.10.031019.
80. Ali M., Adie P., Marrows C.H., Greig D., Hickey B.J., Stamps R.L. Exchange bias using a spin glass // Nat. Mater. 2007. Vol. 6, № 1. P. 70–75 DOI:10.1038/nmat1809.
81. Phan M.H.M.-H., Alonso J., Khurshid H., Lampen-Kelley P., Chandra S., Repa K.S.K.S., Nemati Z., Das R., Iglesias Ó., Srikanth H. Exchange bias effects in iron oxide-based nanoparticle systems // Nanomaterials. 2016. Vol. 6, № 11. P. 1–31 DOI:10.3390/nano6110221.
82. Peddis D., Cannas C., Piccaluga G., Agostinelli E., Fiorani D. Spin-glass-like freezing and enhanced magnetization in ultra-small CoFe2O4 nanoparticles. // Nanotechnology. 2010. Vol. 21, № 12. P. 125705 DOI:10.1088/0957-4484/21/12/125705.
83. Negi D.S., Sharona H., Bhat U., Palchoudhury S., Gupta A., Datta R. Surface spin canting in F e3 O4 and CoF e2 O4 nanoparticles probed by high-resolution electron energy loss spectroscopy // Phys. Rev. B. 2017. Vol. 95, № 17. P. 1–10

DOI:10.1103/PhysRevB.95.174444.

84. Moon S.H., Noh S.H., Lee J.H., Shin T.H., Lim Y., Cheon J. Ultrathin Interface Regime of Core–Shell Magnetic Nanoparticles for Effective Magnetism Tailoring // Nano Lett. 2017. Vol. 17, № 2. P. 800–804 DOI:10.1021/acs.nanolett.6b04016.
85. Brown W.F. Thermal fluctuations of a single-domain particle // Phys. Rev. 1963. Vol. 130, № 5. P. 1677–1686 DOI:10.1103/PhysRev.130.1677.
86. Jeun M., Kim Y.J., Park K.H., Paek S.H., Bae S. Physical Contribution of Néel and Brown Relaxation to Interpreting Intracellular Hyperthermia Characteristics Using Superparamagnetic Nanofluids. 2013. Vol. 13, № 8. P. 5719–5725 DOI:10.1166/jnn.2013.7524.
87. Dormann J.L., Bessais L., Fiorani D. A dynamic study of small interacting particles: superparamagnetic model and spin-glass laws // J. Phys. C Solid State Phys. 1988. Vol. 21, № 10. P. 2015 DOI:10.1088/0022-3719/21/10/019.
88. Hansen M.F.F., Mørup S. Estimation of blocking temperatures from ZFC/FC curves // J. Magn. Magn. Mater. 1999. Vol. 203, № 1–3. P. 214–216 DOI:10.1016/S0304-8853(99)00238-3.
89. Concas G., Congiu F., Muscas G., Peddis D. Determination of Blocking Temperature in Magnetization and Mössbauer Time Scale: A Functional Form Approach // J. Phys. Chem. C. 2017. Vol. 121, № 30. P. 16541–16548 DOI:10.1021/acs.jpcc.7b01748.
90. Chantrell R., Popplewell J., Charles S. Measurements of particle size distribution parameters in ferrofluids // IEEE Trans. Magn. 1978. Vol. 14, № 5. P. 975–977 DOI:10.1109/TMAG.1978.1059918.
91. Moya C., Iglesias Ó., Batlle X., Labarta A. Quantification of Dipolar Interactions in Fe3-xO4 Nanoparticles // J. Phys. Chem. C. 2015. Vol. 119, № 42. P. 24142–24148 DOI:10.1021/acs.jpcc.5b07516.
92. Bender P., Bogart L.K., Posth O., Szczerba W., Rogers S.E., Castro A., Nilsson L., Zeng L.J., Sugunan A., Sommertune J., Fornara A., González-Alonso D., Fernández Barquín L., Johansson C. Structural and magnetic properties of multi-

core nanoparticles analysed using a generalised numerical inversion method // Sci. Rep. Nature Publishing Group, 2017. Vol. 7, № March. P. 1–14 DOI:10.1038/srep45990.

93. Bender P., Balceris C., Ludwig F., Posth O., Bogart L.K., Szczerba W., Castro A., Nilsson L., Costo R., Gavilán H., González-Alonso D., Pedro I. De, Barquin L.F., Johansson C. Distribution functions of magnetic nanoparticles determined by a numerical inversion method // New J. Phys. IOP Publishing, 2017. Vol. 19, № 7 DOI:10.1088/1367-2630/aa73b4.
94. Van Rijssel J., Kuipers B.W.M., Erné B.H. Non-regularized inversion method from light scattering applied to ferrofluid magnetization curves for magnetic size distribution analysis // J. Magn. Magn. Mater. Elsevier, 2014. Vol. 353. P. 110–115 DOI:10.1016/j.jmmm.2013.10.025.
95. Xi H., Gao K.-Z., Shi Y., Xue S. Precessional dynamics of single-domain magnetic nanoparticles driven by small ac magnetic fields // J. Phys. D. Appl. Phys. 2006. Vol. 39, № 22. P. 4746–4752 DOI:10.1088/0022-3727/39/22/002.
96. Bruvera I.J., Mendoza Zélis P., Pilar Calatayud M., Goya G.F., Sánchez F.H. Determination of the blocking temperature of magnetic nanoparticles: The good, the bad, and the ugly // J. Appl. Phys. 2015. Vol. 118, № 18. P. 184304 DOI:10.1063/1.4935484.
97. Suber L., Peddis D. Approaches to Synthesis and Characterization of Spherical and Anisometric Metal Oxide Magnetic Nanomaterials // ChemInform. Weinheim, Germany: Wiley-VCH Verlag GmbH & Co. KGaA, 2011. Vol. 4, № 40. P. no-no DOI:10.1002/chin.201140196.
98. El-Hilo M., O'Grady K., Chantrell R.W. Susceptibility phenomena in a fine particle system. I. Concentration dependence of the peak // J. Magn. Magn. Mater. 1992. Vol. 114, № 3. P. 295–306 DOI:10.1016/0304-8853(92)90272-P.
99. Gittleman J.I., Abeles B., Bozowski S. Superparamagnetism and relaxation effects in granular Ni-SiO2 and Ni-Al2O3 films // Phys. Rev. B. 1974. Vol. 9, № 9. P. 3891–3897 DOI:10.1103/PhysRevB.9.3891.
100. Livesey K.L., Ruta S., Anderson N.R., Baldomir D., Chantrell R.W., Serantes D.

Beyond the blocking model to fit nanoparticle ZFC/FC magnetisation curves // Sci. Rep. Springer US, 2018. Vol. 8, № 1. P. 1–9 DOI:10.1038/s41598-018-29501-8.

101. Cullity B.D., Graham C.D. Introduction to Magnetic Materials // Materials Today. Hoboken, NJ, USA: John Wiley & Sons, Inc., 2008. Vol. 12, № 3. 45 p. DOI:10.1002/9780470386323.

102. Micha J.S., Dieny B., Régnard J.R., Jacquot J.F., Sort J. Estimation of the Co nanoparticles size by magnetic measurements in Co/SiO2 discontinuous multilayers // J. Magn. Magn. Mater. 2004. Vol. 272–276, № SUPPL. 1. P. 2003–2004 DOI:10.1016/j.jmmm.2003.12.268.

103. Goya G.F., Berquó T.S., Fonseca F.C., Morales M.P. Static and dynamic magnetic properties of spherical magnetite nanoparticles // J. Appl. Phys. 2003. Vol. 94, № 5. P. 3520–3528 DOI:10.1063/1.1599959.

104. Muscas G., Concas G., Laureti S., Testa A.M., Mathieu R., De Toro J.A., Cannas C., Musinu A., Novak M.A., Sangregorio C., Lee S.S., Peddis D. The interplay between single particle anisotropy and interparticle interactions in ensembles of magnetic nanoparticles // Phys. Chem. Chem. Phys. Royal Society of Chemistry, 2018. Vol. 20, № 45. P. 28634–28643 DOI:10.1039/c8cp03934h.

105. Sánchez E.H., Vasilakaki M., Lee S.S., Normile P.S., Muscas G., Murgia M., Andersson M.S., Singh G., Mathieu R., Nordblad P., Ricci P.C., Peddis D., Trohidou K.N., Nogués J., De Toro J.A. Simultaneous individual and dipolar collective properties in binary assemblies of magnetic nanoparticles. 2019. P. 1–43.

106. Chantrell R.W., El-Hilo M., O’Grady K. Spin-Glass behaviour in fine particle system // IEEE Trans. Magn. 1991. Vol. 27, № 4. P. 3570–3578.

107. Peddis D., Mansilla M. V, Mørup S., Cannas C., Musinu a, Piccaluga G., D’Orazio F., Lucari F., Fiorani D. Spin-canting and magnetic anisotropy in ultrasmall CoFe2O4 nanoparticles. // J. Phys. Chem. B. 2008. Vol. 112, № 29. P. 8507–8513 DOI:10.1021/jp8016634.

108. Mørup S., Bødker F., Hendriksen P. V., Linderoth S. Spin-glass-like ordering of

the magnetic moments of interacting nanosized maghemite particles // Phys. Rev. B. 1995. Vol. 52, № 1. P. 287–294 DOI:10.1103/PhysRevB.52.287.

109. Bleaney B., Hull R.A. The effective susceptibility of a paramagnetic powder // Proc. R. Soc. London. Ser. A. Math. Phys. Sci. 1941. Vol. 178, № 972. P. 86–92 DOI:10.1098/rspa.1941.0045.

110. Normile P.S., Andersson M.S., Mathieu R., Lee S.S., Singh G., De Toro J.A. Demagnetization effects in dense nanoparticle assemblies // Appl. Phys. Lett. 2016. Vol. 109, № 15 DOI:10.1063/1.4964517.

111. Maltoni P., Sarkar T., Barucca G., Varvaro G., Locardi F., Peddis D., Mathieu R. Tuning the magnetic properties of hard-soft SrFe12O19/CoFe2O4 nanostructures via composition/interphase coupling // J. Phys. Chem. C. 2021. Vol. 125, № 10. P. 5927–5936 DOI:10.1021/acs.jpcc.1c00355.

112. Bedanta S., Kleemann W., Petracic O., Kleemann W. Supermagnetism // J. Phys. D. Appl. Phys. Elsevier, 2009. Vol. 42, № 1. P. 013001 DOI:10.1088/0022-3727/42/1/013001.

113. El-Hilo M., Chantrell R.W., O'Grady K. A model of interaction effects in granular magnetic solids // J. Appl. Phys. 1998. Vol. 84, № 9. P. 5114–5122 DOI:10.1063/1.368761.

114. Nordblad P. Competing interaction in magnets: The root of ordered disorder or only frustration? // Phys. Scr. 2013. Vol. 88, № 5 DOI:10.1088/0031-8949/88/05/058301.

115. McCloy J.S. Spin and Ferroic Glasses // Handbook ofGlass. 2019. P. 687–718 DOI:10.1007/978-3-319-93728-1_20.

116. Peddis D., Trohidou K.N., Vasilakaki M., Margaris G., Bellusci M., Varsano F., Hudl M., Yaacoub N., Fiorani D., Nordblad P., Mathieu R. Memory and superposition in a superspin glass // Sci. Rep. Nature Publishing Group UK, 2021. Vol. 11, № 1. P. 1–8 DOI:10.1038/s41598-021-87345-1.

117. Anthony R. West. Solid State Chemistry and its Applications // Solid State Chem and Its Appl / ed. Wiley J., Sons. New York, 1984 DOI:10.1016/0254-0584(84)90072-5.

118. Coey J.M.D. Magnetism and Magnetic Materials. New York: Cambrige university press, 2010. 614 p. DOI:10.1017/CBO9780511845000.

119. Yafet Y., Kittel C. Antiferromagnetic Arrangements in Ferrites // Phys. Rev. 1952. Vol. 87, № 2. P. 290–294 DOI:10.1103/PhysRev.87.290.

120. Sanchez-Lievanos K.R., Stair J.L., Knowles K.E. Cation Distribution in Spinel Ferrite Nanocrystals: Characterization, Impact on their Physical Properties, and Opportunities for Synthetic Control // Inorg. Chem. 2021. Vol. 60, № 7. P. 4291–4305 DOI:10.1021/acs.inorgchem.1c00040.

121. Ade R., Chen Y.S., Huang C.-H., Lin J.G. Large magnetic anisotropy in highly strained epitaxial MgFe 2 O 4 thin films // J. Appl. Phys. AIP Publishing LLC, 2020. Vol. 127, № 11. P. 113904 DOI:10.1063/5.0003542.

122. Frison R., Cernuto G., Cervellino A., Zaharko O., Colonna G.M., Guagliardi A., Masciocchi N. Magnetite–Maghemite Nanoparticles in the 5–15 nm Range: Correlating the Core–Shell Composition and the Surface Structure to the Magnetic Properties. A Total Scattering Study. // Chem. Mater. 2013. Vol. 25, № 23. P. 4820–4827 DOI:10.1021/cm403360f.

123. Baaziz W., Pichon B.P., Fleutot S., Liu Y., Lefevre C., Greneche J.M., Toumi M., Mhiri T., Begin-Colin S. Magnetic iron oxide nanoparticles: Reproducible tuning of the size and nanosized-dependent composition, defects, and spin canting // J. Phys. Chem. C. 2014. Vol. 118, № 7. P. 3795–3810 DOI:10.1021/jp411481p.

124. Bogart L.K., Blanco-Andujar C., Pankhurst Q.A. Environmental oxidative aging of iron oxide nanoparticles // Appl. Phys. Lett. 2018. Vol. 113, № 13. P. 133701 DOI:10.1063/1.5050217.

125. Schwaminger S.P., Syhr C., Berensmeier S. Controlled Synthesis of Magnetic Iron Oxide Nanoparticles: Magnetite or Maghemite? // Crystals. 2020. Vol. 10, № 3. P. 214 DOI:10.3390/cryst10030214.

126. Moyer J.A., Gao R., Schiffer P., Martin L.W. Epitaxial growth of highly-crystalline spinel ferrite thin films on perovskite substrates for all-oxide devices // Sci. Rep. Nature Publishing Group, 2015. Vol. 5, № October 2014. P. 1–11

DOI:10.1038/srep10363.

127. Fabris F., Lima E., Quinteros C., Neñer L., Granada M., Sirena M., Zysler R.D., Troiani H.E., Leborán V., Rivadulla F., Winkler E.L. Tunnel Magnetoresistance in Self-Assemblies of Exchange-Coupled Core/Shell Nanoparticles // Phys. Rev. Appl. American Physical Society, 2019. Vol. 11, № 5. P. 054089 DOI:10.1103/PhysRevApplied.11.054089.
128. Maldonado A.C.M., Winkler E.L., Raineri M., Córdova A.T., Rodríguez L.M., Troiani H.E., Pisciotti M.L.M., Mansilla M.V., Tobia D., Nadal M.S., Torres T.E., De Biasi E., Ramos C.A., Goya G.F., Zysler R.D., Lima E. Free-Radical Formation by the Peroxidase-Like Catalytic Activity of MFe2O4 (M = Fe, Ni, and Mn) Nanoparticles // J. Phys. Chem. C. 2019. Vol. 123, № 33. P. 20617–20627 DOI:10.1021/acs.jpcc.9b05371.
129. Walz F. The Verwey transition - a topical review // J. Phys. Condens. Matter. 2002. Vol. 14, № 12. P. R285–R340 DOI:10.1088/0953-8984/14/12/203.
130. Sharifi Dehsari H., Ksenofontov V., Möller A., Jakob G., Asadi K. Determining Magnetite/Maghemite Composition and Core-Shell Nanostructure from Magnetization Curve for Iron Oxide Nanoparticles // J. Phys. Chem. C. 2018. Vol. 122, № 49. P. 28292–28301 DOI:10.1021/acs.jpcc.8b06927.
131. Néel, Louis. Propriétés magnétiques des ferrites ; ferrimagnétisme et antiferromagnétisme // Ann. Phys. (Paris). 1948. Vol. 12, № 3. P. 137–198 DOI:10.1051/anphys/194812030137.
132. Barrera G., Coisson M., Celegato F., Raghuvanshi S., Mazaleyrat F., Kane S.N.N., Tiberto P. Cation distribution effect on static and dynamic magnetic properties of Co 1-x Zn x Fe 2 O 4 ferrite powders // J. Magn. Magn. Mater. Elsevier B.V., 2018. Vol. 456, № February. P. 372–380 DOI:10.1016/j.jmmm.2018.02.072.
133. Pilania G., Kocevski V., Valdez J.A., Kreller C.R., Uberuaga B.P. Prediction of structure and cation ordering in an ordered normal-inverse double spinel // Commun. Mater. Springer US, 2020. Vol. 1, № 1. P. 1–11 DOI:10.1038/s43246-020-00082-2.

134. Gómez-Polo C., Recarte V., Cervera L., Beato-López J.J., López-García J., Rodríguez-Velamazán J.A., Ugarte M.D., Mendonça E.C., Duque J.G.S. Tailoring the structural and magnetic properties of Co-Zn nanosized ferrites for hyperthermia applications // J. Magn. Magn. Mater. Elsevier B.V., 2018. Vol. 465, № March. P. 211–219 DOI:10.1016/j.jmmm.2018.05.051.

135. Cannas C., Musinu A., Piccaluga G., Fiorani D., Peddis D., Rasmussen H.K., Mørup S. Magnetic properties of cobalt ferrite–silica nanocomposites prepared by a sol-gel autocombustion technique // J. Chem. Phys. 2006. Vol. 125, № 16. P. 164714 DOI:10.1063/1.2354475.

136. Freire R.M., Palma J.L., Michea S., Ramirez R., Baltazar S.E., Denardin J.C. Coercivity dependence of cation distribution in Co-based spinel: Correlating theory and experiments // Inorg. Chem. Front. Royal Society of Chemistry, 2021. Vol. 8, № 2. P. 433–443 DOI:10.1039/d0qi01129k.

137. Ferreiro-Vila E., Iglesias L., Lucas del Pozo I., Varela-Dominguez N., Bui C.T., Rivas-Murias B., Vila-Fungueiriño J.M., Jimenez-Cavero P., Magen C., Morellon L., Pardo V., Rivadulla F. Apparent auxetic to non-auxetic crossover driven by Co 2+ redistribution in CoFe 2 O 4 thin films // APL Mater. 2019. Vol. 7, № 3. P. 031109 DOI:10.1063/1.5087559.

138. Muscas G., Yaacoub N., Concas G., Sayed F., Sayed Hassan R., Greneche J.M., Cannas C., Musinu A., Foglietti V., Casciardi S., Sangregorio C., Peddis D. Evolution of the magnetic structure with chemical composition in spinel iron oxide nanoparticles // Nanoscale. Royal Society of Chemistry, 2015. Vol. 7, № 32. P. 13576–13585 DOI:10.1039/C5NR02723C.

139. Mameli V., Musinu A., Ardu A., Ennas G., Peddis D., Niznansky D., Sangregorio C., Innocenti C., Thanh N.T.K., Cannas C. Studying the effect of Zn-substitution on the magnetic and hyperthermic properties of cobalt ferrite nanoparticles // Nanoscale. Royal Society of Chemistry, 2016. Vol. 8, № 19. P. 10124–10137 DOI:10.1039/C6NR01303A.

140. Peddis D., Cannas C., Musinu A., Ardu A., Orrù F., Fiorani D., Laureti S., Rinaldi D., Muscas G., Concas G., Piccaluga G. Beyond the Effect of Particle

Size: Influence of CoFe2O4 Nanoparticle Arrangements on Magnetic Properties // Chem. Mater. 2013. Vol. 25, № 10. P. 2005–2013 DOI:10.1021/cm303352r.

141. Li D., Yun H., Diroll B.T., Doan-Nguyen V.V.T., Kikkawa J.M., Murray C.B. Synthesis and Size-Selective Precipitation of Monodisperse Nonstoichiometric M x Fe 3– x O 4 (M = Mn, Co) Nanocrystals and Their DC and AC Magnetic Properties // Chem. Mater. 2016. Vol. 28, № 2. P. 480–489 DOI:10.1021/acs.chemmater.5b03280.

142. Cabrera L.I., Somoza Á., Marco J.F., Serna C.J., Puerto Morales M. Synthesis and surface modification of uniform MFe 2O 4 (M = Fe, Mn, and Co) nanoparticles with tunable sizes and functionalities // J. Nanoparticle Res. 2012. Vol. 14, № 6 DOI:10.1007/s11051-012-0873-x.

143. Pereira C., Pereira A.M., Fernandes C., Rocha M., Mendes R., Fernández-García M.P., Guedes A., Tavares P.B., Grenéche J.M., Araújo J.P., Freire C. Superparamagnetic MFe 2O 4 (M = Fe, Co, Mn) nanoparticles: Tuning the particle size and magnetic properties through a novel one-step coprecipitation route // Chem. Mater. 2012 DOI:10.1021/cm300301c.

144. Concas G., Spano G., Cannas C., Musinu A., Peddis D., Piccaluga G. Inversion degree and saturation magnetization of different nanocrystalline cobalt ferrites // J. Magn. Magn. Mater. 2009. Vol. 321, № 12. P. 1893–1897 DOI:10.1016/j.jmmm.2008.12.001.

145. Jang J.T., Nah H., Lee J.-H.H., Moon S.H., Kim M.G., Cheon J. Critical enhancements of MRI contrast and hyperthermic effects by dopant-controlled magnetic nanoparticles // Angew. Chemie Int. Ed. 2009. Vol. 48, № 7. P. 1234–1238 DOI:10.1002/anie.200805149.

146. Lee J.-H.H., Huh Y.-M.M., Jun Y.W., Seo J.W., Jang J.T., Song H.-T.T., Kim S., Cho E.-J.J., Yoon H.-G.G., Suh J.-S.S., Cheon J. Artificially engineered magnetic nanoparticles for ultra-sensitive molecular imaging // Nat. Med. 2007. Vol. 13, № 1. P. 95–99 DOI:10.1038/nm1467.

147. Albino M., Fantechi E., Innocenti C., López-Ortega A., Bonanni V., Campo G., Pineider F., Gurioli M., Arosio P., Orlando T., Bertoni G., de Julián Fernández

C., Lascialfari A., Sangregorio C. Role of Zn 2+ Substitution on the Magnetic, Hyperthermic, and Relaxometric Properties of Cobalt Ferrite Nanoparticles // J. Phys. Chem. C. 2019. Vol. 123, № 10. P. 6148–6157 DOI:10.1021/acs.jpcc.8b10998.

148. Omelyanchik A., Singh G., Volochaev M., Sokolov A., Rodionova V., Peddis D. Tunable magnetic properties of Ni-doped CoFe2O4 nanoparticles prepared by the sol–gel citrate self-combustion method // J. Magn. Magn. Mater. Elsevier B.V., 2019. Vol. 476. P. 387–391 DOI:10.1016/j.jmmm.2018.12.064.

149. Omelyanchik A., Levada K., Pshenichnikov S., Abdolrahim M., Baricic M., Kapitunova A., Galieva A., Sukhikh S., Astakhova L., Antipov S., Fabiano B., Peddis D., Rodionova V. Green Synthesis of Co-Zn Spinel Ferrite Nanoparticles: Magnetic and Intrinsic Antimicrobial Properties // Materials (Basel). 2020. Vol. 13, № 21. P. 5014 DOI:10.3390/ma13215014.

150. Liu X., Liu J., Zhang S., Nan Z., Shi Q. Structural, Magnetic, and Thermodynamic Evolutions of Zn-Doped Fe3O4 Nanoparticles Synthesized Using a One-Step Solvothermal Method // J. Phys. Chem. C. 2016. Vol. 120, № 2. P. 1328–1341 DOI:10.1021/acs.jpcc.5b10618.

151. Petrova E., Kotsikau D., Pankov V. Structural characterization and magnetic properties of sol-gel derived ZnxFe3-xO4 nanoparticles // J. Magn. Magn. Mater. Elsevier, 2015. Vol. 378. P. 429–435 DOI:10.1016/j.jmmm.2014.11.076.

152. Cheng Y.H., Li L.Y., Wang W.H., Liu H., Ren S.W., Cui X.Y., Zheng R.K. Tunable electrical and magnetic properties of half-metallic ZnxFe3−xO4 from first principles // Phys. Chem. Chem. Phys. 2011. Vol. 13, № 48. P. 21243 DOI:10.1039/c1cp22463h.

153. Pilati V., Cabreira Gomes R., Gomide G., Coppola P., Silva F.G., Paula F.L.O.O., Perzynski R., Goya G.F., Aquino R., Depeyrot J. Core/Shell Nanoparticles of Non-Stoichiometric Zn–Mn and Zn–Co Ferrites as Thermosensitive Heat Sources for Magnetic Fluid Hyperthermia // J. Phys. Chem. C. 2018. Vol. 122, № 5. P. 3028–3038 DOI:10.1021/acs.jpcc.7b11014.

154. Tovstolytkin A.I., Kulyk M.M., Kalita V.M., Ryabchenko S.M., Zamorskyi

V.O., Fedorchuk O.P., Solopan S.O., Belous A.G. Nickel-zinc spinel nanoferrites: Magnetic characterization and prospects of the use in self-controlled magnetic hyperthermia // J. Magn. Magn. Mater. Elsevier B.V., 2019. Vol. 473. P. 422–427 DOI:10.1016/j.jmmm.2018.10.075.

155. Viñas S.L., Simeonidis K., Li Z.-A., Ma Z., Myrovali E., Makridis A., Sakellari D., Angelakeris M., Wiedwald U., Spasova M., Farle M. Tuning the magnetism of ferrite nanoparticles // J. Magn. Magn. Mater. 2016. Vol. 415. P. 20–23 DOI:10.1016/j.jmmm.2016.02.098.
156. López-Ortega A., Lottini E., Fernández C.D.J., Sangregorio C. Exploring the Magnetic Properties of Cobalt-Ferrite Nanoparticles for the Development of a Rare-Earth-Free Permanent Magnet // Chem. Mater. 2015. Vol. 27, № 11. P. 4048–4056 DOI:10.1021/acs.chemmater.5b01034.
157. Jovanović S., Spreitzer M., Otoničar M., Jeon J.-H.H., Suvorov D. pH control of magnetic properties in precipitation-hydrothermal-derived CoFe2O4 // J. Alloys Compd. 2014. Vol. 589. P. 271–277 DOI:10.1016/j.jallcom.2013.11.217.
158. Solano E., Frontera C., Puig T., Obradors X., Ricart S., Ros J. Neutron and X-ray diffraction study of ferrite nanocrystals obtained by microwave-assisted growth. A structural comparison with the thermal synthetic route // J. Appl. Crystallogr. 2014. Vol. 47, № 1. P. 414–420 DOI:10.1107/S1600576713032895.
159. Lavorato G., Alzamora M., Contreras C., Burlandy G., Litterst F.J., Baggio-Saitovitch E. Internal Structure and Magnetic Properties in Cobalt Ferrite Nanoparticles: Influence of the Synthesis Method // Part. Part. Syst. Charact. 2019. Vol. 36, № 4. P. 1–11 DOI:10.1002/ppsc.201900061.
160. Šepelák V., Bergmann I., Feldhoff A., Heitjans P., Krumeich F., Menzel D., Litterst F.J., Campbell S.J., Becker K.D. Nanocrystalline nickel ferrite, NiFe2O4: Mechanosynthesis, nonequilibrium cation distribution, canted spin arrangement, and magnetic behavior // J. Phys. Chem. C. 2007. Vol. 111, № 13. P. 5026–5033 DOI:10.1021/jp067620s.
161. Lee J.-H., Jang J., Choi J., Moon S.H., Noh S.-H., Kim J.-G.J.-W.J.-G.J.-W., Kim J.-G.J.-W.J.-G.J.-W., Kim I.-S., Park K.I., Cheon J. Exchange-coupled

magnetic nanoparticles for efficient heat induction // Nat. Nanotechnol. Nature Publishing Group, 2011. Vol. 6, № 7. P. 418–422 DOI:10.1038/nnano.2011.95.

162. Noh S., Moon S.H., Shin T.-H., Lim Y., Cheon J. Recent advances of magneto-thermal capabilities of nanoparticles: From design principles to biomedical applications // Nano Today. Elsevier Ltd, 2017. Vol. 13. P. 61–76 DOI:10.1016/j.nantod.2017.02.006.
163. Vasilakaki M., Trohidou K.N., Nogués J. Enhanced magnetic properties in antiferromagnetic-core/ferrimagnetic-shell nanoparticles // Sci. Rep. 2015. Vol. 5, № April DOI:10.1038/srep09609.
164. Sanna Angotzi M., Mameli V., Cara C., Musinu A., Sangregorio C., Niznansky D., Xin H.L., Vejpravova J., Cannas C. Coupled hard–soft spinel ferrite-based core–shell nanoarchitectures: magnetic properties and heating abilities // Nanoscale Adv. Royal Society of Chemistry, 2020. Vol. 2, № 8. P. 3191–3201 DOI:10.1039/D0NA00134A.
165. López-Ortega A., Estrader M., Salazar-Alvarez G., Estradé S., Golosovsky I. V., Dumas R.K., Keavney D.J., Vasilakaki M., Trohidou K.N., Sort J., Peiró F., Suriñach S., Baró M.D., Nogués J. Strongly exchange coupled inverse ferrimagnetic soft/hard, MnxFe3−xO4/FexMn3−xO4, core/shell heterostructured nanoparticles // Nanoscale. 2012. Vol. 4, № 16. P. 5138 DOI:10.1039/c2nr30986f.
166. Yoon T.J., Lee H., Shao H., Weissleder R. Highly magnetic core-shell nanoparticles with a unique magnetization mechanism // Angew. Chemie - Int. Ed. 2011. Vol. 50, № 20. P. 4663–4666 DOI:10.1002/anie.201100101.
167. Sartori K., Cotin G., Bouillet C., Halté V., Bégin-Colin S., Choueikani F., Pichon B.P. Strong interfacial coupling through exchange interactions in soft/hard core–shell nanoparticles as a function of cationic distribution // Nanoscale. 2019. Vol. 11, № 27. P. 12946–12958 DOI:10.1039/c9nr02323b.
168. Lavorato G.C., Das R., Alonso Masa J., Phan M.-H., Srikanth H. Hybrid magnetic nanoparticles as efficient nanoheaters in biomedical applications // Nanoscale Adv. Royal Society of Chemistry, 2021. Vol. 3, № 4. P. 867–888

DOI:10.1039/D0NA00828A.

169. Vasilakaki M., Binns C., Trohidou K.N. Susceptibility losses in heating of magnetic core/shell nanoparticles for hyperthermia: a Monte Carlo study of shape and size effects // Nanoscale. 2015. Vol. 7, № 17. P. 7753–7762 DOI:10.1039/C4NR07576E.
170. Schärtl W. Current directions in core–shell nanoparticle design // Nanoscale. 2010. Vol. 2, № 6. P. 829 DOI:10.1039/c0nr00028k.
171. Gavrilov-Isaac V., Neveu S., Dupuis V., Taverna D., Gloter A., Cabuil V. Synthesis of Trimagnetic Multishell MnFe 2 O 4 @CoFe 2 O 4 @NiFe 2 O 4 Nanoparticles // Small. 2015. Vol. 11, № 22. P. 2614–2618 DOI:10.1002/smll.201402845.
172. Kim D.-H., Tamada Y., Ono T., Bader S.D., Rozhkova E.A., Novosad V. The Effect of Ligands on FePt–Fe 3 O 4 Core–Shell Magnetic Nanoparticles // J. Nanosci. Nanotechnol. 2014. Vol. 14, № 3. P. 2648–2652 DOI:10.1166/jnn.2014.8471.
173. Estrader M., López-Ortega A., Golosovsky I. V., Estradé S., Roca A.G., Salazar-Alvarez G., López-Conesa L., Tobia D., Winkler E., Ardisson J.D., Macedo W.A.A., Morphis A., Vasilakaki M., Trohidou K.N., Gukasov A., Mirebeau I., Makarova O.L., Zysler R.D., Peiró F., Baró M.D., Bergström L., Nogués J. Origin of the large dispersion of magnetic properties in nanostructured oxides: FexO/Fe3O4 nanoparticles as a case study // Nanoscale. Royal Society of Chemistry, 2015. Vol. 7, № 7. P. 3002–3015 DOI:10.1039/c4nr06351a.
174. Lavorato G., Winkler E., Rivas-Murias B., Rivadulla F. Thickness dependence of exchange coupling in epitaxial Fe3O4/CoFe2O4 soft/hard magnetic bilayers // Phys. Rev. B. 2016. Vol. 94. P. 054405 DOI:10.1103/PhysRevB.94.054405.
175. Noh S.H., Na W., Jang J.T., Lee J.-H.H., Lee E.J., Moon S.H., Lim Y., Shin J.-S.S., Cheon J. Nanoscale magnetism control via surface and exchange anisotropy for optimized ferrimagnetic hysteresis // Nano Lett. 2012. Vol. 12, № 7. P. 3716–3721 DOI:10.1021/nl301499u.
176. Polishchuk D., Nedelko N., Solopan S., Ślawska-Waniewska A., Zamorskyi V.,

Tovstolytkin A., Belous A. Profound Interfacial Effects in CoFe2O4/Fe3O4 and Fe3O4/CoFe2O4 Core/Shell Nanoparticles // Nanoscale Res. Lett. 2018. Vol. 13, № 1. P. 67 DOI:10.1186/s11671-018-2481-x.

177. Song Q., Zhang Z.J. Controlled synthesis and magnetic properties of bimagnetic spinel ferrite CoFe 2O 4 and MnFe 2O 4 nanocrystals with core-shell architecture // J. Am. Chem. Soc. 2012. Vol. 134, № 24. P. 10182–10190 DOI:10.1021/ja302856z.

178. Zhang Q., Castellanos-Rubio I., Munshi R., Orue I., Pelaz B., Gries K.I., Parak W.J., Del Pino P., Pralle A. Model Driven Optimization of Magnetic Anisotropy of Exchange-Coupled Core-Shell Ferrite Nanoparticles for Maximal Hysteretic Loss // Chem. Mater. 2015. Vol. 27, № 21. P. 7380–7387 DOI:10.1021/acs.chemmater.5b03261.

179. Trohidou K.N., Soukoulis C.M., Kostikas A., Hadjipanayis G. Size dependence of coercivity of small magnetic particles // J. Magn. Magn. Mater. 1992. Vol. 104–107, № PART 3. P. 1587–1588 DOI:10.1016/0304-8853(92)91465-6.

180. Omelyanchik A., Villa S., Vasilakaki M., Singh G., Ferretti A.M., Ponti A., Canepa F., Margaris G., Trohidou K.N., Peddis D. Interplay between inter- and intraparticle interactions in bi-magnetic core/shell nanoparticles // Nanoscale Adv. Royal Society of Chemistry, 2021. Vol. 3, № 24. P. 6912–6924 DOI:10.1039/D1NA00312G.

181. Lottini E., López-Ortega A., Bertoni G., Turner S., Meledina M., Tendeloo G. Van, De Julián Fernández C., Sangregorio C. Strongly Exchange Coupled Core|Shell Nanoparticles with High Magnetic Anisotropy: A Strategy toward Rare-Earth-Free Permanent Magnets // Chem. Mater. 2016. Vol. 28, № 12. P. 4214–4222 DOI:10.1021/acs.chemmater.6b00623.

182. Laureti S., Del Bianco L., Detlefs B., Agostinelli E., Foglietti V., Peddis D., Testa A.M., Varvaro G., Fiorani D. Interface exchange coupling in a CoPt/NiO bilayer // Thin Solid Films. Elsevier B.V., 2013. Vol. 543. P. 162–166 DOI:10.1016/j.tsf.2012.12.115.

183. Yang M. Da, Ho C.H., Ruta S., Chantrell R., Krycka K., Hovorka O., Chen F.R.,

Lai P.S., Lai C.H. Magnetic Interaction of Multifunctional Core–Shell Nanoparticles for Highly Effective Theranostics // Adv. Mater. 2018. Vol. 30, № 50. P. 1802444 DOI:10.1002/adma.201802444.

184. Fabris F., Lohr J., Lima E., de Almeida A.A., Troiani H.E., Rodríguez L.M., Vásquez Mansilla M., Aguirre M.H., Goya G.F., Rinaldi D., Ghirri A., Peddis D., Fiorani D., Zysler R.D., De Biasi E., Winkler E.L. Adjusting the Néel relaxation time of Fe 3 O 4 /Zn x Co 1− x Fe 2 O 4 core/shell nanoparticles for optimal heat generation in magnetic hyperthermia // Nanotechnology. IOP Publishing, 2021. Vol. 32, № 6. P. 065703 DOI:10.1088/1361-6528/abc386.
185. Baaziz W., Pichon B.P., Lefevre C., Ulhaq-Bouillet C., Greneche J.M., Toumi M., Mhiri T., Bégin-Colin S. High exchange bias in Fe3-δO4@CoO core shell nanoparticles synthesized by a one-pot seed-mediated growth method // J. Phys. Chem. C. 2013. Vol. 117, № 21. P. 11436–11443 DOI:10.1021/jp402823h.
186. Lavorato G.C., Lima E., Tobia D., Fiorani D., Troiani H.E., Zysler R.D., Winkler E.L. Size effects in bimagnetic CoO/CoFe2O4 core/shell nanoparticles. // Nanotechnology. IOP Publishing, 2014. Vol. 25, № 35. P. 355704 DOI:10.1088/0957-4484/25/35/355704.
187. Sartori K., Choueikani F., Gloter A., Begin-Colin S., Taverna D., Pichon B.P. Room Temperature Blocked Magnetic Nanoparticles Based on Ferrite Promoted by a Three-Step Thermal Decomposition Process: rapid-communication // J. Am. Chem. Soc. American Chemical Society, 2019. Vol. 141, № 25. P. 9783–9787 DOI:10.1021/jacs.9b03965.
188. Margaris G., Trohidou K.N., Nogués J. Mesoscopic model for the simulation of large arrays of Bi-magnetic core/shell nanoparticles // Adv. Mater. 2012. Vol. 24, № 31. P. 4331–4336 DOI:10.1002/adma.201200615.
189. Massart R.R. Preparation of aqueous magnetic liquids in alkaline and acidic media // IEEE Trans. Magn. 1981. Vol. 17, № 2. P. 1247–1248 DOI:10.1109/TMAG.1981.1061188.
190. Omelyanchik A., da Silva F.G., Gomide G., Kozenkov I., Depeyrot J., Aquino R., Campos A.F.C., Fiorani D., Peddis D., Rodionova V., Jovanović S. Effect of

citric acid on the morpho-structural and magnetic properties of ultrasmall iron oxide nanoparticles // J. Alloys Compd. 2021. Vol. 883. P. 160779 DOI:10.1016/j.jallcom.2021.160779.

191. Sun S., Zeng H., Robinson D.B., Raoux S., Rice P.M., Wang S.X., Li G. Monodisperse MFe 2 O 4 (M = Fe, Co, Mn) Nanoparticles // J. Am. Chem. Soc. 2004. Vol. 126, № 1. P. 273–279 DOI:10.1021/ja0380852.

192. Omelyanchik A., Villa S., Singh G., Rodionova V., Laureti S., Canepa F., Peddis D. Magnetic Properties of Bi-Magnetic Core/Shell Nanoparticles: The Case of Thin Shells // Magnetochemistry. 2021. Vol. 7, № 11. P. 146 DOI:10.3390/magnetochemistry7110146.

193. Peddis D., Orrù F., Ardu A., Cannas C., Musinu A., Piccaluga G. Interparticle Interactions and Magnetic Anisotropy in Cobalt Ferrite Nanoparticles: Influence of Molecular Coating // Chem. Mater. 2012. Vol. 24, № 6. P. 1062–1071 DOI:10.1021/cm203280y.

194. Muscas G., Singh G., Glomm W.R., Mathieu R., Kumar P.A., Concas G., Agostinelli E., Peddis D. Tuning the size and shape of oxide nanoparticles by controlling oxygen content in the reaction environment: Morphological analysis by aspect maps // Chem. Mater. 2015. Vol. 27, № 6. P. 1982–1990 DOI:10.1021/cm5038815.

195. Sandler S.E., Fellows B.D., Mefford O.T., Thompson Mefford O. Best Practices for Characterization of Magnetic Nanoparticles for Biomedical Applications // Anal. Chem. 2019. Vol. 91, № 22. P. 14159–14169 DOI:10.1021/acs.analchem.9b03518.

196. Muscas G., Jovanovi S., Vukomanovi M., Spreitzer M., Peddis D., Jovanović S., Vukomanović M., Spreitzer M., Peddis D., Jovanovi S., Vukomanovi M., Spreitzer M., Peddis D. Zn-doped cobalt ferrite: Tuning the interactions by chemical composition // J. Alloys Compd. 2019. Vol. 796, № May. P. 203–209 DOI:10.1016/j.jallcom.2019.04.308.

197. Brown W.F. Theory of the Approach to Magnetic Saturation // Phys. Rev. 1940. Vol. 58, № 8. P. 736–743 DOI:10.1103/PhysRev.58.736.

198. Devi E.C., Soibam I. Law of Approach to Saturation in Mn–Zn Ferrite Nanoparticles // J. Supercond. Nov. Magn. Journal of Superconductivity and Novel Magnetism, 2019. Vol. 32, № 5. P. 1293–1298 DOI:10.1007/s10948-018-4823-4.

199. Komogortsev S. V., Iskhakov R.S. Law of approach to magnetic saturation in nanocrystalline and amorphous ferromagnets with improved transition behavior between power-law regimes // J. Magn. Magn. Mater. Elsevier B.V., 2017. Vol. 440, № December 2016. P. 213–216 DOI:10.1016/j.jmmm.2016.12.145.

200. Muscas G., Concas G., Cannas C., Musinu A., Ardu A., Orru F., Fiorani D., Laureti S., Rinaldi D., Piccaluga G., Peddis D. Magnetic Properties of Small Magnetite Nanocrystals // J. Phisical Chem. C. 2013. Vol. 114, № 44. P. 23378–23384.

201. Bertotti G. Hysteresis in Magnetism // Hysteresis in Magnetism. Elsevier, 1998. xiii–xvii p. DOI:10.1016/B978-0-12-093270-2.X5048-X.

202. Wohlfarth E.P. Relations between Different Modes of Acquisition of the Remanent Magnetization of Ferromagnetic Particles // J. Appl. Phys. 1958. Vol. 29, № 3. P. 595–596 DOI:10.1063/1.1723232.

203. Laureti S., Varvaro G., Testa A.M., Fiorani D., Agostinelli E., Piccaluga G., Musinu A., Ardu A., Peddis D. Magnetic interactions in silica coated nanoporous assemblies of CoFe 2 O 4 nanoparticles with cubic magnetic anisotropy // Nanotechnology. 2010. Vol. 21, № 31. P. 315701 DOI:10.1088/0957-4484/21/31/315701.

204. Kelly P.E., O’Grady K., Mayo P.I. Switching mechanisms in cobalt phosphorus thin films // International Magnetics Conference. IEEE, 1989. Vol. 25, № 5. P. HA5–HA5 DOI:10.1109/INTMAG.1989.690222.

205. Peddis D., Jonsson P.E., Varvaro G., Laureti S., Jönsson P.E.P.E., Laureti S., Varvaro G. Magnetic interactions: A tool to modify the magnetic properties of materials based on nanoparticles // Frontiers of Nanoscience / ed. Binns C. Oxford, UK: Elsevier B.V, 2014. Vol. 6. P. 129–188 DOI:10.1016/B978-0-08-098353-0.00004-X.

206. Wohlfarth E.P. Magnetic properties of single domain ferromagnetic particles // J. Magn. Magn. Mater. 1983. Vol. 39, № 1–2. P. 39–44 DOI:10.1016/0304-8853(83)90393-1.

207. Tournus F., Tamion A., Hillion A., Dupuis V. Anisotropy evolution of nanoparticles under annealing: Benefits of isothermal remanent magnetization simulation // J. Magn. Magn. Mater. 2016. Vol. 419. P. 1–4 DOI:10.1016/j.jmmm.2016.06.005.

208. Peddis D., Hudl M., Binns C., Fiorani D., Nordblad P. Aging experiments in a superspin glass system of Co particles in Mn matrix // J. Phys. Conf. Ser. 2010. Vol. 200, № SECTION 7 DOI:10.1088/1742-6596/200/7/072074.

209. De Toro J.A., Normile P.S., Lee S.S., Salazar D., Cheong J.L., Muñiz P., Riveiro J.M., Hillenkamp M., Tournus F., Tamion A., Nordblad P. Controlled Close-Packing of Ferrimagnetic Nanoparticles: An Assessment of the Role of Interparticle Superexchange Versus Dipolar Interactions // J. Phys. Chem. C. 2013. Vol. 117, № 19. P. 10213–10219 DOI:10.1021/jp402444x.

210. Néel L. Théorie du traînage magnétique des substances massives dans le domaine de Rayleigh // J. Phys. le Radium. 1950. Vol. 11, № 2. P. 49–61 DOI:10.1051/jphysrad:0195000110204900.

211. Martnez Huerta J.M., De La Torre Medina J., Piraux L., Encinas A. Self consistent measurement and removal of the dipolar interaction field in magnetic particle assemblies and the determination of their intrinsic switching field distribution // J. Appl. Phys. 2012. Vol. 111, № 8 DOI:10.1063/1.4704397.

212. He H.Y. Structural and Magnetic Property of Co1-xNixFe2O4 Nanoparticles Synthesized by Hydrothermal Method // Int. J. Appl. Ceram. Technol. 2013. Vol. 11, № 4. P. 1–11 DOI:10.1111/ijac.12071.

213. Downs R.T., Hall-Wallace M. The American Mineralogist crystal structure database // Am. Mineral. 2003. Vol. 88, № 1. P. 247–250.

214. Ryu B.H., Chang H.J., Choi Y.M., Kong K.J., Lee J.-O.O., Kim C.G., Jung H.-K.K., Byun J.-H.H. Preparation of Co1-xNixFe2O4 nanoparticles by coprecipitation method // Phys. Status Solidi Appl. Res. 2004. Vol. 201, № 8. P.

1855–1858 DOI:10.1002/pssa.200304669.

215. Geshev J., Viegas A.D.C., Schmidt J.E. Negative remanent magnetization of fine particles with competing cubic and uniaxial anisotropies // J. Appl. Phys. 1998. Vol. 84, № 3. P. 1488–1492 DOI:10.1063/1.368214.
216. Andersen H.L., Granados-Miralles C., Saura-Múzquiz M., Stingaciu M., Larsen J., Søndergaard-Pedersen F., Ahlburg J.V., Keller L., Frandsen C., Christensen M. Enhanced intrinsic saturation magnetization of Zn x Co 1-x Fe 2 O 4 nanocrystallites with metastable spinel inversion // Mater. Chem. Front. 2019. Vol. 3, № 4. P. 668–679 DOI:10.1039/c9qm00012g.
217. Tahar L. Ben, Basti H., Herbst F., Smiri L.S., Quisefit J.P., Yaacoub N., Grenèche J.M., Ammar S. Co 1-xZn xFe 2O 4 ($0 \leq x \leq 1$) nanocrystalline solid solution prepared by the polyol method: Characterization and magnetic properties // Mater. Res. Bull. 2012. Vol. 47, № 9. P. 2590–2598 DOI:10.1016/j.materresbull.2012.04.080.
218. Cobos M.A., de la Presa P., Llorente I., Alonso J.M., Garciá-Escorial A., Marín P., Hernando A., Jiménez J.A., García-Escorial A., Marín P., Hernando A., Jiménez J.A. Magnetic Phase Diagram of Nanostructured Zinc Ferrite as a Function of Inversion Degree Î // J. Phys. Chem. C. 2019. Vol. 123, № 28. P. 17472–17482 DOI:10.1021/acs.jpcc.9b02180.
219. Yaseneva P., Bowker M., Hutchings G. Structural and magnetic properties of Zn-substituted cobalt ferrites prepared by co-precipitation method // Phys. Chem. Chem. Phys. 2011. Vol. 13, № 41. P. 18609–18614 DOI:10.1039/c1cp21516g.
220. Apostolov A., Apostolova I., Wesselinowa J. Specific absorption rate in Zn-doted ferrites for self-controlled magnetic hyperthermia // Eur. Phys. J. B. 2019. Vol. 92, № 3 DOI:10.1140/epjb/e2019-90567-2.
221. Jovanović S., Spreitzer M., Tramšek M., Trontelj Z., Suvorov D. Effect of oleic acid concentration on the physicochemical properties of cobalt ferrite nanoparticles // J. Phys. Chem. C. 2014 DOI:10.1021/jp500578f.
222. Tadmor R., Rosensweig R.E., Frey J., Klein J. Resolving the puzzle of ferrofluid dispersants // Langmuir. 2000 DOI:10.1021/la0009137.

223. Ayyappan S., Philip J., Raj B. Effect of digestion time on size and magnetic properties of spinel CoFe2O4 nanoparticles // J. Phys. Chem. C. 2009 DOI:10.1021/jp8083875.

224. Mørup S., Hansen M.F., Frandsen C. 1.04 Magnetic Nanoparticles // Comprehensive Nanoscience and Nanotechnology. Elsevier, 2019. № June. P. 89–140 DOI:10.1016/B978-0-12-803581-8.11338-4.

225. Соболев А.В., Пресняков И.А. Магнетизм и основы мессбауэровской спектроскопии.Часть I. Природа эффекта Мессбауэра. Электрические сверхтонкие взаимодействия. Учебное пособие. Moscow: Отдел печати Химического факультета МГУ Москва, 2011.

226. Walker M., Mayo P.I., O'Grady K., Charles S.W., Chantrell R.W. The magnetic properties of single-domain particles with cubic anisotropy. I. Hysteresis loops // J. Phys. Condens. Matter. 1993. Vol. 5, № 17. P. 2779–2792 DOI:10.1088/0953-8984/5/17/012.

227. Coppola P., da Silva F.G., Gomide G., Paula F.L.O., Campos A.F.C., Perzynski R., Kern C., Depeyrot J., Aquino R. Hydrothermal synthesis of mixed zinc–cobalt ferrite nanoparticles: structural and magnetic properties // J. Nanoparticle Res. Springer Netherlands, 2016. Vol. 18, № 5. P. 1–15 DOI:10.1007/s11051-016-3430-1.

228. Batlle X., Pérez N., Guardia P., Iglesias O., Labarta A., Bartolomé F., Garca L.M., Bartolomé J., Roca A.G., Morales M.P., Serna C.J. Magnetic nanoparticles with bulklike properties (invited) // J. Appl. Phys. 2011. Vol. 109, № 7. P. 1–7 DOI:10.1063/1.3559504.

229. Anaconda Software Distribution. Computer software. Vers. 2-2.4.0. Anaconda [Electronic resource]. 2016. URL: https://anaconda.com.

230. Topkaya R., Baykal A., Demir A. Yafet-Kittel-type magnetic order in Zn-substituted cobalt ferrite nanoparticles with uniaxial anisotropy // J. Nanoparticle Res. 2013. Vol. 15, № 1 DOI:10.1007/s11051-012-1359-6.

231. Brice-Profeta S., Arrio M.A., Tronc E., Menguy N., Letard I., Cartier Dit Moulin C., Noguès M., Chanéac C., Jolivet J.P., Sainctavit P. Magnetic order in γ-Fe2O3

nanoparticles: A XMCD study // J. Magn. Magn. Mater. 2005. Vol. 288. P. 354–365 DOI:10.1016/j.jmmm.2004.09.120.

232. Peddis D., Yaacoub N., Ferretti M., Martinelli A., Piccaluga G., Musinu A., Cannas C., Navarra G., Greneche J.M., Fiorani D. Cationic distribution and spin canting in CoFe2O4 nanoparticles. // J. Phys. Condens. Matter. 2011. Vol. 23, № 42. P. 426004 DOI:10.1088/0953-8984/23/42/426004.

233. Coduri M., Masala P., Bianco L. Del, Spizzo F., Ceresoli D., Castellano C., Cappelli S., Oliva C., Checchia S., Allieta M., Szabo D.V., Schlabach S., Hagelstein M., Ferrero C., Scavini M. Local structure and magnetism of Fe2O3 maghemite nanocrystals: The role of crystal dimension // Nanomaterials. 2020. Vol. 10, № 5 DOI:10.3390/nano10050867.

234. Abdolrahimi M., Vasilakaki M., Slimani S., Ntallis N., Varvaro G., Laureti S., Meneghini C., Trohidou K.N., Fiorani D., Peddis D. Magnetism of Nanoparticles: Effect of the Organic Coating // Nanomaterials. 2021. Vol. 11, № 7. P. 1787 DOI:10.3390/nano11071787.

235. Batlle X., Moya C., Escoda-Torroella M., Iglesias Ò., Fraile Rodríguez A., Labarta A. Magnetic nanoparticles: From the nanostructure to the physical properties // J. Magn. Magn. Mater. 2022. Vol. 543, № May 2021. P. 168594 DOI:10.1016/j.jmmm.2021.168594.

236. Sartori K., Gailly D., Bouillet C., Grenèche J.M., Dueñas-Ramirez P., Begin-Colin S., Choueikani F., Pichon B.P. Increasing the size of Fe3-δO4 Nanoparticles by Performing a Multistep Seed-Mediated Growth Approach // Cryst. Growth Des. 2020. Vol. 20, № 3. P. 1572–1582 DOI:10.1021/acs.cgd.9b01300.

237. Linderoth S., Hendriksen P. V., Bødker F., Wells S., Davies K., Charles S.W., Mørup S. On spin-canting in maghemite particles // J. Appl. Phys. 1994. Vol. 75, № 10. P. 6583–6585 DOI:10.1063/1.356902.

238. Coey J.M.D.D. Noncollinear spin arrangement in ultrafine ferrimagnetic crystallites // Phys. Rev. Lett. American Physical Society, 1971. Vol. 27, № 17. P. 1140 DOI:10.1103/PhysRevLett.27.1140.

239. Fiorani D., Testa A.M., Lucari F., D’Orazio F., Romero H. Magnetic properties of maghemite nanoparticle systems: Surface anisotropy and interparticle interaction effects // Phys. B Condens. Matter. 2002. Vol. 320, № 1–4. P. 122–126 DOI:10.1016/S0921-4526(02)00659-2.
240. Thamm S., Hesse J. A simple plot indicating interactions between single-domain particles // J. Magn. Magn. Mater. 1996. Vol. 154, № 2. P. 254–262 DOI:10.1016/0304-8853(95)00585-4.
241. De Toro J.A., Vasilakaki M., Lee S.S., Andersson M.S., Normile P.S., Yaacoub N., Murray P., Sánchez E.H., Muñiz P., Peddis D., Mathieu R., Liu K., Geshev J., Trohidou K.N., Nogués J. Remanence plots as a probe of spin disorder in magnetic nanoparticles // Chem. Mater. 2017. Vol. 29, № 19. P. 8258–8268 DOI:10.1021/acs.chemmater.7b02522.
242. Khurshid H., Lampen-Kelley P., Iglesias Ò., Alonso J., Phan M.-H.H., Sun C.-J.J., Saboungi M.-L.L., Srikanth H. Spin-glass-like freezing of inner and outer surface layers in hollow γ-Fe2O3 nanoparticles // Sci. Rep. Nature Publishing Group, 2015. Vol. 5, № 500. P. 15054 DOI:10.1038/srep15054.
243. Del Bianco L., Spizzo F., Barucca G., Marangoni G., Sgarbossa P. Glassy magnetic behavior and correlation length in nanogranular Fe-oxide and Au/Fe-oxide samples // Materials (Basel). 2019. Vol. 12, № 23. P. 1–15 DOI:10.3390/ma12233958.
244. Vasilakaki M., Margaris G., Peddis D., Mathieu R., Yaacoub N., Fiorani D., Trohidou K. Monte Carlo study of the superspin glass behavior of interacting ultrasmall ferrimagnetic nanoparticles // Phys. Rev. B. American Physical Society, 2018. Vol. 97, № 9. P. 2–7 DOI:10.1103/PhysRevB.97.094413.
245. Hansen M.F., Mørup S. Models for the dynamics of interacting magnetic nanoparticles // J. Magn. Magn. Mater. 1998. Vol. 184, № 3. P. L262-274 DOI:10.1016/S0304-8853(97)01165-7.
246. Vasilakaki M., Trohidou K.N., Peddis D., Fiorani D., Mathieu R., Hudl M., Nordblad P., Binns C., Baker S. Memory effects on the magnetic behavior of assemblies of nanoparticles with ferromagnetic core/antiferromagnetic shell

morphology // Phys. Rev. B - Condens. Matter Mater. Phys. 2013. Vol. 88, № 14. P. 1–5 DOI:10.1103/PhysRevB.88.140402.

247. Nam D.N.H., Nordblad P., Mathieu R., Jo P., Jönsson P. Memory and superposition in a spin glass // Phys. Rev. B. American Physical Society, 2001. Vol. 63, № 9. P. 92401 DOI:10.1103/PhysRevB.63.092401.

248. Nogués J., Sort J., Langlais V., Skumryev V., Suriñach S., Muñoz J.S., Baró M.D. Exchange bias in nanostructures // Phys. Rep. 2005. Vol. 422, № 3. P. 65–117 DOI:10.1016/j.physrep.2005.08.004.

249. Ghoshani M., Sánchez E.H., Lee S.S., Singh G., Yaacoub N., Peddis D., Mozaffari M., Binns C., De Toro J.A., Normile P.S. On the detection of surface spin freezing in iron oxide nanoparticles and its long-term evolution under ambient oxidation // Nanotechnology. IOP Publishing, 2021. Vol. 32, № 6. P. 065704 DOI:10.1088/1361-6528/abc50a.

250. Binns C., Qureshi M.T., Peddis D., Baker S.H., Howes P.B., Boatwright A., Cavill S.A., Dhesi S.S., Lari L., Kröger R., Langridge S. Exchange bias in Fe@Cr core-shell nanoparticles // Nano Lett. 2013. Vol. 13, № 7. P. 3334–3339 DOI:10.1021/nl401587t.

251. Dormann J.L., Fiorani D., Tronc E., Chimie L. De, Matiere D., Pierre U., Jussieu P. Magnetic Relaxation in Fine-Particle Systems // Adv Chem Phys. New York: Wiley, 2007. Vol. 98. P. 283–494 DOI:10.1002/9780470141571.ch4.

252. Lavorato G.C., Peddis D., Lima E., Troiani H.E., Agostinelli E., Fiorani D., Zysler R.D., Winkler E.L. Magnetic Interactions and Energy Barrier Enhancement in Core/Shell Bimagnetic Nanoparticles // J. Phys. Chem. C. 2015. Vol. 119, № 27. P. 15755–15762 DOI:10.1021/acs.jpcc.5b04448.

253. Liu C., Zou B., Rondinone A.J., Zhang Z.J. Chemical Control of Superparamagnetic Properties of Magnesium and Cobalt Spinel Ferrite Nanoparticles through Atomic Level Magnetic Couplings // J. Am. Chem. Soc. 2000. Vol. 122, № 26. P. 6263–6267.

254. Rondinone A.J., Liu C., Zhang Z.J. Determination of Magnetic Anisotropy Distribution and Anisotropy Constant of Manganese Spinel Ferrite Nanoparticles

// J. Phys. Chem. B. 2001. Vol. 105. P. 7967–7971.

255. Calero-Diaz Del Castillo V.L., Rinaldi C. Effect of sample concentration on the determination of the anisotropy constant of magnetic nanoparticles // IEEE Trans. Magn. 2010. Vol. 46, № 3 PART 2. P. 852–859 DOI:10.1109/TMAG.2009.2032240.
256. Pacakova B., Kubickova S., Reznickova A., Niznansky D., Vejpravova J. Spinel Ferrite Nanoparticles: Correlation of Structure and Magnetism // Magnetic Spinels - Synthesis, Properties and Applications. InTech, 2017 DOI:10.5772/66074.
257. Sharifi I., Shokrollahi H., Doroodmand M.M., Safi R. Magnetic and structural studies on CoFe 2O 4 nanoparticles synthesized by co-precipitation, normal micelles and reverse micelles methods // J. Magn. Magn. Mater. Elsevier, 2012. Vol. 324, № 10. P. 1854–1861 DOI:10.1016/j.jmmm.2012.01.015.
258. Peddis D., Mansilla M. V., Mørup S., Cannas C., Musinu A., Piccaluga G., D’Orazio F., Lucari F., Fiorani D. Spin-Canting and Magnetic Anisotropy in Ultrasmall CoFe 2 O 4 Nanoparticles // J. Phys. Chem. B. 2008. Vol. 112, № 29. P. 8507–8513 DOI:10.1021/jp8016634.
259. Peddis D. Magnetic Properties of Spinel Ferrite Nanoparticles : Influence of the Magnetic Structure // Magnetic Nanoparticle Assemblies / ed. Kalliopi N. Trohidou. Singapore: Pan Stanford, 2014. Vol. 7. P. 159–198 DOI:10.4032/9789814411974.
260. Pérez N., Guardia P., Roca A.G., Morales M.P., Serna C.J., Iglesias O., Bartolomé F., García L.M., Batlle X., Labarta A. Surface anisotropy broadening of the energy barrier distribution in magnetic nanoparticles. // Nanotechnology. 2008. Vol. 19, № 47. P. 475704 DOI:10.1088/0957-4484/19/47/475704.
261. El-Hilo M., Bsoul I. Interaction effects on the coercivity and fluctuation field in granular powder magnetic systems // Phys. B Condens. Matter. 2007. Vol. 389, № 2. P. 311–316 DOI:10.1016/j.physb.2006.07.003.
262. Silva F.G. da, Depeyrot J., Campos A.F.C., Aquino R., Fiorani D., Peddis D. Structural and Magnetic Properties of Spinel Ferrite Nanoparticles // J. Nanosci.

Nanotechnol. 2019. Vol. 19, № 8. P. 4888–4902 DOI:10.1166/jnn.2019.16877.

263. Talone A., Ruggiero L., Slimani S., Imperatori P., Barucca G., Ricci M.A., Sodo A., Peddis D. Magnetic mesoporous silica nanostructures: investigation of magnetic properties // Nanotechnology. 2020. Vol. 31, № 46. P. 465707 DOI:10.1088/1361-6528/abac7c.
264. Manna P.K., Yusuf S.M. Two interface effects: Exchange bias and magnetic proximity // Phys. Rep. Elsevier B.V., 2014. Vol. 535, № 2. P. 61–99 DOI:10.1016/j.physrep.2013.10.002.
265. Gavrilov-Isaac V., Neveu S., Dupuis V., Taverna D., Gloter A., Cabuil V. Synthesis of trimagnetic multishell MnFe2O4@CoFe2O4@NiFe2O4 nanoparticles // Small. 2015. Vol. 11, № 22. P. 2614–2618 DOI:10.1002/smll.201402845.
266. Moskowitz B.M. Hitchhiker’s Guide to Magnetism // Environ. Magn. Work. 1991. Vol. 279, № 1. P. 48 DOI:10.1038/nm1005-1051.
267. Kechrakos D., Trohidou K. Magnetic properties of dipolar interacting single-domain particles // Phys. Rev. B. 1998. Vol. 58, № 18. P. 12169–12177 DOI:10.1103/PhysRevB.58.12169.
268. Kodama R.H., Makhlouf S.A., Berkowitz A.E. Finite Size Effects in Antiferromagnetic NiO Nanoparticles // Phys. Rev. Lett. 1997. Vol. 79, № 7. P. 1393–1396 DOI:10.1103/PhysRevLett.79.1393.
269. Walker M., Mayo P.I., O’Grady K.O., Charles S.W., Chantrell R.W. The magnetic properties of single-domain particles with cubic anisotropy. II. Remanence curves // J. Phys. Condens. Matter. 1993. Vol. 5, № 17. P. 2793–2808 DOI:10.1088/0953-8984/5/17/013.
270. Kelly P.E., O’Grady K., Mayo P.I., Chantrell R.W. Switching mechanisms in cobalt-phosphorus thin films // IEEE Transactions on Magnetics. IEEE, 1989. Vol. 25, № 5. P. HA5–HA5 DOI:10.1109/INTMAG.1989.690222.
271. Peddis D., Laureti S., Mansilla M. V., Agostinelli E., Varvaro G., Cannas C., Fiorani D. Exchange Bias in CoFe2O4/NiO nanocomposites // Superlattices Microstruct. Elsevier Ltd, 2009. Vol. 46, № 1–2. P. 125–129

DOI:10.1016/j.spmi.2008.10.042.

272. Wohlfarth E.P. The coefficient of magnetic viscosity // J. Phys. F Met. Phys. 1984. Vol. 14, № 8. P. L155–L159 DOI:10.1088/0305-4608/14/8/005.
273. McDonagh B.H., Singh G., Hak S., Bandyopadhyay S., Augestad I.L., Peddis D., Sandvig I., Sandvig A., Glomm W.R. L-DOPA-Coated Manganese Oxide Nanoparticles as Dual MRI Contrast Agents and Drug-Delivery Vehicles // Small. 2016. Vol. 12, № 3. P. 301–306 DOI:10.1002/smll.201502545.
274. Yin Y., Rioux R.M., Erdonmez C.K., Hughes S., Somorjai G., Alivisatos A.P. Formation of hollow nanocrystals through the nanoscale Kirkendall effect. // Science. 2004. Vol. 304, № April. P. 711–714 DOI:10.1126/science.1096566.
275. Yin Y., Erdonmez C.K., Cabot A., Hughes S., Alivisatos A.P. Colloidal synthesis of hollow cobalt sulfide nanocrystals // Adv. Funct. Mater. 2006. Vol. 16, № 11. P. 1389–1399 DOI:10.1002/adfm.200600256.
276. An K., Kwon S.G., Park M., Na H. Bin, Baik S.I., Yu J.H., Kim D., Son J.S., Kim Y.W., Song I.C., Moon W.K., Park H.M., Hyeon T. Synthesis of uniform hollow oxide nanoparticles through nanoscale acid etching // Nano Lett. 2008. Vol. 8, № 12. P. 4252–4258 DOI:10.1021/nl8019467.